

University of Southampton Research Repository

Copyright © and Moral Rights for this thesis and, where applicable, any accompanying data are retained by the author and/or other copyright owners. A copy can be downloaded for personal non-commercial research or study, without prior permission or charge. This thesis and the accompanying data cannot be reproduced or quoted extensively from without first obtaining permission in writing from the copyright holder/s. The content of the thesis and accompanying research data (where applicable) must not be changed in any way or sold commercially in any format or medium without the formal permission of the copyright holder/s.

When referring to this thesis and any accompanying data, full bibliographic details must be given, e.g.

Thesis: Author (Year of Submission) "Full thesis title", University of Southampton, name of the University Faculty or School or Department, PhD Thesis, pagination.

Data: Author (Year) Title. URI [dataset]

UNIVERSITY OF SOUTHAMPTON

On Convection and Stability of some Welding and Solidification
Processes

Author: Michael Anthony Sharpe

For Doctor of Philosophy

Faculty of Mathematical Studies

June 2000

Trust in the LORD with all your heart
and lean not on your own understanding;
in all you ways acknowledge Him and He will make your paths
straight.

Proverbs 3:5,6.

Every journey has an end,
when at the worst affairs will mend,
dark the dawn when day in nigh,
hustle your horse and don't say die!

Iolanthe, W.S. Gilbert.

UNIVERSITY OF SOUTHAMPTON

ABSTRACT

FACULTY OF MATHEMATICAL STUDIES

Doctor of Philosophy

ON CONVECTION AND STABILITY OF SOME WELDING AND SOLIDIFICATION
PROCESSES

by Michael Anthony Sharpe

In this thesis a variety of problems are considered, the first of which is associated with the welding process. Experiments indicate that the shape of a weld pool is influenced by convection in the liquid metal. In recent years it has been shown that this convection is crucially affected by the Marangoni (or thermocapillary) force. Recently Craine and Belgrove ([30], [7]) have developed a two-dimensional, axisymmetric model which includes the Marangoni force on the free surface of a semi-infinite region of liquid steel when a point source of current and heat is incident on the free surface. An asymptotic solution to this problem is obtained in this thesis, and the surface tension gradient with respect to temperature, $\partial\gamma/\partial T$, a parameter which is crucial to the magnitude of the Marangoni force, is found to affect every coefficient in the leading and first order asymptotic expansions. In various theoretical and experimental models purely poloidal flow bifurcates to a rotating flow. To investigate this possibility for our flow a linear stability analysis is performed on a numerically obtained poloidal solution for the flow and temperature distribution in a hemisphere (a model first derived in [7]). For the azimuthal stability mode $m = 0$ the equation governing the linear stability of the rotating motion is found to decouple from the corresponding poloidal equations. The poloidal and azimuthal stability equations both become unstable at different critical currents dependent on the sign and magnitude of $\partial\gamma/\partial T$. An investigation of the eigenvectors indicates the onset of instability near to the point source. For the upper modes instability occurs only when $m = 1$ and in a very small region of parameter space.

In the second part of this thesis a freezing sphere problem with flow is used to compare a sharp interface Stefan model and a diffuse interface phase-field model. Firstly a Stefan model that includes a disparity between the density of the solid and liquid phases is derived and solved numerically. This model is compared with a recent phase-field model with flow, derived by Anderson *et al.* in [2]. In this thesis the one-dimensional isotropic version of Anderson's model is obtained in spherical polar coordinates and using certain simplifications when the dimensionless thickness of the interface ε_S is vanishingly small a leading order asymptotic expression reproduces the Stefan model with flow. The phase-field model is subsequently modified and solved numerically, and the results are compared with the sharp interface model. Close agreement is observed between these models when $\varepsilon_S \leq 0.01$.

Contents

1	Introduction to chapters 1 to 5 : Welding models	1
2	Asymptotic analysis of a semi-infinite flow model with large negative surface tension gradient	17
2.1	Introduction	17
2.2	Numerical model	22
2.2.1	Method of numerical solution	25
2.3	Discussion	25
2.4	Asymptotic model	27
2.4.1	Main fluid region	28
2.4.2	Free surface shear layer	33
2.4.3	Matching	36
2.5	Method of solution	40
2.6	Results and discussion	42
3	Steady state solution in a hemisphere	49
3.1	Introduction	49
3.2	The differential equations	50
3.3	Boundary conditions	53
3.4	Finite differences	54
3.5	Results	56
4	Linear stability analysis	62
4.1	Introduction	62
4.2	Derivation of linear system of equations	63
4.3	Boundary conditions	70
4.3.1	Origin ($\lambda = 0$)	70

4.3.2	Outer hemisphere ($\lambda = 1$)	71
4.3.3	Axis of symmetry ($\eta = 0$)	72
4.3.4	Free surface ($\eta = 1$)	74
4.3.5	Corners	75
4.3.6	Problem statement	76
4.4	Finite differences	77
4.4.1	Azimuthal system	83
4.4.2	Poloidal system	87
4.5	Method of solution	92
4.6	Results and discussion	95
4.6.1	Azimuthal stability problem	95
4.6.2	Poloidal system	100
5	Higher modes of stability	107
5.1	Introduction	107
5.2	Derivation of linear system of equations for the azimuthal modes $m \neq 0$. . .	108
5.3	Boundary conditions	112
5.3.1	Point source ($\lambda = 0$)	112
5.3.2	Outer hemisphere ($\lambda = 1$)	112
5.3.3	Axis of symmetry ($\eta = 0$)	113
5.3.4	Free surface ($\eta = 1$)	113
5.3.5	Woods boundary condition on $\lambda = 1$	113
5.3.6	Finite difference scheme	116
5.3.7	Method of solution	116
5.4	Results and discussion	117
6	Introduction to chapters 6 to 10 : Solidification models	119
7	Sharp interface Stefan model with flow	134
7.1	Introduction	134
7.2	Derivation	134
7.2.1	Liquid phase	134
7.2.2	Solid phase	135
7.2.3	Interfacial boundary conditions	136
7.3	Non-dimensionalisation	138

7.4	Tracking of the interface	140
7.5	Finite differences	141
7.6	Boundary conditions	143
7.7	Method of solution	143
7.8	Results and discussion	145
8	Sharp interface limit of the phase-field equations due to Anderson, McFadden and Wheeler	156
8.1	Introduction	156
8.2	Asymptotic limit of phase-field equations without flow	157
8.2.1	Non-dimensionalisations	160
8.2.2	Perturbation expansion	161
8.2.3	Outer expansion	162
8.2.4	Inner expansion	163
8.2.5	Matching	164
8.3	Asymptotic limit of phase-field equations with flow	168
8.3.1	Perturbation expansion	171
8.3.2	Scaling of the pressure and viscosities	173
8.3.3	Outer expansion	174
8.3.4	Inner expansion	176
8.3.5	Problem statement	184
9	Numerical results	186
9.1	Introduction	186
9.2	Phase-field equations without flow	186
9.2.1	Finite differences	188
9.2.2	Boundary conditions	189
9.2.3	Solution method	190
9.2.4	Results and discussion	192
9.3	Phase-field equations with flow	195
9.3.1	Finite differences	196
9.3.2	Boundary conditions	198
9.3.3	Solution method	198
9.3.4	Results and discussion	199

10 Conclusions	205
A Outer and inner asymptotic expansions of the phase-field equations with flow	210
A.1 Outer expansion	210
A.2 Inner expansion	212
B Derivation and asymptotic expansion of Clausius-Clapeyron relation	216
B.1 Derivation of Clausius-Clapeyron equation from phase-field equation	216
B.2 Expansion of Clausius-Clapeyron equation in Δ/ρ_s	222

Acknowledgements

I would like to thank my supervisors R.E. Craine and A.A. Wheeler for their help, support and encouragement throughout my period of study. First and foremost however I must thank my God and saviour Jesus Christ without whom I would not have been able to work at all. His presence and support have been invaluable to me, especially during the difficult times. I would also especially like to thank my parents for their support and prayers on my behalf. Other friends who have supported and encouraged me throughout my time here include Vincent Ooi, Dave Morrish, Ian and Sue Edwards, John and Cherry Balchin and all those with whom I have had the pleasure of sharing an office. There are many more people whose support has been of great benefit, their names I will not list here but I would like to say thankyou to all of you. I would also like to take this opportunity to thank E.P.S.R.C. for their supporting grant and C.P. Please for some helpful suggestions.

Chapter 1

Introduction to chapters 1 to 5 : Welding models

In the first five chapters of this thesis problems associated with the welding process are considered. Welding is a commonly used industrial process which joins together pieces of material, usually metal. Fusion welding is a process which fuses together pieces of material by melting their adjoining surfaces and, therefore, it requires a strong heat source to create a liquid weld pool. Common heat sources include chemical flames, electric arcs, electron beams and laser beams.

Carbon arc welding was first patented in 1885 by Bernardos and Olezewski. An electric arc is formed between a carbon electrode and a work piece which acts as an anode. The arc welding process was later augmented by various technical improvements, one of the most significant was the addition of an inert gas shield to prevent contamination of the weld by exposure to the atmosphere, since it was found that absorption of atmospheric nitrogen created brittle welds. An overview of electric arc welding can be found in [64] and general reviews of arc welding, which include engineering arc physics applications, can be found in [49] and [48]. A recent review by Kannatey-Asibu [58] summarises key developments in the field and includes an extensive literature review of welding processes.

There are many different welding processes in current use, the most important are listed below.

- Submerged Arc Welding (SAW) uses either an alternating (ac) or a direct (dc) current. In this process the arc is maintained in a cavity of molten flux formed from a granular material. SAW is suitable for automatic welding.
- Shielded Metal Arc Welding (SMAW) uses either ac or dc and during manual operation short lengths of flux coated wire are fed into the weld pool. SMAW is used in all

engineering fields.

- Gas Metal Arc Welding (GMAW), or an equivalent process known as Magnesium Inert Gas Welding (MIGW), uses flux which is enclosed in a tubular electrode of small diameter. The flux is protected by a gas shield and continuously fed through a gun. Both GMAW and MIGW are used in general welding purposes.
- Pulsed Gas Tungsten Arc Welding (GTAW), or an equivalent process known as Tungsten Inert Gas Welding (TIGW), uses an arc which is maintained between a non-consumable tungsten anode and the workpiece. The high frequency pulse of inert gas improves the stiffness of the arc. The GTAW and TIGW processes are used in all engineering fields.
- Electron Beam Welding (EBW) is an automatic welding process in a vacuum in which a cathode emits a beam of electrons and no metal transfer occurs. The EBW process is commonly used in the nuclear and aerospace industries.
- Laser Beam Welding (LBW), apart from the different energy source, is essentially the same as EBW. In addition to the uses listed for EBW, however, LBW is also used for cutting non-metallic materials.

Older welding processes, such as SAW and SMAW, are difficult to observe. However, welding physics has advanced greatly over the years and the newer processes, such as GMAW and TIGW, are easier to view.

To develop a mathematical model of the welding process the relative importance of heat conduction and convection must be assessed. Intuitively one might expect heat conduction to be the most important. However, when arc-welding steel the value of the Peclet number¹, $P_e = \rho\nu Lc_p/\kappa$, which measures the relative importance of convection compared with conduction, can range from about 10 to over 1000. Therefore, for TIGW of steel (and, for that matter, many other metals) convection rather than conduction will usually determine the temperature distribution and, consequently, the size and shape of the weld pool. Furthermore, the Reynolds number for TIGW is usually approximately $100A$ and, therefore, the flow is likely to be laminar. To accurately model the welding process a description of the laminar fluid motion is required. To achieve this the forces acting on the liquid must be included.

In the arc welding process the motion inside the weld pool can be caused by the following forces:

- a Lorentz (electromagnetic) force created by the interaction between the applied electric current and its self-induced magnetic field or, occasionally, with an applied magnetic field;

¹Here ρ represents density, ν the viscosity, L a typical length scale, c_p the specific heat at constant pressure and κ the thermal conductivity.

- a buoyancy force due to internal temperature differences causing changes in the density of the molten metal;
- a Marangoni, or thermocapillary, (surface tension) force on the free surface due to the variation of surface tension with temperature;
- a plasma jet force, caused by the jet of inert gas flowing over the free surface of the pool.

Schematic diagrams in which the forces act are displayed in figure 1.1. Clearly all these forces

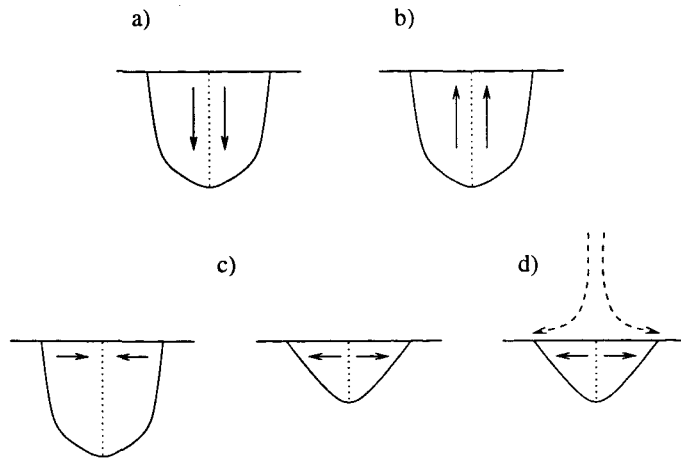


Figure 1.1: Forces in the weld pool: (a) Lorentz (electromagnetic) force caused by the current and the self-induced magnetic field, (b) Buoyancy force due to temperature distribution, (c) Marangoni (thermocapillary) force on the free surface which can cause inward or outward flow on the free surface, (d) Plasma jet force over the surface of the weld pool. A figure similar to this is used in [77].

do not have a significant effect on the fluid motion and for non-arc welding processes (such as EBW and LBW for example) the Lorentz and plasma jet forces do not arise.

In the 1940's the first attempt was made to model the welding process by considering a point source of heat traversing the surface of a semi-infinite block of stationary material [92]. There have been many extensions to this work which exclude material motion. However, experimental results of Woods and Milner [136] indicated that there is motion inside the liquid metal pool formed beneath a tungsten welding arc, primarily caused by the action of the Lorentz force. By examining the mixing of dissimilar metal droplets in the pool these authors found that a symmetrical current path produced a double circulation in the weld pool, but pure rotation was obtained when the current flow was markedly asymmetric. Further, they discovered that materials such as iron and steel produced more rapid motion and this was attributed to the high melting points of these materials. It was also noticed

that the speeds in the weld pool increased with the square of the current. Mills also showed experimentally, see [76], that the shape of the weld pool in GTAW is primarily influenced by the flow patterns in the liquid metal. Using an electric arc which stayed constant, he found that the depth to width ratio of a weld pool could vary by up to 80%, thereby confirming the prediction obtained from evaluating the range of values for Pe , namely that convection rather than conduction will usually determine the size and shape of the weld pool.

Models of arc welding which include fluid motion but consider the simpler case of a semi-infinite region of fluid have been developed by many authors (e.g. Lundquist [73], Sozou *et al.* [110], [111], [112], [113], and [114], Shercliff [99], Bojarevics [9], [10] and [12], Lancaster [65], Belgrove [7]), because of their relative simplicity when compared with models which consider a finite region of fluid. Maecker [74] made initial progress on this problem by performing an approximate analysis, assuming uniform applied current density and a semi-infinite, incompressible, isothermal, electrically conducting, inviscid fluid (IIEI fluid). Lundquist [73] obtained steady solutions to the flow of a semi-infinite viscous (IIEV) fluid due to a point source of current at the free surface by ignoring the inertia forces. Shercliff [99] considered an IIEI fluid using a point source of current, and included convection due to the Lorentz force. He observed that the solution to this model was related to an exact solution of the Navier-Stokes equations for a jet flow initiated by a point source of momentum in an infinite uniform fluid [118]. However, Shercliff's axi-symmetric model produced singularities in the velocity field along the axis of symmetry for all values of the imposed current.

Sozou [110] extended Shercliff's model to include viscosity (considering a IIEV fluid) and obtained a similarity solution for the non-linear, steady-state problem, by assuming that the velocity field was small and, therefore, its effect on the electromagnetic field was negligible. At very low applied currents the addition of viscosity prevented the development of axial singularities. However, on increasing the current an axial jet developed in the fluid, leading to velocity singularities on the axis of symmetry when the Sozou parameter, K , reached a critical value K_{crit} . When the plane boundary is a wall $K_{crit} = 300.1$ which, for steel, corresponds to a critical current, J_{crit} , of approximately $3.7A$. On the other hand when the plane boundary is a free surface $K_{crit} = 94.1$, which corresponds to a critical current, J_{crit} , of approximately $2.06A$ for steel. The parameter K , later called *the parameter of electrically induced vortex flow* [13], is defined by

$$K = \frac{\mu_0 J_0^2}{2\pi^2 \rho \nu^2}, \quad (1.1)$$

where μ_0 is the permeability of free space, J_0 the total applied electric current, ρ the density and ν the kinematic viscosity of the fluid.

In [114] Sozou and English relaxed the 'small velocity field' assumption in [110] by allowing the velocity to affect the electromagnetic field in a IIEV fluid. Their numerical results indicate that the inclusion of induced currents increases the range of K in which a solution exists.

However, the breakdown in the solution was not eliminated by the inclusion of this effect and, furthermore, the increase in K_{crit} (and thereby J_{crit}) is extremely small when realistic material parameter values are used. To address the discrepancy between the large values of K observed in experiments and the small values of K_{crit} obtained in the earlier models, Sozou [113] investigated the effect on the flow field of using a current distribution comprising partly of a circular cylindrical column of current and partly of a current radiating from a point on the surface of an IIEV fluid which occupied a conical region, and then a semi-infinite region. He found that the value of the critical breakdown current J_{crit} could be significantly increased by using this type of current distribution. He also pointed out the inadequate geometry of the semi-infinite model when comparing with experimental results (such as those obtained in [136]). Sozou and Pickering [115] considered the unsteady semi-infinite problem of [110] to study the streamlines of the developing flow field in an IIEV fluid. They discovered that these streamlines were closed loops around a stagnation point which moves away from the point source to infinity at a speed proportional to $t^{-1/2}$, the inverse square root of the time variable. These authors also determined that within a radius r of the point source a steady state value for the non-dimensional streamfunction was established within a time $t = r^2/\nu$, where ν is the coefficient of kinematic viscosity.

In [13] Bojarevics *et al.* discussed in detail a paper by Bojarevics [9], in which the viscous forces in the region of the jet are increased by including a narrow rigid cone centred on the axis of symmetry, to represent a submerged conical electrode in an IIEV fluid. The breakdown in the steady-state solution at low currents, which was encountered by Sozou [110], was avoided by applying the no-slip condition on this new conical electrode, and solutions were obtained up to an unspecified maximum value of K in excess of 8000. Bojarevics also considered the inverse, but geometrically identical case, where the electric current was supplied to the point source on the plane surface of the liquid (which was either a rigid wall or a free surface) from the axial cone. This second situation is displayed in figure 1.2, where the direction of current flow is labelled ‘reversed current J ’. In this figure the angle θ is measured from the axis of symmetry ($\theta = 0$) to the free surface ($\theta = \pi/2$). Bojarevics was able to obtain a numerical solution for the diverging flow described by this model for any large value of K and, furthermore, in [10] he constructs an asymptotic solution for this model for large K .

The use of a semi-infinite geometry is a severe simplification in the theoretical models described above, as observed by Sozou and English [113]. When a finite region of fluid is considered, however, a similarity solution is no longer possible and the resulting system of equations must be solved numerically.

Sozou and Pickering [116] extended the earlier work of Sozou [110] by considering only a hemispherical region of fluid, with the imposed current source placed at the centre of the hemisphere’s surface. A steady-state similarity solution, similar to that obtained by

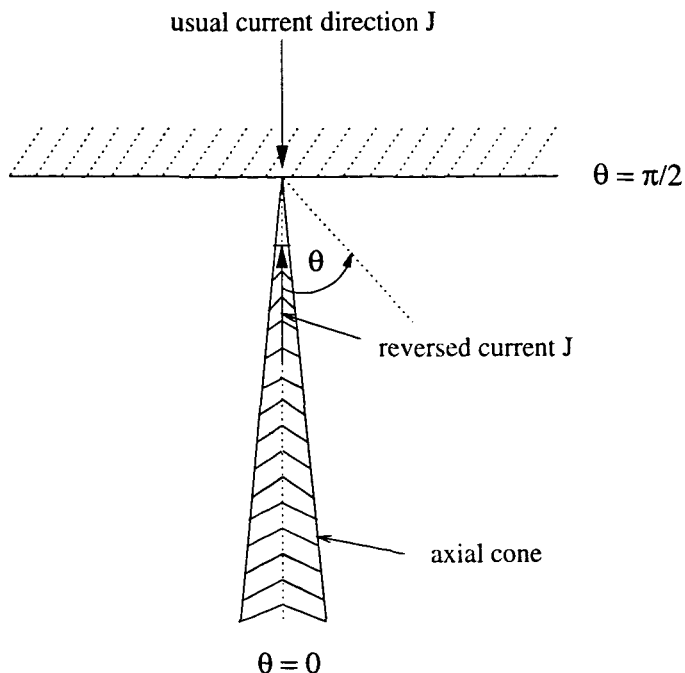


Figure 1.2: Current flows with an axial cone, the regime used in [9], [10] and [13]

Sozou [110], was no longer possible, but a numerical solution to the governing equations was found. However, the numerical method the authors used in [116] did not produce solutions at currents close to the value of K_{crit} obtained in the earlier semi-infinite model ([110]), due to large velocity gradients occurring in the axial region near the spherical surface.

Rosenthal's [92] early steady-state model in a semi-infinite medium, which considers a travelling point source of heat, ignores both convective and radiative heat flow and uses average material properties, was extended by Eagar and Tsai [39] to include a distributed Gaussian heat distribution. These authors claimed that their model was capable of explaining most of the experimental scatter observed in practical investigations. Many other authors have also extended the work of Sozou and Pickering to consider different current inputs at the free surface. Andrews and Craine [4] considered the flow in a hemisphere of IIEV fluid for small currents (i.e. ignoring the non-linear inertia terms in the Navier-Stokes equations) due to various distributed current sources across the plane surface ($\theta = \pi/2$) of the hemisphere. More specifically they considered a point source placed a distance a above the plane surface and a ring sink of radius b centred on the axis of symmetry below this surface. The authors found that varying the current distributions produced qualitatively different flow patterns. Atthey [5] considered the situation where a metallic plate of constant thickness contained a hemispherical pool of IIEV liquid metal of a smaller radius. A Gaussian current distribution, which approximates the real current distribution in an arc, was then applied on the free surface of the pool and drawn off at the periphery of the metallic plate. The numerical

procedure adopted by Atthey was convergent for very large values of K ($\sim 10^5$) and the intensity of the flow was observed to fall off as the thickness of the plate was increased. Results were obtained for a number of different plate thicknesses and pool radii.

Another prescribed pool shape which has been investigated by some authors is that of an oblate spheroid. In [117] Sozou and Pickering considered the case where current is discharged from a circular electrode which is at the centre of the free surface ($\theta = \pi/2$) of such a spheroid of IIEV fluid. They introduced a similar assumption to Andrews and Craine [4], that the velocities are small, and so ignored the non-linear inertial term in the Navier-Stokes equation. The non-linear problem, which includes the inertia term, was considered later by Ajayi, Sozou and Pickering [1]. By increasing the size of the area through which the current was discharged the velocities in the spheroid considered in [1] were observed to vary.

All the theoretical models described so far have only accounted for the Lorentz force and ignored the plasma jet, buoyancy and Marangoni forces. The experimental evidence of Lin and Eagar [71] for example, indicates that overlooking the plasma jet force is not an important oversight. At current values over 300A, however, the authors observed from the experiments that the surface of a weld pool of stainless steel becomes markedly depressed, although the analytical results in [71] indicated that arc pressure only influences the weld pool geometry when the current exceeds 500A. Therefore, the pressure of the arc cannot account for the change in the shape of the free surface for currents of approximately 300A. Instead the change was attributed to circumferential convection within the pool, and the authors argued in [71] that the effect of surface tension on the surface depression was unimportant. The size of the depression in the surface of the pool at a current of 240A is very small, but in [91] Rokhlin stated that between current values of 240A and 300A the depression in the surface of the pool increased by more than five times. Clearly the plasma jet force is not important in many theoretical models, especially those which model the welding arc as a point source since these models cannot obtain solutions at large values of the imposed current. In addition, by neglecting the buoyancy and Marangoni forces these models also, in effect, assume that the pool of liquid metal is isothermal. However, although a theoretical argument can be made for excluding the buoyancy force, it has been shown that the Marangoni force is far from insignificant.

Heiple and Roper [51] studied the effect of adding surface active elements (sulphur and selenium) to iron and stainless steel and showed that the surface tension forces in molten iron can be significantly changed by introducing 40-60ppm (parts per million) of sulphur, oxygen or selenium. The surface tension gradient with respect to temperature ($\partial\gamma/\partial T$) for molten iron is usually negative, in which case the Marangoni force, if it dominates the others, causes the molten metal to flow outwards from the source on the free surface, producing wide shallow welds. However, upon introducing the aforementioned trace elements a positive

surface tension gradient is produced suggesting inward flow towards the source and deeper pools. Later, Zacharia *et al.* [141] showed that fluid motion in the weld pool is further influenced by the temperature distribution on the surface of the pool. Values of the surface tension as a function of temperature were determined experimentally by Keene *et al.* [59] for four different transition metals, namely gold, cobalt, iron and nickel, and type 316 stainless steel. During TIGW this latter type of steel is known to portray different weld penetrations when the constituent parts of each sample are apparently identical. The results in [59] indicated that the differences between the weld-ability of different samples of steel 316 could be related to the surface properties of the melts caused by the presence, or otherwise, of small amounts of surface active elements. For samples of type 316 steel with large and small depth to width ratios (thereby exhibiting good and poor weld-abilities respectively) Keene *et al.* measured $\partial\gamma/\partial T$ to be $8 \times 10^{-5} Nm^{-1}K^{-1}$ and $-3 \times 10^{-4} Nm^{-1}K^{-1}$ respectively. These experiments indicate the crucial role often played by the surface tension forces.

The effect of the Marangoni (also known as the thermocapillary) surface force on fluid flow in the weld pool has been the subject of much experimental investigation since the paper of Heiple and Roper [51]. Consequently some of the recent papers concerning this subject will be outlined below.

In [77] Mills *et al.* discussed recent developments in Marangoni effects associated with welding. These authors concluded that weld penetration in steel using GTAW, TIGW, EBW and LBW techniques is determined by the direction and magnitude of the fluid flow in the weld pool. This flow is, in turn, controlled by the thermocapillary (Marangoni) forces which are dependent on the sulphur content in the sample of steel. The authors also discussed the effects of arc wander and other surface properties. In [100] Shirali and Mills considered the effect on the weld pool of changing various welding parameters such as current, speed, arc-length and electrode geometry. In [100] the authors confirm the proposition of Heiple and Burgardt [15], namely that any increase in the temperature gradient increases both the magnitude of the thermocapillary force and the weld penetration in a high sulphur sample of steel, but decreases the weld penetration in a low sulphur sample. Shirali and Mills also showed that increasing the arc length decreases the weld penetration, but increasing the energy of the arc increases the weld penetration. Motivated by the use of thin walled tubes in the chemical and nuclear industries, Scheller *et al.* [96] considered the influence that the sulphur content has upon thin strips of stainless steel. They confirmed that increasing the content of sulphur, or the linear energy, increases the weld penetration in thin strips of material, thereby allowing a faster welding speed. However, they observed that this advantage is offset by the inferior workability and corrosion resistance of high sulphur steel, which is of course an important consideration in the chemical and nuclear industries. Ishizaki *et al.* [57] performed various experiments to study the convection in molten hemispherical and cylindrical pools

of liquid mercury. In [57] the authors investigated the effects of other forces by applying a hot rod or a jet of hot dry air or ether saturated vapour at room temperature to the centre of the free surface of a hemispherical pool of water in a block of ice. Using these methods the authors demonstrated that a variety of different flow patterns were possible, including inward, outward and more complicated flow patterns. They found that the Marangoni force and its associated surface tension gradient, rather than the shear stress from the air flow, governed the direction of the flow.

To investigate how the presence of the gas tungsten arc affects the welding process, in addition to the effects of normal heat conduction and fluid flow, Pierce *et al.* [84] compared the GTAW method with the non-arc EBW method using two different samples of stainless steel, one containing a high sulphur concentration and the other a low sulphur concentration. These authors found that the GTA and EB welds were both qualitatively similar, demonstrating that Marangoni (thermocapillary) flow and normal convection are the dominant factors in the weld pool. However, they observed growing differences between the two sets of results as the arc power was increased. This effect they attributed to gas motion in the arc plasma, an effect which is not present in EBW.

In [56] Hsieh *et al.* examined the effect of minor surface active elements and the electrode shielding gas on the penetration of stainless steel during TIGW. These authors also found that traces of sulphur or oxygen increased the depth to width ratio of the weld, whereas increasing the aluminium content of the base metal produced the opposite effect since aluminium, which is not a surface active element, is a strong de-oxidant. They also observed that the addition of 1% oxygen or 5% hydrogen to the shielding gas significantly increased the depth to width ratio.

Lee *et al.* [67] considered the effect of a thermocapillary (Marangoni) flow in the EBW process, showing both experimentally and theoretically that this force dominates the fluid flow. Using a dimensionless relationship between heat and mass transfer in the weld pool, Murray *et al.* [78] obtained an analytical expression for the depth of the weld pool in GMAW and compared these results with the experimental evidence.

Over the years since Heiple and Roper's pioneering work there have been various theoretical models which incorporate a surface Marangoni force.

One of the first theoretical models to include the independent contribution of surface tension to the flow of an incompressible, thermally and electrically conducting, inviscid fluid (ITEV fluid) in a weld pool was proposed by the Japanese researchers Yokoya and Matsunawa [138], using material parameters for iron. Using a numerical approach they investigated the effects caused by a non-zero surface tension gradient on the fluid motion in a semicylindrical basin of liquid metal in which current and heat is supplied by a semi-cylindrical submerged electrode on the axis of symmetry. The authors concluded that the Marangoni force on the

free surface has a significant effect on convection and temperature distribution within the pool.

Another early calculation which incorporated the Marangoni effect was due to Oreper and Szekely [79], who used a distributed source of current and heat on the free surface of a ITEV fluid and solved the unsteady temperature and heat phase-change problem using the material properties of steel. Since that work various other models incorporating the thermocapillary free surface force have been developed, see for example Matsunawa *et al.* [75], Zacharia [140], Ravindran *et al.* [86], and, very recently, Priede, Cramer and Bojarevics *et al.* [85] and Chung and Wei [27].

Matsunawa *et al.* [75] developed an unsteady numerical model for heat and mass transfer in a growing pool of ITEV fluid. The authors included Lorentz, Marangoni and buoyancy forces and also an aerodynamic free surface shear force, comparing the individual and combined contribution of these forces to the penetration shape. In addition these authors considered the effect of using different arc lengths, obtaining a two-loop flow structure² when the arc length was comparatively short. (An experimental study of electrode geometry and arc length in TIGW can be found in [53].) Matsunawa *et al.* also observed that the fastest flow speeds were caused by the surface forces (i.e. Marangoni and aerodynamic drag) and that high heat and current density cause deep penetration, whereas a shallow pool occurs when the heat and current density is lower.

In [65] Lancaster proposed a model which extended the steady-state, semi-infinite model of Sozou [110] to an ITEV fluid by including the Marangoni force on the free surface caused by a superimposed prescribed spherically symmetric temperature distribution.

In [140] Zacharia *et al.* outlined a finite difference model for a stationary welding torch in GTAW and LBW. These authors considered the unsteady case, in which the position of the solid/liquid interface is determined by the energy equation. In their model the surface tension gradient is expressed as a function of both the surface temperature and the amount of surface active element present, and the heat source is approximated by a Gaussian distribution. Their model confirmed that in GTAW the heat transfer and depth to width ratio of the weld pool are determined by convection in the liquid pool. To avoid the deleterious effect on the properties of the weld due to the addition of sulphur, Zacharia *et al.* suggested an alternative, namely that the advantage of a narrower, deeper weld pool which is obtained from a uniformly positive value for $\partial\gamma/\partial T$ could be achieved by increasing the surface temperature. In [141] Zacharia *et al.* compared the size and shape of the fusion zone position predicted by the numerical model in [140] with the corresponding results emanating from experiments on type 304 stainless steel, obtaining excellent agreement for both the GTAW and LBW processes.

²The different types of flow structure which are observed in both experimental and theoretical models are discussed in more detail in the introduction to chapter 2.

Ravindran *et al.* [86] used the Galerkin finite element solution method in a model describing the stationary, steady-state LBW process for an ITEV fluid. The position of the solid-liquid interface was determined from the conservation of energy equation, and the heat source was approximated as a beam of finite radius on the free (flat) surface, on which various constant values for the surface tension gradient were applied. This model showed that on the free surface the buoyancy force is much smaller than the thermocapillary force, and the latter totally dominates the flow patterns in the absence of a magnetic field. (In the LBW process the magnetic field is absent, so there is no Lorentz force acting).

Belgrove and Craine ([7], [30]) extended the model of Lancaster in [65] by assuming that the arc was represented by a point source of current and heat, and then solved Sozou's problem together with the coupled temperature equation, including the Marangoni force on the free surface. Since it has been shown both theoretically [138] and experimentally [77] that the presence of small quantities of surfactants in a molten metal causes large changes in the value of the surface tension gradient with respect to temperature, $\partial\gamma/\partial T$, it is not surprising that the introduction in [7] of thermal terms and a Marangoni force into Sozou's problem significantly affects the current at which breakdown occurs. Belgrove and Craine found that a negative surface tension gradient gives rise to a Marangoni force which opposes the Lorentz force, and consequently the development of axial singularities, and hence K_{crit} increases as the magnitude of the negative surface tension is increased. On the other hand, when the surface tension gradient is positive the corresponding Marangoni force reinforces the Lorentz force and K_{crit} is reduced below the value obtained by Sozou in [110].

The numerical solutions found by Belgrove [7] for the steady flow induced by a stationary point source of current and heat on the free surface of a semi-infinite expanse of ITEV fluid, due to the presence of Lorentz and Marangoni forces, are very useful. These numerical results indicate the existence of solutions, for an applied point source for currents up to 60A (and, therefore, large values of K) and for large negative surface tension gradients, using the appropriate parameter values of liquid steel. The use of the phrase 'large negative surface tension gradient' may be misleading in this context, since comparing the chosen values of $\partial\gamma/\partial T$ in [7] to those obtained by Keene *et al.* [59], who measured $\partial\gamma/\partial T$ to be $8 \times 10^{-3} Nm^{-1} K^{-1}$ and $-3 \times 10^{-4} Nm^{-1} K^{-1}$ (for steels with large and small depth to width ratios respectively), a 'large' negative surface tension gradient in this thesis means one that is approximately $O(10^{-4})$. In chapter 2 of this thesis we obtain an asymptotic solution of the model developed in [7] and [30] when the surface tension gradient is large and negative, since this allows us to validate the numerical solutions and provide a greater understanding of the relative importance of the forces involved.

Very recently Priede, Cramer and Bojarevics *et al.* [85] performed an experimental and numerical study of thermocapillary convection in liquid gallium, with small amounts of a

surface active element present at the free surface of the liquid, obtaining similar velocity profiles in both their numerical work and experimental results.

Chung and Wei [27] considered a two-dimensional, unsteady model for welding dissimilar metals with a moving source. This model incorporates Marangoni effects on the (assumed flat) free surface of an ITEV fluid. The position of the solid-liquid interface was determined with the energy equation incorporating a latent heat term, whilst the material parameters in the liquid mixture were obtained using a linear volumetric fraction. Chung and Wei obtained results for different metals and different magnitudes of the Marangoni force, comparing their results with experimental observations.

In chapter 3 of this thesis we outline a model for the stationary, steady-state flow in a hemispherical pool of liquid steel, modelled as an ITEV fluid, due to the application of a point source of heat and current on the liquid's surface. This model was recently investigated by Belgrove [7] and includes both a buoyancy force and the thermocapillary (or Marangoni) force. The results are interesting since they describe how the Marangoni force on the free surface affects the breakdown currents observed in the papers of Sozou and his co-workers (e.g. [115]).

In the last two decades the use of external magnetic fields to control liquid metals has become widespread in the metallurgical industry. By applying an external magnetic field the electrically induced flow can be controlled and this method is apparently used (see [13]) for controlling electric arcs and electro-slag processes. (In the electro-slag process a melting electrode is continuously fed into the area in which the slag³ melts.) In addition to the poloidal flow the external magnetic field causes the fluid to rotate relative to the axis of symmetry. This rotation will attempt to generate a (diverging) flow from the point source out along the plane free surface ($\theta = \pi/2$ in figure 1.2) due to the centrifugal forces. The converging axial flow, which leads to axial singularities, is reduced by the centrifugal forces generated by this motion and if the applied electric field is sufficiently strong these forces can reverse the fluid motion.

In [130] and [31] Craine and Weatherill studied the effect of an external magnetic field on the flow induced in a hemisphere of IIEV fluid by a distributed source of current. In this case the azimuthal rotating flow reduced, or even reversed, the velocity of the poloidal flow.

In [13] Bojarevics *et al.* described an experiment which demonstrates that azimuthal rotation can occur without the imposition of an external magnetic field. In this experiment a small current-carrying electrode situated at the centre of the free surface of a copper bowl of mercury drives a poloidal motion in the fluid. When $J > 15A$ poloidal flow, which converged towards the electrode on the free surface, was accompanied by azimuthal rotation. However, up to a maximum current of 1500A no azimuthal motion was observed when the poloidal

³Slag is the waste material on the top of a liquid metal pool.

flow was diverging away from the source on the free surface.

In [12] Bojarevics and Shcherbinin demonstrated that intense rotation can be achieved in the semi-infinite point source model of Sozou [110], without any externally applied magnetic field, by using an applied azimuthal forcing term kJ^2 , where k is a fixed small parameter. They observed that in this situation the streamlines of the model are similar to those produced by flow to a sink remote from the surface $\theta = \pi/2$, and noted that this type of sink flow, such as that which occurs in a bath tub, has a tendency to rotate in the azimuthal direction. As a critical current value was reached, corresponding to K_{crit} in Sozou's model [110], they found that the azimuthal flow increased dramatically for small k and breakdown was subsequently avoided. However, when considering the reversed current case in which current is supplied by an immersed electrode along $\theta = 0$ (see figure 1.2), small azimuthal disturbances were retarded so that a rotating flow could not be maintained. In [13] Bojarevics *et al.* discussed a paper by Bojarevics and Millere [11] where the authors considered the azimuthal perturbation problem of [12] in a hemisphere (of radius R), with the current diverging radially from a small hemispherical electrode (of radius $R_1 < R$). The authors observed similar results to the semi-infinite point source problem considered in [12]. However, their study was hindered by non-converging numerical methods due to the large velocity gradients near the hemispherical electrode (a problem similar to that encountered by Sozou and Pickering in [116]).

In a recent review article [34] Davidson discussed some recent research in metallurgical MHD including magnetic mixing (used in casting to avoid anisotropic solidification), due to an applied rotating magnetic field, and magnetic damping by an applied static magnetic field. Davidson also discussed in a recent paper [35] the relationship between the poloidal and azimuthal flows, i.e. the flows in spherical polar co-ordinates in the (r, θ) plane and ϕ direction respectively.

In chapters 4 and 5 of this thesis we investigate the linear stability ([26], [38]) of the coupled heat and fluid flow model with surface tension, presented in chapter 3. Many years ago Rayleigh, Reynolds and others all recognised the importance of hydrodynamic stability. Reynold's series of experiments, described in [89], on the transition to turbulent flow in a pipe, is often used to introduce the instability of flows and from these experiments he derived the dimensional number we know today as the *Reynolds number*, Re . In general terms hydrodynamic stability determines whether a given laminar flow (in our case the model presented in chapter 3) is unstable, and if it is then the theory can be used to determine whether the flow becomes turbulent or bifurcates to another laminar flow. The *method of normal modes*, which was introduced to fluid dynamics by Lord Rayleigh [87], is used in chapters 4 and 5, where the approach is discussed further. In these chapters attention is confined to perturbations in the ϕ direction of the form $e^{\sigma t + im\phi}$, where m is called the azimuthal mode of stability.

Using a geometrical optics method Lifschitz found that all axi-symmetric, non-viscous, incompressible, poloidal, stagnation point flows are unstable to perturbations of short wavelength (see [70]). The model presented in chapter 3, however, includes viscosity which will damp any perturbations.

Various classical examples of how linear stability has been applied to inviscid and viscous flows driven by a variety of forcing terms are presented and discussed in [26] and [38]. Some of these models are outlined below.

- Instability of the laminar flow of liquid in a pipe (Poiseuille flow) was first investigated by Reynolds over a hundred years ago.
- Thermal instability occurs when a horizontal layer of stationary fluid is heated from below causing thermal convection (known as Bénard convection) due to the destabilising effect of buoyancy. Rayleigh showed that this instability occurs when a dimensionless parameter, known today as the *Rayleigh number* Ra , exceeds a critical value.
- The effect of rotation, or curvature of streamlines can cause centrifugal instability. Examples include Couette flow (i.e. the flow which occurs between two rotating coaxial cylinders), boundary layer flow on a concave wall and flow in a curved channel. Taylor observed steady secondary flow in the form of toroidal vortices when he performed experiments using two coaxial cylinders with the inner one rotating at a critical value of a non-dimensional parameter known today as the *Taylor number* T_c .
- Thermal instability in fluid spheres and spherical shells.
- Steady two-dimensional flows with parallel streamlines. These types of flow were investigated by Reynolds who observed that the development of instability depended crucially upon the velocity distribution. The inviscid theory was characterised by Rayleigh, whereas consideration of the viscous theory lead to, what became known as, the Orr-Sommerfeld equation.

External forces such as surface tension and magnetohydrodynamic forces usually tend to stabilise fluid flow since they act to inhibit the fluid motion. (In the thermal instability problem outlined above the surface tension on the free surface of the fluid must clearly affect the fluid motion, especially when the fluid layer is very thin.) The stability of some of these models when using an electrically conducting fluid in the presence of a magnetic field is discussed further in [26], Chandrasekhar's textbook on Hydromagnetic Stability.

More recently Wilson [135] considered the effect of a uniform vertical magnetic field on the onset of steady Bénard-Marangoni convection in a layer of conducting liquid heated from below. He investigated the cases when the free surface was deformable and then non-deformable, and introduced various non-dimensional parameters. Wilson found that the

Crispation number, C_r , (the ratio of viscous force to surface tension force at the reference temperature), and the Bond number, B_o , (the ratio of gravitational force to surface tension force at the reference temperature), play a critical role in determining the onset of steady convection.

Gardner *et al.* [45] investigated the linear stability of the flow which develops in the fluid filling a narrow gap between two concentric spheres at different surface temperatures. The experimental results of various authors indicate that steady axi-symmetric flow occurs below a critical Grashof number whereas a quasi-periodic, axi-symmetric flow pattern develops above this critical value, which is dependent upon the Prandtl number and the gap width. The authors of [45] conjectured that the transition in the flow pattern is due to a bifurcation. They found that below a critical Prandtl number a linear stability analysis of an analytical solution to this problem, expressed as a truncated power series in the gap width, indicated the development of an axi-symmetric oscillatory instability with mode $m = 0$. On the other hand, above this critical value instability occurred due to the development of a steady secondary flow with mode $m = 2$. A first approximation to this secondary flow was obtained from a critical eigenvector. In chapter 4 we use a similar method to obtain a first approximation to a secondary flow. The relevant theory is outlined in chapter 4.

Linear stability analysis has been applied to many diverse, physically motivated models over the years, some of which are relevant to the welding models discussed above. A very recent review paper by Shtern and Hussain [106] has discussed the various features of flow breakdown in rotating flows due to singularity development in the velocity field and bifurcation. The authors have discussed a number of recent papers and related the topic to a variety of subject areas including electro-vortex flows, as studied by Bojarevics and his colleagues [13], and the earlier work of Sozou [110]. Over recent years a variety of papers on swirling flows and the bifurcation of purely poloidal flows to a rotational flow have been published by Shtern and his co-workers ([41], [101], [102], [103], [104], [105]). Much of this work is based on an application which occurs in electro-spray processes. In the latter process the flow of an IIEV liquid in an electromagnetic field is driven by radial shear stresses on the inner surfaces of a cone. In [102] Goldshtik *et al.* showed that above a critical Reynolds number a supercritical pitchfork bifurcation from a non-swirling to a swirling flow is possible. Extending this paper Shtern and Barrero [103] found that a similar bifurcation to self swirling flow occurred when the flow was caused by a body force. Shtern and Barrero extended their investigation to include a half-space of IIEV liquid driven by an electromagnetic point source of current, following the model of Sozou [110] which admits a similarity solution. In this latter case they found that the azimuthal motion dominated over the poloidal flow and the number of flow loops in the half-space increased with the applied current. In [104] Shtern and Hussain considered the instability of steady, three-dimensional, axi-symmetric, ITEV flows with divergent streamlines

near a plane surface or a conical surface. One case considered in [104] is the flow in a half-space arising from Marangoni convection induced by a point source of heat on the surface of the liquid. With a linear stability analysis Shtern and Hussain found that the diverging poloidal flow bifurcates to a rotating flow at a critical Reynolds number for azimuthal modes $m = 2, 3, \dots$. However, this critical Reynolds number is influenced in a non-trivial manner by the value of the Prandtl number.

The linear stability of the model discussed in chapter 3 of this thesis is investigated in chapter 4 for the azimuthal mode $m = 0$ and in chapter 5 for the higher modes $m = 1, 2$ and 3. It is worth noting that it was shown in [7] that the solution obtained in chapter 2 can never bifurcate to a rotating flow.

Steel is an extremely important welding material and hence throughout the first five chapters of this thesis all numerical solutions will be calculated using the parameter values for this material. The results are really being calculated, however, for a general ITEV fluid using particular values of the non-dimensional parameters in the problem and, therefore, all the results could be linked to other materials with appropriate changes to the values of the applied current and the magnitude of the surface tension gradient.

Chapter 2

Asymptotic analysis of a semi-infinite flow model with large negative surface tension gradient

2.1 Introduction

Recently Belgrove [7] and Craine and Belgrove [30] extended an earlier welding model by Lancaster [65], by considering the steady state motion of a semi-infinite region of incompressible, thermally and electrically conducting viscous fluid (ITEV fluid) due to stationary coincident point sources of heat and current on the free surface. This model includes a Marangoni force on the free surface and solves the coupled Navier-Stokes and temperature equations. These authors obtained solutions for positive and negative surface tension gradients. They found that solutions exist for large¹ negative surface tension gradients at large values of the imposed current J and, consequently, at large values of the *parameter of electrically induced vortex flow* K .

In this chapter we construct an asymptotic solution of the model developed in [7] and [30] for a large negative surface tension gradient using the non-dimensional parameter K as a large parameter. Firstly, however, an asymptotic solution, derived by Bojarevics, to a semi-infinite welding model is discussed.

Using the non-dimensional parameter K , Bojarevics [10] constructed an asymptotic solution to an earlier model [9] which altered the semi-infinite problem of Sozou [110] by placing a narrow, rigid cone on the axis of symmetry to increase the action of the viscous forces

¹The use of the term *large* may be misleading in this context since comparing the chosen values of $\partial\gamma/\partial T$ in [7] with measurements in steel by Keene *et al.* [59] a large negative surface tension gradient in this thesis means one that is approximately $O(10^{-4})$.

in the axial jet. With this addition Bojarevics was able to obtain solutions for very large values of K . Bojarevics' model describes the flow of a semi-infinite region of incompressible, isothermal, electrically conducting viscous fluid (IIEV fluid) under the influence of a Lorentz force produced by the application of a point source of current at the point of intersection between the axis of symmetry and the free surface. By reducing the conical angle of the cone to zero Bojarevics was also able to obtain results for an infinitely thin wire on the symmetry axis. Figure 2.1 depicts the situation, where spherical polar co-ordinates (r, θ, ϕ) have been

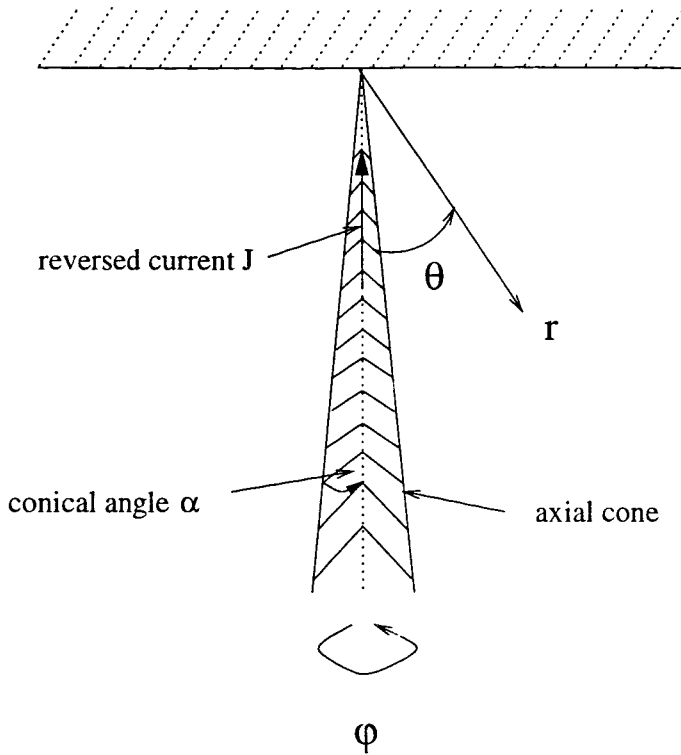


Figure 2.1: Spherical polar coordinates with the origin at the base of a cone placed on the axis of symmetry.

introduced with the origin at the apex of the cone. This figure shows 'reversed current flow' (the situation defined in chapter 1, where an electric current is supplied to the point source on the plane surface of the liquid, $\theta = \pi/2$, from the axis of symmetry $\theta = 0$). The ensuing flow [9] is directed up along the surface of the cone, and then diverges away from the point source along the plane surface. In his model Bojarevics [9] considered, in turn, the cases where the plane surface at $\theta = \pi/2$ was a rigid wall and then a free surface, obtaining numerical results for very large values of the parameter of electrically induced vortex flow K in each case.

Figures 2.2a and 2.3a (obtained from [13]) show respectively the streamlines $\psi/K = \text{const.}$ for $K = 10^7$ (which corresponds to a current of approximately 1900A in steel) for a rigid wall at $\theta = \pi/2$, and for $K = 10^9$ (which corresponds to a current of approximately 19,000A in

steel) for a free surface at $\theta = \pi/2$, when in both cases the electrode has a conical angle α of 5° . The solutions were found to depend upon the conical angle, and figures 2.2b and 2.3b ([13]) show the streamlines for $K = 10^7$ with a rigid wall at $\theta = \pi/2$, and for $K = 10^9$ with a free surface at $\theta = \pi/2$, when the conical angle is zero (i.e. the current is supplied to the point source along an infinitely thin wire). Notice that when K is large the presence of the central cone has little effect upon the streamlines in the bulk of the molten metal.

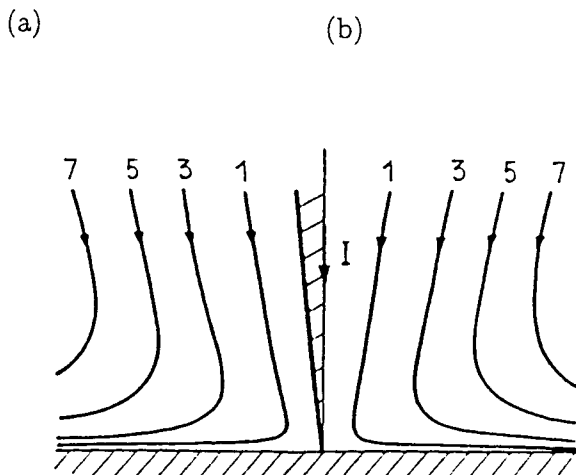


Figure 2.2: Streamlines of the flow with a rigid plane ($K = 10^7$): (a) for the finite size electrode; (b) for the infinitely thin wire. Figure taken from [13].

We now return to the recent model of Belgrove [7] and Craine and Belgrove [30]. These authors have also obtained solutions at high current values, and correspondingly large magnitudes of the parameter K , when the surface tension gradient was negative. The results of Craine and Belgrove showed that three different combinations of flow regimes can occur in the semi-infinite domain of fluid. These three flow regimes are shown schematically in figure 2.4, and the flow structures which result from prescribed values for the current J and the surface tension gradient $\partial\gamma/\partial T$ are indicated on figure 2.5. The latter results were obtained by choosing values for the density ρ , the thermal diffusivity κ , the kinematic viscosity ν and the specific heat at constant pressure c_p which are appropriate for liquid steel, namely

$$\rho = 7000 \text{ kg m}^{-3}, \quad \nu = 6.4 \times 10^{-7} \text{ m}^2 \text{ s}^{-1},$$

$$\kappa = 1.0 \times 10^{-5} \text{ m}^2 \text{ s}^{-1} \quad \text{and} \quad c_p = 600 \text{ J kg}^{-1} \text{ K}^{-1}.$$

In figure 2.5 the region below the dotted curve 2 corresponds to a single loop reverse flow structure (displayed schematically in figure 2.4b) when the ITEV fluid flows up the axis of symmetry (where $\theta = 0$) and diverges away from the point source along the surface (on which

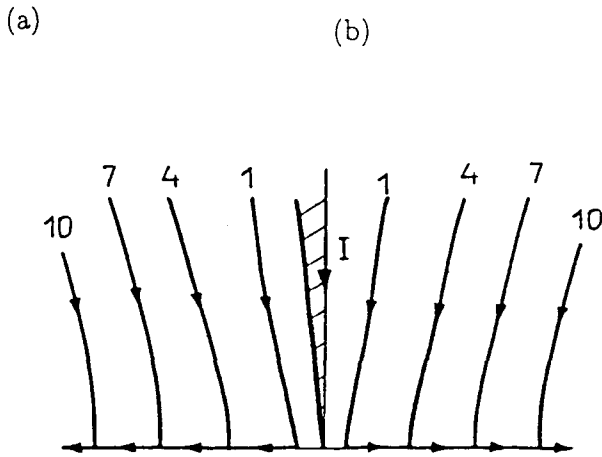
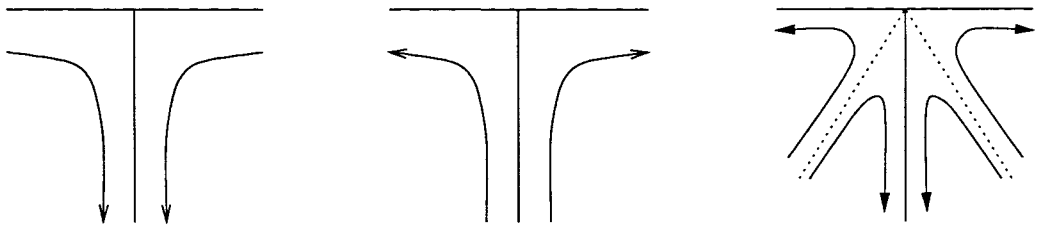


Figure 2.3: Streamlines of the flow with a free surface ($K = 10^9$): (a) for the finite size electrode; (b) for the infinitely thin wire. Figure taken from [13].



a) Inward flow: down axis, in along surface. b) Reverse flow: up axis, out along surface. c) 2-loop flow structure

Figure 2.4: The possible flow structures predicted by the steady-state semi-infinite welding model in [30] and [7].

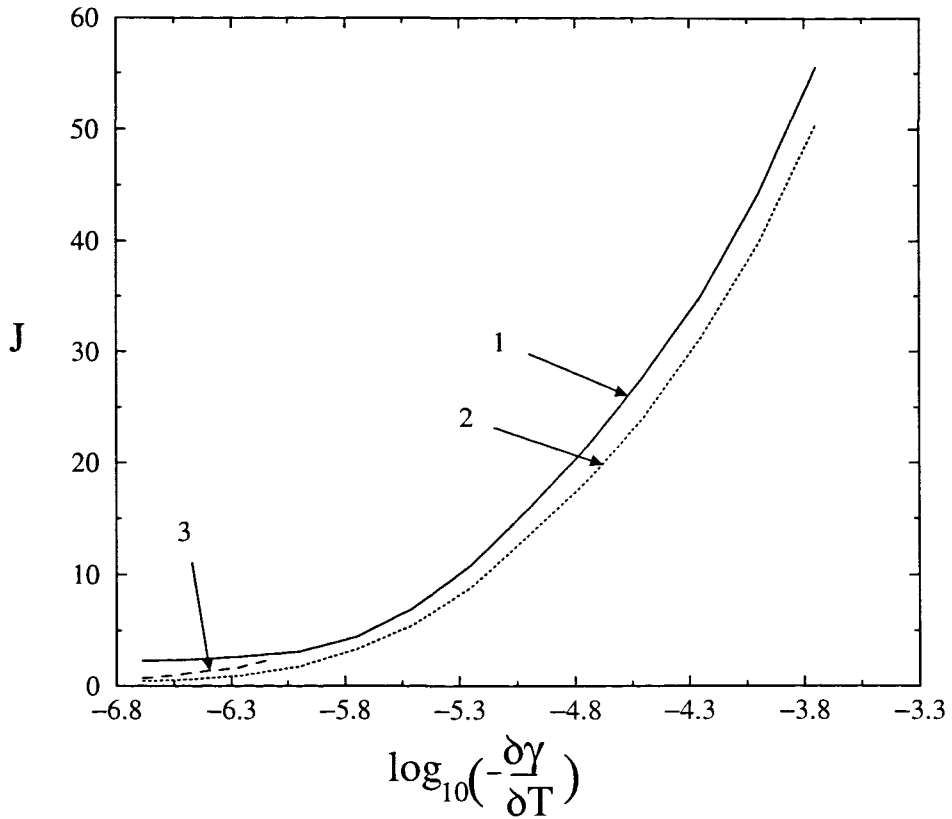


Figure 2.5: Curves in the $(J, \log_{10}(-\partial\gamma/\partial T))$ -plane which separate regions that correspond to different flow regimes in the numerical model described in [7] and [30]. The upper curve indicates model breakdown. A similar figure can be found in the above references.

$\theta = \pi/2$). The region between curves 1 and 2 and to the right of the short curve 3 in figure 2.5 corresponds to a double loop flow structure (displayed schematically in figure 2.4c). In this region the ITEV fluid flows out along the top surface but down the axis of symmetry. Finally the small region between curves 1 and 3 in figure 2.5 corresponds to a single loop inward flow structure (displayed schematically in figure 2.4a) in which the ITEV fluid flows in along the free surface and down the axis of symmetry. Therefore, when the magnitude of the negative surface tension gradient reaches the largest value occurring for real materials the single loop reversed flow structure (figure 2.4b) exists for current values up to approximately $50A$. Curve 1 denotes critical values of the current, J_{crit} , above which the solution breaks down with a fast jet of fluid travelling along the symmetry axis. The figure clearly, shows that J_{crit} is a function of $\partial\gamma/\partial T$, T denoting the temperature.

To understand the relative importance of the competing forces in the model of Craine and Belgrove [30] some asymptotic results for the coupled problem would be very useful and this type of analysis is attempted in section 2.4 for high values of the parameter K and large negative surface tension gradients. First, however, it is necessary to summarise and discuss the formulation of the model and the calculation of numerical results.

2.2 Numerical model

In this section we consider a model which describes the steady state motion and temperature distribution of a semi-infinite region of ITEV fluid due to a stationary point electrode supplying current and heat to the free surface. The surface tension gradient with respect to temperature, $\partial\gamma/\partial T$, creates a large Marangoni (thermocapillary) force on the free surface, outward from the point source when $\partial\gamma/\partial T$ is negative. The surface is assumed flat and buoyancy has been ignored. There is evidence that the exclusion of buoyancy is a reasonable approximation [36], and its omission allows a similarity solution. The viscosity and density coefficients are assumed unchanged by any alterations in temperature. The applied current distribution is assumed spherically symmetric and it is assumed that the current and induced magnetic field remain unchanged by the flow.

With the above assumptions the governing steady state equations are [110]:
the Navier-Stokes equations

$$(\mathbf{v}\cdot\nabla)\mathbf{v} + \frac{1}{\rho}\nabla p - \nu\nabla^2\mathbf{v} - \frac{1}{\rho}\mathbf{J}\times\mathbf{B} = \mathbf{0},$$

where \mathbf{v} denotes velocity, p pressure, \mathbf{J} electric current and \mathbf{B} induced magnetic field;
the incompressibility equation,

$$\nabla\cdot\mathbf{v} = 0;$$

the heat transfer equation,

$$\mathbf{v} \cdot \nabla T = \kappa \nabla^2 T, \quad (2.1)$$

where the term on the left hand side describes heat transfer due to convection and the term on the right represents conductive heat transfer. Viscous heat dissipation and ohmic heating have been ignored since they can be shown to be small.

For a point source of current and heat it can be shown [30] that a similarity solution is possible, with the stream function ψ defined by

$$\psi = \nu r f(\mu)$$

and

$$T = \frac{1}{r} t(\mu),$$

where $\mu = \cos \theta$ and θ represents the angle between the radius and the vertical axis and r is the distance from the point source situated at the origin on the free surface, as shown in figure 2.1.

It follows from the definitions that

$$\mathbf{v} = \frac{\nu}{r} \left(f'(\mu), \frac{1}{(1 - \mu^2)^{\frac{1}{2}}} f(\mu), 0 \right).$$

It is noted that $f(\mu)$ is a non-dimensional function, but with no natural length in the problem $t(\mu)$ remains dimensional.

The MHD (magneto- hydro- dynamic) equations which govern the flow of electrically conducting liquids are well known, [98], and will be quoted in the following summary. The electric current distribution is assumed spherically symmetric and given by

$$\mathbf{J} = \frac{J_0}{2\pi r^2} \hat{\mathbf{r}}, \quad (2.2)$$

where J_0 denotes the total current input. Ampere's law

$$\nabla \times \mathbf{B} = \mu_0 \mathbf{J}, \quad (2.3)$$

where μ_0 represents the permeability of free space, can then be solved analytically to give the self-induced magnetic field

$$\mathbf{B} = \frac{J_0 \mu_0 (1 - \mu)}{2\pi r (1 - \mu^2)^{\frac{1}{2}}} \hat{\boldsymbol{\phi}}, \quad (2.4)$$

assuming that \mathbf{B} remains finite on the axis of symmetry $\mu = 1$.

After substitution for \mathbf{v} , T , \mathbf{B} and \mathbf{J} in the Navier-Stokes and the heat transfer equations, Belgrove and Craine [30] show that the governing equations become

$$f^2(\mu) = 2(1 - \mu^2)f'(\mu) + 4\mu f(\mu) + a\mu^2 + b\mu + c - F(\mu) \quad (2.5)$$

and

$$t'(\mu) = \frac{\nu f(\mu)t(\mu)}{\kappa (1 - \mu^2)}, \quad (2.6)$$

where

$$F(\mu) = K \left[(1 + \mu)^2 \ln(1 + \mu) - \mu \left(1 + \frac{3}{2}\mu \right) \right],$$

a , b and c are constants, a prime denotes differentiation with respect to μ and

$$K = \frac{\mu_0 J_0^2}{2\pi^2 \rho \nu^2}.$$

Note that equation (2.5) is the equation obtained by Sozou [110] for the isothermal case. Sozou notes that if $F(\mu)$ is removed, equation (2.5) becomes identical to that obtained in [118] for the momentum transfer through a viscous jet (a topic which is discussed by Batchelor [6]). Equations (2.5) and (2.6) are solved subject to the following boundary conditions:

no motion across the free surface ($\mu = 0$),

$$v_\theta(0) = 0 \Rightarrow f(0) = 0; \quad (2.7)$$

no fluid crosses the axis of symmetry ($\mu = 1$),

$$v_\theta(1) = 0 \Rightarrow f(1) = 0; \quad (2.8)$$

no heat flux across the top surface ($\mu = 0$),

$$\frac{\partial T}{\partial \theta}(0) = 0 \Rightarrow t'(0) = 0. \quad (2.9)$$

The final boundary condition, derived from the assumption that the shear stress on the free surface arises from the Marangoni force, is

$$f''(0) = -\frac{1}{\rho \nu^2} \frac{\partial \gamma}{\partial T} t(0), \quad (2.10)$$

and this condition couples equation (2.5) to the temperature. Note that condition (2.10) involves $\partial \gamma / \partial T$, the surface tension gradient with respect to temperature, which is assumed constant. By evaluating equation (2.5) at $\mu = 1$ and at $\mu = 0$, and using boundary conditions (2.7) and (2.8), the constants a , b and c can be obtained in terms of $f'(0)$ as follows:

$$a = \frac{K}{2} - 2f'(0), \quad (2.11)$$

$$b = K \left(4 \ln(2) - 3 \right) + 4f'(0), \quad (2.12)$$

$$c = -2f'(0). \quad (2.13)$$

Equation (2.5) is of Ricatti-type and is usually transformed into the second order linear equation

$$u''(\mu) = \frac{u(\mu)}{4(1 - \mu^2)} \left[a\mu^2 + b\mu + c - F(\mu) \right] \quad (2.14)$$

via the transformation

$$f(\mu) = -2(1 - \mu^2) \frac{u'(\mu)}{u(\mu)}.$$

Equation (2.14) must now be solved numerically subject to the boundary conditions

$$u'(0) = 0 \quad \text{and} \quad u(0) = 1. \quad (2.15)$$

Unfortunately the boundary condition (2.10) and the values of the coefficients a , b and c cannot be determined explicitly from the prescribed boundary conditions since $f'(0)$ is unknown and, therefore, in order to calculate the correct value for $f'(0)$ an extra condition is required. In [65] the total heat input has been experimentally found to be approximately six times the current input and this relation is used in our analysis. The heat conducted and convected across a small hemisphere around the origin are given by

$$q_d = -2\pi k \frac{\partial T}{\partial r} \quad \text{and} \quad q_v = 2\pi T c_p \rho v r,$$

where k is the thermal conductivity. The total heat flux is then obtained by integrating with respect to μ between 0 and 1, and hence the additional condition used in this thesis is

$$6J_0 = Q = 2\pi \rho c_p \int_0^1 t(\kappa - \nu f') d\mu. \quad (2.16)$$

2.2.1 Method of numerical solution

Equations (2.14) and (2.6) for $u(\mu)$ and $t(\mu)$ were solved subject to the boundary conditions (2.9), (2.10) and (2.15), using the NAG routine D02BBF. The value of $f'(0)$ was guessed, solutions for u and t were found, and then the initial value $f'(0)$ was altered until the right hand side of equation (2.16) produced a value for Q which was within 0.1% of $6J_0$.

2.3 Discussion

The numerical results of Belgrove [7] revealed that for certain current values and surface tension gradients (which are far from the breakdown value shown on figure 2.5) the temperature profiles are approximately spherical, see figure 2.6². Near the breakdown of the numerical solutions there is more rapid downward flow close to the axis of symmetry and along the free surface. On leaving the current unchanged but increasing the magnitude of the negative surface tension gradient, the isotherms become increasingly aspherical (see figures 2.7 and 2.8). These results suggest a leading order relationship between the conductive and convective methods of heat transfer in regions of large negative surface tension gradient.

²The numbers on figures 2.6 and 2.8 indicate values of $\psi/(\nu L)$ and TL , where L is the length of the horizontal axis.

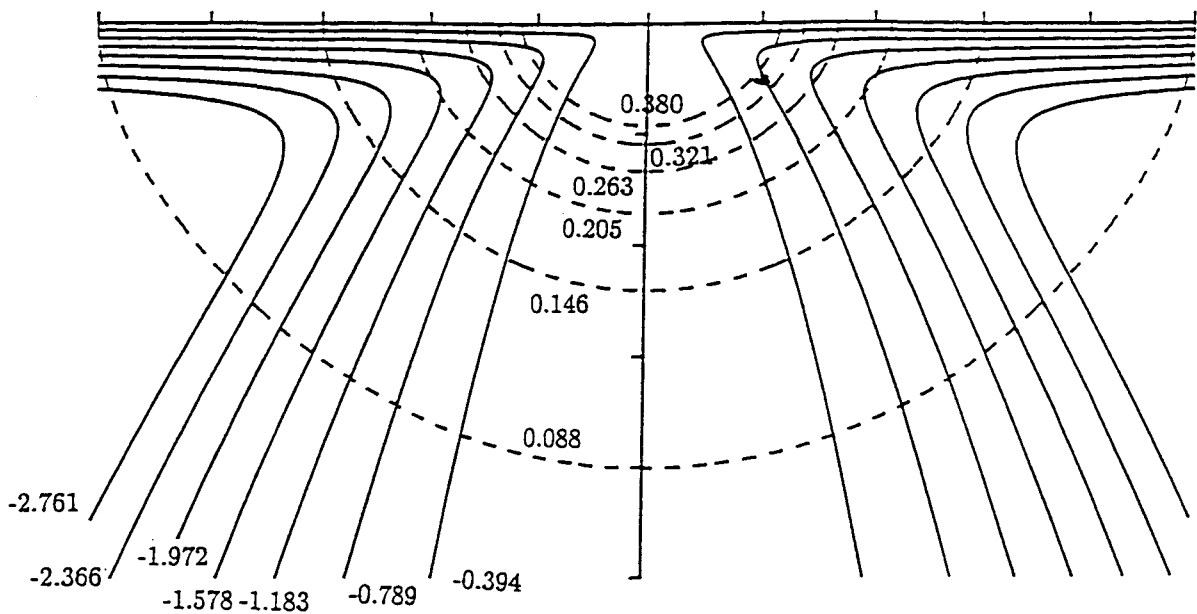


Figure 2.6: Numerical streamlines and isotherms for $K = 271.99$ (i.e. $J_0 = 3.5A$ for steel) and $\partial\gamma/\partial T = -3 \times 10^{-6} NK^{-1}m^{-1}$.

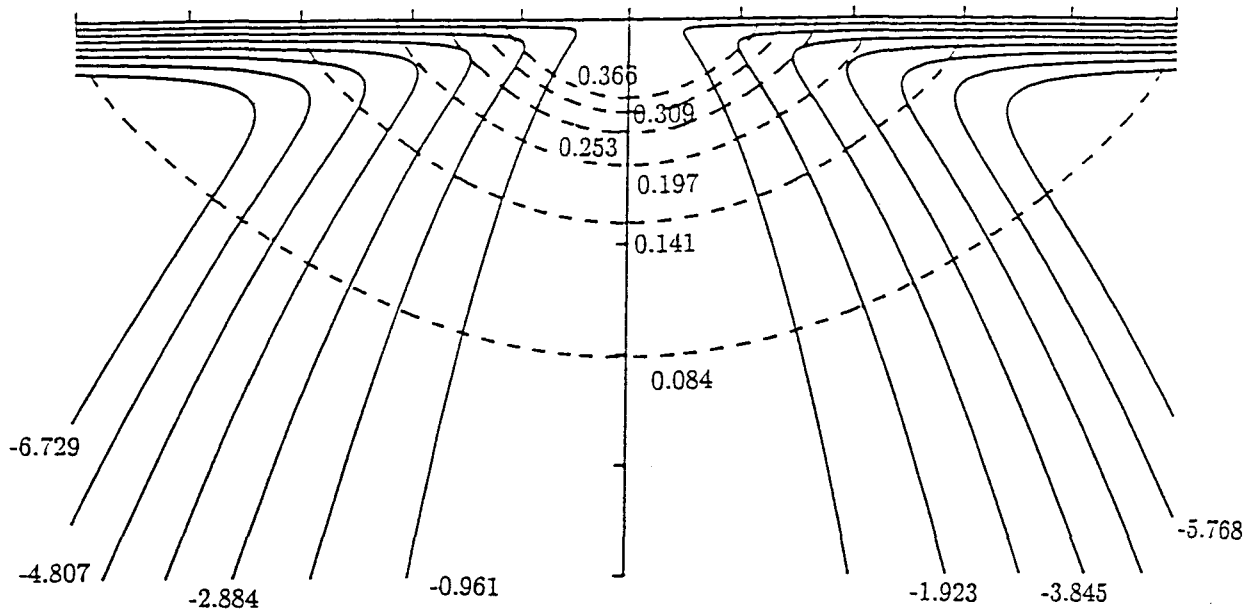


Figure 2.7: Numerical streamlines and isotherms for $K = 271.99$ (i.e. $J_0 = 3.5A$ for steel) and $\partial\gamma/\partial T = -8 \times 10^{-6} NK^{-1}m^{-1}$.

To produce the required balance the value for J_0 , which determines the parameter K , must ensure that the conductive and convective terms are of similar order when there is a large outward Marangoni force.

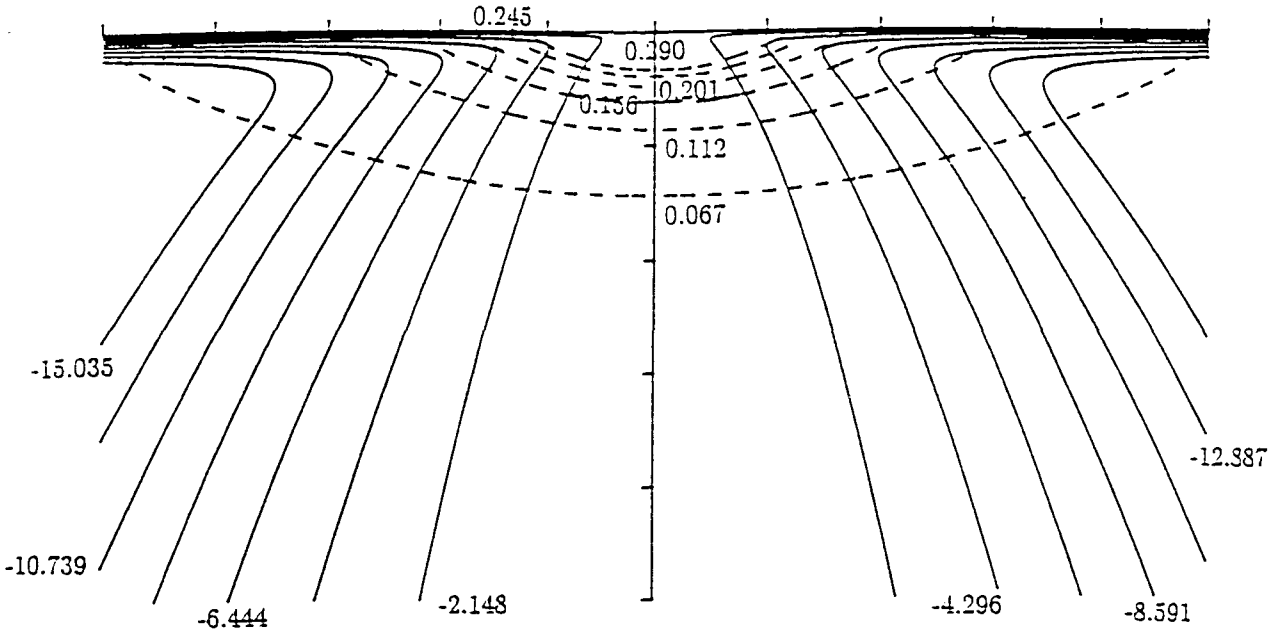


Figure 2.8: Numerical streamlines and isotherms for $K = 271.99$ (i.e. $J_0 = 3.5A$ for steel) and $\partial\gamma/\partial T = -3 \times 10^{-5} NK^{-1}m^{-1}$.

The numerical results suggest that

$$f(\mu) = O(K^{\frac{1}{2}}) \quad (2.17)$$

is a good approximation for the order of magnitude of the non-dimensional stream function. Since the magnitude of the Marangoni force clearly affects the stream function, it seems reasonable to assume that the coefficients a, b and c in equation (2.5) must depend on $\partial\gamma/\partial T$. In this way the surface tension will affect the first approximation to the stream function in an asymptotic analysis, as clearly required by figures 2.6 to 2.8 in which $\partial\gamma/\partial T$ is the only input variable to change.

2.4 Asymptotic model

Figure 2.5 shows that numerical solutions are possible, using the material parameters for steel, when the current is much larger than in the earlier point source isothermal models (see [110]). That is to say point source solutions can now be found for very large values of K , up to approximately 30,000 when $\log_{10}(-\partial\gamma/\partial T) \approx -3.75$. Hence using K as our large

parameter we now attempt an asymptotic analysis of the governing equations described in the previous section when $\partial\gamma/\partial T$ is large and negative and K is also large. Asymptotic analyses are helpful since they provide a deeper understanding of the underlying structure of solutions. It is also hoped that our analysis will produce results that agree with, and hence partially validate, the numerical solutions. Specifically, we look at the region in parameter space where

$$-\frac{1}{\rho\nu^2} \frac{\partial\gamma}{\partial T} = \zeta_1 K^{\frac{3}{2}} \quad (2.18)$$

and

$$\frac{\nu}{\kappa} = \zeta_2 K^{-\frac{1}{2}}, \quad (2.19)$$

when ζ_1 and ζ_2 are both $O(1)$.³ Therefore, using the definition for K given by equation (1.1) in chapter 1, (2.18) and (2.19) are equivalent to

$$\frac{\partial\gamma}{\partial T} = -\zeta_1 \frac{\mu_0^{\frac{3}{2}} J_0^3}{2^{\frac{3}{2}} \rho^{\frac{1}{2}} \pi^3 \nu} \quad \text{and} \quad J_0 = \zeta_2 \frac{2^{\frac{1}{2}} \rho^{\frac{1}{2}} \pi \kappa}{\mu_0^{\frac{1}{2}}}.$$

Figure 2.9 shows lines of constant ζ_1 and ζ_2 , for molten steel. The curve labelled 1 (shown previously in figure 2.5) gives the breakdown current, J_{crit} , for the numerical model. The curve labelled 2 (also in figure 2.5) shows the current at which a transition in flow structure occurs in the numerical solution between a single and double-loop flow structure. Figure 2.9 clearly reveals the region in $J - \partial\gamma/\partial T$ space for which both ζ_1 and ζ_2 are $O(1)$.

The numerical results of Belgrove [7] and Craine and Belgrove [30] suggest that, in the asymptotic solution, for the chosen values of J and $\partial\gamma/\partial T$ the flow should be divided into 2 regions:

- A** - main flow region, valid everywhere except in a thin layer at the free surface;
- B** - narrow viscous shear layer at the free surface, in which $\mu \leq \delta_s$, where δ_s is a positive small parameter.

These regions are shown schematically in figure 2.10.

In the isothermal model considered by Bojarevics [10] the no slip condition at the axis of symmetry ($\mu = 1$) necessitated the use of an additional narrow viscous region near the axis, $1 - \delta_a \leq \mu \leq 1$, where δ_a is another positive small parameter. This axial region is not introduced here because the thermal model investigated in this chapter does not have a no-slip boundary condition on the axis and, more importantly, the numerical results do not indicate any rapid changes in the solutions near this axis.

³For ζ_1 and ζ_2 to be exactly equal to 1 for molten steel (with $\nu = 6.4 \times 10^{-7} m^2 s^{-1}$, $\kappa = 1.0 \times 10^{-5} m^2 s^{-1}$ and $\rho = 7000 Kgm^{-3}$) one requires that $J = 3.34$ (and consequently $K \approx 244$) and $\partial\gamma/\partial T = -1.1 \times 10^{-5} Nm^{-1} K^{-1}$.

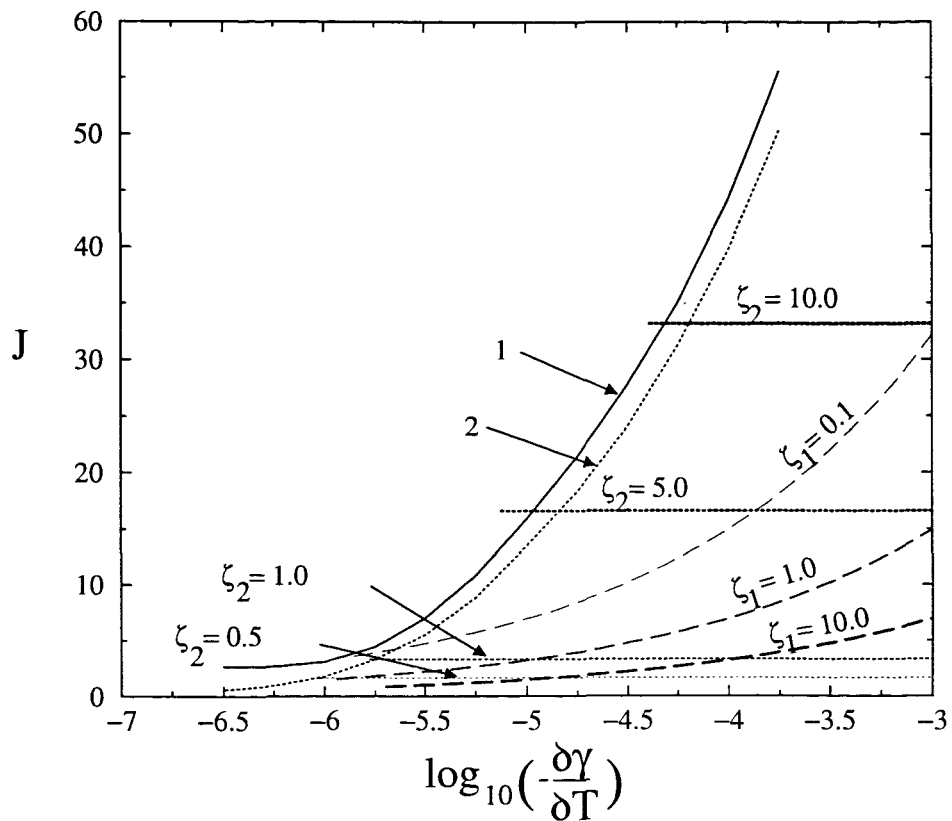


Figure 2.9: Lines of constant ζ_1 and ζ_2 superimposed over figure 2.5.

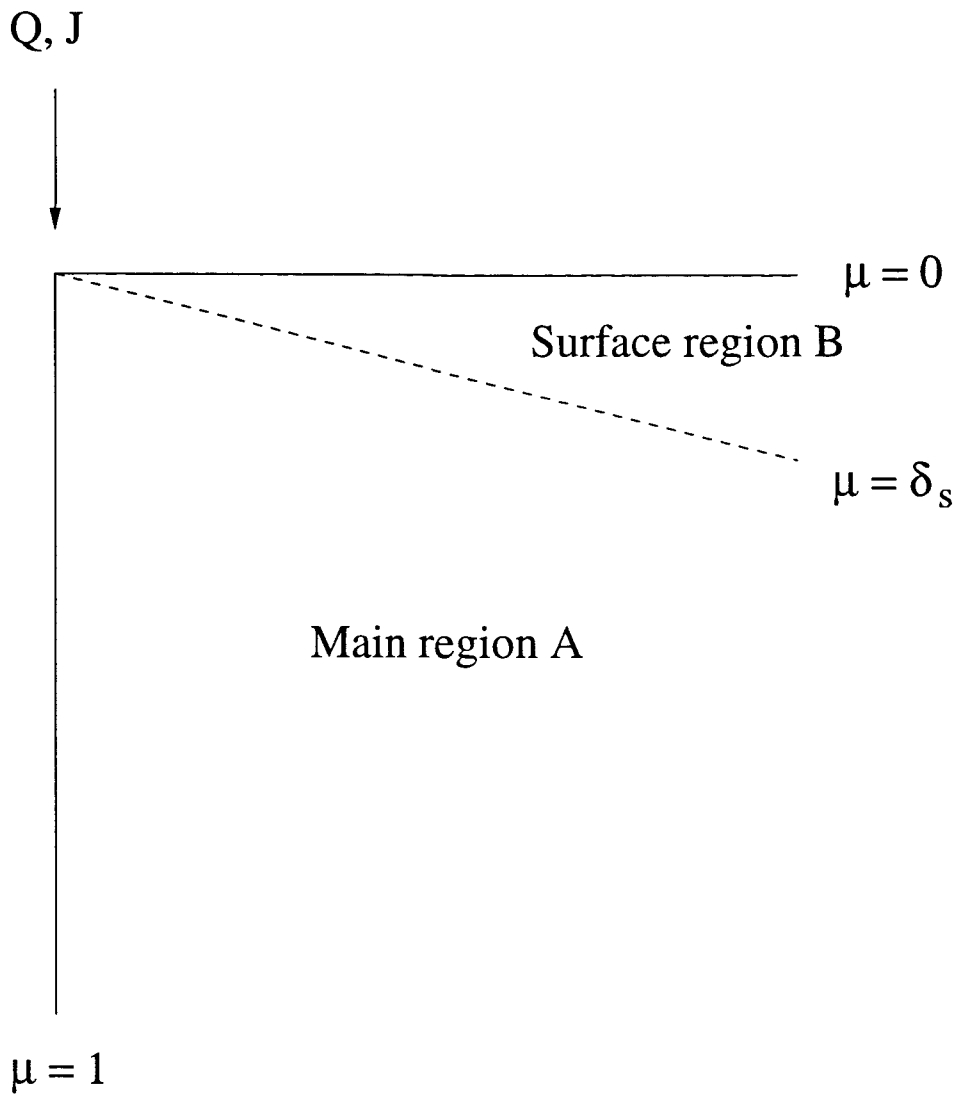


Figure 2.10: Schematic representation of asymptotic regions.

2.4.1 Main fluid region

Asymptotic solutions to equations (2.5) and (2.6) are sought in this section. The non-dimensional stream function f and temperature t are assumed to have regular perturbation expansions with leading and first order terms

$$f(K, \mu) = K^{A_0} f_0(\mu) + K^{A_1} f_1(\mu) + \dots, \quad (2.20)$$

$$t(K, \mu) = K^{B_0} t_0(\mu) + K^{B_1} t_1(\mu) + \dots. \quad (2.21)$$

Since K is large it follows that $A_0 > A_1$ and $B_0 > B_1$. Similarly the constants a , b and c (which are clearly functions of K , by inspection of equations (2.11) to (2.13)) are assumed to have regular perturbation expansions with leading and first order terms

$$a = K a_0 + K^{\frac{1}{2}} a_1 + \dots, \quad b = K b_0 + K^{\frac{1}{2}} b_1 + \dots \quad \text{and} \quad c = K c_0 + K^{\frac{1}{2}} c_1 + \dots. \quad (2.22)$$

Momentum transport equation

Substituting equation (2.20) into equation (2.5), which determines the non-dimensional stream function $f(\mu)$, leads to

$$\begin{aligned} K^{2A_0} f_0^2 + 2K^{A_0+A_1} f_0 f_1 + K^{2A_1} f_1^2 - 2(1 - \mu^2) \left(K^{A_0} f_0' + K^{A_1} f_1' \right) \\ - 4\mu \left(K^{A_0} f_0 + K^{A_1} f_1 \right) + \dots = K \left(a_0 \mu^2 + b_0 \mu + c_0 \right) \\ + K^{A_0} \left(a_1 \mu^2 + b_1 \mu + c_1 \right) - Kr(\mu), \end{aligned} \quad (2.23)$$

where

$$r(\mu) = \left[(1 + \mu)^2 \ln(1 + \mu) - \mu \left(1 + \frac{3}{2} \mu \right) \right]. \quad (2.24)$$

The leading order approximation to $f(\mu)$ is therefore determined by

$$K^{2A_0} f_0^2 = K \left[a_0 \mu^2 + b_0 \mu + c_0 - r(\mu) \right]. \quad (2.25)$$

Hence $A_0 = 1/2$, as expected from comparison with Bojarevics' work in [10], and the numerical results shown in figure 2.8 which were obtained when the parameters satisfied equations (2.18) and (2.19) with $\zeta_1 \approx 1$ and $\zeta_2 \approx 1$. Therefore, with $A_0 = 1/2$ equation (2.25) implies

$$f_0^2 = \left[a_0 \mu^2 + b_0 \mu + c_0 - r(\mu) \right]. \quad (2.26)$$

It should be noted that the solution for f_0 can have a positive or negative square root. For the case of large negative surface tension gradient, the flow is expected to be up the axis of symmetry towards the origin and then diverge outwards along the free surface away from the

point source, as shown in figure 2.4b. This flow structure corresponds to the negative square root solution for f_0 .

The first order approximation to the non-dimensional stream function is determined from

$$2K^{A_0+A_1} f_0 f_1 = K^{A_0} [2(1 - \mu^2) f'_0 + 4\mu f_0 + a_1 \mu^2 + b_1 \mu + c_1], \quad (2.27)$$

which implies that $A_1 = 0$. Using equations (2.26) and (2.27) with $A_0 = 1/2$ and $A_1 = 0$, it follows that

$$f_1 = (1 - \mu^2) \frac{2a_0 \mu + b_0 - r'(\mu)}{2[a_0 \mu^2 + b_0 \mu + c_0 - r(\mu)]} + 2\mu - \frac{a_1 \mu^2 + b_1 \mu + c_1}{2[a_0 \mu^2 + b_0 \mu + c_0 - r(\mu)]^{\frac{1}{2}}}, \quad (2.28)$$

where $r(\mu)$ has been defined by equation (2.24) and

$$r'(\mu) = 2(1 + \mu) \ln(1 + \mu) - 2\mu.$$

Application of the boundary condition $f(1) = 0$ on the axis of symmetry requires that $f_0(1) = 0$ and $f_1(1) = 0$. Hence, taking the limit of equations (2.26) and (2.27) as $\mu \rightarrow 1$, gives

$$a_0 + b_0 + c_0 = r(1) \quad \text{and} \quad a_1 + b_1 + c_1 = 0, \quad (2.29)$$

whilst taking the same limit of the differential of equations (2.26) and (2.27) yields

$$2a_0 + b_0 = r'(1) \quad \text{and} \quad 2a_1 + b_1 = 0. \quad (2.30)$$

Heat transfer equation

In the numerical model the heat transfer equation (2.1) was integrated with respect to μ to obtain

$$t'(\mu) = \frac{\nu f(\mu) t(\mu)}{\kappa (1 - \mu^2)}. \quad (2.31)$$

Substitution of the regular expansion (2.21) for the temperature variable $t(\mu)$ into (2.31) leads to

$$K^{B_0} t'_0 + K^{B_1} t'_1 = \zeta_2 K^{-\frac{1}{2}} \frac{(K^{\frac{1}{2}} f_0 + f_1)(K^{B_0} t_0 + K^{B_1} t_1)}{1 - \mu^2}, \quad (2.32)$$

where equation (2.19) has been used to write ν/κ in terms of the large parameter K . We now choose $B_0 = -1/2$, which is in agreement with the numerical results shown in section 2.3 of this chapter. To leading order, equation (2.32) then gives

$$t'_0 = \zeta_2 \frac{f_0 t_0}{1 - \mu^2} \quad (2.33)$$

which yields the solution

$$t_0(\mu) = C_{t_0} \exp \left[\zeta_2 \int_0^\mu \frac{f_0(\eta)}{1 - \eta^2} d\eta \right], \quad (2.34)$$

where C_{t_0} is a constant of integration. With the obvious choice $B_1 = -1$, equation (2.32) to first order yields⁴

$$t'_1 = \zeta_2 \left[\frac{f_0 t_1 + f_1 t_0}{1 - \mu^2} \right], \quad (2.35)$$

from which it follows that

$$t_1 = t_0 \zeta_2 \int_0^\mu \frac{f_1(\eta)}{1 - \eta^2} d\eta + \frac{C_{t_1}}{C_{t_0}} t_0, \quad (2.36)$$

where C_{t_1} is a constant of integration.

2.4.2 Free surface shear layer

Fluid solution

It is necessary to introduce a stretched variable $\alpha = \alpha(\mu)$ in the thin shear layer near the free surface, $\mu = 0$ [128]. Introduce

$$\alpha = \frac{\mu}{\Delta_s(K)} \quad (2.37)$$

as the stretched variable, where $\Delta_s(K)$ is the small parameter K^{-s} , with $s > 0$. In the shear layer it is assumed that the expansions for f and t take the forms

$$f = K^{\frac{1}{2}} f_{0s}(\mu) + f_{1s}(\mu) + \dots \quad (2.38)$$

$$t = K^{-\frac{1}{2}} t_{0s}(\mu) + K^{-1} t_{1s}(\mu) + \dots, \quad (2.39)$$

which have similar structure in K to the expansions in the main fluid region and so allow the matching to be performed successfully. Using equations (2.22), (2.37), (2.38) and (2.39) equation (2.5) transforms into

$$\begin{aligned} \left(K^{\frac{1}{2}} f_{0s} + f_{1s} \right)^2 &= 2(1 - K^{-2s} \alpha^2) K^s (K^{\frac{1}{2}} f'_{0s} + f'_{1s}) + 4K^{-s} \alpha (K^{\frac{1}{2}} f_{0s} + f_{1s}) \\ &\quad + K \left(a_0 K^{-2s} \alpha^2 + b_0 K^{-s} \alpha + c_0 - r(K^{-s} \alpha) \right) \\ &\quad + K^{\frac{1}{2}} \left(a_1 K^{-2s} \alpha^2 + b_1 K^{-s} \alpha + c_1 \right) \end{aligned} \quad (2.40)$$

where the prime here denotes differentiation with respect to α . Note that the Taylor series expansion of $r(\mu)$ in the shear region, $\delta_s = \alpha/K^s \ll 1$, leads to

$$r(\delta_s) = (1 + \delta_s)^2 \ln(1 + \delta_s) - \delta_s \left(1 + \frac{3}{2} \delta_s \right) = \delta_s^3 + O(\delta_s^4). \quad (2.41)$$

⁴In regions of the $\partial\gamma/\partial T - J$ plane where $\zeta_2 \ll 1$ the conduction term on the left hand side of equation (2.32) is larger than any other term in that equation. Consequently, to leading order,

$$t'_0 = 0$$

and hence the leading order temperature function, $t_0(\mu)$, is constant and the corresponding isotherms are hemispherical. Discussions in section 2.3 of this chapter indicate that when the surface tension gradient is large and negative the leading order terms on the left and right hand sides of equation (2.32) must balance to produce the observed aspherical isotherms, and so the assumption that $\zeta_2 \ll 1$ seems unreasonable.

In the viscous shear layer the linear viscous term, namely the derivative of f in equation (2.5) and consequently equation (2.40), must be retained in order to satisfy the boundary conditions on the free surface. Consequently, the viscous term must have the same order of magnitude as the non-linear inviscid term. This is only possible⁵ if

$$s = \frac{1}{2},$$

in which case the leading and first order approximations to equation (2.40) are

$$f_{0s}^2 = 2f'_{0s} + c_0 \quad (2.42)$$

and

$$2f_{0s}f_{1s} = 2f'_{1s} + \alpha b_0 + c_1, \quad (2.43)$$

respectively. The boundary condition $f(0) = 0$ is equivalent to

$$f_{0s}(0) = 0 \quad \text{and} \quad f_{1s}(0) = 0. \quad (2.44)$$

Applying condition (2.44)₁ to equation (2.42) yields

$$c_0 = -2f'_{0s}(0) \quad (2.45)$$

and applying (2.44)₂ to equation (2.43) yields

$$c_1 = -2f'_{1s}(0) \quad (2.46)$$

Provided $c_0 > 0$ (and therefore $f'_{0s}(0) < 0$, which is true for the reversed flow shown in figure 2.4b), the solution to (2.42) is easily shown to be

$$f_{0s} = \sqrt{c_0} \frac{1 - \exp(\sqrt{c_0}\alpha)}{1 + \exp(\sqrt{c_0}\alpha)}, \quad (2.47)$$

where the new constant of integration has been determined by again applying condition (2.44)₁. Equation (2.47) is the leading approximation to the stream function in the small shear layer at the free surface.

⁵If $s > 1/2$ equation (2.40) leads to

$$f'_{0s} = 0,$$

since the first (viscous) term on the right-hand side of equation (2.40) would not balance with any other term. If $s < 1/2$ then equation (2.40) gives

$$f_{0s}^2 = c_0,$$

since the term on the left-hand side of equation (2.40) would only balance with the constant in the final term on the right hand side. Both cases imply f_{0s} is constant throughout the interfacial region, but condition (2.9) then requires that the constant is zero, which eliminates the necessary surface region. Therefore, $s = 1/2$ is the only possible choice.

A more accurate solution is likely to be obtained by calculating f_{1s} . After substituting from (2.47), equation (2.43) can be solved in a standard way, using an integrating factor, to give

$$f_{1s} = -\frac{1}{2 + \exp(-\sqrt{c_0}\alpha) + \exp(\sqrt{c_0}\alpha)} \times \frac{b_0}{2} \left[\int \left\{ \alpha \exp(-\sqrt{c_0}\alpha) + 2\alpha + \alpha \exp(\sqrt{c_0}\alpha) \right\} d\alpha \right] - \left(\frac{c_1}{2} \right) \frac{1}{2 + \exp(-\sqrt{c_0}\alpha) + \exp(\sqrt{c_0}\alpha)} \int \left\{ \exp(-\sqrt{c_0}\alpha) + \exp(\sqrt{c_0}\alpha) + 2 \right\} d\alpha.$$

The displayed integral can then be integrated by parts to yield

$$f_{1s} = -\frac{b_0}{2c_0} \left[\frac{-\left(\alpha\sqrt{c_0} + 1\right) \exp(-\sqrt{c_0}\alpha) + \alpha^2 c_0 + \left(\alpha\sqrt{c_0} - 1\right) \exp(\sqrt{c_0}\alpha) + 2}{2 + \exp(-\sqrt{c_0}\alpha) + \exp(\sqrt{c_0}\alpha)} - \left(\frac{c_1}{2\sqrt{c_0}} \right) \frac{2\alpha - \exp(-\sqrt{c_0}\alpha) + \exp(\sqrt{c_0}\alpha)}{2 + \exp(-\sqrt{c_0}\alpha) + \exp(\sqrt{c_0}\alpha)} \right], \quad (2.48)$$

where the constant of integration has been determined by applying condition (2.44)₂.

Thermal solution

The temperature in the shear layer is found using a similar method to that outlined above. The viscous and thermal shear layers are assumed to have the same width, so in the thermal layer we introduce

$$\alpha = \frac{\mu}{K^{-\frac{1}{2}}} \quad (2.49)$$

Substituting equation (2.49) into (2.6) leads to

$$K^{\frac{1}{2}} \left(K^{-\frac{1}{2}} t'_{0s} + K^{-1} t'_{1s} \right) = \zeta_2 K^{-\frac{1}{2}} \frac{\left(K^{\frac{1}{2}} f_{0s} + f_{1s} \right) \left(K^{-\frac{1}{2}} t_{0s} + K^{-1} t_{1s} \right)}{1 - \left(K^{-\frac{1}{2}} \alpha \right)^2}. \quad (2.50)$$

In this case the leading and first order approximations to equation (2.50) are

$$t'_{0s} = 0 \quad (2.51)$$

and

$$t'_{1s} = \zeta_2 f_{0s} t_{0s}, \quad (2.52)$$

whereas boundary condition (2.9) ($t'(0) = 0$) leads to the conditions

$$t'_{0s}(0) = 0 \quad \text{and} \quad t'_{1s}(0) = 0. \quad (2.53)$$

Equation (2.51) implies that

$$t_{0s} = t_{0s}(0) \quad (2.54)$$

where $t_{0s}(0)$ is a constant. Integrating equation (2.52) yields

$$t_{1s} = \zeta_2 t_{0s}(0) \left[\sqrt{c_0} \alpha - \ln \left(1 + \exp(\sqrt{c_0} \alpha) \right)^2 \right] + t_{1s}(0) + \zeta_2 t_{0s}(0) \ln(4) \quad (2.55)$$

where $t_{1s}(0)$ is a constant of integration.

The final boundary condition (2.10), for the shear stress on the free surface, can be rewritten using the asymptotic expansions described above as

$$K \left(K^{\frac{1}{2}} f''_{0s}(0) + f''_{1s}(0) \right) = \zeta_1 K^{\frac{3}{2}} \left(K^{-\frac{1}{2}} t_{0s}(0) + K^{-1} t_{1s}(0) \right). \quad (2.56)$$

Therefore, the leading order and first order boundary conditions emanating from (2.56) are

$$f''_{0s}(0) = 0$$

⁶and

$$f''_{1s}(0) = \zeta_1 t_{0s}(0),$$

respectively.

Equation (2.51) reveals that to leading order the temperature is constant throughout the surface layer.

Observe that taking the limit as $\alpha \rightarrow 0$ of the differential with respect to α of equation (2.43) leads to

$$b_0 = -2f''_{1s}(0) = -2\zeta_1 t_{0s}(0), \quad (2.57)$$

since $f_{1s}(0) = 0$ (condition (2.44)₂). Therefore using equations (2.29)₁ and (2.30)₁ we obtain

$$a_0 = \frac{r'(1)}{2} + \zeta_1 t_{0s}(0) \quad \text{and} \quad c_0 = r(1) - \frac{r'(1)}{2} + \zeta_1 t_{0s}(0). \quad (2.58)$$

Using (2.45) it is clear that equations (2.57) and (2.58) are the leading order expansions of equations (2.11) to (2.13). Similarly, using (2.46), the first order expansions of equations (2.11) to (2.13) give

$$a_1 = \zeta_1 t_{1s}(0), \quad b_1 = -2\zeta_1 t_{1s}(0) \quad \text{and} \quad c_1 = \zeta_1 t_{1s}(0). \quad (2.59)$$

2.4.3 Matching

To obtain the remaining constants C_{t_0} and C_{t_1} in equations (2.34) and (2.36) in terms of $t_{1s}(0)$ we match the leading and first order expressions for the stream function. We adopt Van Dyke's [128] approach by using the *asymptotic matching principle*:

$$\begin{aligned} &\text{The } m\text{-term inner expansion of (the } n\text{-term outer expansion)} = \\ &\text{the } n\text{-term outer expansion of (the } m\text{-term inner expansion),} \end{aligned}$$

⁶Note that the equation $f''_{0s} = 0$ is consistent with the limit of the differential of equation (2.42) as $\alpha \rightarrow 0$.

and choosing $m = n = 2$. In our work *outer* refers to the main fluid region, whereas *inner* refers to the surface shear layer.

It follows from equations (2.34) and (2.36) in section 2.4.1 that the 2-term outer expansion, in inner variables, is

$$\begin{aligned}
K^{-\frac{1}{2}}t_0(K^{-\frac{1}{2}}\alpha) + K^{-1}t_1(K^{-\frac{1}{2}}\alpha) &= K^{-\frac{1}{2}}C_{t_0} \exp \left[\zeta_2 \int_0^{K^{-\frac{1}{2}}\alpha} \frac{f_0(K^{-\frac{1}{2}}\alpha)}{1 - K^{-1}\alpha^2} d(K^{-\frac{1}{2}}\alpha) \right] \\
&+ K^{-1}t_0(K^{-\frac{1}{2}}\alpha)\zeta_2 \int_0^{K^{-\frac{1}{2}}\alpha} \frac{f_1(K^{-\frac{1}{2}}\alpha)}{1 - K^{-1}\alpha^2} d(K^{-\frac{1}{2}}\alpha) \\
&+ K^{-1} \frac{C_{t_1}}{C_{t_0}} t_0(K^{-\frac{1}{2}}\alpha). \tag{2.60}
\end{aligned}$$

Expanding in a Taylor series in the small parameter $K^{-\frac{1}{2}}$, it is easily shown that the 2-term inner expansion of the 2-term outer solution is

$$K^{-\frac{1}{2}}t_0(K^{-\frac{1}{2}}\alpha) + K^{-1}t_1(K^{-\frac{1}{2}}\alpha) = C_{t_0}K^{-\frac{1}{2}} + \left(-C_{t_0}\zeta_2\sqrt{c_0}\alpha + C_{t_1} \right) K^{-1}. \tag{2.61}$$

Similarly the 2-term inner expansion, in outer variables, can be written as

$$\begin{aligned}
K^{-\frac{1}{2}}t_{0s}(\mu) + K^{-1}t_{1s}(\mu) &= t_{0s}(0)K^{-\frac{1}{2}} + \left(t_{1s}(0) + \zeta_2 t_{0s}(0) \ln(4) \right) K^{-1} \\
&+ \zeta_2 t_{0s}(0) \left[\sqrt{c_0 K} - 2 \ln \left(1 + \exp(\sqrt{c_0 K} \mu) \right) \right] K^{-1} \tag{2.62}
\end{aligned}$$

which on expansion gives the leading two terms in the form

$$t_{0s}(0)K^{-\frac{1}{2}} + \left(-\zeta_2 t_{0s}(0)\sqrt{c_0 K} \mu + 2 \ln(2)\zeta_2 t_{0s}(0) + t_{1s}(0) \right) K^{-1}. \tag{2.63}$$

Therefore, writing (2.63) in terms of α and equating with (2.61) gives

$$C_{t_0} = t_{0s}(0) \quad \text{and} \quad C_{t_1} = 2 \ln(2)\zeta_2 t_{0s}(0) + t_{1s}(0). \tag{2.64}$$

A composite solution, which is uniformly valid over the entire region, is obtained from the addition of the inner and outer expansions and subtraction of the common parts of the leading and first order expansions in the two regions. Therefore, the approximate first order solution for f is

$$f_c(\mu) = K^{\frac{1}{2}}f_{0c} + f_{1c} = K^{\frac{1}{2}} \left(f_0 + f_{0s} + \sqrt{c_0} \right) + \left(f_1 + f_{1s} + \frac{b_0}{2c_0} \left((c_0 K)^{\frac{1}{2}} \mu - 1 \right) + \frac{c_1}{2\sqrt{c_0}} \right), \tag{2.65}$$

where f_{0c} and f_{1c} denote the leading and first order composite asymptotic approximations of the non-dimensional stream function. With the calculated expressions for f_0 , f_1 , f_{0s} and f_{1s} , the composite asymptotic solution for the non-dimensional stream function (for large magnitude negative surface tension gradient and large non-dimensional parameter K) can be

written explicitly as

$$\begin{aligned}
f_c(\mu) = & K^{\frac{1}{2}} \left\{ - \left(a_0 \mu^2 + b_0 \mu + c_0 - r(\mu) \right)^{\frac{1}{2}} + \sqrt{c_0} \left(\frac{1 - \exp \left((c_0 K)^{\frac{1}{2}} \mu \right)}{1 + \exp \left((c_0 K)^{\frac{1}{2}} \mu \right)} \right) + \sqrt{c_0} \right\} \\
& + \left(1 - \mu^2 \right) \frac{2a_0 \mu + b_0 - r'(\mu)}{2(a_0 \mu^2 + b_0 \mu + c_0 - r(\mu))} - \frac{a_1 \mu^2 + b_1 \mu + c_1}{2[a_0 \mu^2 + b_0 \mu + c_0 - r(\mu)]^{\frac{1}{2}}} \\
& + 2\mu + \frac{b_0}{2c_0} \left((c_0 K)^{\frac{1}{2}} \mu - 1 \right) + \frac{c_1}{2\sqrt{c_0}} \\
& - \frac{b_0}{2c_0 \left(2 \exp \left(- (c_0 K)^{\frac{1}{2}} \mu \right) + \exp \left(- 2(c_0 K)^{\frac{1}{2}} \mu \right) + 1 \right)} \\
& \times \left[- \left((c_0 K)^{\frac{1}{2}} \mu + 1 \right) \exp \left(- 2(c_0 K)^{\frac{1}{2}} \mu \right) \right. \\
& \quad \left. + (c_0 K \mu^2 + 2) \exp \left(- (c_0 K)^{\frac{1}{2}} \mu \right) + \left((c_0 K)^{\frac{1}{2}} \mu - 1 \right) \right] \\
& - \frac{c_1}{2\sqrt{c_0}} \frac{2K^{\frac{1}{2}} \mu - \exp(-\sqrt{c_0 K} \mu) + \exp(\sqrt{c_0 K} \mu)}{2 + \exp(-\sqrt{c_0 K} \mu) + \exp(\sqrt{c_0 K} \mu)}. \tag{2.66}
\end{aligned}$$

Similarly the approximate first order solution for t is

$$\begin{aligned}
t_c(\mu) &= K^{-\frac{1}{2}} t_{0c} + K^{-1} t_{1c} \tag{2.67} \\
&= K^{-\frac{1}{2}} \left(t_0 + t_{0s} - t_{0s}(0) \right) + K^{-1} \left(t_1 + t_{1s} + \zeta_2 t_{0s}(0) \left\{ \sqrt{c_0 K} \mu - 2 \ln(2) \right\} - t_{1s}(0) \right).
\end{aligned}$$

where t_{0c} and t_{1c} denote the leading and first order composite approximation for the temperature. With the calculated expressions for t_0 , t_1 , t_{0s} and t_{1s} , the composite asymptotic solution for the temperature (for large magnitude negative surface tension gradient and large non-dimensional parameter K) can be written explicitly as

$$\begin{aligned}
t_c(\mu) = & K^{-\frac{1}{2}} \left\{ t_{0s}(0) \exp \left[\zeta_2 \int_0^\mu \frac{f_0(\nu)}{1 - \nu^2} d\nu \right] \right\} \\
& + K^{-1} \left\{ t_0(\mu) \zeta_2 \int_0^\mu \frac{f_1(\nu)}{1 - \nu^2} d\nu + \frac{\left(t_{1s}(0) + 2 \ln(2) \zeta_2 t_{0s}(0) \right)}{t_{0s}(0)} t_0(\mu) \right. \\
& \quad \left. + 2 \zeta_2 t_{0s}(0) \left[\sqrt{c_0 K} - \ln \left(1 + \exp(\sqrt{c_0 K} \mu) \right) \right] \right\} \tag{2.68}
\end{aligned}$$

The constants $t_{0s}(0)$ and $t_{1s}(0)$ remain to be calculated. As discussed earlier, in this thesis this final boundary condition is taken to be the one used by Belgrove [7], since it has been shown in experiments, [65], that the applied current J_0 and heat input Q_{in} are approximately related by the equation

$$6J_0 = Q_{in}.$$

This assumption is again used here, and provides the extra condition

$$6J_0 = Q_{in} = 2\pi k \int_0^1 t(\mu) \left(1 - \frac{\nu}{\kappa} f'(\mu)\right) d\mu, \quad (2.69)$$

where $k = \rho c_p \kappa$ denotes the thermal conduction coefficient. With the aid of equations (2.19) and (2.66), equation (2.69) can be written as

$$\begin{aligned} \frac{3J_0}{\pi k} = & K^{-\frac{1}{2}} \left[\int_{\varepsilon}^1 t_0(\mu) (1 - \zeta_2 f'_0(\mu)) d\mu - \zeta_2 \int_0^{K^{\frac{1}{2}\varepsilon}} t_{0s}(\alpha) f'_{0s}(\alpha) d\alpha \right] \\ & + K^{-1} \left[\int_{\varepsilon}^1 \left\{ t_1(\mu) [1 - \zeta_2 f'_0(\mu)] - \zeta_2 t_0(\mu) f'_1(\mu) \right\} d\mu \right. \\ & \left. + \int_0^{K^{\frac{1}{2}\varepsilon}} \left\{ t_{0s}(\alpha) [1 - \zeta_2 f'_{1s}(\alpha)] - \zeta_2 t_{1s}(\alpha) f'_{0s}(\alpha) \right\} d\alpha \right] \quad (2.70) \end{aligned}$$

to leading and first order, where ε is a small parameter denoting the thickness of the shear layer. Taking the limit $\varepsilon \rightarrow 0$ in the lower bound of the first integral and $K^{\frac{1}{2}\varepsilon} \rightarrow \infty$ in the upper bound of the second integral, the leading order expression

$$\frac{3J_0 K^{\frac{1}{2}}}{\pi k} = \int_0^1 t_0(\mu) (1 - \zeta_2 f'_0(\mu)) d\mu + \sqrt{c_0} \zeta_2 t_{0s}(0), \quad (2.71)$$

gives a non-linear equation for $t_{0s}(0)$. Incorporating the remaining sections of the integrals, introduced by the approximations $\varepsilon \rightarrow 0$ and $K^{\frac{1}{2}\varepsilon} \rightarrow \infty$ in the leading order expression, into the equation for the first order, we obtain

$$\begin{aligned} 0 = & \int_{\varepsilon}^1 \left\{ t_1(\mu) (1 - \zeta_2 f'_0(\mu)) - \zeta_2 t_0(\mu) f'_1(\mu) \right\} d\mu + K^{\frac{1}{2}} \varepsilon t_{0s}(0) \\ & + \zeta_2 t_{0s}(0) \left[\frac{b_0}{2c_0} (\sqrt{c_0} K^{\frac{1}{2}} \varepsilon - 1) - \frac{c_1}{2\sqrt{c_0}} \right] - \zeta_2 \int_0^{K^{\frac{1}{2}\varepsilon}} t_{1s}(\alpha) f'_{0s}(\alpha) d\alpha \\ & - K^{\frac{1}{2}} \int_0^{\varepsilon} t_0(\mu) (1 - \zeta_2 f'_0(\mu)) d\mu + K^{\frac{1}{2}} \int_{K^{\frac{1}{2}\varepsilon}}^{\infty} \zeta_2 t_{0s}(\alpha) f'_{0s}(\alpha) d\alpha. \quad (2.72) \end{aligned}$$

The final integral term in (2.72) can be expressed as

$$-\frac{2\zeta_2 t_{0s}(0) \sqrt{c_0 K}}{1 + \exp(\sqrt{c_0 K} \varepsilon)} \quad \text{which clearly tends to zero when } K^{\frac{1}{2}} \text{ is large.}$$

Similarly, by expanding in powers of μ

$$-K^{\frac{1}{2}} \int_0^{\varepsilon} t_0(\mu) (1 - \zeta_2 f'_0(\mu)) d\mu = -K^{\frac{1}{2}} \varepsilon t_{0s}(0) \left(1 + \zeta_2 \frac{b_0}{2\sqrt{c_0}} \right),$$

to leading order. Incorporating these results in (2.72) yields

$$\begin{aligned} 0 = & \int_0^1 \left\{ t_1(\mu) (1 - \zeta_2 f'_0(\mu)) - \zeta_2 t_0(\mu) f'_1(\mu) \right\} d\mu - \zeta_2 \int_0^{\infty} t_{1s}(\alpha) f'_{0s}(\alpha) d\alpha \\ & - \zeta_2 t_{0s}(0) \frac{b_0}{2c_0} - \zeta_2 t_{0s}(0) \frac{c_1}{2\sqrt{c_0}}, \quad (2.73) \end{aligned}$$

where again we have taken the limit $\varepsilon \rightarrow 0$ in the lower bound of the first integral and $K^{\frac{1}{2}}\varepsilon \rightarrow \infty$ in the upper bound of the second integral. Using integration by parts it can be clearly shown that

$$\int_0^\infty t_{1s}(\alpha) f'_{0s}(\alpha) d\alpha = 2\zeta_2 t_{0s}(0) \sqrt{c_0} [1 - \ln(2)] - \sqrt{c_0} t_{1s}(0),$$

therefore equation (2.73) can be rearranged to yield

$$\begin{aligned} t_{1s}(0) = & - \left[\int_0^1 t_0(\mu) \left\{ \left[\ln(-f_0(\mu)) - \ln(1 - \mu^2) + 2 \ln(2) \zeta_2 \right] (1 - \zeta_2 f'_0(\mu)) \right. \right. \\ & \left. \left. - \zeta_2 \left[(1 - \mu^2) \frac{f'_0(\mu)}{f_0(\mu)} \right]' - 2\zeta_2 \right\} d\mu \right. \\ & \left. - 2\zeta_2 t_{0s}(0) \sqrt{c_0} (1 - \ln(2)) - t_{0s}(0) \frac{b_0}{2c_0} \right] \\ & \times \left[\int_0^1 t_0(\mu) \left\{ \left(-\frac{\zeta_1 \zeta_2}{2} \int_0^\mu \frac{(\nu - 1)^2}{(1 - \nu^2) f_0(\nu)} d\nu + \frac{1}{t_{0s}(0)} \right) (1 - \zeta_2 f'_0(\mu)) \right. \right. \\ & \left. \left. + \frac{\zeta_1 \zeta_2}{2} (\mu - 1) \left(\frac{2f_0(\mu) - (\mu - 1) f'_0(\mu)}{f_0^2(\mu)} \right) \right\} d\mu + \zeta_2 \sqrt{c_0} - \frac{\zeta_1 \zeta_2}{2\sqrt{c_0}} t_{0s}(0) \right]^{-1} \end{aligned} \quad (2.74)$$

a linear integral expression for $t_{1s}(0)$.

2.5 Method of solution

Equations (2.66), (2.68), (2.71) and (2.74) are solved simultaneously for steel for prescribed fixed values of the current J_0 and surface tension gradient $\partial\gamma/\partial T$. To evaluate the temperature distribution and stream function across the entire region the constants $t_{0s}(0)$ and $t_{1s}(0)$ must be calculated. An iterative process is employed to determine $t_{0s}(0)$ from (2.71), to a specified tolerance, for given values of surface tension gradient and current. Then $t_{1s}(0)$ can be determined by evaluating (2.74). The initial value of $t_{0s}(0)$ is guessed and f'_0 is evaluated using equation (2.25), then to evaluate t_0 the integral on the right hand side of equation (2.34) is calculated via the NAG routine D01AJF, using a range of 100 points equally spaced in μ between 0 and 1. Finally the outer integral in equation (2.71) is then integrated numerically over the entire range of $\mu \in [0, 1)$ ⁷ by the NAG routine D01GAF. This routine supplies values of the integrand at $\mu = \mu_m$ where $m \in [1, 999]$ and $\mu_m \in [0, 1)$. The value of $t_{0s}(0)$ is then altered until equation (2.71) is satisfied to within a specified tolerance of 1×10^{-5} . This tolerance level is comparable to the error introduced by the numerical integration. Further reduction in the value of the tolerance produced no distinguishable change in the results. The value calculated for $t_{0s}(0)$ is finally substituted into equations (2.74), (2.66) and (2.68) and

⁷Since the integrand in (2.34) contains a singularity at $\mu = 1$ equations (2.34) and (2.71) cannot be simply evaluated there. To avoid this complication the integral is evaluated over the interval $\mu \in [0, 1 - \delta]$ where $\delta = 1/100$ and we have denoted this by the range $\mu \in [0, 1)$.

the composite solutions for f and t are then plotted as functions of μ . Figure 2.11 summarises the program structure.

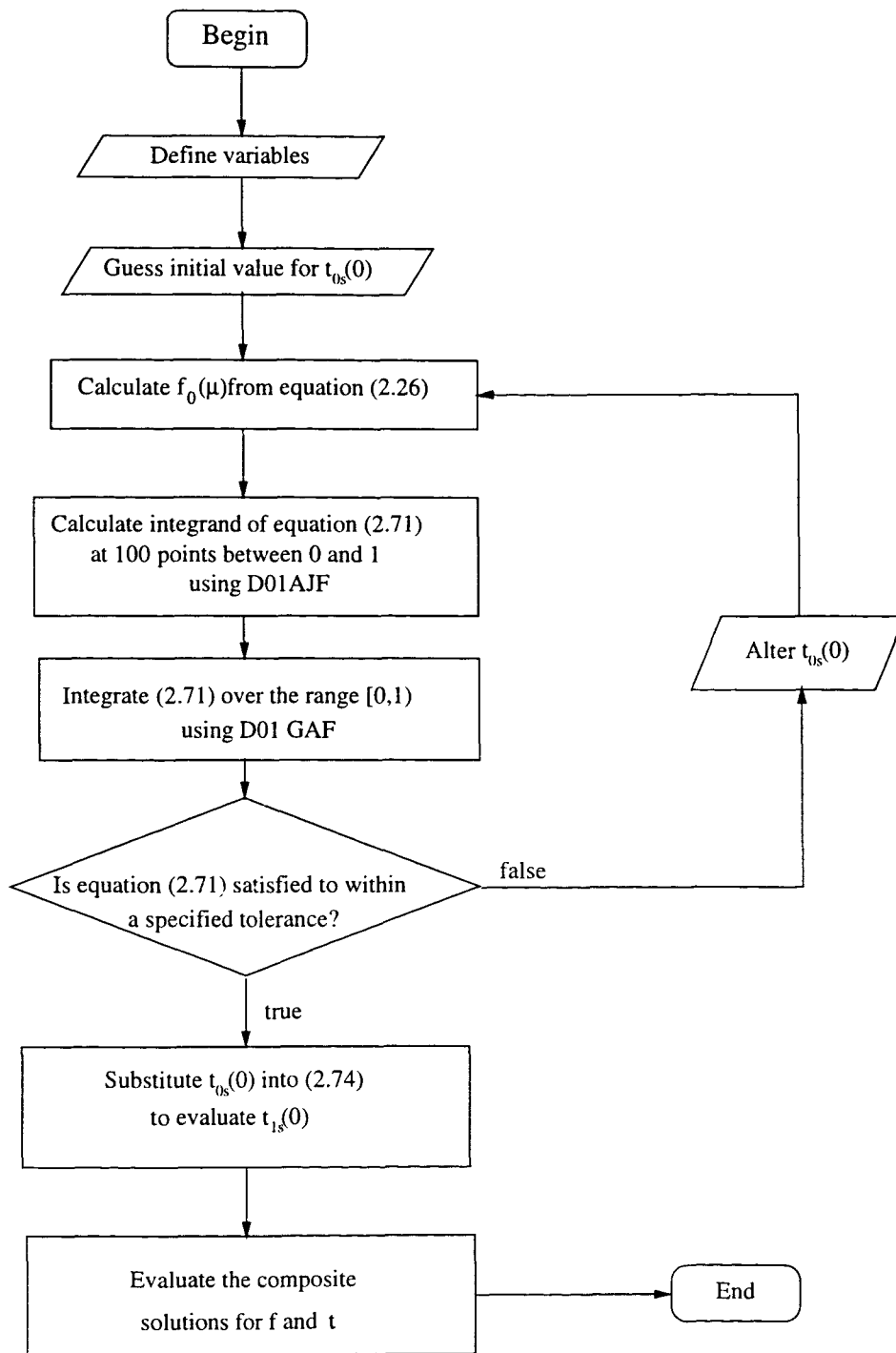


Figure 2.11: Program structure

2.6 Results and discussion

In all the results discussed in this section the values chosen for ν , κ , ρ and c_p are again

$$\rho = 7000 \text{kgm}^{-3}, \quad \nu = 6.4 \times 10^{-7} \text{m}^2 \text{s}^{-1},$$

$$\kappa = 1.0 \times 10^{-5} \text{m}^2 \text{s}^{-1} \quad \text{and} \quad c_p = 600 \text{Jkg}^{-1} \text{K}^{-1}.$$

These values are appropriate for liquid steel. The temperature will be highest at the origin and since we are restricting attention to $\partial\gamma/\partial T < 0$ the Marangoni force will try to make the fluid on the free surface flow away from the point source. The actual direction of flow, however, will depend on the relative magnitudes of the Marangoni and the other forces. In the model outlined in section 2.2 of this chapter three flow structures were possible for negative surface tension gradient, and these were shown schematically in figure 2.4. For the values of the parameters assumed above, however, the asymptotic model will only give one flow structure, namely the outward flowing single loop structure described in figure 2.4 as reversed flow.

Figures 2.12 and 2.13 display the values of $f(\mu)$ and $t(\mu)$, which are proportional to the stream function and the temperature respectively, for both the full numerical model and the composite asymptotic solution (given by equations (2.66) and (2.68) respectively), when $\partial\gamma/\partial T = -3 \times 10^{-5} \text{Nm}^{-1} \text{K}^{-1}$ and $K = 271.99$ (i.e. $J_0 = 3.5A$ for steel). With these parameter values it is easily calculated that $\zeta_1 = 2.3325$ and $\zeta_2 = 1.0555$.

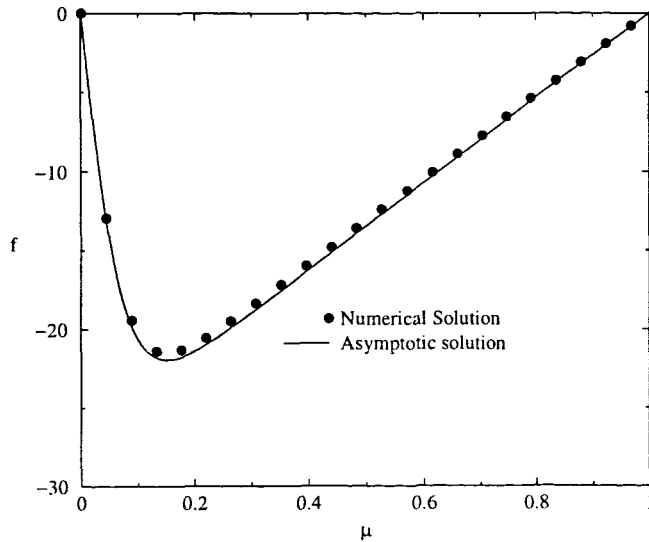


Figure 2.12: Variation of f with μ for the asymptotic and numerical solutions when $K = 271.99$ (i.e. $J_0 = 3.5A$ for steel) and $\partial\gamma/\partial T = -3 \times 10^{-5} \text{Nm}^{-1} \text{K}^{-1}$.

Figure 2.12 shows a strong outward flow near the top surface, flowing away from the point source. The temperature profile is clearly dependent on the polar angle θ , as is clearly

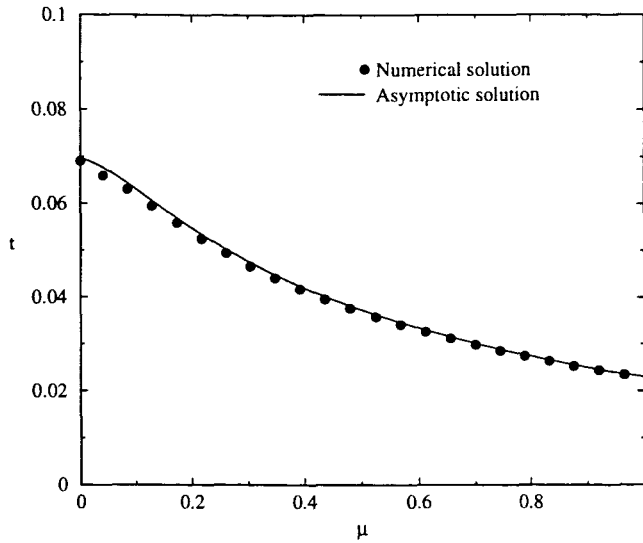


Figure 2.13: Variation of t with μ for the asymptotic and numerical solutions when $K = 271.99$ (i.e. $J_0 = 3.5A$ for steel) and $\partial\gamma/\partial T = -3 \times 10^{-5} Nm^{-1} K^{-1}$.

observed in figure 2.13. Both figures show very good agreement between the full numerical solution and the first order composite asymptotic solutions derived in section 2.4.3.

When the magnitude of the negative surface tension gradient $\partial\gamma/\partial T$ is reduced, but the value of J_0 is kept constant, the error between the asymptotic approximation and the numerical solution becomes more pronounced. Figures 2.14 and 2.15 show the numerical and asymptotic solutions to $f(\mu)$ and $t(\mu)$ respectively when $\partial\gamma/\partial T = -3 \times 10^{-6} Nm^{-1} K^{-1}$ and $J_0 = 3.5A$. These parameter values correspond to $\zeta_1 = 0.2335$ and $\zeta_2 = 1.0555$ and inspection of figure 2.9 shows that these choices place the solution just inside the surface tension dominated single loop region shown in figure 2.5. Being near the edge of this region, with a value for ζ_1 not close to 1, it is not surprising that some errors appear.

It is clear from figures 2.14 and 2.15 that the asymptotic solution is less accurate than for the previous case, especially for the temperature. However, it is expected that the accuracy could be improved by retaining more terms in the expansions.

As mentioned above the chosen values for the parameters J_0 and $\partial\gamma/\partial T$, and the associated values for ζ_1 and ζ_2 , place us close to the region of parameter space where a 2-loop flow develops (see figure 2.4c). This is confirmed by the fact that a slight increase in the value of the current in the numerical solution leads to the development of a two-loop flow structure, indicating that the surface tension forces no longer dominate the problem. Since the Lorentz-dominated counter rotating loop first develops near the axis of symmetry it is not surprising to see differences between the asymptotic approximation and numerical solution for both the streamfunction and temperature, visible in figures 2.14 and 2.15 as $\mu \rightarrow 1$.

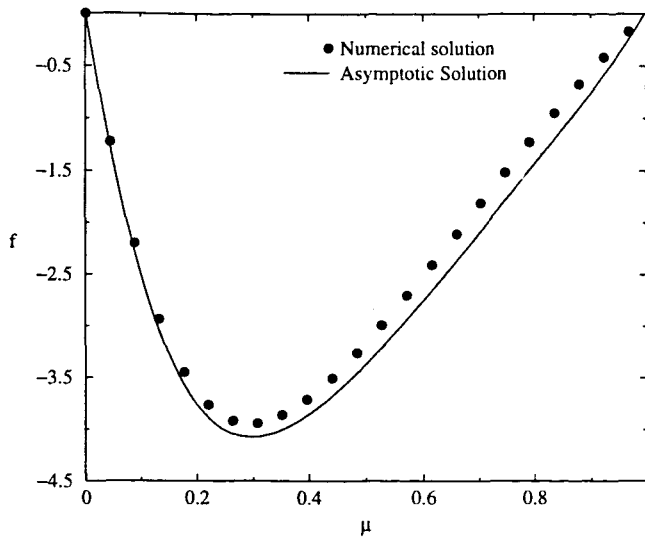


Figure 2.14: Variation of f with μ for the asymptotic and numerical solutions when $K = 271.99$ (i.e. $J_0 = 3.5A$ for steel) and $\partial\gamma/\partial T = -3 \times 10^{-6} Nm^{-1} K^{-1}$.

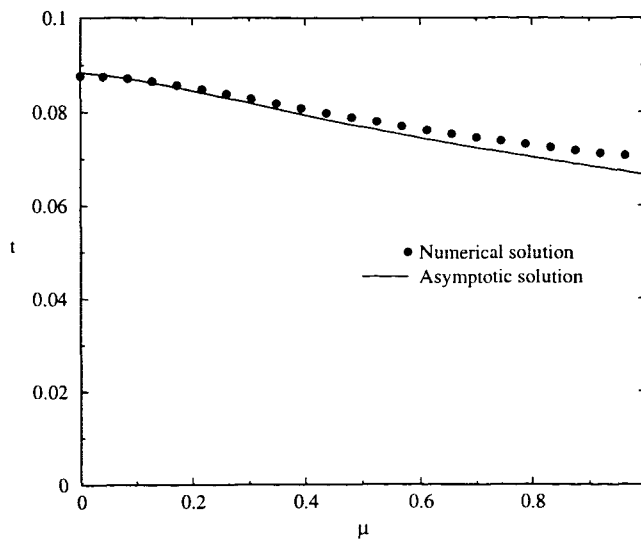


Figure 2.15: Variation of t with μ for the asymptotic and numerical solutions when $K = 271.99$ (i.e. $J_0 = 3.5A$ for steel) and $\partial\gamma/\partial T = -3 \times 10^{-6} Nm^{-1} K^{-1}$.

Figures 2.16 and 2.17 show profiles of f and t , proportional to the stream function and temperature, for the case $\partial\gamma/\partial T = -8 \times 10^{-6} Nm^{-1}K^{-1}$ and $J = 3.5A$ (corresponding to $\zeta_1 = 0.62201$ and $\zeta_2 = 1.0555$), i.e. a magnitude of $\partial\gamma/\partial T$ between the two previous values. Predictably the maximum error in both the temperature distribution and stream function lies between those obtained in the previous two cases.

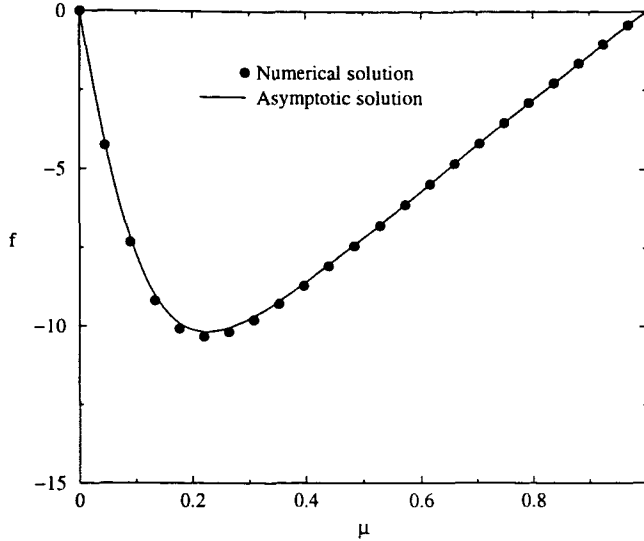


Figure 2.16: Variation of f with μ for the asymptotic and numerical solutions when $K = 271.99$ (i.e. $J_0 = 3.5A$ for steel) and $\partial\gamma/\partial T = -8 \times 10^{-6} Nm^{-1}K^{-1}$.

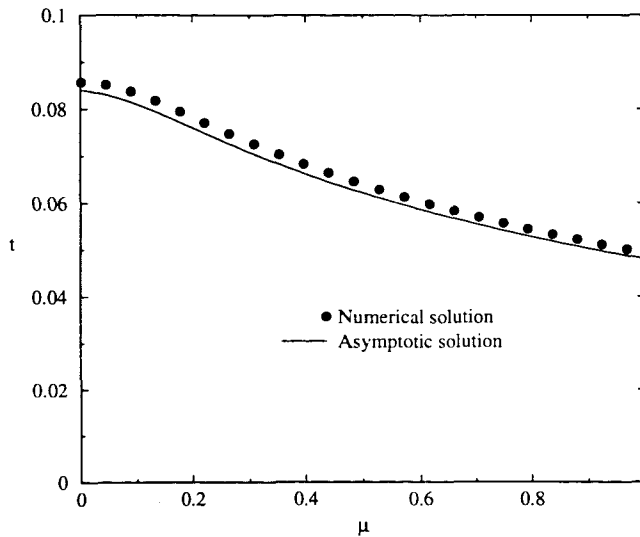


Figure 2.17: Variation of t with μ for the asymptotic and numerical solutions when $K = 271.99$ (i.e. $J_0 = 3.5A$ for steel) and $\partial\gamma/\partial T = -8 \times 10^{-6} Nm^{-1}K^{-1}$.

So far we have only shown examples of the asymptotic approximation for a fixed current

of $J_0 = 3.5A$. Increasing the current, and thereby the value of the large parameter K , should yield an accurate asymptotic approximation provided ζ_1 and ζ_2 remain $O(1)$. To confirm our view, graphs comparing the numerical and asymptotic solutions for the functions f and t , when $\partial\gamma/\partial T = -3 \times 10^{-5} Nm^{-1} K^{-1}$ and $J = 5.6A$, are shown in figures 2.18 and 2.19. These parameter values correspond to $\zeta_1 = 0.5695$ and $\zeta_2 = 1.6888$.

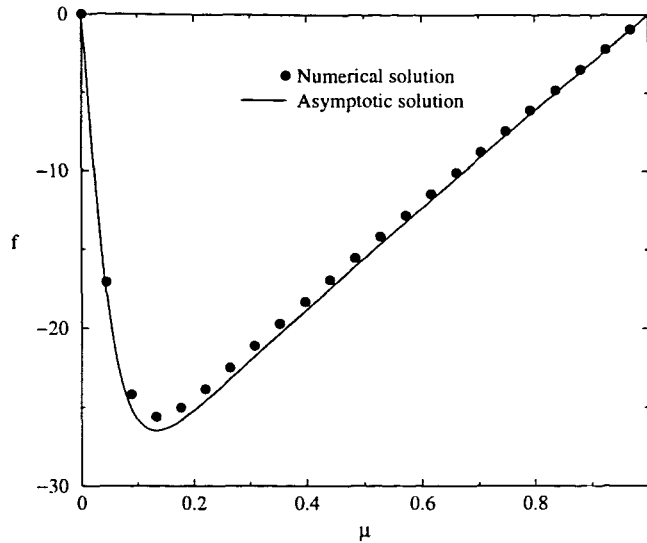


Figure 2.18: Variation of f with μ for asymptotic and numerical solutions when $K = 696.3$ (i.e. $J_0 = 5.6A$ for steel) and $\partial\gamma/\partial T = -3 \times 10^{-5} Nm^{-1} K^{-1}$.

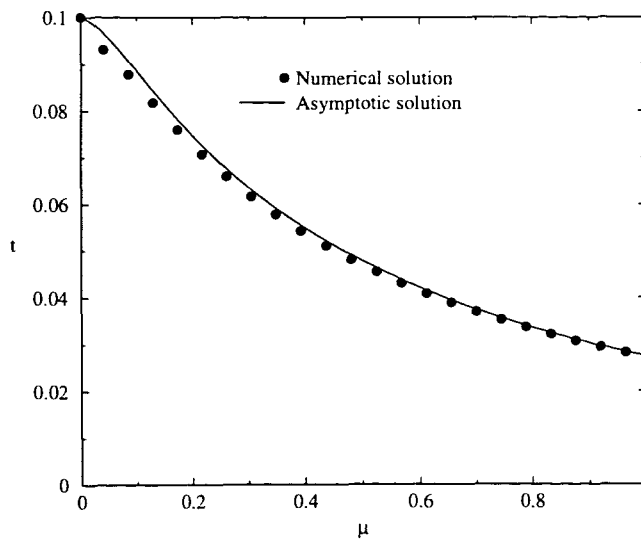


Figure 2.19: Variation of t with μ for the asymptotic and numerical solutions when $K = 696.3$ (i.e. $J_0 = 5.6A$ for steel) and $\partial\gamma/\partial T = -3 \times 10^{-5} Nm^{-1} K^{-1}$.

Discussion

Very good agreement between the asymptotic and numerical solutions has been obtained when ζ_1 and ζ_2 are both $O(1)$. When ζ_1 and ζ_2 differ from unity, however, the assumptions under which the asymptotic model was derived do not remain valid and hence, not surprisingly, the asymptotic solutions are less accurate.

At very low currents and low magnitudes of $\partial\gamma/\partial T$ the isotherms are quite flat. On increasing the current the isotherms become more spherical, since the effect of the surface tension force is negated by the increasing Lorentz force. Starting from a position in $(\partial\gamma/\partial T, J)$ -parameter space which leads to approximately spherical isotherms (as shown, for example, in figure 2.6) and then increasing the current, the Lorentz force begins to affect the flow structure by creating a second counter rotating loop close to the axis of symmetry ($\mu = 1$).

Note that breakdown of the asymptotic solution can be linked to the development of a double loop flow structure in the numerical solution, where a counter rotating Lorentz dominated loop appears near the axis of symmetry. When the second loop appears the stream function in the numerical model will change sign close to the axis of symmetry. In the asymptotic model, however, this change in sign is impossible since, in the main fluid region

$$g_0(\mu) = -\left(a_0\mu^2 + b_0\mu + c_0 - r(\mu)\right)^{\frac{1}{2}}, \quad (2.75)$$

which is always one-signed and negative provided the solution is real. Breakdown of the asymptotic solution clearly occurs if

$$a_0\mu^2 + b_0\mu + c_0 - r(\mu) < 0, \quad (2.76)$$

which, with the use of equations (2.58)₁, (2.57) and (2.58)₂, is equivalent to

$$\zeta_1 t_0(0) < \frac{-2\left(2\ln(2) - 1\right)\mu^2 - 2\mu - 3\mu^2 + 2(1 + \mu)^2 \ln(1 + \mu) + 3 - 4\ln(2)}{2(\mu - 1)^2}. \quad (2.77)$$

It is easily shown that the right-hand side of equation (2.77) increases monotonically with μ and has its maximum value when $\mu = 1$. Both the numerator and denominator on the right-hand side of (2.77) vanish as $\mu \rightarrow 1$. Applying L'Hôpital's rule twice then gives the condition for breakdown as

$$\zeta_1 t_0(0) < 1 - \ln(2). \quad (2.78)$$

If the above inequality is satisfied then a real streamfunction does not exist in the asymptotic solution.

To conclude let us consider the results for the breakdown current. For a comparatively large negative surface tension gradient at low currents (but large K) the resulting Marangoni force creates outward flow on the free surface with a consequential upward flow, towards the point

source, along the axis of symmetry (shown in figure 2.4b). When the current is increased the larger Lorentz force causes the fluid velocity on the axis to slow down, and eventually reverse its direction, thereby creating a second counter rotating loop near this axis. It is well known from the results in [110] for a zero surface tension gradient (for which the Marangoni force is absent) that breakdown occurs due to the existence of a fluid jet down the axis of symmetry when the current is low, 2.05A for steel. The presence of surface tension on the free surface causes little change to Sozou's method of singularity development [110] once flow down the axis of symmetry has been achieved. It is not a surprise, therefore, that figure 2.5 reveals that the values of the applied current at which downward axial flows develop are very close to those values of the current at which breakdown occurs and the difference between these current values (i.e. curves 1 and 2 in figure 2.5) is relatively constant over a wide range of values of $-\partial\gamma/\partial T$.

Chapter 3

Steady state solution in a hemisphere

3.1 Introduction

In addition to obtaining a steady similarity solution for the temperature and stream function in a semi-infinite region of incompressible, thermally and electrically conducting viscous (ITEV) fluid due to a stationary point source of current and heat, Belgrove [7] also considered flow inside a hemispherical region. He solved this problem in a finite region numerically, also including the buoyancy force which has been shown to affect the shape of the weld pool, [12].

A problem encountered by experimentalists is the large standard deviation of a given parameter in a weld, say its depth, when an experiment is repeated under supposedly identical conditions. One possible cause is the existence of multiple steady-state solutions. In an attempt to increase our understanding of the problem, Belgrove [7] carried out a linear stability analysis of the solution inside a hemispherical weld-pool. No analytical solution is possible for the underlying steady-state situation so Belgrove had to adopt a full numerical solution to this problem and the associated stability analysis (for modes $m = 1, 2, 3$). Due to some errors in his lengthy code, however, Belgrove's stability results were slightly inaccurate. In chapter 4 of this thesis the analysis for the $m = 0$ azimuthal stability mode is investigated (this important case was not considered by Belgrove), whilst in chapter 5 Belgrove's results for the low non-zero modes of stability, $m = 1, 2$ and 3 , are reworked, corrected and extended.

Before any stability analysis can be attempted the underlying flow must be determined and in this chapter, therefore, a brief description of Belgrove's work for determining the flow inside a hemisphere of liquid metal is presented. Figure 3.1 shows the main geometrical features of the problem.

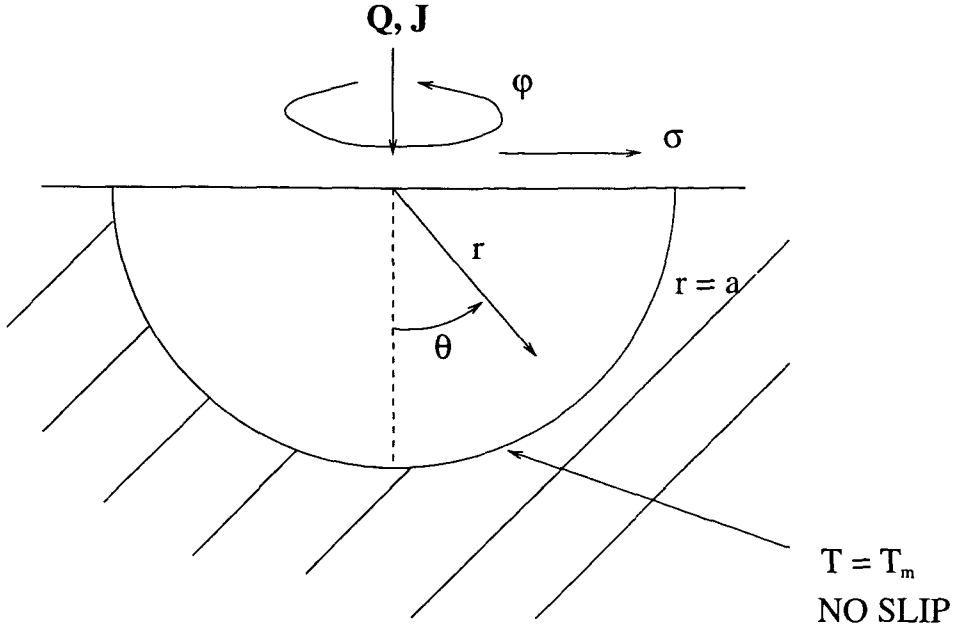


Figure 3.1: Geometry of the hemispherical flow model

Our model includes the electro-magnetic force (due to the current and its interaction with the self induced magnetic field), the Marangoni force on the free surface (due to the variation of the surface tension with temperature) and the buoyancy force (caused by density variations within the pool). The top (free) surface is assumed flat and a stationary point source of heat and current is placed on this surface at the centre of the hemisphere. The liquid is treated as a ITEV Newtonian fluid, the viscosity coefficient is assumed to be constant and the applied current and heat distributions are assumed to be spherically symmetric. The Boussinesq approximation is also used so the density is constant except in the buoyancy term where a linear variation in temperature is assumed. The current and induced magnetic field are further assumed to remain unchanged by the fluid flow, and these assumptions ensure that analytical expressions for the magnetic field and electro-motive force can be derived. No azimuthal rotation of the fluid is included at this stage.

3.2 The differential equations

The governing steady-state equations are:

the Navier-Stokes equations

$$-\mathbf{F}_B + \rho(\mathbf{v} \cdot \nabla)\mathbf{v} + \nabla p - \rho\nu\nabla^2\mathbf{v} - \mathbf{J} \times \mathbf{B} = 0, \quad (3.1)$$

where

$\rho(\mathbf{v} \cdot \nabla)\mathbf{v}$ denotes the inertial force, ∇p the pressure gradient, $\rho\nu\nabla^2\mathbf{v}$ the viscous force,

$\mathbf{J} \times \mathbf{B}$ the electro-magnetic force and \mathbf{F}_B the buoyancy force;

the incompressibility equation

$$\nabla \cdot \mathbf{v} = 0; \quad (3.2)$$

the heat transfer equation

$$\mathbf{v} \cdot \nabla T = \kappa \nabla^2 T + \epsilon_\nu + \epsilon_o, \quad (3.3)$$

where $\kappa \nabla^2 T$ represents heat transfer due to conduction and ϵ_ν, ϵ_o denote viscous dissipation and ohmic heating respectively. The last two terms are small and will be ignored.

We introduce the spherical polar coordinate system (r, θ, ϕ) as shown in figure 3.1. The axis of symmetry and free surface are given, therefore, on $\theta = 0$ and $\pi/2$ respectively and the point source of heat and current is located at $r = 0$. The unit vectors in each of the coordinate directions at any point are denoted by $\hat{\mathbf{r}}, \hat{\boldsymbol{\theta}}$ and $\hat{\boldsymbol{\phi}}$ respectively.

A Stokes stream function ψ is introduced and expressed in the form

$$\psi = \nu r g(\mu, \lambda),$$

where $\lambda = r/a$ (a is the radius of the hemisphere) and $\mu = \cos \theta$. Assuming that the fluid flow is axisymmetric with no azimuthal component, the velocity \mathbf{v} is connected to the stream function by

$$\mathbf{v} = \nabla \times \left(0, 0, \frac{\psi}{r \sin \theta} \right). \quad (3.4)$$

Substituting for ψ it then follows that

$$\mathbf{v} = -\frac{\nu}{r} \left(g_\mu, \frac{g + \lambda g_\lambda}{(1 - \mu^2)^{\frac{1}{2}}}, 0 \right), \quad (3.5)$$

where in this equation and throughout the remainder of the chapter the subscripts μ and λ denote partial derivatives with respect to those variables.

The temperature T is written

$$T = \frac{T_m a}{r} t(\mu, \lambda), \quad (3.6)$$

where T_m is the melting temperature (which we take to be 1700K for steel) and t is non-dimensional. With the Boussinesq approximation the buoyancy force, \mathbf{F}_B , has the form

$$\mathbf{F}_B = -(\rho - \rho_m) g_e \mathbf{e}_z, \quad (3.7)$$

where g_e represents the acceleration due to gravity, ρ_m is the density of the metal at its melting temperature and $\mathbf{e}_z = -(\hat{\mathbf{r}} \cos \theta - \hat{\boldsymbol{\theta}} \sin \theta)$ is the unit vector in the upward vertical direction. The change in density is approximated by the expression

$$\rho - \rho_m = -\rho \beta \left(\frac{T_m a t}{r} - T_m \right). \quad (3.8)$$

where β is the coefficient of expansion of the liquid metal.

The MHD (magneto- hydro- dynamic) equations which govern the flow of electrically conducting liquids are summarised by equations (2.2), (2.3) and (2.4). Using equations (3.5), (3.6), (3.7), (2.2) and (2.4), the curl of equation (3.1) becomes

$$(1 - \mu^2)f_{\mu\mu} - 4\mu f_{\mu} + \lambda^2 f_{\lambda\lambda} - 2\lambda f_{\lambda} - \frac{K}{1 + \mu} + R_r \lambda^2 (-\lambda t_{\lambda} + t + \mu t_{\mu}) = 3f g_{\mu} + g f_{\mu} + \lambda(f_{\mu} g_{\lambda} - f_{\lambda} g_{\mu}), \quad (3.9)$$

where

$$f = g_{\mu\mu} + \frac{(2\lambda g_{\lambda} + \lambda^2 g_{\lambda\lambda})}{(1 - \mu^2)} = \frac{-r^2}{\nu(1 - \mu^2)^{\frac{1}{2}}} (\nabla \times \mathbf{v})_{\phi}. \quad (3.10)$$

The quantity $(\nabla \times \mathbf{v})_{\phi}$ represents the ϕ -component of $\nabla \times \mathbf{v}$. The *parameter of electrically induced vortical flow* K is defined in chapter 1 by

$$K = \frac{J_0^2 \mu_0}{2\pi^2 \nu^2 \rho}$$

and R_r , related to the Rayleigh number, is defined by

$$R_r = \frac{g_e \beta T_m a^3}{\nu^2}. \quad (3.11)$$

Dropping the viscous dissipation and ohmic heating terms the temperature equation (3.3) reduces to

$$P_r [-(\lambda t_{\lambda} - t)g_{\mu} + (g + \lambda g_{\lambda})t_{\mu}] = \lambda^2 t_{\lambda\lambda} - 2\mu t_{\mu} + (1 - \mu^2)t_{\mu\mu}, \quad (3.12)$$

where P_r is the Prandtl number defined by

$$P_r = \frac{\nu}{\kappa}.$$

The equations are then transformed, following Sozou and Pickering [115], by defining a new variable

$$\eta = (1 - \mu)^{\frac{1}{2}}. \quad (3.13)$$

This transformation ensures that the governing differential equations are elliptic throughout the region of interest. The introduction of η also improves the distribution of grid lines in the hemisphere since equal spacing in the η variable corresponds fairly closely to equal spacing in θ , whereas equal spacing in μ leads to very unequal spacing in θ . The distribution of grid lines is discussed in detail in chapter 4.

To denote this change of variable the dependent variables $f(\mu, \lambda)$, $g(\mu, \lambda)$ and $t(\mu, \lambda)$ are replaced by $f(\eta, \lambda)$, $g(\eta, \lambda)$ and $t(\eta, \lambda)$ respectively. With these changes the governing system, comprising equations (3.9), (3.10) and (3.12), becomes

$$(2 - \eta^2)f_{\eta\eta} + (2\lambda g_{\lambda} + 2g + 6 - 7\eta^2)\frac{f_{\eta}}{\eta} + 4\lambda^2 f_{\lambda\lambda} - 2\lambda\left(\frac{g_{\eta}}{\eta} + 4\right)f_{\lambda} + 6\frac{g_{\eta}f}{\eta} - \frac{4K}{2 - \eta^2} + R_r \lambda^2 \left[-\lambda t_{\lambda} + t - \frac{1 - \eta^2}{2\eta} t_{\eta} \right] = 0, \quad (3.14)$$

$$-f - \frac{\mathbf{g}_\eta}{4\eta^3} + \frac{\mathbf{g}_{\eta\eta}}{4\eta^2} + \frac{(2\lambda\mathbf{g}_\lambda + \lambda^2\mathbf{g}_{\lambda\lambda})}{(2 - \eta^2)\eta^2} = 0 \quad (3.15)$$

and

$$-\frac{1}{2\eta}\mathbf{g}_\eta(\lambda t_\lambda - t) + \frac{1}{2\eta}t_\eta(\mathbf{g} + \lambda\mathbf{g}_\lambda) + \frac{1}{P_r}\left[\lambda^2 t_{\lambda\lambda} + \frac{(2 - 3\eta^2)}{4\eta}t_\eta + \frac{(2 - \eta^2)}{4}t_{\eta\eta}\right] = 0, \quad (3.16)$$

where the subscript η denotes differentiation with respect to that variable. Note also that the free surface now becomes $\eta = 1$ and the axis is $\eta = 0$.

3.3 Boundary conditions

The boundary conditions to be applied to the differential equations (3.14), (3.15) and (3.16) are listed below, with reasons for their validity.

Velocity

$$\mathbf{v} \text{ is finite on the axis of symmetry} \quad \mathbf{g}(0, \lambda) = 0; \quad (3.17)$$

$$\text{no slip on the hemispherical boundary} \quad \mathbf{g}(\eta, 1) = 0, \quad \mathbf{g}_\lambda(\eta, 1) = 0; \quad (3.18)$$

$$\text{no velocity perpendicular to the free surface} \quad \mathbf{g}(1, \lambda) = 0; \quad (3.19)$$

the flow at the origin approaches the similarity solution described in section 2.2 of chapter 2 for flow in a semi-infinite region

$$\mathbf{g}(\eta, 0) = g^0(\mu), \quad (3.20)$$

$$f(\eta, 0) = g^0_{\mu\mu}(\mu); \quad (3.21)$$

the derivative of the non-dimensional vorticity function f is

$$\text{finite on the axis } \theta = 0 \text{ (by symmetry)} \quad f_\eta(0, \lambda) = 0; \quad (3.22)$$

$$(3.15) \text{ evaluated on } \lambda = 1 \quad f(\eta, 1) = \frac{\mathbf{g}_{\lambda\lambda}}{\eta^2(2 - \eta^2)}; \quad (3.23)$$

$$(3.15) \text{ evaluated on } \eta = 0 \text{ and } \lambda = 1 \quad f(0, 1) = \frac{1}{4}\mathbf{g}_{\eta\eta\lambda\lambda}. \quad (3.24)$$

In addition, by considering the surface stresses on the free surface of the weld pool it is easily seen that

$$\sigma_{r\theta} = \rho\nu\left(\frac{1}{r}\frac{\partial v_r}{\partial\theta} - \frac{v_\theta}{r} + \frac{\partial v_\theta}{\partial r}\right) = \frac{\partial\gamma}{\partial r} = \frac{\partial\gamma}{\partial T}\frac{\partial T}{\partial r}, \quad (3.25)$$

from which it follows that a further boundary condition to be satisfied on the surface $\eta = 1$ is

$$f(1, \lambda) = \gamma_T\left(\lambda t_\lambda(1, \lambda) - t(1, \lambda)\right),$$

where the parameter γ_T is defined by

$$\gamma_T = \frac{T_m a}{\rho \nu^2} \frac{\partial \gamma}{\partial T}.$$

With the earlier choices of material parameters for steel it follows that when $\partial \gamma / \partial T \approx 10^{-7}$ the parameter $\gamma_T \approx 10^2$.

Temperature

$$\text{No heat flux across the free surface} \quad t_\eta(0, \lambda) = 0; \quad (3.26)$$

$$\text{no heat flux across the axis of symmetry} \quad t_\eta(1, \lambda) = 0; \quad (3.27)$$

$$\text{the temperature on the hemisphere is the melting temperature} \quad t(\eta, 1) = 1; \quad (3.28)$$

$$t \text{ tends to the similarity solution described in section 2.2 at the origin } t(\eta, 0) = t^0(\mu). \quad (3.29)$$

All the boundary conditions stated above were used by Belgrove in [7].

3.4 Finite differences

The finite difference method used here to solve the system of equations and boundary conditions is the same as that adopted by Belgrove. His method has been fully discussed in [7], so only a brief summary is given here. The grid points used are equally spaced in both the λ and η directions. All second derivatives are approximated by central differences, whereas the first derivative of a variable is approximated by the Leonard QUI (quadratic upstream interpolation) method [68] in the equation which is being used to update the value of that variable. Elsewhere, central differences are employed to approximate first derivatives. Therefore, Leonard's method is used to approximate f_λ and f_η in equation (3.14), g_λ and g_η in equation (3.15) and t_λ and t_η in equation (3.16) but central differences are used for all other derivatives.

Leonard's method avoids both the stability problems associated with using central differences for first derivatives and the inaccuracies of upstream numerical diffusion, and a brief discussion follows. Consider the differential equation

$$\frac{\partial \phi}{\partial t} = -u \frac{\partial \phi}{\partial x} + d \frac{\partial^2 \phi}{\partial x^2} + S, \quad (3.30)$$

where ϕ , t , u , x and d denote a material variable, time, velocity, spatial position and the (positive) diffusion coefficient respectively. The quantity S represents any other source or transport terms and may involve derivatives of variables other than ϕ . Expressing the first derivative $\partial \phi / \partial x$ in equation (3.30) in terms of standard one-sided differences, namely

$$\frac{\partial \phi}{\partial x} = \frac{\phi_{x+dx} - \phi_x}{\delta x}$$

when using forward (downwind) differencing and

$$\frac{\partial\phi}{\partial x} = \frac{\phi_x - \phi_{x-dx}}{\delta x}$$

when using backward (upwind) differencing, leads to discretisation errors

$$+\frac{u}{2} \frac{dx}{\delta x} \frac{\partial^2\phi}{\partial x^2} \quad \text{and} \quad -\frac{u}{2} \frac{dx}{\delta x} \frac{\partial^2\phi}{\partial x^2} \quad (3.31)$$

respectively. Therefore, using backward differences when u is large and positive, or using forward differences when u is large and negative, may result in errors which completely swamp the diffusion terms present in equation (3.30).

The QUI (Quadratic Upstream Interpolation) method of Leonard [68] replaces $-u\partial\phi/\partial x$ in (3.30) with

$$-u \left[\frac{2\phi_{x+dx} + 3\phi_x - 6\phi_{x-dx} + \phi_{x-2dx}}{6\delta x} \right] \quad \text{when} \quad u > 0 \quad (3.32)$$

and

$$-u \left[\frac{-\phi_{x+2dx} + 6\phi_{x+dx} - 3\phi_x - 2\phi_{x-dx}}{6\delta x} \right] \quad \text{when} \quad u < 0. \quad (3.33)$$

Using these expressions leads to a discretisation error of $O(\delta x^3)$. Discretisations (3.32) and (3.33) are a modification of the QUICK scheme outlined in both [68] and [44]. Although Leonard presents his method in one-dimension, Fletcher [44] discusses some papers where it has been successfully used in three dimensions, where it has been applied to the driven cavity problem in [122] and [83] for instance.

On the boundaries where a variable is unknown, fictitious points outside the region are used wherever possible, to avoid the use of one-sided derivatives. For a comprehensive list of all the discretised boundary conditions see [7].

The solution method employed in [7] and this thesis is to solve the system of equations using SUR (successive under-relaxation). Firstly, the similarity solution for flow in a semi-infinite region is calculated to obtain the values for g , f and t at $\lambda = 0$. Then f and g are initially set to zero everywhere else and t is given a linear profile from the origin to its known value on the outer hemisphere. In a single SUR sweep new values for the unknowns are then calculated at every grid point. When the maximum percentage change in any of the variables is less than 0.002% the iterative process is stopped.

Results were obtained using a grid size of 61×61 and a convergence tolerance of 0.002%. Increasing the number of points in the grid produced a very small maximum percentage change in f , g and T at any grid point. The convergence process was checked by calculating the error residues of the variables f , g and T at each grid point from equations (3.14), (3.15) and (3.16) for particular values of the parameters. The 2-norms of the error residues of equations (3.14), (3.15) and (3.16) over every grid point in the mesh were found to be

$O(10^{-6})$, $O(10^{-7})$ and $O(10^{-11})$ respectively. (The infinity norms of equations (3.14), (3.15) and (3.16) were calculated as $O(10^{-6})$, $O(10^{-9})$ and $O(10^{-12})$ respectively, and the approximate orders of magnitude for the variables f , g and T were $O(10)$, $O(10^{-2})$ and $O(1)$ respectively.)

3.5 Results

There are three forces acting within the hemisphere:-

- a buoyancy force (with $\beta = 1.25 \times 10^{-4} K^{-1}$, a realistic value for liquid steel),
- a Lorentz force, namely the $\mathbf{J} \times \mathbf{B}$ term in equation (3.1) and
- a Marangoni force arising from $\partial\gamma/\partial T$.

The Lorentz force creates a flow which is directed towards the source on the free surface and then down the axis of symmetry (away from the source). The buoyancy force usually seems to oppose the Lorentz force, whereas the Marangoni force reinforces the Lorentz force when $\partial\gamma/\partial T$ is positive but opposes the Lorentz force when $\partial\gamma/\partial T$ is negative. Therefore, when the value of $\partial\gamma/\partial T$ is positive but very small, the flow is largely governed by the buoyancy force when the current is small. However, on increasing the applied current and keeping the other parameters constant the Lorentz force grows until it dominates the other forces. These two situations are shown in figures 3.2 and 3.3 respectively. The Reynolds number Re , a dimensionless quantity which measures the ratio of momentum to viscous forces, is given by $\rho v L / \nu^1$ and for these flows its value is 7 and 80 respectively, both sufficiently low for the flow to be laminar.

As the value of $\partial\gamma/\partial T$ increases from its small positive value, the size of the loop created by the buoyancy force at low currents decreases and eventually disappears. Figure 3.4 shows the qualitative flow structure for positive $\partial\gamma/\partial T$. The dotted line represents the breakdown current for the similarity solution of the semi-infinite model, at a given value of $\partial\gamma/\partial T$, whereas the upper solid line denotes the corresponding breakdown current J_{crit} for the numerical solution in the hemisphere, the problem which has been outlined in this chapter. The lower solid line in figure 3.4 indicates the boundary between the parameter values resulting in flows in the hemisphere consisting of one loop (region 1, in which the Lorentz and surface tension forces dominate as in figure 3.3) and those consisting of two loops (region 2, in which the buoyancy force leads to a loop rotating in the opposite direction, as in figure 3.2).

¹here v denotes velocity, ν the viscosity, L a typical length scale and ρ the density

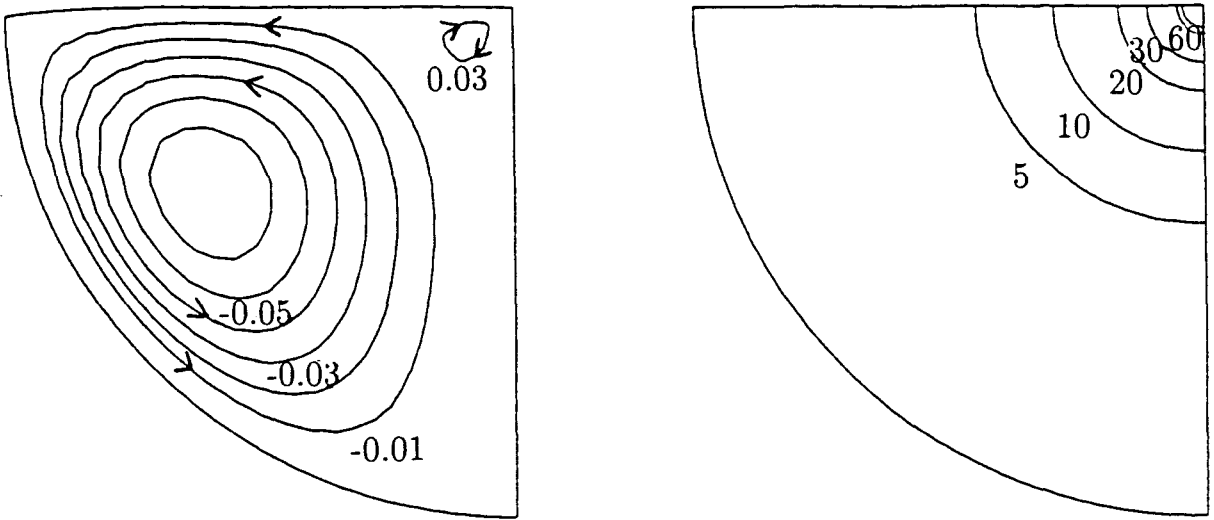


Figure 3.2: (a) Streamlines and (b) isotherms for $K = 22.2$ (i.e. $J = 1.0A$ for steel), $\beta = 1.25 \times 10^{-4} K^{-1}$ and $\partial\gamma/\partial T = 10^{-7} Nm^{-1} K^{-1}$

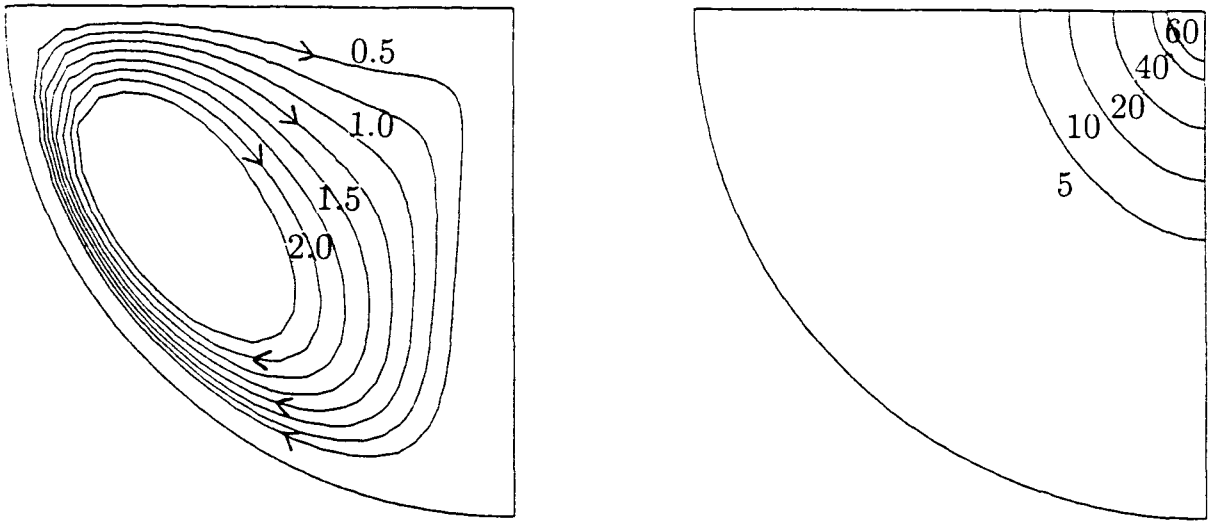


Figure 3.3: (a) Streamlines and (b) isotherms for $K = 71.9$ (i.e. $J = 1.8A$ for steel), $\beta = 1.25 \times 10^{-4} K^{-1}$ and $\partial\gamma/\partial T = 10^{-7} Nm^{-1} K^{-1}$

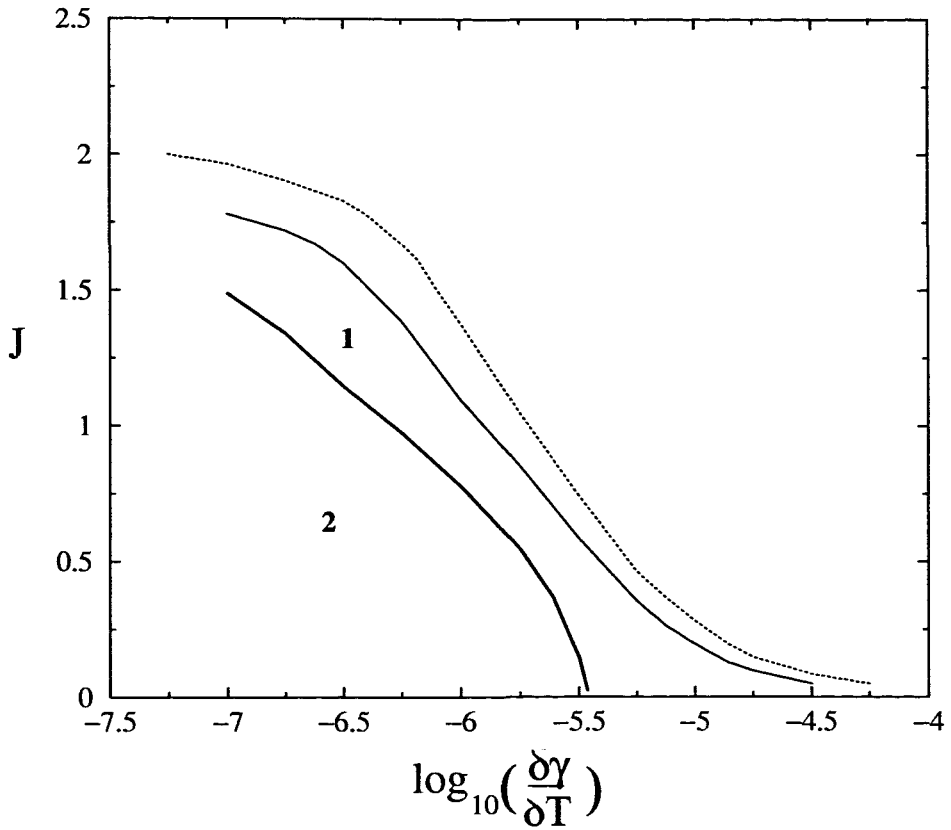


Figure 3.4: Qualitative flow structure for the steady-state flow model in a hemisphere with positive $\partial\gamma/\partial T$. The lower solid curves represent the transition between a one- and a two-loop flow structure. The upper solid and dotted lines represent the breakdown currents as a function of $\partial\gamma/\partial T$ for the hemispherical and semi-infinite models respectively.

When the value of $\partial\gamma/\partial T$ is negative the Marangoni force reinforces the buoyancy force and, therefore, at low currents a single loop is produced which flows up the axis of symmetry and away from the source on the free surface. As the current is increased the Lorentz force produces a counter rotating loop near the origin. These situations are shown in figures 3.5 and 3.6. The Reynolds numbers for these flows are 5 and 28 respectively.

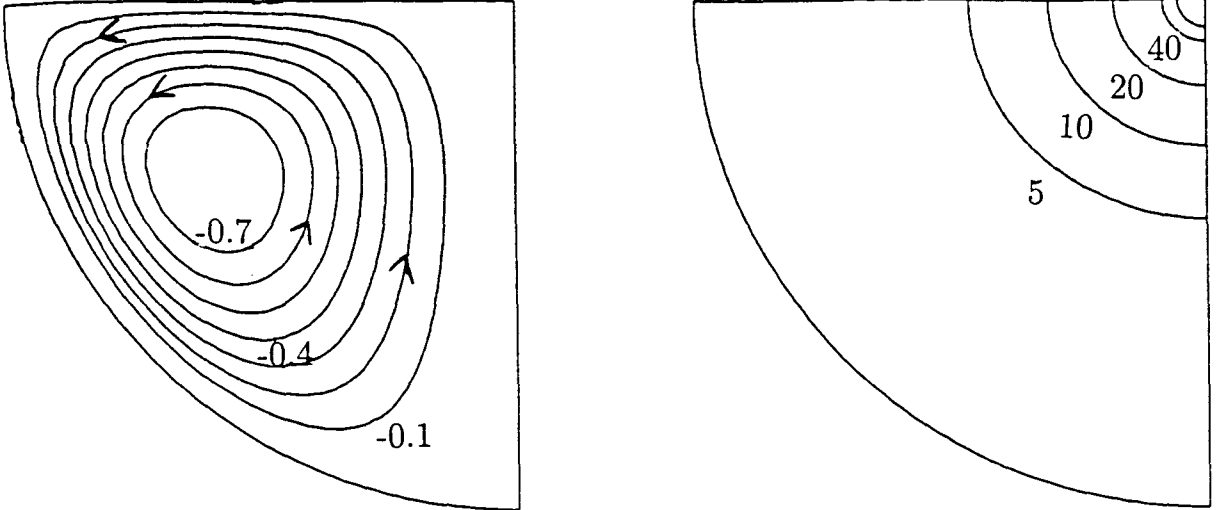


Figure 3.5: (a) Streamlines and (b) isotherms, for $K = 22.2$ (i.e. $J = 1.0A$ for steel), $\beta = 1.25 \times 10^{-4}K^{-1}$ and $\partial\gamma/\partial T = -2 \times 10^{-7}Nm^{-1}K^{-1}$.

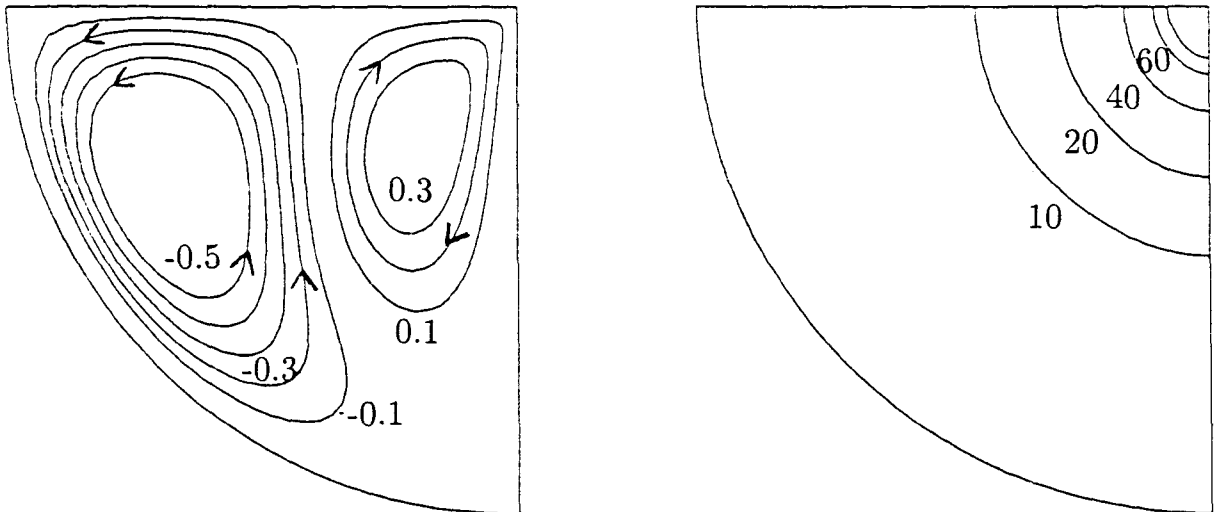


Figure 3.6: (a) Streamlines and (b) isotherms, for $K = 88.8$ (i.e. $J = 2.0A$ for steel), $\beta = 1.25 \times 10^{-4}K^{-1}$ and $\partial\gamma/\partial T = -2 \times 10^{-7}Nm^{-1}K^{-1}$.

When the value of $\partial\gamma/\partial T$ is large and negative and the current, and hence the Lorentz force, is less important, a strong jet flows away from the point source along the top surface of the weld-pool (see figure 3.7). For this case the maximum Reynolds number is 450, which again indicates laminar flow.

Results for the breakdown current J_{crit} when $\partial\gamma/\partial T$ is negative are displayed in figure 3.8. The dotted line again corresponds to the breakdown current for the similarity solution

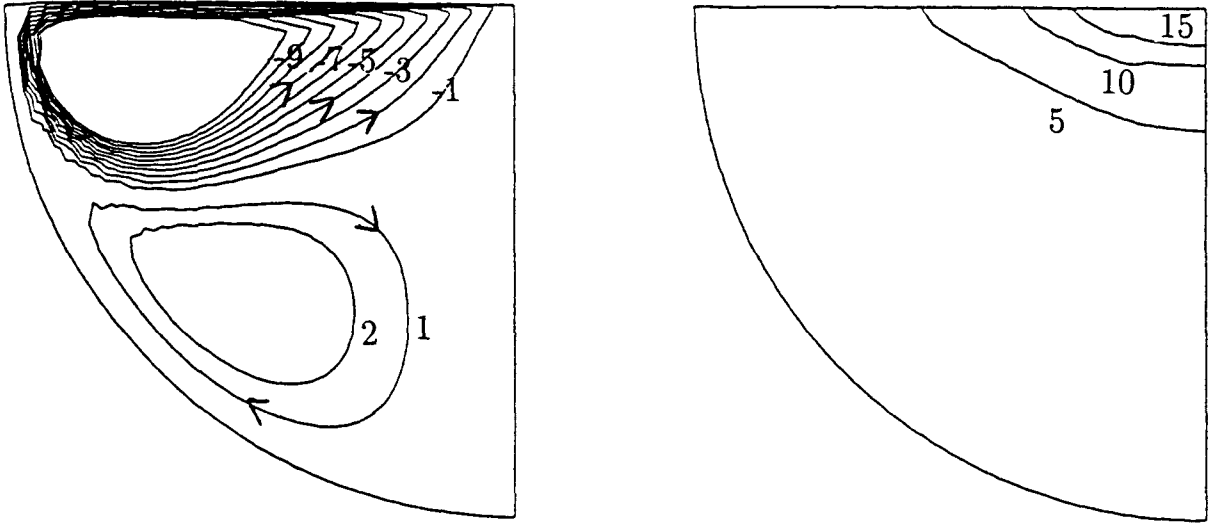


Figure 3.7: (a) Streamlines and (b) isotherms for $K = 22.2$ (i.e. $J = 1.0A$ for steel), $\beta = 1.25 \times 10^{-4} K^{-1}$ and $\partial\gamma/\partial T = -1 \times 10^{-4} Nm^{-1} K^{-1}$

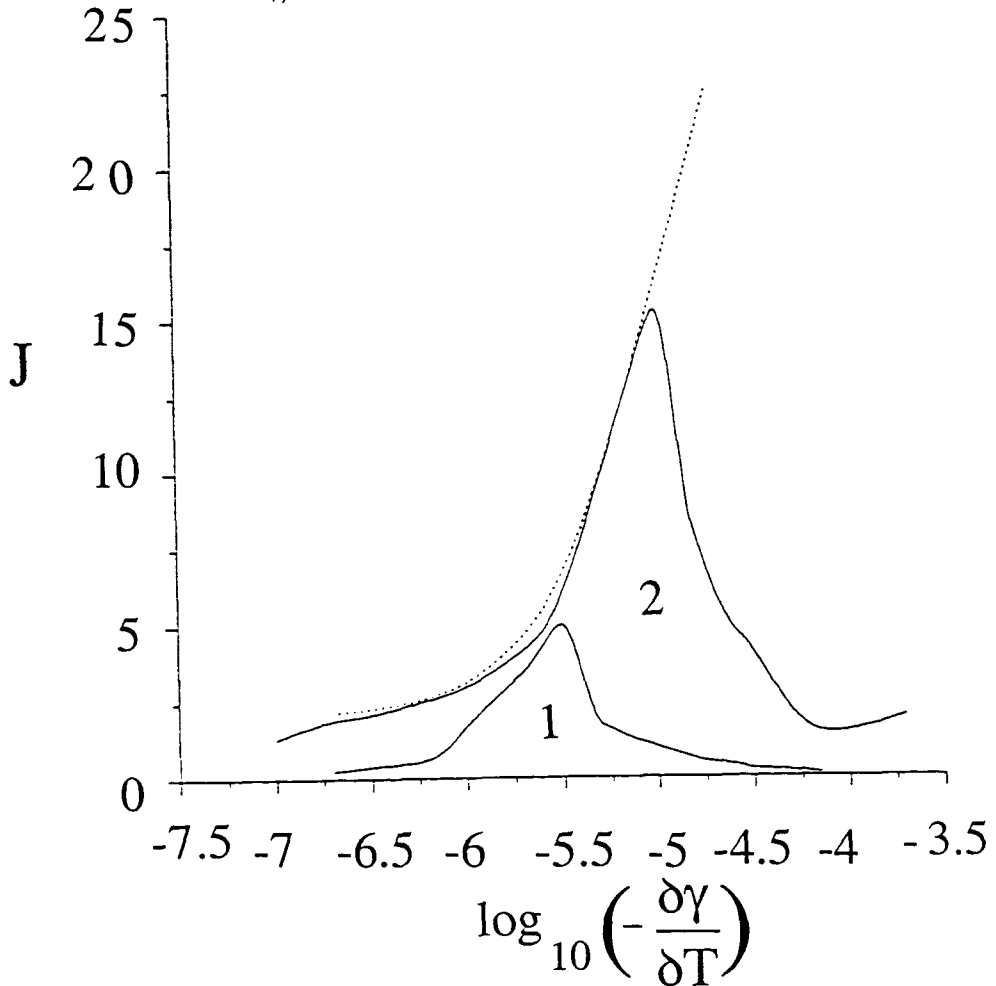


Figure 3.8: Qualitative flow structure for the steady-state hemispherical flow model with negative $\partial\gamma/\partial T$. The lower solid line represents the transition between a one- and a two-loop flow structure. The upper solid and dotted lines represent the breakdown currents, as a function of $\partial\gamma/\partial T$, for the hemispherical and semi-infinite models respectively.

of the semi-infinite model (figure 2.5 in chapter 2), whereas the upper solid line denotes the breakdown current for numerical solutions in the hemisphere. The lower solid line in figure 3.8 separates regions in $J - \log_{10}(\partial\gamma/\partial T)$ space with solutions consisting of one loop (region 1, where the buoyancy and surface tension forces dominate as in figure 3.5) from those consisting of two loops (region 2, where the Lorentz force produces a counter rotating loop as seen in figure 3.6).

The magnitude of the isotherms is directly related to the magnitude of the applied current J . When J is large the temperature within the weld-pool is large and conversely when J is small the temperature in the pool is also small. On the other hand the shape of the temperature profiles is governed by the magnitude of the Reynolds number Re . In figure 3.7, $\partial\gamma/\partial T$ is large and negative and, therefore, the Marangoni force is strong. As a result both the velocity and the corresponding Re are large. A large Reynolds number also occurs in figure 3.3 since the Marangoni force reinforces the Lorentz force and fast axial flow is produced. We can clearly see the non-spherical nature of the isotherms in figure 3.3 and 3.7. In the remaining figures, however, the isotherms are more spherical because in these figures the Reynolds numbers are small.

To conclude it should be pointed out that there are two possible reasons for the breakdown in the numerical solution in the hemisphere. At a given $\partial\gamma/\partial T$ solutions were obtained at low currents, but they could not be found when the current exceeded the critical current value J_{crit} . For these positive, and small negative, values of $\partial\gamma/\partial T$ the loss of convergence seems to arise from the development of infinite axial velocities, as found in the isothermal case [110]. On the other hand, for large negative values of the surface tension gradient the Reynolds number is approaching 1000 at the breakdown current and the loss of convergence may be indicating turbulence and instability in the numerical scheme.

Chapter 4

Linear stability analysis

4.1 Introduction

In this chapter the stability of the flow in a hemisphere discussed in the previous chapter is investigated, by performing a linear stability analysis [38]. In his thesis Belgrove [7] started the investigation of the stability of this problem by looking for solutions proportional to $e^{im\phi}$, where ϕ is the usual azimuthal angle in spherical polar coordinates, and obtaining results for the mode $m = 1$. Unfortunately, the method he used to derive the algebraic system rendered him unable to investigate the first normal mode of stability ($m = 0$), which is probably the most important. Following Belgrove, in this chapter and chapter 5 we assume that the *principle of exchange of stabilities* is valid, namely that the marginal stability modes with vanishing real part also have zero complex part.

Before embarking on a stability analysis we briefly outline the method of normal modes for studying oscillations and instability. In this method, further details of which can be obtained in [26], [38] and [37], a known solution to a set of equations is perturbed, and in a linear stability analysis products of these perturbations are neglected in the resulting system. The perturbations are then resolved into independent components, or modes, varying with time t in the form $e^{\sigma t}$, for some generally complex constant σ which is to be determined. In general terms we wish to determine whether the predicted flow can be achieved in reality (i.e. the linear stability analysis attempts to distinguish stable from unstable patterns of predicted flow). The sign of the real part of the constant σ determines whether the disturbances die away, persist with a similar magnitude, or grow to such an extent that the basic flow becomes a different laminar, or a turbulent, flow.

A complete linear stability analysis requires us to examine the response to all possible small disturbances. By the *method of normal modes* this is achieved by resolving the small disturbances into modes, chosen by considering the geometry and symmetry of the system.

Each mode satisfies the system of linear equations and therefore may be considered separately¹. Distinguishing the different modes by the symbol m , the perturbation \bar{u} may be written symbolically as

$$\bar{u}(r, \theta, \phi, t) = \int \tilde{\tilde{u}}_m(r, \theta, \phi, t) dm,$$

and the time dependence is then eliminated by seeking solutions of the form

$$\tilde{\tilde{u}}_m(r, \theta, \phi, t) = \tilde{u}_m(r, \theta, \phi)e^{\sigma_m t}.$$

The constant σ_m will be different for each normal mode distinguished by m .

In this thesis it is assumed that the mode of the perturbation is separable in the azimuthal direction, given by $\hat{\phi}$ in spherical polar co-ordinates, and hence

$$\tilde{u}_m(r, \theta, \phi)e^{\sigma_m t} = \bar{u}_m(r, \theta)e^{\sigma_m t + im\phi}.$$

The standard procedure is to write σ_m as $\sigma_m = \sigma_m^{(r)} + i\sigma_m^{(i)}$ where $\sigma_m^{(r)}$ and $\sigma_m^{(i)}$ denote the real and imaginary parts of σ_m respectively. It should be emphasised, however, that for the solution to be stable at particular parameter values, every $\sigma_m^{(r)}$ must be less than zero for every mode, i.e. every value of m . The parameter values which lead to solutions where the maximum $\sigma_n^{(r)}$ is zero indicate curves of marginal and neutral stability for a particular mode $m = n$. On a neutral stability curve there is one, or more, mode(s) where $\sigma_n^{(r)}$ equals zero, however in the neighbourhood of this curve all the remaining modes have $\sigma_m^{(r)}$ less than zero. On the other hand, on a marginal stability curve there is one, or more, mode(s) where $\sigma_n^{(r)}$ equals zero, however on one side of the curve all modes have negative real part where as on the other side of the curve one or more modes have $\sigma_n^{(r)}$ greater than zero.

In the welding problem there will be instabilities at currents just exceeding the critical current, J_c , at which instability first arises for a given value of $\partial\gamma/\partial T$, but by definition there will be no instabilities for current values less than J_c . If $\sigma_m^{(i)} \neq 0$ as $\sigma_m^{(r)} \rightarrow 0$, then an oscillatory instability (or over-stability) arises. This term was first used by Eddington [40] in 1926. On the other hand, if $\sigma_m^{(i)} = 0$ as $\sigma_m^{(r)} \rightarrow 0$, there is said to be an *exchange of stabilities*, and instability sets in as a steady secondary flow. The *principle of exchange of stabilities* assumes that exchange of stability occurs due to steady secondary flows only. It is not possible to check the behaviour of $\sigma_m^{(r)}$ and $\sigma_m^{(i)}$ for all possible m , and in practice only the simplest modes are investigated. In this chapter we consider the lowest possible azimuthal mode of stability $m = 0$.

4.2 Derivation of linear system of equations

Following the discussion above the velocity \mathbf{v} and temperature T are expressed:

¹In this chapter we consider the lowest possible mode of stability $m = 0$ for a perturbation which is chosen to be separable in ϕ . The modes $m = 1, 2$ and 3 are considered in chapter 5.

$$\begin{aligned}\mathbf{v} &= \mathbf{u} + \bar{\mathbf{v}}, \\ T &= T_0 + \bar{T},\end{aligned}\tag{4.1}$$

where \mathbf{u} represents the steady state velocity solution,

$\bar{\mathbf{v}}$ denotes a small perturbation to the steady state solution,

T_0 is the steady state temperature solution,

\bar{T} is a small perturbation to the steady state temperature solution.

The variables \mathbf{u} and T_0 satisfy the steady state equations considered in chapter 3. Taking the curl of the unsteady momentum-transport equation (which is given in its steady form by equation (3.1) in chapter 3) gives

$$\begin{aligned}\nabla \times \frac{\partial \mathbf{v}}{\partial t} &= \nabla \times \left[\mathbf{v} \times (\nabla \times \mathbf{v}) \right] - \nu \nabla \times \nabla \times \nabla \times \mathbf{v} + \\ &\quad \frac{1}{\rho} \nabla \times \mathbf{F}_B + \frac{1}{\rho} \nabla \times (\mathbf{J} \times \mathbf{B}).\end{aligned}\tag{4.2}$$

Using equations (4.1) and removing the stationary solution and any term containing products of perturbations, equation (4.2) leads to

$$\begin{aligned}\nabla \times \left[\mathbf{u} \times (\nabla \times \bar{\mathbf{v}}) \right] + \nabla \times \left[\bar{\mathbf{v}} \times (\nabla \times \mathbf{u}) \right] - \nu \nabla \times \nabla \times \nabla \times \bar{\mathbf{v}} \\ + \frac{1}{\rho} \nabla \times \bar{\mathbf{F}}_B = \frac{\partial}{\partial t} (\nabla \times \bar{\mathbf{v}}).\end{aligned}\tag{4.3}$$

In this equation $\bar{\mathbf{F}}_B$ denotes the buoyancy force caused by the temperature perturbation.

In the underlying flow in a hemisphere outlined in the previous chapter the velocity and temperature were determined by calculating the functions $\psi = \psi(\eta, \lambda)$ and $t = t(\eta, \lambda)$. Following the discussion in the previous section the perturbations are assumed to depend on ϕ through the separable term $e^{im\phi}$, where m denotes the mode of stability. Therefore, the perturbations can be written as

$$\bar{T} = \bar{\tilde{T}}(\eta, \lambda)e^{(im\phi + \sigma t)} \quad \text{and} \quad \bar{\psi} = \bar{\tilde{\psi}}(\eta, \lambda)e^{(im\phi + \sigma t)}$$

which reduce to

$$\bar{\psi} = \bar{\tilde{\psi}}(\eta, \lambda)e^{\sigma t} \quad \text{and} \quad \bar{T} = \bar{\tilde{T}}(\eta, \lambda)e^{\sigma t}.\tag{4.4}$$

for the mode of vibration $m = 0$. Writing $\sigma = \sigma^{(r)} + i\sigma^{(i)}$, solutions are sought for $\sigma^{(r)} = 0$ and these represent marginal or neutral stability solutions depending on the sign of $\sigma^{(r)}$ in the neighbouring parameter space, as described in section 4.1.

Note that in (4.4), and the following sections, a $\bar{\quad}$ on top of a variable denotes a poloidal perturbation variable, (i.e. in the (r, θ) plane only). In an analogous way $\tilde{\quad}$ denotes an

azimuthal perturbation variable (i.e. in the ϕ -direction) and a $\tilde{}$ denotes the part of the perturbation variable that is independent of t and ϕ as shown in equation (4.4). Any variable without a superposed bar or tilde denotes a ‘main flow’ variable, which of course is known inside the hemisphere from the solution to the steady state flow model described in chapter 3.

Flow equation

The model describing steady flow in a hemisphere, outlined in chapter 3, assumes that the fluid is incompressible, satisfying

$$\nabla \cdot \mathbf{u} = 0,$$

and that the flow is axisymmetric. These conditions imply the existence of a stream function $\psi(\theta, r)$ which can be non-dimensionalised and written

$$\psi = a\lambda\nu g(\eta, \lambda). \quad (4.5)$$

Since it is assumed that the fluid is incompressible it follows that $\nabla \cdot \bar{\mathbf{v}} = 0$ and therefore the perturbation velocity can also be found from a stream function $\bar{\psi}$, non-dimensionalised by

$$\bar{\psi} = a\lambda\nu\bar{g}(\eta, \lambda). \quad (4.6)$$

Since the velocity in the underlying flow in the hemisphere, \mathbf{u} , is connected to the stream function ψ by

$$\mathbf{u} = \nabla \times \left(0, 0, \frac{\psi}{a\lambda \sin \theta} \right),$$

it follows that, with respect to a spherical polar coordinate system,

$$\mathbf{u} = - \left(\frac{1}{-2(a\lambda)^2\eta} \psi_{\eta}, \frac{1}{a\lambda\eta(2-\eta^2)^{\frac{1}{2}}} \psi_r, 0 \right) = -\frac{\nu}{a\lambda} \left(\frac{-1}{2\eta} g_{\eta}, \frac{g + \lambda g_{\lambda}}{\eta(2-\eta^2)^{\frac{1}{2}}}, 0 \right) \quad (4.7)$$

defines the velocity of the underlying flow in terms of $g(\lambda, \eta)$. Similarly, connecting the poloidal components of the perturbation velocity $\bar{\mathbf{v}}$ to the streamfunction $\bar{\psi}$ by

$$\bar{\mathbf{v}} = \nabla \times \left(0, 0, \frac{\bar{\psi}}{a\lambda \sin \theta} \right),$$

it follows that $\bar{\mathbf{v}}$ can be expressed

$$\bar{\mathbf{v}} = (\bar{v}_r, \bar{v}_{\theta}, \bar{v}_{\phi}) = -\frac{\nu}{a\lambda} \left(\frac{-1}{2\eta} \bar{g}_{\eta}, \frac{\bar{g} + \lambda \bar{g}_{\lambda}}{\eta(2-\eta^2)^{\frac{1}{2}}}, \bar{v}_{\phi} \right). \quad (4.8)$$

The perturbation velocity in the azimuthal direction \bar{v}_{ϕ} is now expressed in terms of the non dimensional function $\bar{g}(\eta, \lambda)$ through

$$\bar{v}_{\phi} = \frac{\nu \bar{g}}{a\lambda\eta(2-\eta^2)^{\frac{1}{2}}}. \quad (4.9)$$

For convenience $\bar{\mathbf{v}}$ is written as

$$\bar{\mathbf{v}} = \bar{\mathbf{v}}_1 + \bar{\mathbf{v}}_2,$$

where $\bar{\mathbf{v}}_1$ is the two-dimensional ‘poloidal perturbation velocity’ $(\bar{v}_r, \bar{v}_\theta, 0)$ and $\bar{\mathbf{v}}_2$ denotes the ‘azimuthal perturbation velocity’ $(0, 0, \bar{v}_\phi)$.

It is easily shown from equation (4.8) that

$$\nabla \times \bar{\mathbf{v}}_1 = -\frac{\nu\eta(2-\eta^2)^{\frac{1}{2}}}{(a\lambda)^2} \bar{f} \hat{\phi}, \quad (4.10)$$

where $\hat{\phi}$ denotes the unit vector in the ϕ direction and the vorticity perturbation function, \bar{f} , is defined by

$$\bar{f} = \frac{1}{(2\eta)^2} \bar{g}_{\eta\eta} - \frac{1}{4\eta^3} \bar{g}_\eta + \frac{2\lambda\bar{g}_\lambda + \lambda^2\bar{g}_{\lambda\lambda}}{\eta^2(2-\eta^2)} = -(\nabla \times \bar{\mathbf{v}}_1)_\phi \frac{(\lambda a)^2}{\nu\eta(2-\eta^2)^{\frac{1}{2}}}. \quad (4.11)$$

Similarly, the azimuthal vorticity perturbation function², $\bar{\bar{f}}$, is defined by

$$\bar{\bar{f}} = \frac{1}{(2\eta)^2 a \lambda} \bar{\bar{g}}_{\eta\eta} - \frac{1}{4\eta^3 a \lambda} \bar{\bar{g}}_\eta + \frac{\lambda \bar{\bar{g}}_{\lambda\lambda}}{a \eta^2 (2-\eta^2)} = -(\nabla \times \nabla \times \bar{\mathbf{v}}_2)_\phi \frac{(\lambda a)^2}{\nu\eta(2-\eta^2)^{\frac{1}{2}}}. \quad (4.12)$$

Direct calculation from the definition of $\bar{\mathbf{v}}_2$ shows that

$$\nabla \times \bar{\mathbf{v}}_2 = -\frac{\nu}{(a\lambda)^2} \left(\frac{-1}{2\eta} \bar{\bar{g}}_\eta, \frac{\lambda}{\eta(2-\eta^2)^{\frac{1}{2}}} \bar{\bar{g}}_\lambda, 0 \right), \quad (4.13)$$

and with the use of equation (4.10) the total perturbation vorticity $\nabla \times \bar{\mathbf{v}}$ can be written

$$\nabla \times \bar{\mathbf{v}} = -\frac{\nu}{(a\lambda)^2} \left(\frac{-1}{2\eta} \bar{\bar{g}}_\eta, \frac{\lambda}{\eta(2-\eta^2)^{\frac{1}{2}}} \bar{\bar{g}}_\lambda, \eta(2-\eta^2)^{\frac{1}{2}} \bar{f} \right). \quad (4.14)$$

After two further differentiations it follows that

$$\begin{aligned} \nabla \times \nabla \times \nabla \times \bar{\mathbf{v}} &= \frac{\nu}{(a\lambda)^3} \left(\frac{-\eta(2-\eta^2)}{2} \bar{\bar{f}}_\eta - 2(1-\eta^2) \bar{f} \right) \hat{\mathbf{r}} \\ &+ \frac{\nu\eta(2-\eta^2)^{\frac{1}{2}}}{(a\lambda)^3} \left(\lambda \bar{\bar{f}}_\lambda - \bar{f} \right) \hat{\boldsymbol{\theta}} \\ &+ \frac{\nu\eta(2-\eta^2)^{\frac{1}{2}}}{(a\lambda)^4} \left(\lambda^2 \bar{f}_{\lambda\lambda} - 2\lambda \bar{f}_\lambda + \frac{(2-\eta^2)}{4} \bar{f}_{\eta\eta} + \frac{(6-7\eta^2)}{4\eta} \bar{f}_\eta \right) \hat{\phi}. \end{aligned} \quad (4.15)$$

where $\hat{\mathbf{r}}$ and $\hat{\boldsymbol{\theta}}$ denote the unit vectors in the r and θ directions. Using (4.14) it can be shown that

$$\begin{aligned} \mathbf{u} \times (\nabla \times \bar{\mathbf{v}}) &= \frac{\nu^2}{(a\lambda)^3} (g + \lambda g_\lambda) \bar{f} \hat{\mathbf{r}} + \frac{\nu^2(2-\eta^2)^{\frac{1}{2}}}{2(a\lambda)^3} g_\eta \bar{f} \hat{\boldsymbol{\theta}} \\ &- \frac{\nu^2}{2\eta^2(2-\eta^2)^{\frac{1}{2}}(a\lambda)^3} (\lambda g_\eta \bar{\bar{g}}_\lambda - \bar{\bar{g}}_\eta (g + \lambda g_\lambda)) \hat{\phi}, \end{aligned} \quad (4.16)$$

²It should be noted that, unlike \bar{g} , $\bar{\bar{f}}$ is dimensional as can be clearly seen by inspection of (4.12). This is not a problem, however, since in the final system of equations $\bar{\bar{f}}$ is everywhere replaced by \bar{g} using (4.12).

from which it follows that

$$\begin{aligned}
\nabla \times [\mathbf{u} \times (\nabla \times \bar{\mathbf{v}})] &= -\frac{\nu^2}{4\eta^2(a\lambda)^4} \left[\lambda \mathbf{g}_{\eta\eta} \bar{g}_\lambda - \bar{g}_\eta \mathbf{g}_\eta - \frac{\lambda}{\eta} \mathbf{g}_\eta \bar{g}_\lambda - \bar{g}_{\eta\eta} \mathbf{g} \right. \\
&\quad \left. + \left(\frac{\lambda}{\eta} \mathbf{g}_\lambda + \frac{1}{\eta} \mathbf{g} - \lambda \mathbf{g}_{\lambda\eta} \right) \bar{g}_\eta - \lambda \mathbf{g}_\lambda \bar{g}_{\eta\eta} + \lambda \mathbf{g}_\eta \bar{g}_{\lambda\eta} \right] \hat{\mathbf{r}} \\
&\quad + \frac{\nu^2}{(a\lambda)^4 2\eta^2 (2 - \eta^2)^{\frac{1}{2}}} \left[\lambda^2 \mathbf{g}_\eta \bar{g}_{\lambda\lambda} + \lambda (\lambda \mathbf{g}_{\lambda\eta} - \mathbf{g}_\eta) \bar{g}_\lambda \right. \\
&\quad \left. + (2\mathbf{g} - \lambda^2 \mathbf{g}_{\lambda\lambda}) \bar{g}_\eta - \lambda (\mathbf{g} + \lambda \mathbf{g}_\lambda) \bar{g}_{\eta\lambda} \right] \hat{\boldsymbol{\theta}} \\
&\quad - \frac{\nu^2 (2 - \eta^2)^{\frac{1}{2}}}{2(a\lambda)^4} \left[-\lambda \mathbf{g}_\eta \bar{f}_\lambda + 3\mathbf{g}_\eta \bar{f} + \bar{f}_\eta \mathbf{g} + \lambda \bar{f}_\eta \mathbf{g}_\lambda \right] \hat{\boldsymbol{\phi}}. \tag{4.17}
\end{aligned}$$

Taking the curl of equation (4.7) leads to

$$\nabla \times \mathbf{u} = -\frac{\nu\eta(2 - \eta^2)^{\frac{1}{2}}}{(a\lambda)^2} f \hat{\boldsymbol{\phi}}, \tag{4.18}$$

and further manipulation gives

$$\nabla \times [\bar{\mathbf{v}} \times (\nabla \times \mathbf{u})] = -\frac{\nu^2(2 - \eta^2)^{\frac{1}{2}}}{2(a\lambda)^4} [-\lambda \bar{g}_\eta f_\lambda + 3\bar{g}_\eta f + (\bar{g} + \lambda \bar{g}_\lambda) f_\eta] \hat{\boldsymbol{\phi}}. \tag{4.19}$$

Finally, the buoyancy term can be expressed in terms of θ as

$$\frac{1}{\rho} \bar{\mathbf{F}}_{\mathbf{B}} = \beta g_e T_m (\cos \theta, -\sin \theta, 0) \bar{\mathbf{T}}, \tag{4.20}$$

and hence

$$\frac{1}{\rho} \nabla \times \bar{\mathbf{F}}_{\mathbf{B}} = \frac{-\beta g_e \eta (2 - \eta^2)^{\frac{1}{2}} T_m}{a\lambda} \left[\frac{1 - \eta^2}{2\eta} \bar{\mathbf{T}}_\eta + \lambda \bar{\mathbf{T}}_\lambda \right] \hat{\boldsymbol{\phi}}, \tag{4.21}$$

where θ has been expressed in terms of η .

Writing the variables as separable in t and ϕ , according to equation (4.4), and using equation (4.14), the right-hand side of equation (4.3) is transformed for the $m = 0$ mode to

$$\frac{\partial}{\partial t} (\nabla \times \bar{\mathbf{v}}) = -\frac{\sigma\nu}{(a\lambda)^2} e^{\sigma t} \left(-\frac{1}{2\eta} \bar{\bar{g}}_\eta, \frac{\lambda}{\eta(2 - \eta^2)^{\frac{1}{2}}} \bar{\bar{g}}_\lambda, \eta(2 - \eta^2)^{\frac{1}{2}} \bar{\bar{f}} \right). \tag{4.22}$$

Using equations (4.15), (4.17), (4.19), (4.21) and (4.22), the three components of the vector equation (4.3) yield:

$\hat{\mathbf{r}}$ -component,

$$\begin{aligned}
\left(-\frac{1}{2\eta} \mathbf{g}_{\eta\eta} + \frac{1}{2\eta^2} \mathbf{g}_\eta \right) \lambda \bar{\bar{g}}_\lambda + (\mathbf{g} + \lambda \mathbf{g}_\lambda) \left(\frac{1}{2\eta} \bar{\bar{g}}_{\eta\eta} - \frac{1}{2\eta^2} \bar{\bar{g}}_\eta \right) + \frac{\mathbf{g}_\eta}{2\eta} \left(-\lambda \bar{\bar{g}}_{\lambda\eta} + \bar{\bar{g}}_\eta \right) + \frac{\lambda \mathbf{g}_{\lambda\eta}}{2\eta} \bar{\bar{g}}_\eta \\
+ a\lambda\eta^2(2 - \eta^2) \bar{\bar{f}}_\eta + 4a\lambda\eta(1 - \eta^2) \bar{\bar{f}} = \lambda^2 \sigma_1 \bar{\bar{g}}_\eta, \tag{4.23}
\end{aligned}$$

$\hat{\theta}$ -component,

$$-\frac{\mathfrak{g}_\eta \lambda}{2\eta} \bar{\bar{g}}_\lambda + \frac{1}{2\eta} \left[(-\lambda \bar{\bar{g}}_{\lambda\eta} + \bar{\bar{g}}_\eta) \mathfrak{g} - \lambda^2 \bar{\bar{g}}_{\lambda\eta} \mathfrak{g}_\lambda \right] + \frac{\lambda^2}{2\eta} \mathfrak{g}_{\lambda\eta} \bar{\bar{g}}_\lambda - \frac{\lambda^2 \mathfrak{g}_{\lambda\lambda}}{2\eta} \bar{\bar{g}}_\eta + \frac{\mathfrak{g}_\eta \lambda^2}{2\eta} \bar{\bar{g}}_{\lambda\lambda} + \frac{\mathfrak{g}}{2\eta} \bar{\bar{g}}_\eta - a\lambda\eta^2(2 - \eta^2)(\lambda \bar{\bar{f}}_\lambda - \bar{\bar{f}}) = -\lambda^3 \sigma_1 \bar{\bar{g}}_\lambda, \quad (4.24)$$

$\hat{\phi}$ -component,

$$\frac{\lambda \mathfrak{g}_\eta}{2\eta} \bar{\bar{f}}_\lambda - \frac{3}{2\eta} \mathfrak{g}_\eta \bar{\bar{f}} - \frac{(\mathfrak{g} + \lambda \mathfrak{g}_\lambda)}{2\eta} \bar{\bar{f}}_\eta + \frac{\lambda \mathfrak{f}_\lambda}{2\eta} \bar{\bar{g}}_\eta - \frac{3\mathfrak{f}}{2\eta} \bar{\bar{g}}_\eta - \frac{\mathfrak{f}_\eta}{2\eta} (\bar{\bar{g}} + \lambda \bar{\bar{g}}_\lambda) - \lambda^2 \bar{\bar{f}}_{\lambda\lambda} + 2\lambda \bar{\bar{f}}_\lambda - \frac{(2 - \eta^2)}{4} \bar{\bar{f}}_{\eta\eta} - \frac{(6 - 7\eta^2)}{4\eta} \bar{\bar{f}}_\eta - R_r \lambda^3 \left(\frac{1 - \eta^2}{2\eta} \bar{\bar{T}}_\eta + \lambda \bar{\bar{T}}_\lambda \right) = -\lambda^2 \sigma_1 \bar{\bar{f}}, \quad (4.25)$$

where R_r has been defined by equation (3.11) and

$$\sigma_1 = \frac{\sigma a^2}{\nu} \quad (4.26)$$

is the non-dimensional form of the eigenvalue σ .

Integrating equation (4.23) with respect to η yields

$$-\frac{\lambda \mathfrak{g}_\eta}{2\eta} \bar{\bar{g}}_\lambda + \frac{\bar{\bar{g}}_\eta}{2\eta} (\mathfrak{g} + \lambda \mathfrak{g}_\lambda) + a\lambda\eta^2(2 - \eta^2) \bar{\bar{f}} = A(\lambda) + \lambda^2 \sigma_1 \bar{\bar{g}}, \quad (4.27)$$

where $A(\lambda)$ is an arbitrary function of λ . On the other hand dividing equation (4.24) by $-a\lambda^3$ and integrating with respect to λ also leads to equation (4.27) with a constant of integration $B(\eta)$. Comparing this latter equation with (4.27) requires that $A(\lambda) = B(\eta) = \text{const}$. Using the boundary conditions introduced in section 4.3 it can be shown that this constant is zero. Hence we put $A = 0$ and note that equations (4.23), (4.24) and (4.27) all convey the same information. As a result the two equations (4.23) and (4.24) are discarded in favour of the single equation (4.27).

Temperature equation

Next the correct equation for the temperature perturbation must be found. The unsteady form of the heat transfer equation, given in its steady form by equation (2.1), is

$$\frac{\partial T}{\partial t} + \mathbf{v} \cdot \nabla T = \kappa \nabla^2 T, \quad (4.28)$$

where $T = T_0 + \bar{T}$ and $\mathbf{v} = \mathbf{u} + \bar{\mathbf{v}}$ from (4.1). Substituting these definitions into equation (4.28), removing the steady-state solution and ignoring any terms that are quadratic in the perturbations, yields

$$\frac{\partial \bar{T}}{\partial t} + \bar{\mathbf{v}} \cdot \nabla T_0 + \mathbf{u} \cdot \nabla \bar{T} = \kappa \nabla^2 \bar{T}. \quad (4.29)$$

The steady state temperature distribution is denoted by

$$T_0 = \frac{T_m}{\lambda} t(\eta, \lambda)$$

and the small temperature perturbation \bar{T} is expressed

$$\bar{T} = T_m \tilde{\bar{T}}(\eta, \lambda) e^{\sigma t},$$

and it is then easily shown that

$$\nabla T_0 = \frac{T_m}{a\lambda^2} (\lambda t_\lambda - t) \hat{\mathbf{r}} + \frac{(2 - \eta^2)^{\frac{1}{2}} T_m}{2(a\lambda^2)} t_\eta \hat{\boldsymbol{\theta}}, \quad (4.30)$$

$$\bar{\mathbf{v}} \cdot \nabla T_0 = \frac{-\nu T_m}{2\eta a^2 \lambda^3} \left[\tilde{\bar{g}}_\eta (t - \lambda t_\lambda) + t_\eta (\tilde{\bar{g}} + \lambda \tilde{\bar{g}}_\lambda) \right] e^{\sigma t}, \quad (4.31)$$

$$\nabla \bar{T} = \frac{T_m}{a} \tilde{\bar{T}}_\lambda e^{\sigma t} \hat{\mathbf{r}} + \frac{(2 - \eta^2)^{\frac{1}{2}} T_m}{2a\lambda} \tilde{\bar{T}}_\eta e^{\sigma t} \hat{\boldsymbol{\theta}}, \quad (4.32)$$

$$\mathbf{u} \cdot \nabla \bar{T} = \frac{\nu T_m}{a^2 \lambda} \left[\frac{\mathbf{g}_\eta}{2\eta} \tilde{\bar{T}}_\lambda - \left(\frac{\mathbf{g}}{\lambda} + \mathbf{g}_\lambda \right) \frac{\tilde{\bar{T}}_\eta}{2\eta} \right] e^{\sigma t}, \quad (4.33)$$

$$\frac{\partial \bar{T}}{\partial t} = \sigma T_m \tilde{\bar{T}} e^{\sigma t}, \quad (4.34)$$

$$\nabla^2 \bar{T} = \frac{T_m e^{\sigma t}}{(a\lambda)^2} \left[\lambda^2 \tilde{\bar{T}}_{\lambda\lambda} + 2\lambda \tilde{\bar{T}}_\lambda + \frac{(2 - 3\eta^2)}{4\eta} \tilde{\bar{T}}_\eta + \frac{(2 - \eta^2)}{4} \tilde{\bar{T}}_{\eta\eta} \right]. \quad (4.35)$$

With these results equation (4.29) becomes

$$\begin{aligned} & -2\eta P_r \left[\lambda^2 \tilde{\bar{T}}_{\lambda\lambda} + 2\lambda \tilde{\bar{T}}_\lambda + \frac{(2 - 3\eta^2)}{4\eta} \tilde{\bar{T}}_\eta + \frac{(2 - \eta^2)}{4} \tilde{\bar{T}}_{\eta\eta} \right] \\ & - \tilde{\bar{g}}_\eta \left(\frac{t}{\lambda} - t_\lambda \right) - t_\eta \left(\frac{\tilde{\bar{g}}}{\lambda} + \tilde{\bar{g}}_\lambda \right) + \lambda \mathbf{g}_\eta \tilde{\bar{T}}_\lambda - \left(\mathbf{g} + \lambda \mathbf{g}_\lambda \right) \tilde{\bar{T}}_\eta = -2\eta \lambda^2 \sigma_1 \tilde{\bar{T}}. \end{aligned} \quad (4.36)$$

A complete set of differential equations governing the linear stability analysis for the mode $m = 0$ has not yet been determined, however, since the current system contains three linear partial differential equations, (4.25), (4.27) and (4.36), in the five unknowns $\tilde{\bar{f}}$, $\tilde{\bar{f}}$, $\tilde{\bar{g}}$, $\tilde{\bar{g}}$ and $\tilde{\bar{T}}$. The variables t , g and f which appear in the coefficients of these equations are known, of course, since they are the ‘main flow’ variables calculated from the steady-state hemispherical flow model discussed in chapter 3. Equation (4.27) is a first order partial differential equation in η and λ , whereas equations (4.25) and (4.36) are both second order differential equations in the same variables. The variable $\tilde{\bar{f}}$ is eliminated from the system by using the second order differential equation (4.12). This reduces the number of unknown variables to four but at the same time it transforms (4.27) into a second order differential equation for $\tilde{\bar{g}}$. In an analogous way equation (4.11) could be used to eliminate $\tilde{\bar{f}}$ from equation (4.25). However, this would create a fourth order partial differential equation in $\tilde{\bar{g}}$ which is much more difficult to solve, and so equation (4.11) is retained in the system. The system that will be solved,

therefore, consists of the four linear partial differential equations (4.11), (4.25), (4.27 revised) and (4.36) in the four unknowns \tilde{f} , $\tilde{\tilde{g}}$, \tilde{g} and \tilde{T} . This linear system is:

$$-2\eta\tilde{f} - \frac{1}{2\eta^2}\tilde{\tilde{g}}_\eta + \frac{4\lambda}{\eta(2-\eta^2)}\tilde{\tilde{g}}_\lambda + \frac{1}{2\eta}\tilde{\tilde{g}}_{\eta\eta} + \frac{2\lambda^2}{\eta(2-\eta^2)}\tilde{\tilde{g}}_{\lambda\lambda} = 0, \quad (4.37)$$

$$\begin{aligned} 3\mathfrak{g}_\eta\tilde{f} + \frac{\eta(2-\eta^2)}{2}\tilde{f}_{\eta\eta} + \left(3 - \frac{7}{2}\eta^2 + \mathfrak{g} + \lambda\mathfrak{g}_\lambda\right)\tilde{f}_\eta - \lambda(4\eta + \mathfrak{g}_\eta)\tilde{f}_\lambda \\ + 2\eta\lambda^2\tilde{f}_{\lambda\lambda} + (3f - \lambda f_\lambda)\tilde{\tilde{g}}_\eta + \lambda f_\eta\tilde{\tilde{g}}_\lambda + f_\eta\tilde{\tilde{g}} \\ + R_r\lambda^3(1-\eta^2)\tilde{T}_\eta + 2\eta\lambda^4 R_r\tilde{T}_\lambda = 2\eta\lambda^2\sigma_1\tilde{f}, \end{aligned} \quad (4.38)$$

$$\frac{(\eta^2-2)\eta}{2}\tilde{\tilde{g}}_{\eta\eta} + \left[\frac{2-\eta^2}{2} - (\mathfrak{g} + \lambda\mathfrak{g}_\lambda)\right]\tilde{\tilde{g}}_\eta + \lambda\mathfrak{g}_\eta\tilde{\tilde{g}}_\lambda - 2\lambda^2\eta\tilde{\tilde{g}}_{\lambda\lambda} = -2\eta\lambda^2\sigma_1\tilde{\tilde{g}}, \quad (4.39)$$

$$\begin{aligned} \left(\frac{t}{\lambda} - t_\lambda\right)\tilde{g}_\eta + t_\eta\tilde{g}_\lambda + \frac{t_\eta}{\lambda}\tilde{g} + (4\eta\lambda P_r - \lambda\mathfrak{g}_\lambda)\tilde{T}_\lambda + 2\eta P_r\lambda^2\tilde{T}_{\lambda\lambda} \\ + P_r\frac{\eta(2-\eta^2)}{2}\tilde{T}_{\eta\eta} + \left[\mathfrak{g} + \lambda\mathfrak{g}_\lambda + P_r\left(\frac{2-3\eta^2}{2}\right)\right]\tilde{T}_\eta = 2\eta\lambda^2\sigma_1\tilde{T}. \end{aligned} \quad (4.40)$$

4.3 Boundary conditions

The system of differential equations derived in section 4.2 must be solved subject to boundary conditions on $\lambda = 0$, $\lambda = 1$, $\eta = 0$ and $\eta = 1$. The appropriate conditions are considered in the following sections.

4.3.1 Origin ($\lambda = 0$)

No perturbations from the flow are allowed at the origin and therefore

$$\tilde{v}_r : \quad \lim_{\lambda \rightarrow 0} \left(\frac{\nu\tilde{g}_\eta}{2a\lambda\eta} \right) = 0, \quad (4.41)$$

$$\tilde{v}_\theta : \quad \lim_{\lambda \rightarrow 0} \left(\frac{-\nu(\tilde{g} + \lambda\tilde{g}_\lambda)}{a\lambda\eta(2-\eta^2)^{\frac{1}{2}}} \right) = 0, \quad (4.42)$$

$$\tilde{v}_\phi : \quad \lim_{\lambda \rightarrow 0} \left(\frac{\nu\tilde{\tilde{g}}}{a\lambda\eta(2-\eta^2)^{\frac{1}{2}}} \right) = 0. \quad (4.43)$$

Since the perturbation velocities must be finite it follows that

$$\bar{\bar{g}}(\eta, 0) = 0 \quad \text{and} \quad \bar{\bar{g}}'(\eta, 0) = 0. \quad (4.44)$$

In a similar way no perturbation of the temperature is allowed at the origin, hence

$$\bar{\bar{T}}(\eta, 0) = 0. \quad (4.45)$$

Finally, equation (4.11) leads to

$$\bar{\bar{f}}(\eta, 0) = \lim_{\lambda \rightarrow 0} \left(\frac{1}{(2\eta)^2} \bar{\bar{g}}_{\eta\eta} - \frac{1}{4\eta^3} \bar{\bar{g}}_{\eta} + \frac{2\lambda \bar{\bar{g}}_{\lambda} + \lambda^2 \bar{\bar{g}}_{\lambda\lambda}}{\eta^2(2 - \eta^2)} \right),$$

from which it follows that

$$\bar{\bar{f}}(\eta, 0) = 0. \quad (4.46)$$

4.3.2 Outer hemisphere ($\lambda = 1$)

The no-slip boundary condition at the solid-liquid boundary requires that both the velocity and its associated perturbation are zero on this hemispherical surface. Therefore, it is necessary that for $0 \leq \eta \leq 1$

$$\bar{\bar{v}}_r : \quad \lim_{\lambda \rightarrow 1} \left(\frac{\nu}{2a\lambda\eta} \bar{\bar{g}}_{\eta} \right) = 0, \quad (4.47)$$

$$\bar{\bar{v}}_{\theta} : \quad \lim_{\lambda \rightarrow 1} \left(\frac{-\nu(\bar{\bar{g}} + \lambda \bar{\bar{g}}_{\lambda})}{a\lambda\eta(2 - \eta^2)^{\frac{1}{2}}} \right) = 0, \quad (4.48)$$

$$\bar{\bar{v}}_{\phi} : \quad \lim_{\lambda \rightarrow 1} \left(\frac{\nu \bar{\bar{g}}}{a\lambda\eta(2 - \eta^2)^{\frac{1}{2}}} \right) = 0. \quad (4.49)$$

The above results require that

$$\bar{\bar{g}}(\eta, 1) = 0 \quad \text{and} \quad \bar{\bar{g}}'(\eta, 1) = C_0, \quad (4.50)$$

where C_0 is an unknown constant. It follows immediately that all the derivatives of $\bar{\bar{g}}$ and $\bar{\bar{g}}'$ with respect to η are identically zero on $\lambda = 1$.

The outer boundary is at the melting temperature T_m , therefore

$$\bar{\bar{T}}(\eta, 1) = 0 \quad (4.51)$$

by definition.

It seems natural to complete the boundary conditions on the outer hemisphere by evaluating (4.38) when $\lambda = 1$, to give

$$\left(\frac{3}{2\eta} - \frac{7\eta}{4} \right) \bar{\bar{f}}_{\eta} + \bar{\bar{f}}_{\lambda\lambda} + \frac{2 - \eta^2}{4} \bar{\bar{f}}_{\eta\eta} + R_r \bar{\bar{T}}_{\lambda} - 2\bar{\bar{f}}_{\lambda} = \lambda^2 \sigma_1 \bar{\bar{f}}. \quad (4.52)$$

This boundary condition is discussed further in section 4.4.2.

4.3.3 Axis of symmetry ($\eta = 0$)

No flow occurs across the axis of symmetry in the steady-state solution, so it seems natural to assume that there is no velocity perturbation across this axis and hence

$$\bar{v}_\theta(0, \lambda) = -\frac{\nu}{a\lambda} \lim_{\eta \rightarrow 0} \left[\frac{\bar{g} + \lambda \bar{g}_\lambda}{\eta(2 - \eta^2)^{\frac{1}{2}}} \right] = 0. \quad (4.53)$$

The latter is equivalent to

$$\lim_{\eta \rightarrow 0} \left(\frac{\frac{\partial}{\partial \lambda} [\lambda \bar{g}]}{\eta(2 - \eta^2)^{\frac{1}{2}}} \right) = 0,$$

which requires that

$$\bar{g}(0, \lambda) = \frac{C_1}{\lambda}, \quad (4.54)$$

where C_1 is an unknown constant.

The vorticity, $\bar{\omega}$ created by the perturbation velocities can be expressed in the form

$$\begin{aligned} \bar{\omega} = \nabla \times \bar{\mathbf{v}} = & \frac{1}{a} \left(\frac{(2 - \eta^2)^{\frac{1}{2}}}{2\lambda} \frac{\partial \bar{v}_\phi}{\partial \eta} + \frac{(1 - \eta^2)}{\lambda \eta (2 - \eta^2)^{\frac{1}{2}}} \bar{v}_\phi \right) \hat{\mathbf{r}} \\ & - \frac{1}{a} \left(\frac{\bar{v}_\phi}{\lambda} + \frac{\partial \bar{v}_\phi}{\partial \lambda} \right) \hat{\boldsymbol{\theta}} \\ & + \frac{1}{a} \left(\frac{\bar{v}_\theta}{\lambda} + \frac{\partial \bar{v}_\theta}{\partial \lambda} - \frac{(2 - \eta^2)^{\frac{1}{2}}}{2\lambda} \frac{\partial \bar{v}_r}{\partial \eta} \right) \hat{\boldsymbol{\phi}}. \end{aligned} \quad (4.55)$$

Taking the limit of (4.55) on the axis of symmetry, and using $\bar{v}_\theta = 0$ there, leads to

$$\lim_{\eta \rightarrow 0} \bar{\omega} = \frac{1}{\sqrt{2}a\lambda} \lim_{\eta \rightarrow 0} \left(\frac{\partial \bar{v}_\phi}{\partial \eta} + \frac{\bar{v}_\phi}{\eta} \right) \hat{\mathbf{r}} - \frac{1}{a\lambda} \lim_{\eta \rightarrow 0} \left(\frac{\partial \bar{v}_\phi}{\partial \lambda} + \frac{\bar{v}_\phi}{\lambda} \right) \hat{\boldsymbol{\theta}} + \frac{1}{\sqrt{2}a\lambda} \lim_{\eta \rightarrow 0} \left(\frac{\partial \bar{v}_r}{\partial \eta} \right) \hat{\boldsymbol{\phi}}. \quad (4.56)$$

Requiring $\bar{\omega}$ to be finite on the axis then yields

$$\bar{v}_\phi(0, \lambda) = \frac{\nu}{a\lambda} \lim_{\eta \rightarrow 0} \left(\frac{\bar{g}(\eta, \lambda)}{\eta(2 - \eta^2)^{\frac{1}{2}}} \right) = 0, \quad (4.57)$$

which implies

$$\bar{g}(0, \lambda) = 0. \quad (4.58)$$

Since the solution is axisymmetric there is no heat flux across the axis of symmetry. Hence we assume that there is no heat flux across the axis of symmetry arising from the temperature perturbation variable \bar{T} , and so

$$\bar{T}_\eta(0, \lambda) = 0. \quad (4.59)$$

The symmetry of the problem also implies

$$\bar{f}_\eta(0, \lambda) = 0. \quad (4.60)$$

It is further assumed that $\nabla \times \bar{\mathbf{v}}_1$ remains finite on the axis, where equation (4.11) shows that

$$\nabla \times \bar{\mathbf{v}}_1 = -\frac{\nu}{(a\lambda)^2} \left(-\frac{(2-\eta^2)^{\frac{1}{2}}}{4\eta^2} \tilde{\tilde{g}}_\eta + \frac{(2-\eta^2)^{\frac{1}{2}}}{4\eta} \tilde{\tilde{g}}_{\eta\eta} + \frac{2\lambda}{\eta(2-\eta^2)^{\frac{1}{2}}} \tilde{\tilde{g}}_\lambda + \frac{\lambda^2}{\eta(2-\eta^2)^{\frac{1}{2}}} \tilde{\tilde{g}}_{\lambda\lambda} \right). \quad (4.61)$$

The first term on the right hand side of equation (4.61) is clearly the most singular in η , and hence we require

$$\tilde{\tilde{g}}_\eta(0, \lambda) = 0. \quad (4.62)$$

Using L'Hôpital's rule on this first term, equation (4.61) then implies

$$\nabla \times \bar{\mathbf{v}}_1 = -\frac{\nu}{(a\lambda)^2} \left(\frac{(2-\eta^2)^{\frac{1}{2}}}{8\eta} \tilde{\tilde{g}}_{\eta\eta} + \frac{2\lambda}{\eta(2-\eta^2)^{\frac{1}{2}}} \tilde{\tilde{g}}_\lambda + \frac{\lambda^2}{\eta(2-\eta^2)^{\frac{1}{2}}} \tilde{\tilde{g}}_{\lambda\lambda} \right). \quad (4.63)$$

It will be shown in equation (4.77) that the constant C_1 in equation (4.54) is identically zero, and hence all derivatives of $\tilde{\tilde{g}}$ with respect to λ are zero on the axis $\eta = 0$. As a consequence, the numerators in the second and third terms on the right hand side of equation (4.63) vanish on $\eta = 0$, and to preserve the finite nature of the whole equation it is necessary that

$$\tilde{\tilde{g}}_{\eta\eta}(0, \lambda) = 0. \quad (4.64)$$

A further condition that must hold on the axis of symmetry can be obtained from equation (4.38), which on dividing by η gives

$$\begin{aligned} & \left(\frac{f_\eta}{\eta} \right) \tilde{\tilde{g}} + \left(\frac{\lambda f_\eta}{\eta} \right) \tilde{\tilde{g}}_\lambda + \left(\frac{3f - \lambda f_\lambda}{\eta} \right) \tilde{\tilde{g}}_\eta + \left(\frac{3g_\eta}{\eta} \right) \tilde{\tilde{f}} - \left(4\lambda + \frac{\lambda}{\eta} g_\eta \right) \tilde{\tilde{f}}_\lambda \\ & + \left(\frac{g + \lambda g_\lambda + 3}{\eta} - \frac{7}{2\eta} \right) \tilde{\tilde{f}}_\eta + 2\lambda^2 \tilde{\tilde{f}}_{\lambda\lambda} + \left(\frac{2-\eta^2}{2} \right) \tilde{\tilde{f}}_{\eta\eta} + R_r 2\lambda^4 \tilde{\tilde{T}}_\lambda \\ & + \left(\frac{R_r(1-\eta^2)\lambda^3}{\eta} \right) \tilde{\tilde{T}}_\eta = 2\lambda^2 \sigma_1 \tilde{\tilde{f}}. \end{aligned}$$

Taking the limit of the latter as $\eta \rightarrow 0$ and using conditions (4.58), (4.59), (4.60), (4.62), (4.64) and L'Hôpital's rule, where appropriate, transforms the above equation to

$$-2\lambda \tilde{\tilde{f}}_\lambda + \lambda^2 \tilde{\tilde{f}}_{\lambda\lambda} + 2\tilde{\tilde{f}}_{\eta\eta} + R_r \lambda^4 \tilde{\tilde{T}}_\lambda + \frac{R_r \lambda^3}{2} \tilde{\tilde{T}}_{\eta\eta} = \lambda^2 \sigma_1 \tilde{\tilde{f}} \quad \text{on } \eta = 0. \quad (4.65)$$

In an analogous way another condition that must hold on the axis of symmetry can be obtained from equation (4.40), divided by 2η ,

$$\begin{aligned} & \frac{t_\eta}{2\eta\lambda} \tilde{\tilde{g}} + \frac{t_\eta}{2\eta} \tilde{\tilde{g}}_\lambda + \left(\frac{t - \lambda t_\lambda}{2\eta\lambda} \right) \tilde{\tilde{g}}_\eta + \left(2P_r \lambda - \lambda \frac{g_\lambda}{2\eta} \right) \tilde{\tilde{T}}_\lambda + \left[\frac{P_r(2-\eta^2)}{4} \right] \tilde{\tilde{T}}_{\eta\eta} \\ & + \left[P_r \left(\frac{1}{2\eta} - \frac{3\eta}{4} \right) + \frac{g}{2\eta} + \frac{\lambda g_\lambda}{2\eta} \right] \tilde{\tilde{T}}_\eta + \lambda^2 P_r \tilde{\tilde{T}}_{\lambda\lambda} = \lambda^2 \sigma_1 \tilde{\tilde{T}}. \end{aligned}$$

Applying boundary conditions (4.54), (4.58), (4.59), (4.60), (4.62) and (4.64) as $\eta \rightarrow 0$ and again using L'Hôpital's rule, where necessary, transforms the above equation into

$$P_r \lambda^2 \tilde{\tilde{T}}_{\lambda\lambda} + P_r \tilde{\tilde{T}}_{\eta\eta} + 2\lambda P_r \tilde{\tilde{T}}_{\lambda} = \lambda^2 \sigma_1 \tilde{\tilde{T}} \quad \text{on } \eta = 0. \quad (4.66)$$

4.3.4 Free surface ($\eta = 1$)

It is assumed that there is no velocity perturbation perpendicular to the free surface. Therefore, it is required that

$$\tilde{v}_\theta(1, \lambda) = -\frac{\nu}{a} \lim_{\eta \rightarrow 1} \left(\frac{\tilde{g} + \lambda \tilde{g}_\lambda}{\lambda \eta (2 - \eta^2)^{\frac{1}{2}}} \right) = 0, \quad (4.67)$$

which in an analogous way to (4.54) implies

$$\tilde{g}(1, \lambda) = \frac{C_2}{\lambda}, \quad (4.68)$$

where C_2 is an unknown constant.

The general forms for the components of the shear stress on the free surface are given by

$$\sigma_{\phi\theta} = -\frac{\rho\nu}{a\lambda} \left(\frac{-(2 - \eta^2)^{\frac{1}{2}}}{2} \frac{\partial v_\phi}{\partial \eta} + \frac{(1 - \eta^2)}{\eta(2 - \eta^2)^{\frac{1}{2}}} v_\phi \right) \quad (4.69)$$

and

$$\sigma_{r\theta} = \rho\nu \left(\frac{1}{r} \frac{\partial v_r}{\partial \theta} - \frac{v_\theta}{r} + \frac{\partial v_\theta}{\partial r} \right) = \frac{\partial \gamma}{\partial T} \frac{\partial T}{\partial r}. \quad (4.70)$$

The assumed axisymmetric nature of the Marangoni force implies that $\sigma_{\phi\theta} = 0$ on $\eta = 1$, and it follows with the use of (4.69) and (4.9) that

$$\tilde{\tilde{g}}_\eta(1, \lambda) = 0. \quad (4.71)$$

It is also assumed that there is no heat flux across the free surface, so

$$\tilde{\tilde{T}}_\eta(1, \lambda) = 0. \quad (4.72)$$

The constant term in equation (4.68) will be shown in section 4.3.5 to be zero and, therefore, on the free surface all derivatives of \tilde{g} with respect to λ are also identically zero. Using these results and (4.72), the temperature equation (4.40) reduces to

$$\left(\frac{t - \lambda t_\lambda}{2\lambda} \right) \tilde{\tilde{g}}_\eta + \left(2\lambda P_r - \lambda \frac{g_\lambda}{2} \right) \tilde{\tilde{T}}_\lambda + P_r \lambda^2 \tilde{\tilde{T}}_{\lambda\lambda} + \frac{P_r}{4} \tilde{\tilde{T}}_{\eta\eta} = \lambda^2 \sigma_1 \tilde{\tilde{T}} \quad \text{on } \eta = 1, \quad (4.73)$$

and equation (4.38) yields

$$\begin{aligned} \left(\frac{3f - \lambda f_\lambda}{2} \right) \tilde{\tilde{g}}_\eta + \frac{3}{2} g_\eta \tilde{\tilde{f}} - \left(2\lambda + \frac{\lambda}{2} g_\eta \right) \tilde{\tilde{f}}_\lambda - \frac{1}{4} \tilde{\tilde{f}}_\eta + \lambda^2 \tilde{\tilde{f}}_{\lambda\lambda} \\ + \frac{1}{4} \tilde{\tilde{f}}_{\eta\eta} + R_r \lambda^4 \tilde{\tilde{T}}_\lambda = \lambda^2 \sigma_1 \tilde{\tilde{f}} \quad \text{on } \eta = 1. \end{aligned} \quad (4.74)$$

In a similar way with the use of equation (4.71), equation (4.39) implies

$$-\frac{1}{2}\tilde{\tilde{g}}_{\eta\eta} + \lambda\tilde{\tilde{g}}_{\eta\lambda} - 2\lambda^2\tilde{\tilde{g}}_{\lambda\lambda} = -2\lambda^2\sigma_1\tilde{\tilde{g}} \quad \text{on } \eta = 1. \quad (4.75)$$

4.3.5 Corners

In obtaining equations (4.64) and (4.74) above we have assumed that the constants C_0 , C_1 and C_2 , introduced in equations (4.50)₂, (4.54) and (4.68) respectively, are all zero. These assumptions can be verified by considering the system of equations in the ‘‘corners’’ of the hemisphere, where $(\eta, \lambda) \rightarrow (1, 1)$, $(0, 1)$ and $(0, 0)$ in turn.

First consider equations (4.50)₂ and (4.68) at the point $(\eta, \lambda) = (1, 1)$. Consistency requires that

$$\lim_{\eta \rightarrow 1} [\tilde{\tilde{g}}(\eta, 1)] = \lim_{\lambda \rightarrow 1} [\tilde{\tilde{g}}(1, \lambda)],$$

in which case

$$C_0 = \lim_{\lambda \rightarrow 1} \left(\frac{C_2}{\lambda} \right) = C_2. \quad (4.76)$$

Similarly, taking the limits of equations (4.44)₁ and (4.54) as $(\eta, \lambda) \rightarrow (0, 0)$ we obtain

$$\lim_{\eta \rightarrow 0} [\tilde{\tilde{g}}(\eta, 0)] = \lim_{\lambda \rightarrow 0} [\tilde{\tilde{g}}(0, \lambda)], \quad (4.77)$$

which requires that $C_1 = 0$. In a similar way, considering $\tilde{\tilde{g}}$ at the bottom corner where $(\eta, \lambda) \rightarrow (0, 1)$ leads to $C_0 = 0$. Hence result (4.76) gives $C_2 = 0$, and all three constants C_0 , C_1 and C_2 are zero.

The knowledge obtained above for the variables at the corner points allows the boundary conditions to be simplified. At the corner where the hemisphere intersects with the axis of symmetry (i.e. $\lambda = 1$, $\eta = 0$) the boundary conditions (4.50) and (4.51) on the outer hemisphere hold, so

$$\tilde{\tilde{T}}(0, 1) = 0, \quad \tilde{\tilde{g}}(0, 1) = 0 \quad \text{and} \quad \tilde{\tilde{g}}'(0, 1) = 0. \quad (4.78)$$

We now consider an expression for $\tilde{\tilde{f}}$ in the same corner of the grid. Equation (4.11) on the axis of symmetry gives

$$\tilde{\tilde{f}} = -\frac{1}{4\eta^3}\tilde{\tilde{g}}_{\eta} + \frac{1}{4\eta^2}\tilde{\tilde{g}}_{\eta\eta} + \frac{2\lambda}{\eta^2(2-\eta^2)}\tilde{\tilde{g}}_{\lambda} + \frac{\lambda^2}{\eta^2(2-\eta^2)}\tilde{\tilde{g}}_{\lambda\lambda}. \quad (4.79)$$

Recall equations (4.62) and (4.64) then, using L'Hôpital's rule on the first term of equation (4.79), it follows that

$$\tilde{\tilde{f}}(0, 1) = \lim_{\eta \rightarrow 0} \left[\frac{1}{6\eta^2}\tilde{\tilde{g}}_{\eta\eta}(\eta, 1) + \frac{2}{\eta^2(2-\eta^2)}\tilde{\tilde{g}}_{\lambda}(\eta, 1) + \frac{1}{\eta^2(2-\eta^2)}\tilde{\tilde{g}}_{\lambda\lambda}(\eta, 1) \right]. \quad (4.80)$$

L'Hôpital's rule can then be employed again to transform equation (4.80) to

$$\tilde{f}(0, 1) = \lim_{\eta \rightarrow 0} \left[\frac{1}{12\eta} \tilde{g}_{\eta\eta\eta}(\eta, 1) + \frac{2}{4\eta(1-\eta^2)} \tilde{g}_{\lambda\eta}(\eta, 1) + \frac{1}{4\eta(1-\eta^2)} \tilde{g}_{\lambda\lambda\eta}(\eta, 1) \right], \quad (4.81)$$

where the numerators in the second and third terms are zero on the axis (from (4.62)). Since the point $(\eta, \lambda) = (0, 1)$ lies on the hemisphere $\lambda = 1$, where \tilde{g} and all its derivatives with respect to η are zero, it follows that

$$\tilde{g}_{\eta\eta\eta}(0, 1) = 0 \quad (4.82)$$

and, after one further application of L'Hôpital's rule, equation (4.81) gives

$$\tilde{f}(0, 1) = \lim_{\eta \rightarrow 0} \left[\frac{1}{12} \tilde{g}_{\eta\eta\eta}(\eta, 1) + \frac{1}{2} \tilde{g}_{\lambda\eta}(\eta, 1) + \frac{1}{4} \tilde{g}_{\lambda\lambda\eta}(\eta, 1) \right]. \quad (4.83)$$

Since the second and third terms on the right hand side of this equation clearly vanish on the axis (from equation (4.64)) and, as discussed above, all derivatives of \tilde{g} with respect to η are zero, (4.83) simplifies to

$$\tilde{f}(0, 1) = 0. \quad (4.84)$$

Finally at the corner where the hemisphere intersects with the free surface (i.e. $\eta = 1$, $\lambda = 1$) the boundary conditions on both the outer hemisphere and the free surface can be applied. The only remaining unknown in this corner is $\tilde{f}(1, 1)$ but applying the boundary conditions (4.50)₂ and (4.68) when $C_0 = C_2 = 0$ to equation (4.37) immediately leads to

$$\tilde{f}(1, 1) = 0. \quad (4.85)$$

4.3.6 Problem statement

Assuming the principle of exchange of stabilities, solutions are sought when $\sigma = 0$, therefore the complete system of equations in the four unknowns \tilde{f} , \tilde{g} , \tilde{g} and \tilde{T} which govern the linear stability of the flow determined in chapter 3, for the mode $m = 0$, is written as:

$$\frac{(\eta^2 - 2)\eta}{2} \tilde{g}_{\eta\eta} + \left[\frac{2 - \eta^2}{2} - (g + \lambda g_\lambda) \right] \tilde{g}_\eta + \lambda g_\eta \tilde{g}_\lambda - 2\lambda^2 \eta \tilde{g}_{\lambda\lambda} = 0, \quad (4.86)$$

$$-2\eta \tilde{f} - \frac{1}{2\eta^2} \tilde{g}_\eta + \frac{4\lambda}{\eta(2 - \eta^2)} \tilde{g}_\lambda + \frac{1}{2\eta} \tilde{g}_{\eta\eta} + \frac{2\lambda^2}{\eta(2 - \eta^2)} \tilde{g}_{\lambda\lambda} = 0, \quad (4.87)$$

$$\begin{aligned} \left(\frac{t}{\lambda} - t_\lambda \right) \tilde{g}_\eta + t_\eta \tilde{g}_\lambda + \frac{t_\eta}{\lambda} \tilde{g} + (4\eta\lambda P_r - \lambda g_\lambda) \tilde{T}_\lambda + 2\eta P_r \lambda^2 \tilde{T}_{\lambda\lambda} \\ + P_r \frac{\eta(2 - \eta^2)}{2} \tilde{T}_{\eta\eta} + \left[g + \lambda g_\lambda + P_r \left(\frac{2 - 3\eta^2}{2} \right) \right] \tilde{T}_\eta = 0, \end{aligned} \quad (4.88)$$

$$\begin{aligned}
3g_\eta \tilde{f} + \frac{\eta(2-\eta^2)}{2} \tilde{f}_{\eta\eta} + \left(3 - \frac{7}{2}\eta^2 + g + \lambda g_\lambda\right) \tilde{f}_\eta - \lambda(4\eta + g_\eta) \tilde{f}_\lambda \\
+ 2\eta\lambda^2 \tilde{f}_{\lambda\lambda} + (3f - \lambda f_\lambda) \tilde{g}_\eta + \lambda f_\eta \tilde{g}_\lambda + f_\eta \tilde{g} \\
+ R_r \lambda^3 (1 - \eta^2) \tilde{T}_\eta + 2\eta\lambda^4 R_r \tilde{T}_\lambda = 0.
\end{aligned} \tag{4.89}$$

The above equations must be solved subject to the boundary conditions

$$\tilde{g}(\eta, 1) = \tilde{g}(\eta, 0) = \tilde{g}(0, \lambda) = \tilde{g}_\eta(1, \lambda) = 0, \tag{4.90}$$

$$-\frac{1}{2} \tilde{g}_{\eta\eta} + \lambda g_\eta \tilde{g}_\lambda - 2\lambda^2 \tilde{g}_{\lambda\lambda} = 0 \quad \text{on } \eta = 1, \tag{4.91}$$

$$\tilde{g}(\eta, 1) = \tilde{g}_\lambda(\eta, 1) = \tilde{g}(\eta, 0) = \tilde{g}(0, \lambda) = \tilde{g}_\eta(0, \lambda) = \tilde{g}(1, \lambda) = 0, \tag{4.92}$$

$$\tilde{T}(\eta, 1) = \tilde{T}(\eta, 0) = \tilde{T}_\eta(0, \lambda) = \tilde{T}_\eta(1, \lambda) = 0, \tag{4.93}$$

$$P_r \lambda^2 \tilde{T}_{\lambda\lambda} + P_r \tilde{T}_{\eta\eta} + 2\lambda P_r \tilde{T}_\lambda = 0 \quad \text{on } \eta = 0, \tag{4.94}$$

$$\left(\frac{t-\lambda t_\lambda}{2\lambda}\right) \tilde{g}_\eta + (2\lambda P_r - \lambda \frac{g_\lambda}{2}) \tilde{T}_\lambda + P_r \lambda^2 \tilde{T}_{\lambda\lambda} + \frac{P_r}{4} \tilde{T}_{\eta\eta} = 0 \quad \text{on } \eta = 1, \tag{4.95}$$

$$\tilde{f}(\eta, 0) = \tilde{f}_\eta(0, \lambda) = 0, \tag{4.96}$$

$$\left(\frac{3}{2\eta} - \frac{7\eta}{4}\right) \tilde{f}_\eta + \tilde{f}_{\lambda\lambda} + \frac{2-\eta^2}{4} \tilde{f}_{\eta\eta} + R_r \tilde{T}_\lambda - 2\tilde{f}_\lambda = 0 \quad \text{on } \lambda = 1, \tag{4.97}$$

$$-2\lambda \tilde{f}_\lambda + \lambda^2 \tilde{f}_{\lambda\lambda} + 2\tilde{f}_{\eta\eta} + R_r \lambda^4 \tilde{T}_\lambda + \frac{R_r \lambda^3}{2} \tilde{T}_{\eta\eta} = 0 \quad \text{on } \eta = 0, \tag{4.98}$$

$$\begin{aligned}
\left(\frac{3f - \lambda f_\lambda}{2}\right) \tilde{g}_\eta + \frac{3}{2} g_\eta \tilde{f} - (2\lambda + \frac{\lambda}{2} g_\eta) \tilde{f}_\lambda - \frac{1}{4} \tilde{f}_\eta + \lambda^2 \tilde{f}_{\lambda\lambda} \\
+ \frac{1}{4} \tilde{f}_{\eta\eta} + R_r \lambda^4 \tilde{T}_\lambda = 0 \quad \text{on } \eta = 1,
\end{aligned} \tag{4.99}$$

$$\tilde{f}(0, 1) = \tilde{f}(1, 1) = 0. \tag{4.100}$$

Before considering the finite difference formulation in section 4.4 note that the partial differential equations (4.87), (4.88) and (4.89) which govern the stability of the poloidal flow have decoupled from equation (4.86), which describes the stability of the azimuthal motion. In general the equations governing the stability of the poloidal flow are linked to the azimuthal stability equation by second order terms. However, since the stability analysis in this chapter is linear, equation (4.86) has totally decoupled from the other three equations (4.87), (4.88) and (4.89). The two systems, which are henceforth referred to as azimuthal and poloidal, will be solved separately inside the hemisphere.

4.4 Finite differences

Equations (4.86), (4.87), (4.88) and (4.89) are written in terms of finite differences and then must be solved in the hemisphere. The grid points used for this linear stability problem

must coincide with nodes where the underlying steady-state flow variables f , g and t are calculated in the hemisphere, so that the coefficients appearing in (4.86) to (4.89) can be computed accurately.

Let us outline the solution procedure. For fixed values of J and $\partial\gamma/\partial T$, the variables f , g and t are calculated from equations (3.14), (3.15) and (3.16) at each mesh point on a 61×61 grid equally spaced in both the η and λ directions. This is the steady-state solution and in the previous chapter a 61×61 grid was found to give reasonable accuracy. Any derivatives of these main flow variables that are required for coefficients of the linear stability equations are approximated by central differencing, using neighbouring points on the 61×61 steady-state mesh. The stability analysis must be performed using grid points which coincide with the points used in determining the steady-state solution, but a 61×61 grid is too large to employ for the stability part since the required computing time proves excessive. Therefore, a coarser grid was used for the stability equations, taking care that grid points on the coarser grid coincided with grid points on the finer underlying mesh on which the steady-state variables had been calculated.

The relative simplicity of the azimuthal system, the single differential equation (4.86), allows the use of a grid with fine spacing near the boundaries, a method suggested by Roache [90]. This grid is shown schematically in figure 4.1, where the size of the mesh in the central region was made relatively coarse to enable the program to have a sensible running time. Figure 4.1 shows equal spacing in θ in both the main and boundary regions. In the following numerical work, however, the grid is equally spaced in η in both regions so before proceeding further we need to check that the position of the grid points in the stability mesh is not unevenly redistributed by the coordinate transformation $\theta \mapsto \eta$.

In figure 4.2 the crosses show the actual distribution of grid points in η , along a grid line where λ is constant, for the situation shown in figure 4.1 in which the θ spacings are separately constant in both the main and boundary regions. These crosses form the slightly curved dashed line displayed in figure 4.2. If the position of the grid points had been invariant under the transformation $\theta \mapsto \eta$, the dashed curve would be coincident with the dots in figure 4.2 which form a straight diagonal line across the figure. The closeness of both lines shows that the distribution of grid points is not significantly affected by the coordinate transformation.

An attempt was made to use the grid shown in figure 4.1 for the poloidal system. The additional complexity of solving a larger system of equations on a grid of varying size produced additional problems, however, and the use of this variable grid was dropped for the poloidal system. In producing our solution for the poloidal equations (4.87), (4.88) and (4.89), therefore, a regular grid (displayed by solid lines in figure 4.3) is used.

In both the poloidal and azimuthal systems the first derivatives in the centre of the pool are approximated using the Quadratic Upstream Interpolation (QUI) method of Leonard [68],

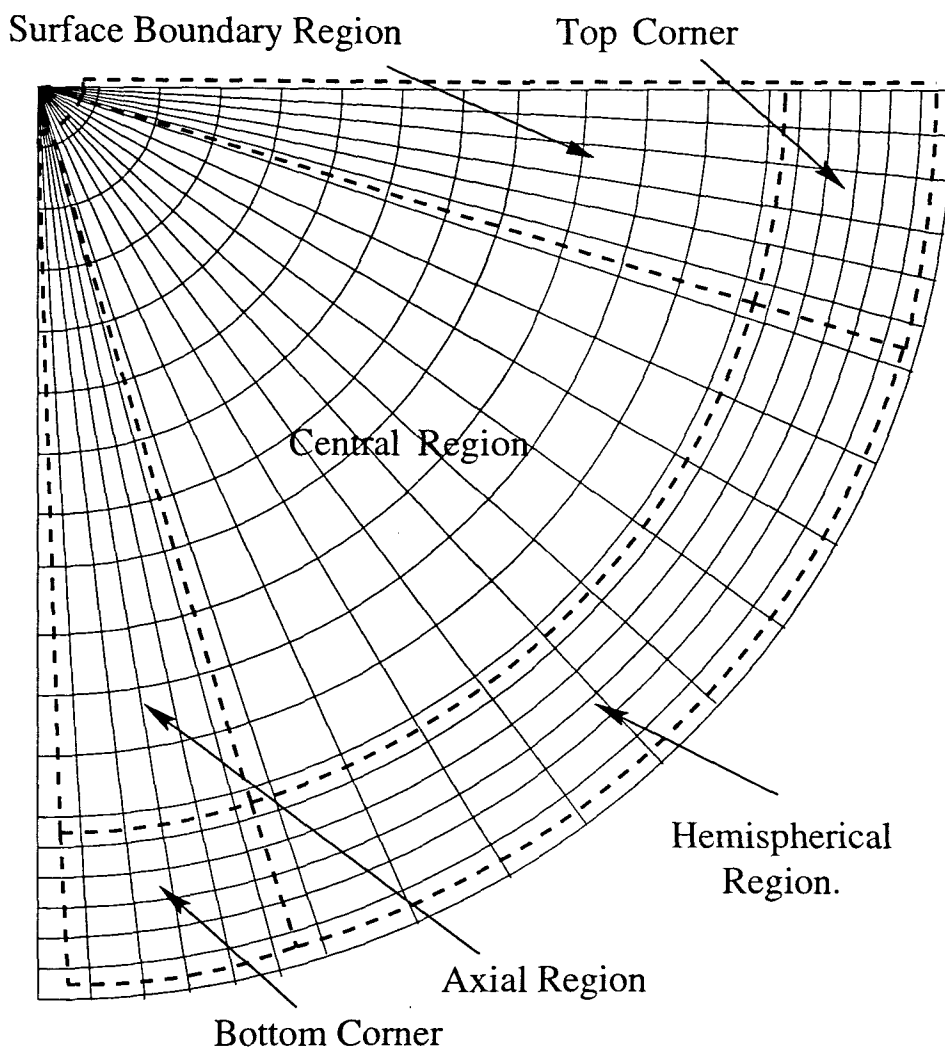


Figure 4.1: Azimuthal stability grid which uses fine spacing near the boundaries.

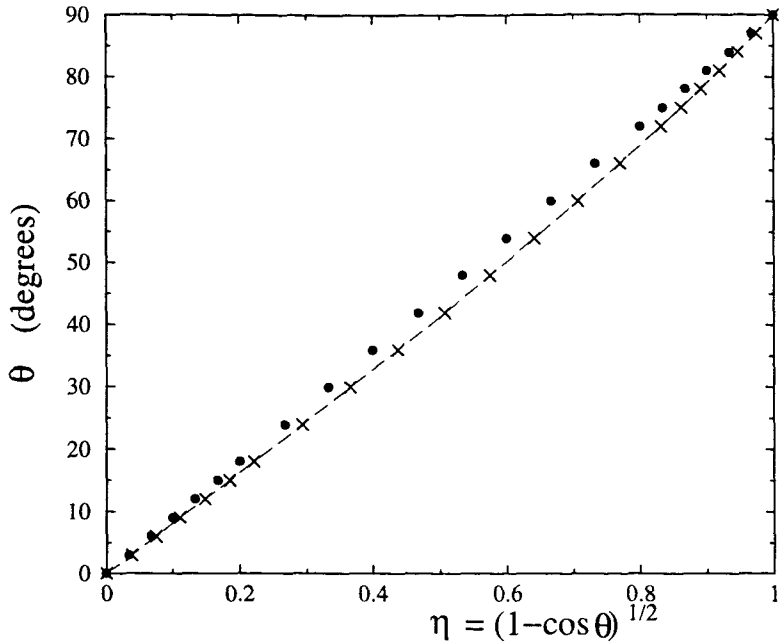


Figure 4.2: Grid point spacing in θ and η along a grid line where λ is constant. \times denote the distribution of grid points in η -space when the distribution in θ -space is constant in the main and boundary regions. \bullet denote the equivalent invariant transformation $\theta \mapsto \eta$.

described in the previous chapter. Near the boundaries the QUI method is used for first derivatives parallel to the boundary, but one-sided differencing [108] is used in the direction perpendicular to the boundary. Remember that near the boundaries the grid lines are closely spaced in the azimuthal system and so the size of the discretisation error associated with one-sided differencing is reduced. Central differencing is used to represent second derivatives everywhere.

On boundaries where a Neumann condition exists fictitious grid points outside the hemisphere are introduced. Fictitious points may also be necessary when using Leonard's method close to a boundary. Using the central difference approximation for the Neumann boundary condition, the fictitious grid points can be written in terms of grid points inside the hemisphere in the usual way. When no Neumann boundary condition exists, however, the fictitious grid points cannot be easily replaced and in this situation one-sided finite difference approximations are used in our solution.

There is a further complication to the finite difference scheme when the grid size is not equally spaced in either the η or λ directions, as in the azimuthal grid shown in figure 4.1. Near the boundaries between regions with different grid sizes considerable care is required and for simplicity, whenever the normal finite difference rules stated above would have required the use of fictitious points inside the central region of the grid shown in figure 4.1, one-sided

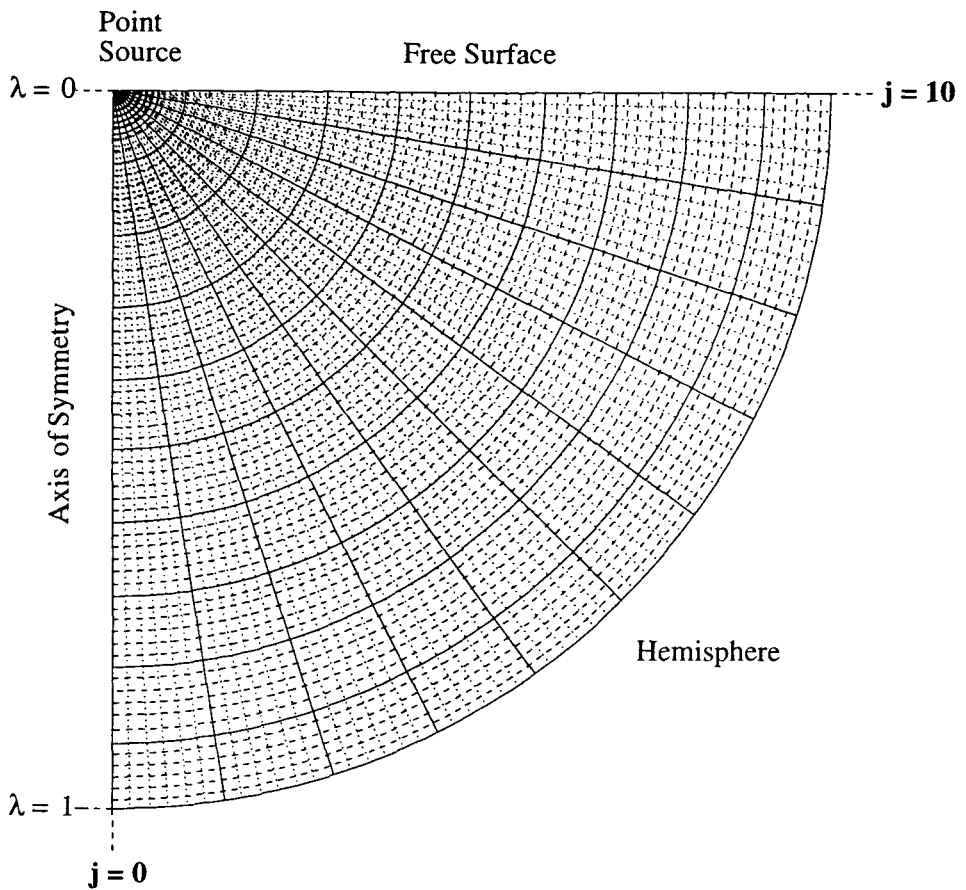
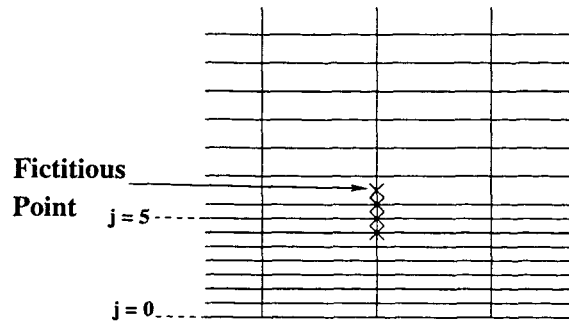
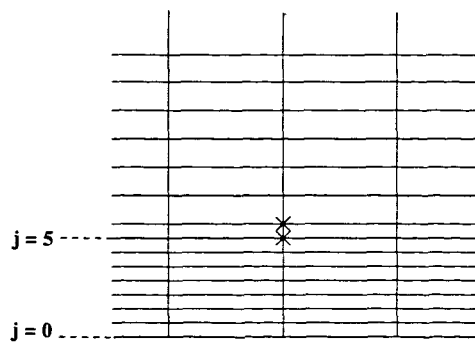


Figure 4.3: The poloidal stability grid, which uses equal spacing in λ and η throughout the hemisphere, is displayed by solid lines. The dotted lines denote the grid on which the steady-state solution, discussed in chapter 3, was calculated.

differences were used to avoid the difficulty. This situation is illustrated by figure 4.4, where in the upper diagram it is shown how the use of Leonard's method close to the transition between grid sizes, would require the introduction of a fictitious point within the central region. Instead of this scheme a simple one-sided difference is used, as shown in the lower diagram of figure 4.4. This change is adopted wherever a transition in the size of the mesh occurs.



Leonard's Method



One-sided differencing

Figure 4.4: Finite difference approximations at the grid size transition (when Leonard's method requires the use of a fictitious point within the central region one-sided finite differencing is used instead).

4.4.1 Azimuthal system

Positions of grid points

The grid used for solving the azimuthal system has been shown in figure 4.1. Note that 17 and 21 points are used in the λ and η directions respectively (i.e. $N_\lambda = 17$ and $N_\eta = 21$), since $\bar{g} = 0$ at the origin where $\lambda = 0$, on the hemisphere where $\lambda = 1$ and on the axis of symmetry where $\eta = 0$, so these points are not included in the grid.

In the central region (see figure 4.1), where constant values are used for $\Delta\lambda$ and $\Delta\eta$, the points are labelled

$$\begin{aligned} \text{for } \lambda = 1/15, 2/15, \dots, 12/15 \quad \text{by } i = 1, 2, \dots, 12 \quad \text{and} \\ \text{for } \eta = 3/15, 4/15, \dots, 12/15 \quad \text{by } j = 6, 7, \dots, 15. \end{aligned}$$

The value of λ at a particular point i and η at a particular point j in this central region are given by

$$\lambda_i = i\Delta\lambda_C \quad \text{and} \quad \eta_j = (j - 3)\Delta\eta_C, \quad (4.101)$$

where $\Delta\lambda_C = \Delta\eta_C = 1/15$. The subscript C refers to the central region.

Figure 4.1 shows that additional grid points are added near the axis, surface and hemispherical boundary by halving the grid spacing along lines perpendicular to the nearby boundary. In the axial region the grid points are labelled as follows:

$$\begin{aligned} \lambda = 1/15, 2/15, \dots, 12/15 \quad \text{by } i = 1, 2, \dots, 12 \quad \text{and} \\ \eta = 1/30, 2/30, \dots, 5/30 \quad \text{by } j = 1, 2, \dots, 5. \end{aligned}$$

The value of λ at a particular point i and η at a particular point j are given by

$$\lambda_i = i\Delta\lambda_A \quad \text{and} \quad \eta_j = j\Delta\eta_A. \quad (4.102)$$

The subscript A refers to the axial boundary region. The distances between mesh points in the λ and η directions are given by $\Delta\lambda_A = \Delta\lambda_C$ and $\Delta\eta_A = \Delta\eta_C/2$, where $\Delta\eta_C$ and $\Delta\lambda_C$ denote the grid spacing used in the central region in the η and λ directions respectively.

In a similar way in the surface boundary region the grid points are labelled:

$$\begin{aligned} \lambda = 1/15, 2/15, \dots, 12/15 \quad \text{as } i = 1, 2, \dots, 12 \quad \text{and} \\ \eta = 25/30, 26/30, \dots, 1 \quad \text{as } j = 16, 17, \dots, 21. \end{aligned}$$

In this region the values of λ and η at a particular point (i, j) are given by

$$\lambda_i = i\Delta\lambda_S \quad \text{and} \quad \eta_j = 6\Delta\eta_A + 9\Delta\eta_C + (j - 15)\Delta\eta_S, \quad (4.103)$$

where the subscript S denotes the surface boundary region. The values of $\Delta\lambda_S$ and $\Delta\eta_S$ are the same as $\Delta\lambda_A$ and $\Delta\eta_A$, that is $\Delta\lambda_C$ and $\Delta\eta_C/2$ respectively.

Turning to the hemispherical boundary region, the identification used is to represent

$$\begin{aligned}\lambda &= 25/30, 26/30, \dots 29/30 \quad \text{by} \quad i = 13, 14, \dots 17 \quad \text{and} \\ \eta &= 3/15, 4/15, \dots 12/15 \quad \text{by} \quad j = 6, 7, \dots 15.\end{aligned}$$

Here the values of λ and η at a particular point (i, j) are given by

$$\lambda_i = 12\Delta\lambda_C + (i - 12)\Delta\lambda_H \quad \text{and} \quad \eta_j = (j - 3)\Delta\eta_H \quad (4.104)$$

where $\Delta\eta_H = \Delta\eta_C$ and $\Delta\lambda_H = \Delta\lambda_C/2$, and the suffix H denotes the hemispherical boundary region.

In the top corner, between the outer hemisphere and the free surface, we represent

$$\begin{aligned}\lambda &= 25/30, 26/30, \dots 29/30 \quad \text{by} \quad i = 13, 14, \dots 17 \quad \text{and} \\ \eta &= 25/30, 26/30, \dots 1 \quad \text{by} \quad j = 16, 17, \dots 21.\end{aligned}$$

The appropriate values of λ and η at the point (i, j) are now

$$\lambda_i = 12\Delta\lambda_C + (i - 12)\Delta\lambda_{SH} \quad \text{and} \quad \eta_j = 6\Delta\eta_A + 9\Delta\eta_C + (j - 15)\Delta\eta_{SH}, \quad (4.105)$$

where $\Delta\eta_{SH} = \Delta\eta_C/2$ and $\Delta\lambda_{SH} = \Delta\lambda_C/2$.

Finally in the bottom corner, between the outer hemisphere and the axis of symmetry, the identification used is to label

$$\begin{aligned}\lambda &= 25/30, 26/30, \dots 29/30 \quad \text{by} \quad i = 13, 14, \dots 17 \quad \text{and} \\ \eta &= 1/30, 2/30, \dots 5/30 \quad \text{by} \quad j = 1, 2, \dots 5,\end{aligned}$$

with the corresponding values of λ and η at (i, j) given by

$$\lambda_i = 12\Delta\lambda_C + (i - 12)\Delta\lambda_{AH} \quad \text{and} \quad \eta_j = j\Delta\eta_{AH}, \quad (4.106)$$

with $\Delta\eta_{AH} = \Delta\eta_C/2$ and $\Delta\lambda_{AH} = \Delta\lambda_C/2$.

Finite difference form of (4.86)

Equation (4.86) is a second order partial differential equation in the perturbation variable \bar{g} with coefficients which depend on the steady-state solution. To obtain the finite difference

form of (4.86) within each region on figure 4.1 the second derivatives of $\bar{\bar{g}}$ are approximated on every internal grid point using central differences to give

$$0 = \frac{\eta_j(\eta_j^2 - 2)}{2} \left(\frac{\bar{\bar{g}}_{j-1} - 2\bar{\bar{g}}_j + \bar{\bar{g}}_{j+1}}{(\Delta\eta_R)^2} \right) + \left(\frac{2 - \eta_j^2}{2} - (\mathfrak{g} + \lambda_i \mathfrak{g}_\lambda) \right) \bar{\bar{g}}_\eta + \lambda_i \mathfrak{g}_\eta \bar{\bar{g}}_\lambda - 2\lambda_i^2 \eta_j \left(\frac{\bar{\bar{g}}_{i-1} - 2\bar{\bar{g}}_i + \bar{\bar{g}}_{i+1}}{(\Delta\lambda_R)^2} \right), \quad (4.107)$$

where the grid spacing in the finite difference approximations and the values of λ_i and η_j are dependent on the region, denoted by the subscript R , in which they are evaluated. For example, in the central region the subscript R is replaced by C , and η_j and λ_i by equation (4.101). The variable $\bar{\bar{g}}(\eta, \lambda)$ evaluated at (η_j, λ_i) is usually denoted by $\bar{\bar{g}}_{i,j}$. This notation is a little unwieldy, however, and for brevity we have dropped one subscript from the finite difference derivative approximations in equation (4.107) and most of the following working in this chapter. To illustrate the simplification of notation consider the central difference approximation for $\bar{\bar{g}}_{\eta\eta}$, namely

$$\frac{\bar{\bar{g}}_{i,j-1} - 2\bar{\bar{g}}_{i,j} + \bar{\bar{g}}_{i,j+1}}{(\Delta\eta_R)^2}, \quad \text{which is written as } \frac{\bar{\bar{g}}_{j-1} - 2\bar{\bar{g}}_j + \bar{\bar{g}}_{j+1}}{(\Delta\eta_R)^2}$$

in equation (4.107). An analogous procedure is generally adopted for all derivatives with respect to λ , when the j subscript is dropped from the explicit finite difference representations.

Over most of the grid the first derivatives $\bar{\bar{g}}_\eta$ and $\bar{\bar{g}}_\lambda$ are approximated using Leonard's method. To illustrate the procedure consider the term in (4.107) involving $\bar{\bar{g}}_\eta$, and write its coefficient as $a(\eta, \lambda)$. Central differences are used for any derivatives appearing in a , so

$$a_{i,j} = \frac{2 - (\eta_j)^2}{2} - \left(\mathfrak{g}_i + \lambda_i \frac{\mathfrak{g}_{i+1} - \mathfrak{g}_{i-1}}{2\Delta\lambda_R} \right).$$

Since the coefficient of $\bar{\bar{g}}_{\eta\eta}$ in the equation is negative, if at a given point $a_{i,j} < 0$ the derivative $\bar{\bar{g}}_\eta$ at that point is approximated by

$$\frac{-\bar{\bar{g}}_{j+2} + 6\bar{\bar{g}}_{j+1} - 3\bar{\bar{g}}_j - 2\bar{\bar{g}}_{j-1}}{6\Delta\eta_R},$$

whereas if $a_{i,j} > 0$ the derivative is written

$$\frac{2\bar{\bar{g}}_{j+1} + 3\bar{\bar{g}}_j - 6\bar{\bar{g}}_{j-1} + \bar{\bar{g}}_{j-2}}{6\Delta\eta_R}.$$

An analogous procedure is used for the term involving $\bar{\bar{g}}_\lambda$.

The expected direction of flow is parallel to the boundaries rather than perpendicular to them. For simplicity therefore one-sided differences, instead of Leonard's method, are used to approximate the first derivative $\partial/\partial\eta$ inside the axial and surface boundary regions. This

simpler approximation should be reasonable since the grid is finely spaced along lines in the η direction near these boundaries and velocities in this direction should be small. In the axial boundary region the coefficient of $\bar{\bar{g}}_\eta$ can be written

$$a_{i,j} = \frac{2 - (\eta_j)^2}{2} - \left(g_{i,j} + \lambda_i \frac{g_{i+1} - g_{i-1}}{2\Delta\lambda_A} \right),$$

where η_j and λ_i are given by equation (4.102) if $i < 13$ and equation (4.106) otherwise.

When $a_{i,j} < 0$ we use

$$\bar{\bar{g}}_\eta = \frac{\bar{\bar{g}}_{j+1} - \bar{\bar{g}}_j}{\Delta\eta_A},$$

whereas if $a_{i,j} > 0$ then we introduce

$$\bar{\bar{g}}_\eta = \frac{\bar{\bar{g}}_j - \bar{\bar{g}}_{j-1}}{\Delta\eta_A}.$$

An identical method is used in the surface boundary region, except that the subscript S replaces the subscript A in the approximations above, and λ_i , η_j are given by equation (4.103) if $i < 13$ and (4.105) otherwise.

In the outer hemispherical region the coefficient of $\bar{\bar{g}}_\lambda$ in (4.86) can be expressed

$$b_{i,j} = \frac{\lambda_i(g_{j+1} - g_{j-1})}{2\Delta\eta_H},$$

where λ_i is given by equation (4.106) if $j < 6$, (4.104) if $6 \leq j \leq 15$ and (4.105) otherwise.

The derivative $\bar{\bar{g}}_\lambda$ is replaced by

$$\frac{\bar{\bar{g}}_{i+1} - \bar{\bar{g}}_i}{\Delta\lambda_H} \quad \text{when } b_{i,j} < 0,$$

and by

$$\bar{\bar{g}}_\lambda = \frac{\bar{\bar{g}}_i - \bar{\bar{g}}_{i-1}}{\Delta\lambda_H} \quad \text{when } b_{i,j} > 0.$$

The quantity $\bar{\bar{g}}$ vanishes on all boundaries except the free surface. On the latter, equation (4.86) is transformed into equation (4.91) which can be expressed

$$0 = -\frac{\bar{\bar{g}}_{j-1} - \bar{\bar{g}}_j}{(\Delta\eta_S)^2} + \lambda_i g_\eta \bar{\bar{g}}_\lambda - 2\lambda_i^2 \left(\frac{\bar{\bar{g}}_{i-1} - 2\bar{\bar{g}}_i + \bar{\bar{g}}_{i+1}}{(\Delta\lambda_S)^2} \right), \quad (4.108)$$

where λ_i is given by equation (4.103) if $i < 13$ or (4.105) otherwise, and $\bar{\bar{g}}_\lambda$ as described by the preceding paragraph.

Throughout the small corner regions where the grid points are finely spaced in both coordinate directions, one-sided differencing is employed to approximate first derivatives whenever Leonard's method would lead to unwanted fictitious points. Examples of these are points outside the hemisphere which cannot be written in terms of grid points within the hemisphere (usually when there is not a Neumann boundary condition), or fictitious points within the central region as shown in figure 4.4. These cases were discussed earlier in this section. The second derivatives in these situations need no special treatment.

4.4.2 Poloidal system

Position of grid points

The numerical solution of the poloidal system of stability equations is very time consuming, and so the number of grid points chosen is relatively small. In the poloidal system of equations the mesh points are equally spaced throughout the region with eleven points used in the λ direction and eleven points in the η direction, (i.e. $N_\eta = N_\lambda = 11$). An odd number of grid points occurs in both the λ and η directions since poloidal stability variables are required at the origin and on the axis of symmetry and so grid points are needed on $\lambda = 0$ and $\eta = 0$. The poloidal grid is displayed with solid lines in figure 4.3. The grid points are labelled for

$$\begin{aligned}\lambda &= 0, 1/10, \dots 1 \text{ by } i = 0, 1, \dots 10 \text{ and} \\ \eta &= 0, 1/10, \dots 1 \text{ by } j = 0, 1, \dots 10.\end{aligned}$$

The values of λ and η at point (i, j) are given by

$$\lambda_i = i\Delta\lambda \quad \text{and} \quad \eta_j = j\Delta\eta$$

respectively, where throughout the entire grid $\Delta\lambda = 1/10$ and $\Delta\eta = 1/10$. These values of $\Delta\lambda$ and $\Delta\eta$ are used throughout the remainder of this section on the poloidal system.

Finite difference forms of equations (4.87), (4.88) and (4.89)

The bulk of the region is approximated by Leonard's QUI method for first derivatives and central differencing for second derivatives, but special consideration is given to the equations on or near the boundaries.

Consider first equation (4.87) which transforms into

$$\begin{aligned}\left(\frac{1}{2\eta_j}\right) \left(\frac{\tilde{\tilde{g}}_{j+1} - 2\tilde{\tilde{g}}_j + \tilde{\tilde{g}}_{j-1}}{(\Delta\eta)^2}\right) + \left(\frac{2(\lambda_i)^2}{\eta_j(2 - (\eta_j)^2)}\right) \left(\frac{\tilde{\tilde{g}}_{i+1} - 2\tilde{\tilde{g}}_i + \tilde{\tilde{g}}_{i-1}}{(\Delta\lambda)^2}\right) \\ - 2(\eta_j)\tilde{\tilde{f}}_{i,j} - \left(\frac{1}{2(\eta_j)^2}\right)\tilde{\tilde{g}}_\eta + \left(\frac{4\lambda_i}{\eta_j(2 - (\eta_j)^2)}\right)\tilde{\tilde{g}}_\lambda = 0,\end{aligned}\quad (4.109)$$

where the derivatives $\tilde{\tilde{g}}_\lambda$ and $\tilde{\tilde{g}}_\eta$ are approximated by Leonard's method, as shown below. Since

$$\left(\frac{4\lambda_i}{\eta_j(2 - (\eta_j)^2)}\right) \geq 0 \quad \text{for all } \lambda \in (0, 1], \eta \in (0, 1],$$

the derivative $\tilde{\tilde{g}}_\lambda$ is approximated by

$$\frac{-\tilde{\tilde{g}}_{i+2} + 6\tilde{\tilde{g}}_{i+1} - 3\tilde{\tilde{g}}_i - 2\tilde{\tilde{g}}_{i-1}}{6\Delta\lambda}.\quad (4.110)$$

In an analogous way, the coefficient multiplying the derivative $\tilde{\tilde{g}}_\eta$ is always negative and so $\tilde{\tilde{g}}_\eta$ is replaced by

$$\frac{2\tilde{\tilde{g}}_{j+1} + 3\tilde{\tilde{g}}_j - 6\tilde{\tilde{g}}_{j-1} + \tilde{\tilde{g}}_{j-2}}{6\Delta\eta}\quad (4.111)$$

throughout the region.

Next we consider the temperature equation (4.88) which can be written

$$\begin{aligned}
0 = & \left(\frac{t_{j+1} - t_{j-1}}{2\Delta\eta} \right) \tilde{g}_\lambda + \left(\frac{t_{i,j}}{\lambda_i} - \left(\frac{t_{i+1} - t_{i-1}}{2\Delta\lambda} \right) \right) \tilde{g}_\eta \\
& + \left(g_{i,j} + \lambda_i \left(\frac{g_{i+1} - g_{i-1}}{2\Delta\lambda} \right) + P_r \left(\frac{2 - 3(\eta_j)^2}{2} \right) \right) \tilde{T}_\eta \\
& + \left(4\eta_j \lambda_i P_r - \lambda_i \left(\frac{g_{i+1} - g_{i-1}}{2\Delta\lambda} \right) \right) \tilde{T}_\lambda \\
& + \left(P_r \frac{\eta_j [2 - (\eta_j)^2]}{2} \right) \left(\frac{\tilde{T}_{j+1} - 2\tilde{T}_j + \tilde{T}_{j-1}}{(\Delta\eta)^2} \right) \\
& + 2\eta_j P_r (\lambda_i)^2 \left(\frac{\tilde{T}_{i+1} - 2\tilde{T}_i + \tilde{T}_{i-1}}{(\Delta\lambda)^2} \right) + \left(\frac{t_{j+1} - t_{j-1}}{2\Delta\eta\lambda_i} \right) \tilde{g}_{i,j}, \quad (4.112)
\end{aligned}$$

where t_λ , t_η , g_λ have been expressed using central differences. The first derivatives \tilde{T}_η , \tilde{T}_λ are approximated once again by Leonard's QUI method in an analogous way to the method used for the equations above. For the sake of continuity with the steady state solution in the hemisphere, and use of the same discretisation error, the first derivatives \tilde{g}_η and \tilde{g}_λ are also approximated using the QUI method.

Finally, equation (4.89) can be expressed

$$\begin{aligned}
0 = & \left(\frac{\eta_j (2 - (\eta_j)^2)}{2} \right) \left(\frac{\tilde{f}_{j+1} - 2\tilde{f}_j + \tilde{f}_{j-1}}{(\Delta\eta)^2} \right) + 3 \left(\frac{g_{j+1} - g_{j-1}}{2\Delta\eta} \right) \tilde{f}_{i,j} \\
& + \left(3 - \frac{7(\eta_j)^2}{2} + g_{i,j} + (\lambda_i) \frac{g_{i+1} - g_{i-1}}{2\Delta\lambda} \right) \tilde{f}_\eta \\
& + 2\eta_j (\lambda_i)^2 \left(\frac{\tilde{f}_{i+1} - 2\tilde{f}_i + \tilde{f}_{i-1}}{(\Delta\lambda)^2} \right) + \left(3f_{i,j} - (\lambda_i) \frac{f_{i+1} - f_{i-1}}{2\Delta\lambda} \right) \tilde{g}_\eta \\
& + \left((\lambda_i) \frac{f_{j+1} - f_{j-1}}{2\Delta\eta} \right) \tilde{g}_\lambda + \left(\frac{f_{j+1} - f_{j-1}}{2\Delta\eta} \right) \tilde{g}_{i,j} \\
& + R_r (\lambda_i)^3 \left(1 - (\eta_j)^2 \right) \tilde{T}_\eta - \lambda_i \left(4\eta_j + \frac{g_{j+1} - g_{j-1}}{2\Delta\eta} \right) \tilde{f}_\lambda \\
& + 2\eta_j (\lambda_i)^4 R_r \tilde{T}_\lambda, \quad (4.113)
\end{aligned}$$

where the first derivatives \tilde{f}_λ and \tilde{f}_η are again approximated by the QUI scheme and for the sake of continuity so are \tilde{g}_λ , \tilde{g}_η , \tilde{T}_λ and \tilde{T}_η .

Finite difference forms of the poloidal stability boundary conditions (4.94), (4.95), (4.98) and (4.99).

On the free surface, $\eta = 1$, the temperature perturbation function \tilde{T} and vorticity perturbation function \tilde{f} are not prescribed. Using central differences to approximate $\tilde{T}_{\lambda\lambda}$ and $\tilde{T}_{\eta\eta}$

(with the grid point outside the hemisphere removed by the central difference approximation of the Neumann boundary condition) and one-sided differences for \tilde{g}_η , \tilde{f}_η and $\tilde{f}_{\eta\eta}$, the temperature equation (4.95) transforms to

$$0 = \left(\frac{t_{i,j}}{2\lambda_i} - \frac{t_i - t_{i-1}}{4\Delta\lambda} \right) \left(\frac{\tilde{g}_j - \tilde{g}_{j-1}}{2\Delta\eta} \right) + (\lambda_i)^2 P_r \left(\frac{\tilde{T}_{i+1} - 2\tilde{T}_i + \tilde{T}_{i-1}}{(\Delta\lambda)^2} \right) + \left(2\lambda_i P_r - \frac{\lambda_i}{2} \left(\frac{g_i - g_{i-1}}{\Delta\lambda} \right) \right) \tilde{T}_\lambda + \frac{P_r}{2} \left(\frac{-\tilde{T}_j + \tilde{T}_{j-1}}{(\Delta\eta)^2} \right) \quad (4.114)$$

and the vorticity equation, (4.99), similarly becomes

$$0 = \left(\frac{3f_{i,j}}{2} - \frac{\lambda_i(f_{i+1} - f_{i-1})}{4\Delta\lambda} \right) \left(\frac{\tilde{g}_j - \tilde{g}_{j-1}}{\Delta\eta} \right) + \left(\frac{3(g_j - g_{j-1})}{2\Delta\eta} \right) \tilde{f}_{i,j} + R_r(\lambda_i)^4 \tilde{T}_\lambda - \left(2\lambda_i + \frac{\lambda_i}{2} \left(\frac{g_j - g_{j-1}}{\Delta\eta} \right) \right) \tilde{f}_\lambda - \frac{1}{4} \left(\frac{\tilde{f}_j - \tilde{f}_{j-1}}{\Delta\eta} \right) + (\lambda_i)^2 \left(\frac{\tilde{f}_{i+1} - 2\tilde{f}_i + \tilde{f}_{i-1}}{(\Delta\lambda)^2} \right) + \frac{1}{4} \left(\frac{\tilde{f}_{j-2} - 2\tilde{f}_{j-1} + \tilde{f}_j}{(\Delta\eta)^2} \right). \quad (4.115)$$

The first derivatives \tilde{T}_λ and \tilde{f}_λ in equations (4.114) and (4.115) are then approximated by Leonard's QUI method and the resulting finite difference scheme used on $\eta = 1$.

Near the boundaries $\lambda = 0$ and $\lambda = 1$ the first derivatives are written in terms of one-sided differences only when the use of the third order QUI method would require the introduction of fictitious grid points and no Neumann boundary conditions for either \tilde{f} or \tilde{T} exist on $\lambda = 0$ or $\lambda = 1$. On the axis of symmetry, $\eta = 0$, equation (4.94) becomes

$$0 = (\lambda_i)^2 P_r \left(\frac{\tilde{T}_{i-1} - 2\tilde{T}_i + \tilde{T}_{i+1}}{(\Delta\lambda)^2} \right) + 2P_r \left(\frac{\tilde{T}_{j+1} - \tilde{T}_j}{(\Delta\eta)^2} \right) + 2\lambda_i P_r \left(\frac{-\tilde{T}_{i+2} + 6\tilde{T}_{i+1} - 3\tilde{T}_i - 2\tilde{T}_{i-1}}{6\Delta\lambda} \right), \quad (4.116)$$

except on the mesh point where $\lambda = 1 - \Delta\lambda$. For the latter \tilde{T}_λ is approximated by first order differencing.

It remains to determine \tilde{f} on the axis of symmetry. The perturbation \tilde{f} satisfies equation (4.98) when $\eta = 0$ and is approximated by

$$0 = - 2\lambda_i \left(\frac{2\tilde{f}_{i+1} + 3\tilde{f}_i - 6\tilde{f}_{i-1} + \tilde{f}_{i-2}}{6\Delta\lambda} \right) + (\lambda_i)^2 \left(\frac{\tilde{f}_{i+1} - 2\tilde{f}_i + \tilde{f}_{i-1}}{(\Delta\lambda)^2} \right) + 4 \left(\frac{\tilde{f}_{j+1} - \tilde{f}_j}{(\Delta\eta)^2} \right) + R_r(\lambda_i)^3 \left(\frac{\tilde{T}_{j+1} - \tilde{T}_j}{(\Delta\eta)^2} \right) + R_r(\lambda_i)^4 \left(\frac{-\tilde{T}_{i+2} + 6\tilde{T}_{i+1} - 3\tilde{T}_i - 2\tilde{T}_{i-1}}{6\Delta\lambda} \right), \quad (4.117)$$

except on the mesh points where $\lambda = \Delta\lambda$ and $\lambda = 1 - \Delta\lambda$. For the latter two special cases the first derivatives with respect to λ are once again approximated by first order differences, since the QUI method would use values on grid points outside the hemisphere that cannot be written in terms of values on grid points inside the region.

Finite difference form of equation (4.97) on $\lambda = 1$

Investigation revealed that by using the finite difference equation (4.97) on the hemispherical boundary $\lambda = 1$ some positive real eigenvalues σ_1 were produced for all values of the applied current, even very small values. This result is not expected and after some thought and numerical experimentation, different implementations of the boundary conditions applied at the solid hemispherical boundary were explored. A variety of forms of this boundary condition have been proposed by Woods [137], Thom [125] and Pearson [81] but all are derived by using Taylor series expansions of the stream function and vorticity close to the hemispherical boundary.

The Woods boundary condition is stated

$$Q(\eta, 1) = \frac{3}{(\Delta\lambda)^2} \psi(\eta, 1 - \Delta\lambda) - \frac{1}{2} Q(\eta, 1 - \Delta\lambda) + O(h^2), \quad (4.118)$$

where the stream function ψ and vorticity Q are related by $Q = \nabla^2 \psi$. In the work in this thesis for flow in a hemisphere, the Stokes stream function is used for the main and perturbation flow variables and so a revised form of equation (4.118) must be found that follows from our relation

$$Q = \nabla^2 \left(\frac{\psi}{a\lambda\eta(2 - \eta^2)^{\frac{1}{2}}} \right).$$

Since evaluating equation (4.87) on $\lambda = 1$ gives

$$\tilde{f}(\eta, 1) = \frac{\tilde{g}_{\lambda\lambda}(\eta, 1)}{\eta^2(2 - \eta^2)},$$

a relationship similar to (4.118) can be obtained which gives this expression when expanded in a Taylor series in $\Delta\lambda$. This time, however, the boundary condition must be expressed in terms of the non-dimensional vorticity on the solid boundary, $\tilde{f}(\eta, 1)$, and the non-dimensional stream function and vorticity on the adjacent grid point, $\tilde{g}(\eta, 1 - \Delta\lambda)$ and $\tilde{f}(\eta, 1 - \Delta\lambda)$,

Therefore, the Woods boundary condition for a Stokes stream function has the form

$$\begin{aligned} \tilde{f}(\eta, 1) = & \left(\frac{3}{(\Delta\lambda)^2(1 + 2\Delta\lambda)(\eta_j)^2(2 - (\eta_j)^2)} \right) \tilde{g}(\eta, 1 - \Delta\lambda) \\ & - \left(\frac{1}{2(1 + 2\Delta\lambda)} \right) \tilde{f}(\eta, 1 - \Delta\lambda). \end{aligned} \quad (4.119)$$

Using a similar approach it can be shown that the forms of the boundary conditions on the outer hemispherical boundary suggested by Thom and Pearson, for a Stokes stream function,

are

$$\tilde{f}(\eta, 1) \simeq \frac{2\tilde{g}(\eta, 1 - \Delta\lambda)}{(\Delta\lambda)^2(\eta_j)^2[2 - (\eta_j)^2]} \quad (4.120)$$

and

$$\tilde{f}(\eta, 1) \simeq \frac{4\tilde{g}(\eta, 1 - \Delta\lambda)}{(\Delta\lambda)^2(\eta_j)^2[2 - (\eta_j)^2]} - \frac{\tilde{g}(\eta, 1 - 2\Delta\lambda)}{2(\Delta\lambda)^2(\eta_j)^2[2 - (\eta_j)^2]}, \quad (4.121)$$

respectively. Thom's boundary condition (4.120), is the simpler expression. However, the condition has a leading order error of $O(\Delta\lambda)$, whereas the Woods and Pearson boundary conditions preserve the second order error used in most of the discretisation process.

In performing a numerical linear stability analysis every grid point on the stability mesh produces an eigenvalue for each perturbation variable considered at that mesh point. When all the eigenvalues have negative real part the system is said to be stable. On solving the system of equations with \tilde{f} evaluated on the boundary $\lambda = 1$ using equation (4.97), some eigenvalues with positive real part were produced for all values of $\partial\gamma/\partial T$ and J . On replacing equation (4.97) by equations (4.119), (4.120) and (4.121) in turn, however, all the eigenvalues had negative real part when the system was tested at very low currents for a number of different values of $\partial\gamma/\partial T$. Since the Woods boundary condition has been used in the numerical solution for the steady-state solution in the hemisphere it is also the one chosen in the stability analysis in this chapter.

4.5 Method of solution

The existence of solutions to both the azimuthal and poloidal sets of equations must be investigated numerically, since the perturbations cannot be written analytically and the solution to the steady state problem had to be found numerically. The azimuthal stability equation (4.86) with boundary conditions (4.90) and (4.91) (which decoupled from the remaining stability equations when the system was linearised), and the poloidal stability system (4.87), (4.88) and (4.89) subject to the boundary conditions (4.92) to (4.100) (with (4.97) replaced by (4.119)) are solved separately on the grids displayed in figures 4.1 and 4.3 respectively. The solution method in both cases is essentially the same.

Consider first the method for the poloidal system. The governing poloidal stability equations in finite difference form ((4.109), (4.112) and (4.113)), and their corresponding boundary conditions, are written in terms of a matrix \mathbf{A} of coefficients and a vector \mathbf{x} of perturbation functions, over the entire finite difference stability grid on which the perturbations are unknown. The system is expressed

$$\mathbf{A}\mathbf{x} = \mathbf{0}, \quad (4.122)$$

where \mathbf{x} is a vector of the unknown functions \tilde{g} , \tilde{f} and \tilde{T} at each point on the grid of solid lines shown in figure 4.3. The elements in \mathbf{A} are determined from the values of f , g and t (and their derivatives) at each grid point, calculated using the underlying steady-state model discussed in chapter 3.

The overall solution method is as follows. For a given value of $\partial\gamma/\partial T$, the current J is increased from zero in small steps. At each new value of J the steady-state solution in the hemisphere is calculated numerically, and this solution is used to determine the coefficients in the matrix \mathbf{A} . The determinant of \mathbf{A} is then calculated using NAG routine F03AFF. Non-zero solutions for \mathbf{x} exist only when the determinant of \mathbf{A} is identically zero. Investigation revealed that at extremely low currents all the eigenvalues of the system (which correspond to the rate of exponential growth with time of the perturbations) were found to be negative, as expected. Consequently, at these parameter values all disturbances decrease exponentially with time and the problem is stable.

As the current is increased a different steady-state solution is obtained and hence the values of the coefficients change in matrix \mathbf{A} . As a result the magnitudes the eigenvalues associated with the system will also change. If the real part of a single (real) eigenvalue passes through zero then the determinant of \mathbf{A} (calculated via NAG routine F03AFF) will change sign. This feature will always occur since $\det\mathbf{A}$ is proportional to the product of the eigenvalues.

Complex eigenvalues occur in conjugate pairs, and the imaginary part of a complex eigenvalue corresponds to an oscillatory perturbation. When the real part of a complex eigenvalue changes sign, in this chapter due to a change in either $\partial\gamma/\partial T$ or J , the real part of its complex

conjugate must also change sign. In this situation the determinant of \mathbf{A} will not change sign, since the product of a pair of complex conjugate eigenvalues is always positive regardless of the sign of their real part. Therefore, monitoring changes to the sign of the determinant is not sufficient if the system of stability equations is likely to produce complex eigenvalues. In this, and the subsequent chapter, however, we assume the *principle of exchange of stabilities* and look for the simpler case where all the eigenvalues are assumed real.

The program structure that was used to solve the poloidal and azimuthal stability problems is shown in figure 4.5. At the start of the solution process values for $\partial\gamma/\partial T$ and J were entered by the user, together with the size of the current increment to be used later. Then the semi-infinite numerical model described in chapter 2 was solved to obtain the similarity solution. This solution was used in calculating the steady-state solution in the hemisphere, as discussed in chapter 3, from which the elements of matrix \mathbf{A} could be determined. Nag routine F03AFF calculated the determinant of matrix \mathbf{A} and the current was then increased by the previously prescribed incremental step and, provided the current did not exceed some user imposed maximum, the code was re-run. Solving the stability problem on a Sun SPARC5 machine, for a considerable number of discrete values of $\partial\gamma/\partial T$ and J in the region of parameter space where the steady-state model converged, required a running time of at least two weeks. Due to the length of time required to run these simulations the number of results presented in this thesis is relatively small.

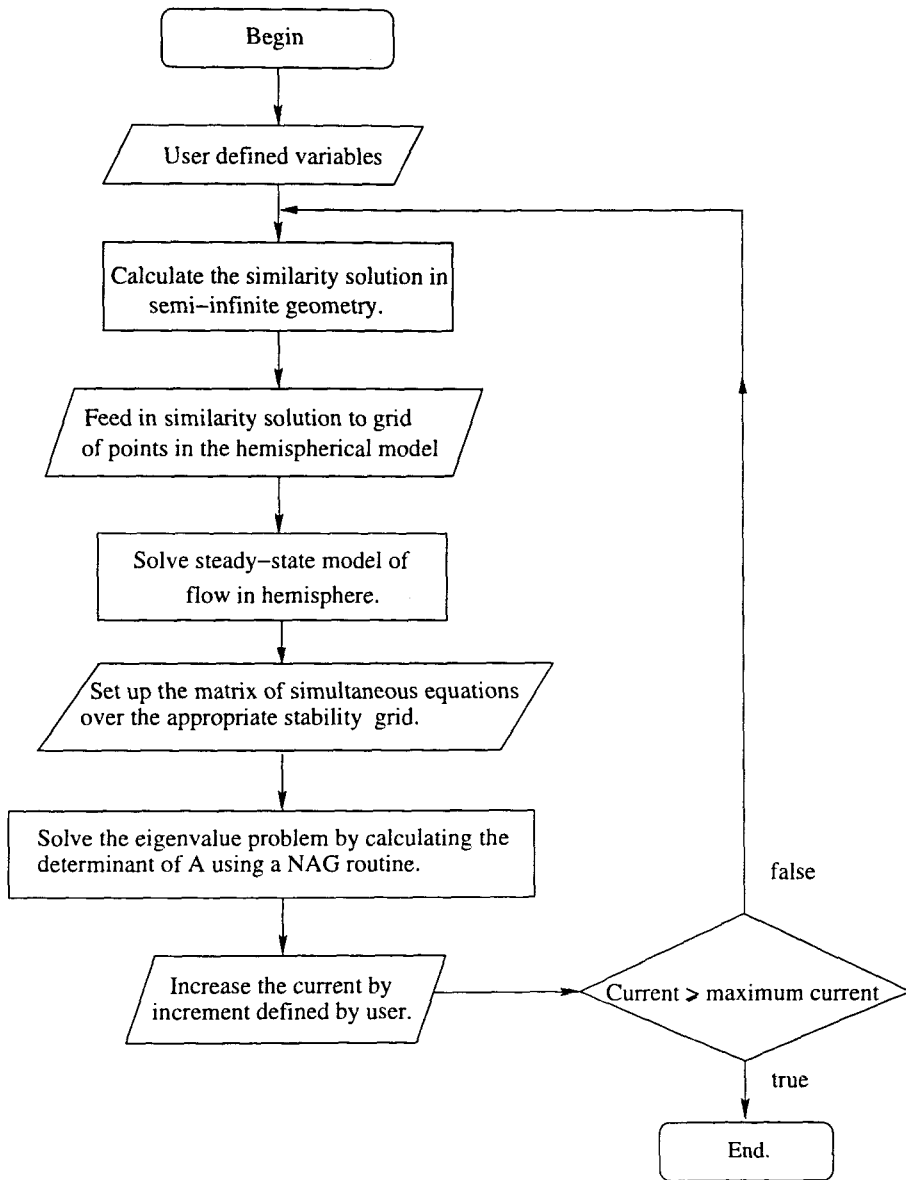


Figure 4.5: Program structure

4.6 Results and discussion

The determinant of \mathbf{A} was calculated for a large number of values of the current, J , and surface tension gradient, $\partial\gamma/\partial T$, for which the underlying steady state model converged. In a set of solutions the surface tension gradient was fixed and the current was then increased in small steps until a current was reached, J_{crit} , for which the steady state solution in the hemisphere failed to converge. Figures 3.4 and 3.8 showed J_{crit} as a function of $\log_{10}(\pm \partial\gamma/\partial T)$ respectively and as discussed then, at currents greater than J_{crit} no solution could be obtained. For each solution determined the determinant was recorded and its values was observed to vary smoothly with the current J as the latter was slowly increased.

The underlying steady-state model was solved on a 61×61 grid in the hemisphere. Numerical experimentation suggested that these solutions were sufficiently accurate for our purposes. The accuracy of the stability curves produced in the figures below is clearly dependent on the incremental step size in the current, and in our results the step size was set to 0.014. As discussed earlier the number of grid points used in the azimuthal and poloidal stability problems was restricted by the running time and capacity of the Sun SPARC5 machine on which the numerical results were calculated. The complicated nature of the formulation of the stability problem discussed here combined with the long running time made extensive checking difficult. However, the accuracy of the results presented were checked by altering the number of grid lines in both the poloidal-stability model and the underlying steady-state model, taking care that mesh points on the two grids remained coincident, and then running the code for various values of $\partial\gamma/\partial T$ and J . In the poloidal-stability case changes in the number of grid points in either the steady-state grid or the poloidal stability grid caused only small changes in the position of the displayed stability curves. The more complicated structure of the finite difference grid for the azimuthal stability problem made changing the size of the stability grid in this case more difficult. However, varying the size of the underlying steady state grid, again caused only small changes in the stability curves when the code was tested for particular values of $\partial\gamma/\partial T$ and J .

4.6.1 Azimuthal stability problem

Figure 4.6 displays the stability of the steady flow to the decoupled azimuthal perturbation when the surface tension gradient is negative. No azimuthal rotational flow was allowed in the steady state model, but an azimuthal perturbation is included and the marginal stability curve therefore corresponds to the development of a rotational component in the flow. The upper solid curves seen on the upper right- and left-hand sides of figure 4.6 show the current values for which the underlying steady-state numerical solution for flow in the hemisphere ceased to be convergent, see figure 3.8. (The steady-state model in chapter 3 was deemed to

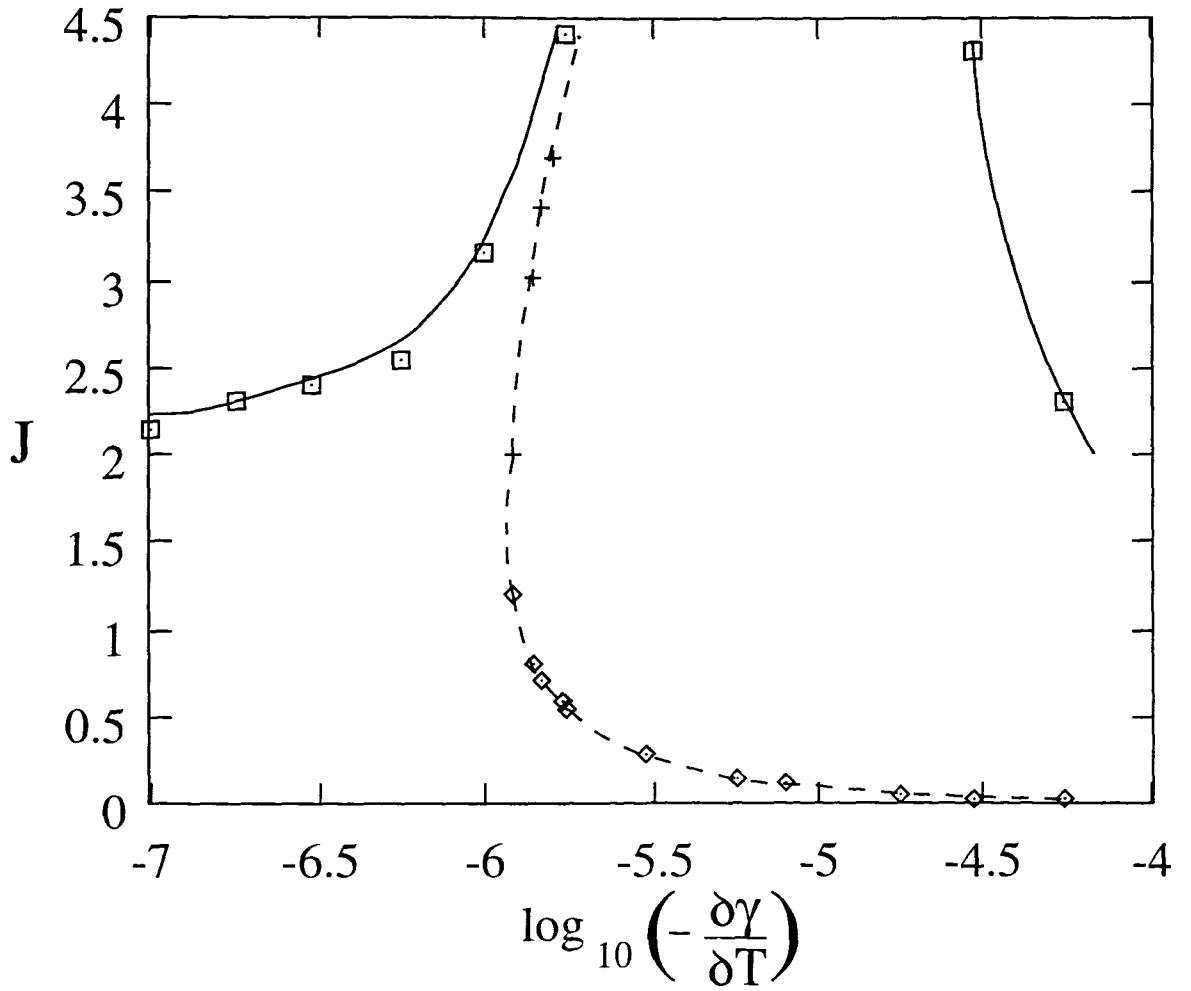


Figure 4.6: Stability and steady-state breakdown curves for the azimuthal system when $\partial\gamma/\partial T < 0$.

be non-convergent if, after 90,000 iterations of the SUR solution algorithm, equations (3.14), (3.15) and (3.16) could not be satisfied to within a tolerance of 0.002%.

At the very small current values below and to the left of the dotted line the model is stable to azimuthal perturbations. The dotted line denotes a marginal stability curve where there exists an exchange of stabilities. When crossing from the left to the right of this dotted line the determinant of \mathbf{A} changes sign and consequently a real eigenvalue passes through zero, thereby becoming positive, and the system becomes unstable to azimuthal perturbations. Careful inspection of figure 4.6 clearly shows that for $J \leq 4.5A$ the region of instability does not extend up to the current values at which the underlying steady state numerical model fails to converge. For currents just below the breakdown value, however, the model is extremely difficult to investigate, since the numerical procedures are very sensitive and lengthy. It should be pointed out that, in [7] the similarity solution obtained for the semi-infinite model (discussed in chapter 2 of this thesis) was shown to be stable for large negative $\partial\gamma/\partial T$ and, therefore, the outward jet predicted here is unstable due to restricting the fluid to being inside a hemisphere.

Figure 4.6 displays the case of negative surface tension gradient. A negative $\partial\gamma/\partial T$ causes an outward flow of fluid on the free surface away from the point source at the origin. As the magnitude of the negative surface tension gradient was increased a strong surface jet, outwards from the source, developed at very small current values in the underlying steady-state flow model described in chapter 3 (see figure 3.7). The dotted line shown in figure 4.6 tends towards zero as the magnitude of $\partial\gamma/\partial T$ increases and this suggests that the instability which develops in the azimuthal system is due to the strong outward Marangoni force, manifest in the stationary model for large values of negative $\partial\gamma/\partial T$ and small currents.

When $\partial\gamma/\partial T$ is positive the Marangoni force tries to create on the free surface an inward flow towards the point source. In this situation the azimuthal linear stability system did not possess any marginal stability curves up to current values close to where the underlying steady-state model failed to converge. It is well known that converging vortices have a tendency to ‘spin up’, and this consideration was applied to the welding problem by Bojarevics in [13] and [12]. As a result of his arguments our model might be expected to possess marginal stability curves just prior to the breakdown of the steady-state model, where an axial jet develops down the axis of symmetry, but because convergence of the steady-state model is difficult to achieve in this region no such curves could be found.

It is hoped that an indication of the region where azimuthal instability first occurs inside the hemisphere can be gained by examining the eigenvector \mathbf{e}_v , corresponding to the first positive eigenvalue. The relevant eigenvector was found by using the NAG routine F02BJF. The solution for \mathbf{e}_v provides a vector of the scaled azimuthal perturbation streamfunction $\bar{g}(\lambda, \eta)$ at each grid point on the azimuthal finite difference mesh displayed in figure 4.1. Note

that the other poloidal perturbations have decoupled, although they will be considered later in this section.

Plots of \mathbf{e}_v are obtained by choosing appropriate values for \bar{g} , and plotting these points using linear interpolation between grid points in the λ and η directions. Curves are fitted through these points. This procedure was quite lengthy and complicated to code since the spacing for the azimuthal stability grid is not constant throughout the hemisphere.

Figure 4.7 shows the secondary flow set up due to the positive eigenvalue which occurs when $\partial\gamma/\partial T = -3.0 \times 10^{-5} Nm^{-1}K^{-1}$ and $J = 0.03A$. The values of the stream function have

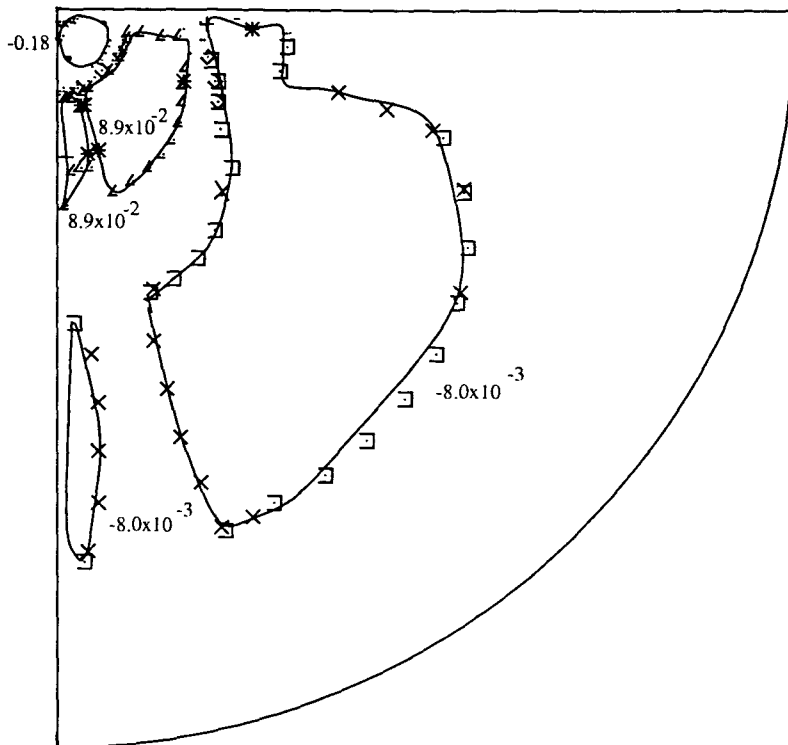


Figure 4.7: Contour plot of $\bar{g}(\lambda, \eta)$ obtained from an evaluation of the azimuthal eigenvector \mathbf{e}_v when $\partial\gamma/\partial T = -3.0 \times 10^{-5} Nm^{-1}K^{-1}$ and $J = 0.03A$.

been scaled in the numerical algorithm and consequently the numbers on the figure only give a relative order of magnitude for the non-dimensional perturbation stream-function $\bar{g}(\lambda, \eta)$ at each grid point. At first sight this figure seems quite complicated but a closer inspection reveals that the maximum flow region occurs close to the point source. This suggests that the breakdown in stability is due to azimuthal rotation near the point source of heat and current. Since the general form of the perturbation for \bar{g} is

$$\bar{g} = \bar{g} e^{(im\phi + \sigma t)},$$

it is clear that the perturbations are independent of ϕ for the mode $m = 0$. (Recall that \bar{g} denotes the non-dimensional stream-function perturbation in the azimuthal direction.) These

perturbations must conform to the principal of conservation of angular momentum, however, so the presence of the strong rotation near the origin creates a slow counter-rotating region in the main bulk of the fluid (see figures 4.7 and 4.8).

Figure 4.8 shows a different secondary flow, corresponding to the positive eigenvalue which occurs when $\partial\gamma/\partial T = -1.78 \times 10^{-6} Nm^{-1} K^{-1}$ and $J = 0.545A$. Once again the eigenvector

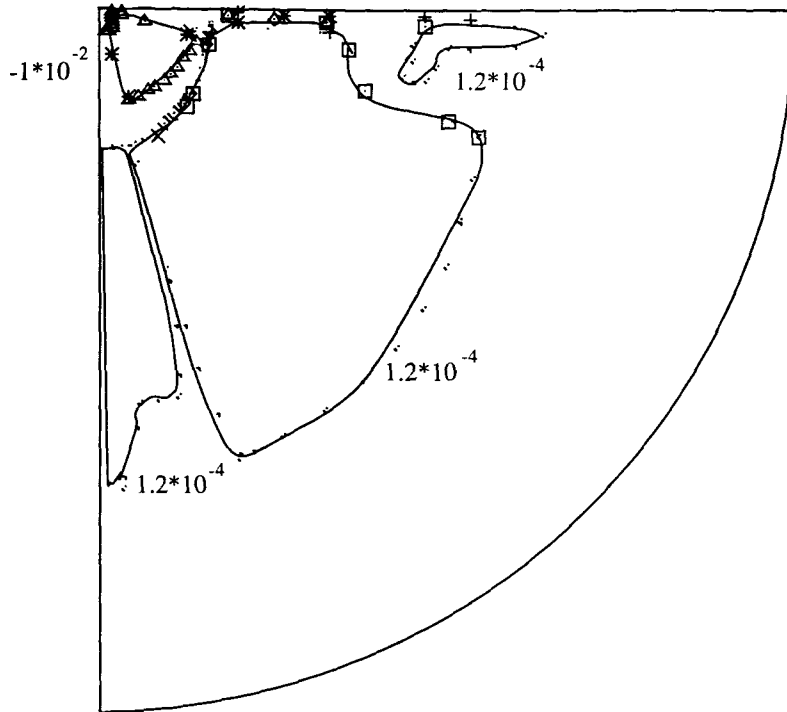


Figure 4.8: Contour plot of $\tilde{g}(\lambda, \eta)$ obtained from an evaluation of the azimuthal eigenvector e_v when $\partial\gamma/\partial T = -1.78 \times 10^{-6} Nm^{-1} K^{-1}$ and $J = 0.545A$.

suggests that instability is due to the development of a large azimuthal rotation at the point source. In a similar way to the preceding case, the main bulk of the fluid rotates slowly in the opposing direction to conserve angular momentum.

4.6.2 Poloidal system

The stability curves for positive surface tension gradient in the poloidal system are described in figure 4.9. The upper curve, labelled 1, shows the current J_{crit} at which the underlying steady state model described in chapter 3 failed to converge (see figure 3.4). At current values exceeding J_{crit} no converged solution to the steady-state model could be obtained. A marginal stability curve was found lying just below curve 1 but it is too close to curve 1 to display on the figure. Curve 2 denotes a change in the sign of the determinant of matrix A . Therefore, within the region on figure 4.9 enclosed by curve 2 there exists one real positive eigenvalue. Between curve 2, the horizontal axis and a curve just below curve 1 no marginal stability curves were found.

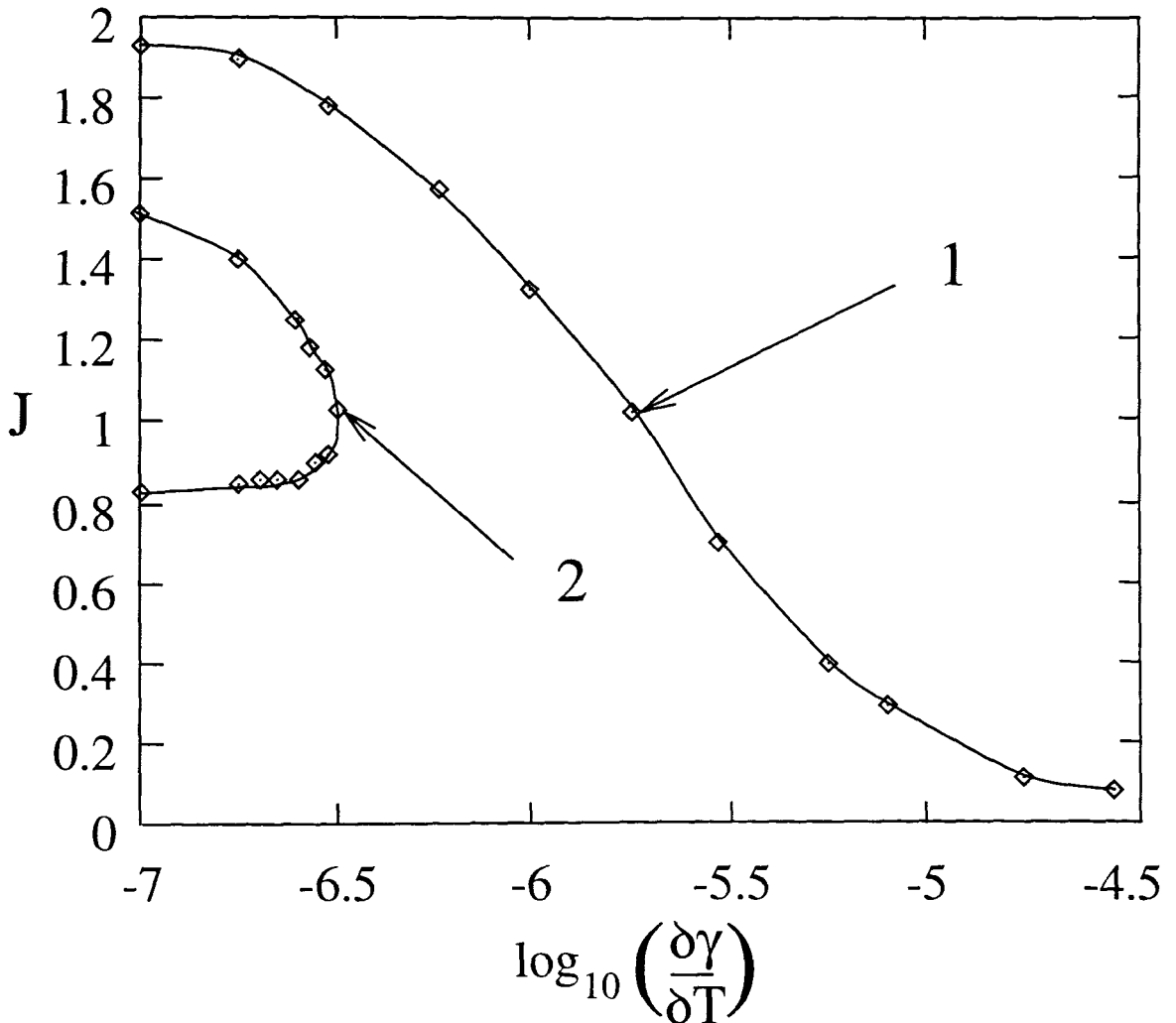


Figure 4.9: Stability and steady-state breakdown curves for poloidal system when $\partial\gamma/\partial T > 0$.

The instability of the basic flow to poloidal disturbances at current values approaching breakdown is not very surprising. When the applied current is small and $\partial\gamma/\partial T > 0$, the

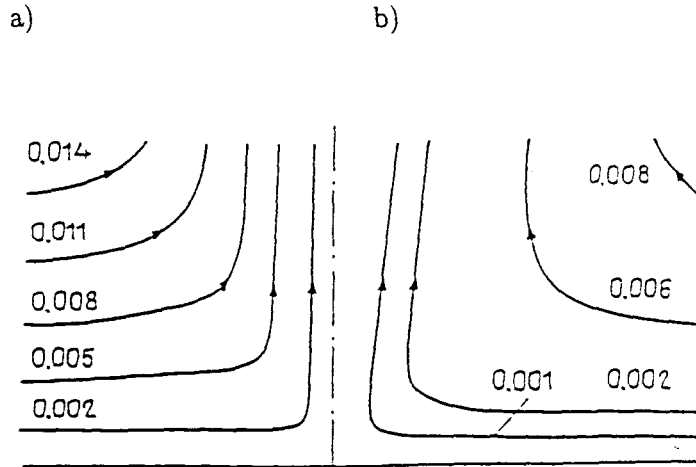


Figure 4.10: Streamlines of a Marangoni free flow a) without rotation for $J = 2.01A$, b) with rotation for $J = 2.10A$ (figure taken from [13]).

underlying flow in the finite hemispherical domain is an axial jet down the axis of symmetry. The jet can become unstable to azimuthal rotations. Once such rotations occur the associated centrifugal force which results will then in turn cause a change in the poloidal flow. This behaviour can be clearly seen in results obtained by Bojarevics [12], [13] for the semi-infinite isothermal model, see figure 4.10. The streamlines in figure 4.10a resemble the flow to a sink remote from the plane surface, yet the converging sink flow reaches a state of intense swirl, even from a small rotational disturbance. Figure 4.10b displays the streamlines at a similar current when this swirl is included. Clearly there is a significant difference in the magnitude and distribution of the poloidal streamlines because of the addition of an azimuthal component to the flow. In [12] Bojarevics *et al.* showed that a state of intense rotation may be achieved from a semi-infinite model similar to that considered in chapter 2 but without surface tension effects. He also showed experimentally the propensity of a converging flow to ‘spin up’. In his experiment a hemispherical copper container was filled with mercury, and supplied by an electric current from a small electrode situated at the centre of the free surface. For currents $\geq 15A$ the observed flow was clearly accompanied by rotation.

Figure 4.11 is a repeat of figure 4.9 but with an additional curve. This curve has been taken from figure 3.4 where it indicates the boundary between parameter values which result in steady-state flows in the hemisphere consisting of one loop and those consisting of two loops (as discussed in chapter 3). It is observed that the upper part of curve 2 in figure 4.11, which encloses an unstable region, lies at current values just prior to the development of a single loop flow structure in the steady-state model, and stability is restored as curve 3 is

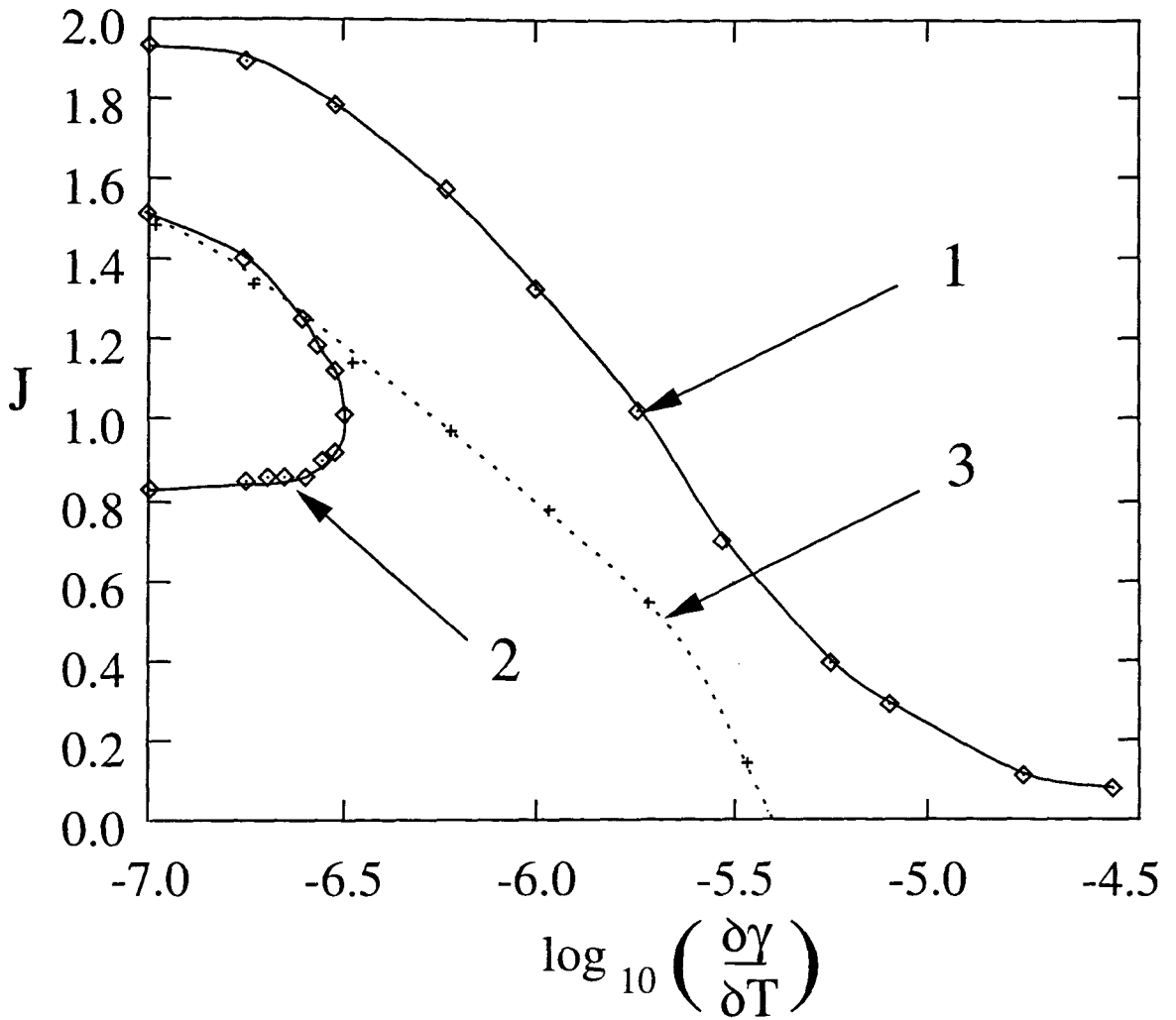


Figure 4.11: Stability, steady-state breakdown and flow-transition curves for poloidal system when $\partial \gamma / \partial T > 0$.

crossed by increasing the current at a fixed value of $\partial\gamma/\partial T$.

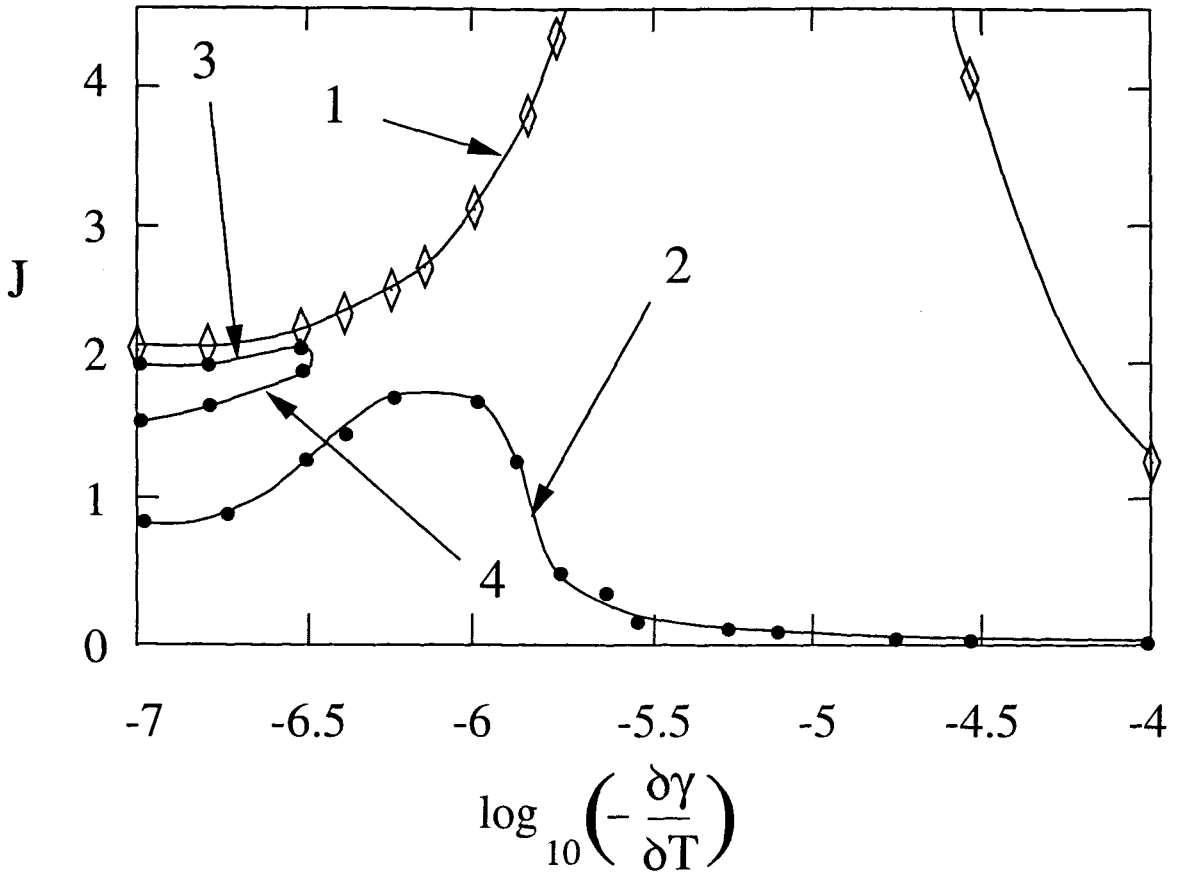


Figure 4.12: Stability and steady-state breakdown curves for the poloidal system when $\partial\gamma/\partial T < 0$.

Figure 4.12 shows the stability curves for the poloidal system when the surface tension gradient is now negative. The curve labelled 1, seen on the upper right- and left-hand sides of the figure, corresponds to the breakdown in convergence of the underlying solution for steady state flow in the hemisphere (considered in chapter 3). At current values above this curve no solution could be obtained for the steady-state model. On the other hand at current values below curve 2 the poloidal system is stable. As curve 2 is crossed, by increasing J at a fixed value of $\partial\gamma/\partial T$, the determinant of matrix \mathbf{A} was observed to change sign and therefore a negative, real eigenvalue passes through zero and becomes positive. This exchange of stability occurs at decreasing current values as $\log_{10}(-\partial\gamma/\partial T)$ increases, to values causing strong outward flow on the free surface (see figure 3.5). The outward jet on the free surface is consequently unstable even at very low applied currents. Curve 4 in figure 4.12 indicates a change in the sign of the determinant of \mathbf{A} . Because figures 4.9 and 4.12 must join smoothly when the value of the surface tension gradient tends toward zero, this curve must join with the upper branch of curve 2 on figure 4.9 and therefore it indicates a region of stability.

However, this region disappears as the magnitude of the negative surface tension gradient is increased because curve 3, which runs parallel to the left-hand part of the breakdown curve 1, corresponds to the development of a marginal stability curve just before the breakdown of the underlying steady-state model.

Figure 4.13 shows the secondary flow corresponding to the eigenvector arising from the positive eigenvalue which occurs where $\partial\gamma/\partial T = -3.0 \times 10^{-5} Nm^{-1}K^{-1}$ and $J = 0.03A$. Once again the values on these plots have been scaled by the numerical algorithm and give

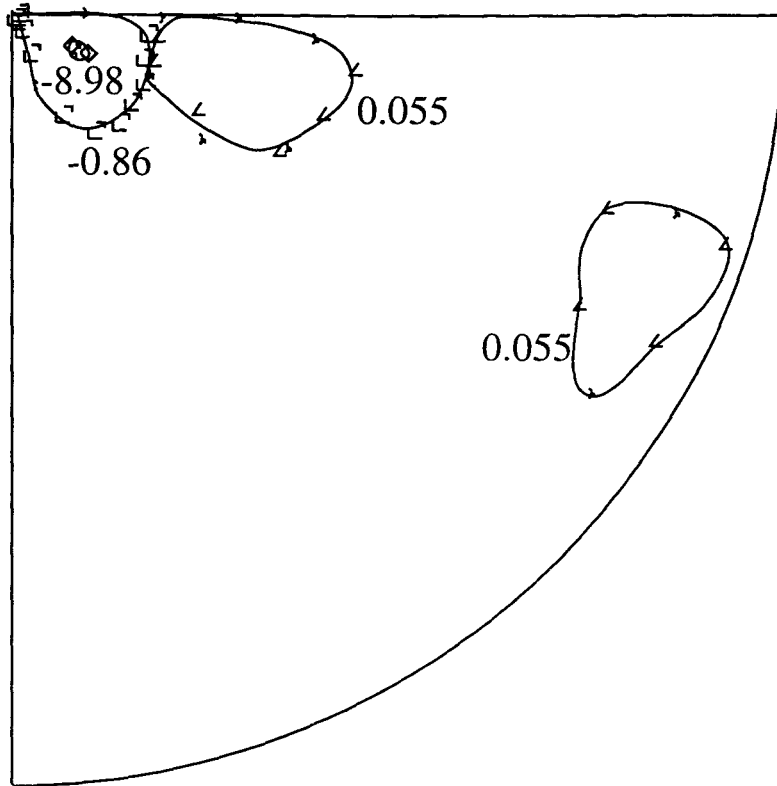


Figure 4.13: Contour plot of $\tilde{g}(\lambda, \eta)$ obtained from an evaluation of the poloidal eigenvector e_v when $\partial\gamma/\partial T = -3 \times 10^{-5} Nm^{-1}K^{-1}$ and $J = 0.03A$.

a relative order of magnitude for the non-dimensional perturbation stream-function $\tilde{g}(\lambda, \eta)$. Figure 4.13 again suggests that instability occurs due to a secondary flow developing near the point source. This is rather unexpected since there is a strong outward flow on the top surface in the underlying steady-state model at these assumed values of $(J, \partial\gamma/\partial T)$, and a diverging flow in a semi-infinite region is stable. Figure 4.13 is consistent, however, with the eigenvectors corresponding to the azimuthal perturbations shown in figures 4.7 and 4.8. Notice that there also exist small counter-rotating loops in figure 4.13 near the free surface and close to the outer hemispherical boundary. As in the previous eigenvector plots all the large perturbations in the non-dimensional stream-function are shown to lie in the upper part

of the hemisphere.

Figure 4.14 shows the secondary flow set up due to the positive eigenvalue which occurs when $\partial\gamma/\partial T = -1.0 \times 10^{-7} Nm^{-1}K^{-1}$ and $J = 0.93A$. At these values of J and $\partial\gamma/\partial T$

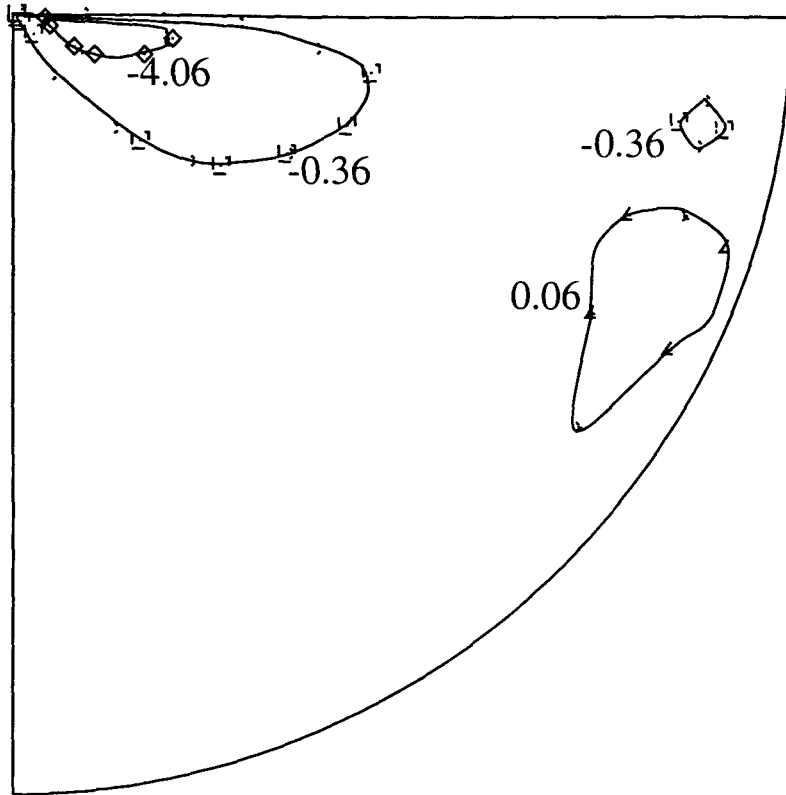


Figure 4.14: Contour plot of $\tilde{g}(\lambda, \eta)$ obtained from an evaluation of the poloidal eigenvector e_v when $\partial\gamma/\partial T = -1 \times 10^{-7} Nm^{-1}K^{-1}$ and $J = 0.93A$.

only a small Marangoni force occurs on the free surface and consequently the steady-state flow structure is qualitatively different from that corresponding to figure 4.13. Figure 4.14 reveals, however, that the secondary flow is once more strongest close to the point source and that there is again a slow counter rotating loop near the outer hemisphere. Note also that the region of negative flow perturbation in figure 4.14 extends a little further along the free surface than in figure 4.13. Both of the eigenvalue plots shown in figures 4.13 and 4.14 suggest that the instability of this model to perturbations of mode $m = 0$ occur near the point source, regardless of the magnitude of the free surface force.

Figure 4.15 shows on the same figure the simplified graphs of the azimuthal and poloidal stability curves for negative $\partial\gamma/\partial T$. Again the upper solid line, labelled 1, denotes the current above which the underlying steady-state model failed to converge. Line 3 was shown in figure 4.6, and discussed there, whilst line 2 was shown on figure 4.12 and discussed at that stage.

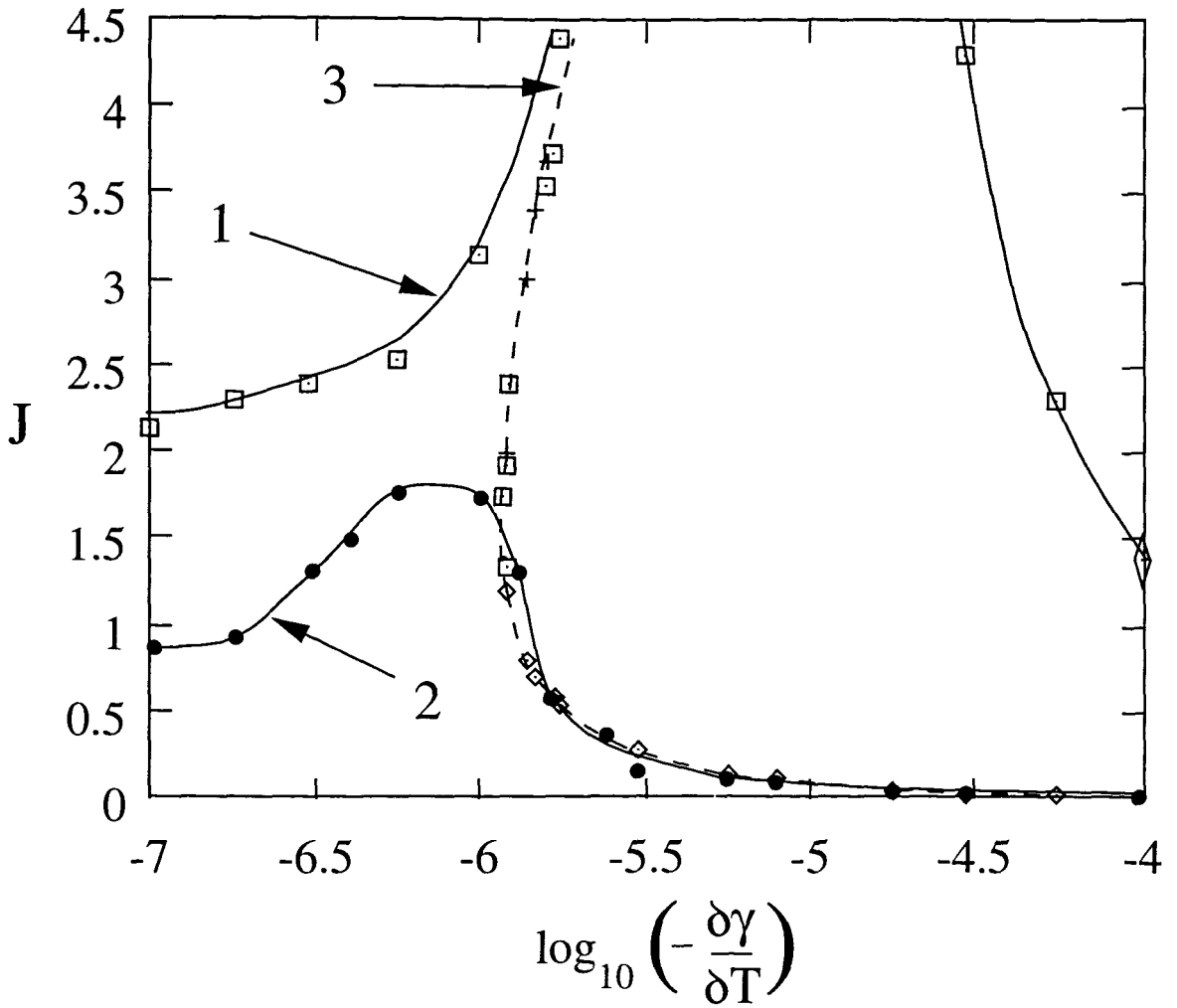


Figure 4.15: Stability and steady-state breakdown curves for azimuthal and poloidal systems when $\partial\gamma/\partial T < 0$.

Chapter 5

Higher modes of stability

5.1 Introduction

The azimuthal stability mode $m = 0$ was considered at length in the previous chapter. For the upper modes of stability, $m \geq 1$, the appropriate system of linear equations can be written in terms of velocity and vorticity perturbation functions. Belgrove [7] derived the system of equations for $m \geq 1$ and investigated the modes $m = 1$ and 2, *assuming the principle of exchange of stabilities*. The perturbation equations can be written in the form

$$\mathbf{A}\mathbf{x} = \sigma\mathbf{B}\mathbf{x},$$

where \mathbf{x} is a vector of the unknown perturbation variables at every point on the stability grid, \mathbf{A} is a matrix of coefficients in the stability equations and σ is the eigenvalue which we introduced in chapter 4. As we will show below all elements in the matrix \mathbf{B} have the same sign wherever we are positioned inside the hemisphere. Therefore, provided all the eigenvalues are real (i.e. assuming the principle of exchange of stabilities) the stability of the system can be monitored by evaluating the determinant of \mathbf{A} at different parameter values in the $(J, \partial\gamma/\partial T)$ -plane. In this case for $m \geq 1$ a change in sign of the determinant of \mathbf{A} occurs only when an eigenvalue of the linear system passes through zero, and becomes positive. This was the method used in chapter 4 where we considered the azimuthal stability mode $m = 0$.

On investigating again the discretisation described in [7], and obtaining approximate solutions, it was found that positive real eigenvalues existed at vanishingly small current values, in contradiction to the assumption made in [7]. Therefore, the problem of the higher modes of stability is reconsidered in this chapter and the revised solution for the stability of the upper modes is presented below.

5.2 Derivation of linear system of equations for the azimuthal modes $m \neq 0$

The derivation and finite difference formulation for the system of equations for the stability modes $m \geq 1$ is essentially the same as [7], but the time dependency has been included in much of the working within this chapter. A further alteration to [7] for the boundary condition on the outer hemisphere $\lambda = 1$ is also required, and in section 5.3.5 the Woods boundary condition is applied in an analogous way to that adopted previously in chapter 4.

As described in chapter 4 the total velocity \mathbf{v} and temperature T are expressed

$$\mathbf{v} = \mathbf{u} + \bar{\mathbf{v}} \quad (5.1)$$

and

$$T = T_0 + \bar{T}, \quad (5.2)$$

where the ‘stationary’ solutions for velocity and temperature are denoted by \mathbf{u} and T_0 and their perturbations are denoted by $\bar{\mathbf{v}}$ and \bar{T} respectively. Substituting (5.2) and (5.1) into the time-dependent form of the curl of the Navier-Stokes equation, and eliminating both the stationary solution and any term containing a quadratic in a small parameter, leads to

$$\frac{\partial \bar{\mathbf{w}}}{\partial t} = \nabla \times (\mathbf{u} \times \bar{\mathbf{w}}) + \nabla \times [\bar{\mathbf{v}} \times (\nabla \times \mathbf{u})] - \nu \nabla \times \nabla \times \bar{\mathbf{w}} + \frac{1}{\rho} \nabla \times \bar{\mathbf{F}}_{\mathbf{B}}. \quad (5.3)$$

In equation (5.3) $\bar{\mathbf{w}}$ represents the perturbation vorticity $\nabla \times \bar{\mathbf{v}}$ and $\bar{\mathbf{F}}_{\mathbf{B}}$ denotes the buoyancy force caused by the temperature perturbation.

The time dependence is again assumed to have the form $e^{\sigma t}$ where σ is written as $\sigma = \sigma^{(\tau)} + i\sigma^{(i)}$, with $\sigma^{(\tau)}$ and $\sigma^{(i)}$ denoting the real and complex parts of σ respectively. We write

$$T_0 = \frac{T_m}{\lambda} t(\eta, \lambda) \quad (5.4)$$

for the steady-state temperature distribution and, since the steady-state flow is incompressible and axi-symmetric, a stream-function ψ can be introduced and non-dimensionalised by

$$\psi = a\lambda\nu g(\eta, \lambda). \quad (5.5)$$

As in the previous chapter the steady state velocity in the hemisphere is related to \mathbf{g} through

$$\mathbf{u} = -\frac{\nu}{a\lambda} \left(-\frac{1}{2\eta} \mathbf{g}_\eta, \frac{\mathbf{g} + \lambda \mathbf{g}_\lambda}{\eta(2 - \eta^2)^{\frac{1}{2}}}, 0 \right). \quad (5.6)$$

The steady state solutions are complicated functions of both λ and η . However, as discussed previously the perturbations are chosen to depend on ϕ through the separable term $e^{im\phi}$,

where m denotes the mode of vibration. Therefore, for the m^{th} mode of vibration the perturbations

$$\bar{\mathbf{w}} = (\bar{w}_r, \bar{w}_\theta, \bar{w}_\phi) \quad \text{and} \quad \bar{\mathbf{v}} = (\bar{v}_r, \bar{v}_\theta, \bar{v}_\phi)$$

can be written as

$$\bar{w}_r = \tilde{w}_r(\eta, \lambda)e^{(im\phi + \sigma t)}, \quad \bar{w}_\theta = \tilde{w}_\theta(\eta, \lambda)e^{(im\phi + \sigma t)}, \quad \bar{w}_\phi = \tilde{w}_\phi(\eta, \lambda)e^{(im\phi + \sigma t)}, \quad (5.7)$$

$$\bar{v}_r = \tilde{v}_r(\eta, \lambda)e^{(im\phi + \sigma t)}, \quad \bar{v}_\theta = \tilde{v}_\theta(\eta, \lambda)e^{(im\phi + \sigma t)}, \quad \bar{v}_\phi = \tilde{v}_\phi(\eta, \lambda)e^{(im\phi + \sigma t)} \quad (5.8)$$

and

$$\bar{T} = T_m \tilde{T}(\eta, \lambda)e^{(im\phi + \sigma t)}. \quad (5.9)$$

The buoyancy term is defined in terms of θ as

$$\bar{\mathbf{F}}_B = \beta \rho g_e T_m (\cos \theta, -\sin \theta, 0) \tilde{T} e^{(im\phi + \sigma t)}. \quad (5.10)$$

Substituting (5.7)₁ to (5.10) into the vector equation (5.3), and cancelling the exponential term, leads to the following expressions for each component:

r-component

$$\begin{aligned} & \frac{im}{a\eta} \left[\frac{(2g_\lambda + \lambda g_{\lambda\lambda})}{(2-\eta^2)} + \frac{1}{4\lambda} \left(g_{\eta\eta} - \frac{g_\eta}{\eta} \right) \right] \tilde{v}_r + \frac{1}{2} \left[\frac{2m^2}{\eta(2-\eta^2)} - (g_\eta + \lambda g_{\lambda\eta}) \right] \tilde{w}_r \\ & + \left[\frac{\lambda(1-\eta^2)}{(2-\eta^2)^{\frac{1}{2}}} \right] \tilde{w}_{\theta,\lambda} - \frac{1}{4} [2(g + \lambda g_\lambda) + 2 - 3\eta^2] \tilde{w}_{r,\eta} - \left[\frac{\eta(2-\eta^2)}{4} \right] \tilde{w}_{r,\eta\eta} \\ & + \frac{(2-\eta^2)^{\frac{1}{2}}}{4} \left[\frac{4(1-\eta^2)}{(2-\eta^2)} - g_{\eta\eta} + \frac{\eta g_\eta}{(2-\eta^2)} \right] \tilde{w}_\theta + \left[\frac{(2-\eta^2)^{\frac{1}{2}}(2\eta - g_\eta)}{4} \right] \tilde{w}_{\theta,\eta} \\ & + \left[\frac{\lambda\eta(2-\eta^2)^{\frac{1}{2}}}{2} \right] \tilde{w}_{\theta,\lambda\eta} + \left[\frac{im}{(2-\eta^2)^{\frac{1}{2}}} \left(1 - \frac{g_\eta}{2\eta} \right) \right] \tilde{w}_\phi + \left[\frac{\lambda im}{(2-\eta^2)^{\frac{1}{2}}} \right] \tilde{w}_{\phi,\lambda} \\ & - \frac{ima\beta g_e T_m \lambda \eta \tilde{T}}{\nu} = \lambda^2 \sigma_1 \eta \tilde{w}_r, \end{aligned} \quad (5.11)$$

θ -component

$$\begin{aligned} & - \frac{ima\beta g_e T_m (1-\eta^2) \tilde{T}}{\nu(2-\eta^2)^{\frac{1}{2}}} + \frac{im}{a\lambda\eta} \left[\frac{(2g_\lambda + \lambda g_{\lambda\lambda})}{(2-\eta^2)^{\frac{1}{2}}} + \frac{1}{4\lambda} \left(g_{\eta\eta} - \frac{g_\eta}{\eta} \right) \right] \tilde{v}_\theta \\ & + \left[\frac{(2g_\lambda + \lambda g_{\lambda\lambda})}{(2-\eta^2)^{\frac{1}{2}}} \right] \tilde{w}_r + \left[\frac{g + \lambda g_\lambda}{(2-\eta^2)^{\frac{1}{2}}} \right] \tilde{w}_{r,\lambda} + \left[\frac{\eta(2-\eta^2)^{\frac{1}{2}}}{2} \right] \tilde{w}_{r,\lambda\eta} \\ & + \left[\frac{m^2}{\lambda\eta(2-\eta^2)} + \frac{g_\lambda\eta}{2} \right] \tilde{w}_\theta + \left[\frac{g_\eta}{2} - 2\eta \right] \tilde{w}_{\theta,\lambda} - \lambda\eta \tilde{w}_{\theta,\lambda\lambda} \\ & + \left[\frac{im(1-\eta^2 + g + \lambda g_\lambda)}{\lambda\eta(2-\eta^2)} \right] \tilde{w}_\phi + \frac{im}{2\lambda} \tilde{w}_{\phi,\eta} = \lambda \sigma_1 \eta \tilde{w}_\theta, \end{aligned} \quad (5.12)$$

ϕ -component

$$\begin{aligned}
& \frac{1}{2a\lambda} \left[\frac{2(1-\eta^2)}{\eta(2-\eta^2)} (2\mathfrak{g}_\lambda + \lambda\mathfrak{g}_{\lambda\lambda}) - 2\mathfrak{g}_{\lambda\eta} - \lambda\mathfrak{g}_{\lambda\lambda\eta} - \frac{(2-\eta^2)}{4\lambda} \mathfrak{g}_{\eta\eta\eta} + \frac{(4-\eta^2)}{4\lambda\eta} \left(\mathfrak{g}_{\eta\eta} - \frac{\mathfrak{g}_\eta}{\eta} \right) \right] \tilde{v}_\theta \\
& - \frac{1}{2a\lambda} \left[\frac{2-\eta^2}{4\lambda} \left(\mathfrak{g}_{\eta\eta} - \frac{\mathfrak{g}_\eta}{\eta} \right) + 2\mathfrak{g}_\lambda + \lambda\mathfrak{g}_{\lambda\lambda} \right] \tilde{v}_{\theta,\eta} + \frac{im}{(2-\eta^2)^{\frac{1}{2}}} \tilde{w}_{r,\lambda} + \frac{im}{2\lambda} \tilde{w}_{\theta,\eta} \\
& + \left[\frac{im(1-\eta^2)}{\lambda\eta(2-\eta^2)} \right] \tilde{w}_\theta + \left[\frac{1}{\lambda\eta(2-\eta^2)} - \frac{\mathfrak{g}_\eta}{2\lambda} + \frac{(1-\eta^2)}{\lambda\eta(2-\eta^2)} (\mathfrak{g} + \lambda\mathfrak{g}_\lambda) \right] \tilde{w}_\phi \\
& + \left[\frac{\mathfrak{g}_\eta}{2} - 2\eta \right] \tilde{w}_{\phi,\lambda} - \lambda\eta \tilde{w}_{\phi,\lambda\lambda} - \left[\frac{\mathfrak{g} + \lambda\mathfrak{g}_\lambda}{2\lambda} + \frac{(2-3\eta^2)}{4\lambda} \right] \tilde{w}_{\phi,\eta} \\
& + \frac{(2-\eta^2)^{\frac{1}{2}}}{a} \left[\frac{1}{4\lambda^2} \left(\mathfrak{g}_{\eta\eta} - \frac{\mathfrak{g}_\eta}{\eta} \right) - \frac{1}{4\lambda} \left(\mathfrak{g}_{\lambda\eta\eta} - \frac{\mathfrak{g}_{\lambda\eta}}{\eta} \right) - \frac{3\mathfrak{g}_{\lambda\lambda} + \lambda\mathfrak{g}_{\lambda\lambda\lambda}}{(2-\eta^2)} \right] \tilde{v}_r \\
& - \frac{(2-\eta^2)^{\frac{1}{2}}}{a} \left[\frac{2\mathfrak{g}_\lambda + \lambda\mathfrak{g}_{\lambda\lambda}}{(2-\eta^2)} + \frac{1}{4\lambda} \left(\mathfrak{g}_{\eta\eta} - \frac{\mathfrak{g}_\eta}{\eta} \right) \right] \tilde{v}_{r,\lambda} - \frac{\eta(2-\eta^2)}{4\lambda} \tilde{w}_{\phi,\eta\eta} \\
& + \left[\frac{a\beta g_e T_m (2-\eta^2)^{\frac{1}{2}} (1-\eta^2)\eta}{2\nu} \right] \tilde{T}_\eta + \left[\frac{a\beta \rho g_e T_m (2-\eta^2)^{\frac{1}{2}} \eta^2 \lambda}{\nu} \right] \tilde{T}_\lambda = \lambda\sigma_1 \eta \tilde{w}_\phi
\end{aligned} \tag{5.13}$$

where

$$\sigma_1 = \frac{a^2}{\nu} \sigma.$$

The vector identity $\nabla \cdot \mathbf{w} = 0$ implies that

$$\tilde{w}_\phi = \frac{i}{m} \left[\eta(2-\eta^2)^{\frac{1}{2}} (2\tilde{w}_r + \lambda\tilde{w}_{r,\lambda}) + (1-\eta^2)\tilde{w}_\theta + \frac{\eta(2-\eta^2)}{2} \tilde{w}_{\theta,\eta} \right], \tag{5.14}$$

and hence \tilde{w}_ϕ and its derivatives can be eliminated from (5.11) and (5.12), yielding

$$\begin{aligned}
& -\frac{m}{a\eta} \left[\frac{2\mathfrak{g}_\lambda + \lambda\mathfrak{g}_{\lambda\lambda}}{(2-\eta^2)} + \frac{1}{4\lambda} \left(\mathfrak{g}_{\eta\eta} - \frac{\mathfrak{g}_\eta}{\eta} \right) \right] \tilde{v}_r - \left[\frac{(\mathfrak{g}_\eta - \lambda\mathfrak{g}_{\lambda\eta})}{2} + \frac{m^2}{\eta(2-\eta^2)} - 2\eta \right] \tilde{w}_r \\
& + \left[-\frac{\mathfrak{g}_\eta}{2} + 4\eta \right] \lambda\tilde{w}_{r,\lambda} + \lambda^2\eta\tilde{w}_{r,\lambda\lambda} + \left[\frac{\mathfrak{g} + \lambda\mathfrak{g}_\lambda}{2} + \frac{(2-3\eta^2)}{4} \right] \tilde{w}_{r,\eta} \\
& + \left[\frac{\eta(2-\eta^2)}{4} \right] \tilde{w}_{r,\eta\eta} + \frac{(2-\eta^2)^{\frac{1}{2}}}{4} \left[-\frac{\mathfrak{g}_\eta}{\eta} + \mathfrak{g}_{\eta\eta} \right] \tilde{w}_\theta + \frac{ma\beta g_e T_m \lambda \eta}{\nu} \tilde{T} = \lambda^2 \sigma_1 \eta \tilde{w}_r
\end{aligned} \tag{5.15}$$

and

$$\begin{aligned}
& -\frac{m}{a\lambda\eta} \left[\frac{2\mathfrak{g}_\lambda + \lambda\mathfrak{g}_{\lambda\lambda}}{(2-\eta^2)} + \frac{1}{4\lambda} \left(\mathfrak{g}_{\eta\eta} - \frac{\mathfrak{g}_\eta}{\eta} \right) \right] \tilde{v}_\theta + \frac{1}{(2-\eta^2)^{\frac{1}{2}}} \left[\frac{2\mathfrak{g}}{\lambda} + \frac{4(1-\eta^2)}{\lambda} - \lambda\mathfrak{g}_{\lambda\lambda} \right] \tilde{w}_r \\
& + \left[\frac{2(1-\eta^2)}{(2-\eta^2)^{\frac{1}{2}}} \right] \tilde{w}_{r,\lambda} + \left[\frac{\eta(2-\eta^2)^{\frac{1}{2}}}{\lambda} \right] \tilde{w}_{r,\eta} + \left[-\frac{\mathfrak{g}_\eta}{\eta} + 2\eta \right] \tilde{w}_{\theta,\lambda} + \lambda\eta\tilde{w}_{\theta,\lambda\lambda} \\
& + \frac{1}{(2-\eta^2)} \left[\frac{(2\eta^4 - 4\eta^2 + 1)}{\lambda\eta} - \frac{m^2}{\lambda\eta} - \frac{(2-\eta^2)}{2} \mathfrak{g}_{\lambda\eta} + \frac{(1-\eta^2)}{\lambda\eta} (\mathfrak{g} + \lambda\mathfrak{g}_\lambda) \right] \tilde{w}_\theta \\
& + \frac{1}{4\lambda} [6 - 7\eta^2 + 2(\mathfrak{g} + \lambda\mathfrak{g}_\lambda)] \tilde{w}_{\theta,\eta} + \left[\frac{\eta(2-\eta^2)}{4\lambda} \right] \tilde{w}_{\theta,\eta\eta} \\
& + \left[\frac{ma\beta g_e T_m (1-\eta^2)}{\nu(2-\eta^2)^{\frac{1}{2}}} \right] \tilde{T} = \lambda\sigma_1 \eta \tilde{w}_\theta,
\end{aligned} \tag{5.16}$$

where $i\tilde{w}_r$ has been substituted for \tilde{w}_r and $i\tilde{w}_\theta$ has been substituted for \tilde{w}_θ .

The relationship between $\tilde{\mathbf{v}}$ and $\tilde{\mathbf{w}}$ is well known and for our coordinate system can be written

$$\begin{aligned} \tilde{\mathbf{w}} = \nabla \times \tilde{\mathbf{v}} = & \frac{1}{a} \left[\frac{(2-\eta^2)^{\frac{1}{2}}}{2\lambda} \tilde{v}_{\phi,\eta} + \frac{1-\eta^2}{\lambda\eta(2-\eta^2)^{\frac{1}{2}}} \tilde{v}_\phi - \frac{im}{\lambda\eta(2-\eta^2)^{\frac{1}{2}}} \tilde{v}_\theta \right] \hat{\mathbf{r}} \\ & + \frac{1}{a} \left[\frac{im}{\lambda\eta(2-\eta^2)^{\frac{1}{2}}} \tilde{v}_r - \frac{\tilde{v}_\phi}{\lambda} - \tilde{v}_{\phi,\lambda} \right] \hat{\boldsymbol{\theta}} + \frac{1}{a} \left[\frac{\tilde{v}_\theta}{\lambda} + \tilde{v}_{\theta,\lambda} - \frac{(2-\eta^2)^{\frac{1}{2}}}{2\lambda} \tilde{v}_{r,\eta} \right] \hat{\boldsymbol{\phi}}. \end{aligned} \quad (5.17)$$

The incompressibility condition is $\nabla \cdot \tilde{\mathbf{v}} = 0$, from which an expression for \tilde{v}_ϕ is obtained in a similar way to (5.14). Then all terms involving \tilde{v}_ϕ and its derivatives can be removed from equation (5.17), leaving the following expressions for the \mathbf{r} and $\boldsymbol{\theta}$ components of the vector:

\mathbf{r} -component

$$\begin{aligned} \tilde{w}_r ma = & \frac{4(1-\eta^2)}{\lambda} \tilde{v}_r + 2(1-\eta^2) \tilde{v}_{r,\lambda} + \frac{\eta(2-\eta^2)}{\lambda} \tilde{v}_{r,\eta} \\ & + \left[\frac{(1-4\eta^2+2\eta^4-m^2)}{\lambda\eta(2-\eta^2)^{\frac{1}{2}}} \right] \tilde{v}_\theta + \left[\frac{(2-\eta^2)^{\frac{1}{2}}(6-7\eta^2)}{4\lambda} \right] \tilde{v}_{\theta,\eta} \\ & + \frac{\eta(2-\eta^2)}{2} \tilde{v}_{r,\lambda\eta} + \frac{\eta(2-\eta^2)^{\frac{3}{2}}}{4\lambda} \tilde{v}_{r,\eta\eta}, \end{aligned} \quad (5.18)$$

$\boldsymbol{\theta}$ -component

$$\begin{aligned} -\tilde{w}_\theta ma = & \frac{(2-\eta^2)^{\frac{1}{2}}}{\lambda} \left[-\frac{m^2}{\eta(2-\eta^2)} + 2\eta \right] \tilde{v}_r + 4\eta(2-\eta^2)^{\frac{1}{2}} \tilde{v}_{r,\lambda} + \lambda\eta(2-\eta^2)^{\frac{1}{2}} \tilde{v}_{r,\lambda\lambda} \\ & + \frac{(1-\eta^2)}{\lambda} \tilde{v}_\theta + (1-\eta^2) \tilde{v}_{\theta,\lambda} + \frac{\eta(2-\eta^2)}{2\lambda} \tilde{v}_{\theta,\eta} + \frac{\eta(2-\eta^2)}{2} \tilde{v}_{\theta,\lambda\eta}. \end{aligned} \quad (5.19)$$

Finally, substituting (5.1) and (5.2) into the unsteady form of the temperature equation (3.3), removing the steady-state solution and ignoring any terms containing a quadratic in a small parameter, leaves

$$\frac{\partial \tilde{T}}{\partial t} + \tilde{\mathbf{v}} \cdot \nabla \frac{T_0}{T_m} + \mathbf{u} \cdot \nabla \tilde{T} = \kappa \nabla^2 \tilde{T}. \quad (5.20)$$

The steady-state and perturbation temperature distributions, T_0 and \tilde{T} respectively, and the steady-state velocity solution \mathbf{u} are given by the general expressions (5.4), (5.9) and (5.6) respectively. These three expressions can be substituted into equation (5.20), together with definitions (5.8) and (5.9), to give

$$\begin{aligned} 2 \left(t_\lambda - \frac{t}{\lambda} \right) \tilde{v}_r + \frac{(2-\eta^2)^{\frac{1}{2}}}{\lambda} t_\eta \tilde{v}_\theta + \frac{\nu g_\eta}{\eta} \tilde{T}_\lambda - \frac{\nu(g+\lambda g_\lambda)}{\lambda\eta} \tilde{T}_\eta \\ - \kappa \left(2\lambda \tilde{T}_{\lambda\lambda} + 4\tilde{T}_\lambda + \frac{(2-3\eta^2)}{2\lambda\eta} \tilde{T}_\eta + \frac{(2-\eta^2)}{2\lambda} \tilde{T}_{\eta\eta} - \frac{2m^2}{\lambda\eta^2(2-\eta^2)} \tilde{T} \right) = 2\nu\lambda\sigma_1 \tilde{T}. \end{aligned} \quad (5.21)$$



5.3 Boundary conditions

The system of differential equations obtained in section 5.2 must be solved subject to boundary conditions on \tilde{v}_r , \tilde{v}_θ , \tilde{v}_ϕ , \tilde{w}_r , \tilde{w}_θ and \tilde{T} on $\lambda = 0$, $\lambda = 1$, $\eta = 0$ and $\eta = 1$. The appropriate conditions are stated below.

5.3.1 Point source ($\lambda = 0$)

No perturbations from the prescribed flow are allowed at the origin, therefore

$$\tilde{v}_r(\eta, 0) = \tilde{v}_\theta(\eta, 0) = \tilde{v}_\phi(\eta, 0) = 0. \quad (5.22)$$

Evaluating equation (5.16) on $\lambda = 0$ and using L'Hôpital's rule wherever appropriate requires that

$$\tilde{v}_{\theta,\lambda}(\eta, 0) = \tilde{w}_\theta(\eta, 0) = \tilde{w}_r(\eta, 0) = 0. \quad (5.23)$$

With the use of (5.23), equation (5.14) gives

$$\tilde{w}_\phi(\eta, 0) = 0. \quad (5.24)$$

No perturbation of the temperature is allowed at the origin, hence

$$\tilde{T}(\eta, 0) = 0. \quad (5.25)$$

5.3.2 Outer hemisphere ($\lambda = 1$)

The no-slip boundary condition on the solid-liquid boundary requires that the velocity components and their associated perturbations are zero on the hemispherical boundary, and hence

$$\tilde{v}_r(\eta, 1) = \tilde{v}_\theta(\eta, 1) = \tilde{v}_\phi(\eta, 1) = 0. \quad (5.26)$$

Evaluating equation (5.17) on $\lambda = 1$ then requires that

$$\tilde{w}_r(\eta, 1) = 0. \quad (5.27)$$

One method of completing the boundary conditions on $\lambda = 1$ is to evaluate equation (5.16) on the outer hemisphere. Employing this equation in the finite difference scheme, however, led to the appearance of positive eigenvalues for all current values, as discussed in the analogous situation in chapter 4. To avoid this difficulty the Woods boundary condition is again adopted on $\lambda = 1$, and this will be discussed further in section 5.3.5.

The outer boundary is at the melting temperature T_m , therefore

$$\tilde{T}(\eta, 1) = 0. \quad (5.28)$$

5.3.3 Axis of symmetry ($\eta = 0$)

No motion is allowed across the axis of symmetry, so we also assume there is no velocity perturbation across it. This assumption is equivalent to

$$\tilde{v}_\theta(0, \lambda) = 0. \quad (5.29)$$

Evaluating (5.17) on $\eta = 0$, and using L'Hôpital's rule where appropriate, requires that

$$\tilde{v}_\phi(0, \lambda) = \tilde{v}_r(0, \lambda) = 0. \quad (5.30)$$

Consequently, satisfying equation (5.15) on $\eta = 0$ requires that

$$\tilde{w}_\theta(0, \lambda) = 0 \quad \text{and} \quad \tilde{w}_r(0, \lambda) = 0, \quad (5.31)$$

and evaluating the temperature equation (5.21) on $\eta = 0$ then gives

$$\tilde{T}(0, \lambda) = 0. \quad (5.32)$$

5.3.4 Free surface ($\eta = 1$)

It is assumed that there is no velocity perturbation perpendicular to the free surface, so

$$\tilde{v}_\theta(1, \lambda) = 0. \quad (5.33)$$

The perturbation to the shear stress components on the free surface satisfy

$$\tilde{\sigma}_{r\theta} = \frac{\rho\nu}{2a\lambda} \tilde{v}_{r,\eta} = \frac{1}{a} \frac{\partial\gamma}{\partial T} \tilde{T}_\lambda \quad \text{and} \quad \tilde{\sigma}_{\phi\theta} = \frac{\rho\nu}{2a\lambda} \tilde{v}_{\phi,\eta} = \rho\nu \tilde{w}_r = 0, \quad (5.34)$$

which imply that

$$\tilde{w}_r(1, \lambda) = 0 \quad \text{and} \quad \frac{\partial\tilde{v}_r}{\partial\eta} = \frac{2\lambda}{\rho\nu} \frac{\partial\gamma}{\partial T} \tilde{T}_\lambda \quad \text{on} \quad \eta = 1. \quad (5.35)$$

Finally, equations (5.16) and (5.21) are used on the free surface $\eta = 1$ to complete the set of boundary conditions.

5.3.5 Woods boundary condition on $\lambda = 1$

Investigation reveals that evaluating equation (5.16) on the hemispherical boundary $\lambda = 1$ and using the resulting condition in the governing system produces some positive non-dimensional eigenvalues σ_1 for all current values. These eigenvalues were not detected by Belgrove [7]. As mentioned earlier the difficulty is removed when use is made of the Woods boundary condition [137] on the outer hemisphere. In the previous chapter this condition was shown to give

$$\tilde{f}(\eta, 1) = \frac{3}{\eta^2(2 - \eta^2)(1 + 2\Delta\lambda)(\Delta\lambda)^2} \tilde{g}(\eta, 1 - \Delta\lambda) - \frac{1}{2(1 + 2\Delta\lambda)} \tilde{f}(\eta, 1 - \Delta\lambda), \quad (5.36)$$

when higher order terms are neglected. In the system of linear equations for $m \geq 1$ being considered in this chapter, however, different perturbation functions, namely the velocity and vorticity functions, are used and hence $\tilde{f}(\eta, \lambda)$ and $\tilde{g}(\eta, \lambda)$ must be expressed in terms of \tilde{v}_r and \tilde{w}_ϕ . The ϕ -component of the vorticity \tilde{w}_ϕ can be expressed

$$\tilde{w}_\phi = -\frac{\eta(2-\eta^2)^{\frac{1}{2}}\nu}{(a\lambda)^2} \tilde{f}(\eta, \lambda), \quad (5.37)$$

and substituting (5.37) into equation (5.36) gives

$$\begin{aligned} -\eta(2-\eta^2)^{\frac{1}{2}}a^2\tilde{w}_\phi(\eta, 1) &= \frac{3\nu}{(\Delta\lambda)^2(1+2\Delta\lambda)}\tilde{g}(\eta, 1-\Delta\lambda) \\ &+ \frac{\eta(2-\eta^2)^{\frac{1}{2}}a^2(1-\Delta\lambda)^2}{2(1+2\Delta\lambda)}\tilde{w}_\phi(\eta, 1-\Delta\lambda). \end{aligned} \quad (5.38)$$

The function $g(\eta, \lambda)$ can be written in terms of \tilde{v}_r via the relation

$$\tilde{v}_r = \left(\frac{\nu}{2a\lambda\eta}\right)\tilde{g}_\eta, \quad (5.39)$$

which can then be used in the equation formed by differentiating (5.38) with respect to η to give

$$\begin{aligned} -\frac{(2-\eta^2)^{\frac{1}{2}}a}{2(1-\Delta\lambda)}\tilde{w}_{\phi,\eta}(\eta, 1) + \frac{a(\eta^2-1)}{(2-\eta^2)^{\frac{1}{2}}\eta(1-\Delta\lambda)}\tilde{w}_\phi(\eta, 1) &= \\ \frac{3}{(\Delta\lambda)^2(1+2\Delta\lambda)}\tilde{v}_r(\eta, 1-\Delta\lambda) + \frac{(2-\eta^2)^{\frac{1}{2}}a(1-\Delta\lambda)}{4(1+2\Delta\lambda)}\tilde{w}_{\phi,\eta}(\eta, 1-\Delta\lambda) \\ + \frac{(1-\eta^2)a(1-\Delta\lambda)}{\eta(2-\eta^2)^{\frac{1}{2}}2(1+2\Delta\lambda)}\tilde{w}_\phi(\eta, 1-\Delta\lambda). \end{aligned} \quad (5.40)$$

Using equation (5.14), \tilde{w}_ϕ and $\tilde{w}_{\phi,\eta}$ can be eliminated from (5.40) since, after substituting $i\tilde{w}_r$ for \tilde{v}_r and $i\tilde{w}_\theta$ for \tilde{w}_θ

$$-m\tilde{w}_\phi = \eta(2-\eta^2)^{\frac{1}{2}}(2\tilde{w}_r + \lambda\tilde{w}_{r,\lambda}) + (1-\eta^2)\tilde{w}_\theta + \frac{\eta(2-\eta^2)}{2}\tilde{w}_{\theta,\eta}$$

and

$$\begin{aligned} -m\tilde{w}_{\phi,\eta} &= \left((2-\eta^2)^{\frac{1}{2}} - \eta^2(2-\eta^2)^{-\frac{1}{2}}\right)(2\tilde{w}_r + \lambda\tilde{w}_{r,\lambda}) + 2\eta(2-\eta^2)^{\frac{1}{2}}(\tilde{w}_{r,\eta} \\ &+ \lambda\tilde{w}_{r,\lambda\eta}) - 2\eta\tilde{w}_\theta + \left(2 - \frac{5}{2}\eta^2\right)\tilde{w}_{\theta,\eta} + \frac{\eta}{2}(2-\eta^2)\tilde{w}_{\theta,\eta\eta}. \end{aligned}$$

Therefore, the condition

$$\begin{aligned} 2a(1-\eta^2)\tilde{w}_{r,\lambda}(\eta, 1) + \frac{a\eta}{2}(2-\eta^2)\tilde{w}_{r,\lambda\eta}(\eta, 1) + \frac{a(2\eta^4 - 4\eta^2 + 1)}{\eta(2-\eta^2)^{\frac{1}{2}}}\tilde{w}_\theta(\eta, 1) \\ + \frac{a}{4}(2-\eta^2)^{\frac{1}{2}}(6-7\eta^2)\tilde{w}_{\theta,\eta}(\eta, 1) + \frac{a}{4}\eta(2-\eta^2)^{\frac{3}{2}}\tilde{w}_{\theta,\eta\eta}(\eta, 1) \end{aligned}$$

$$\begin{aligned}
& -\frac{3m(1-\Delta\lambda)}{(\Delta\lambda)^2(1+2\Delta\lambda)}\tilde{v}_r(\eta, 1-\Delta\lambda) + \frac{2a(1-\Delta\lambda)^2(1-\eta^2)}{(1+2\Delta\lambda)}\tilde{w}_r(\eta, 1-\Delta\lambda) \\
& + \frac{a(1-\eta^2)(1-\Delta\lambda)^3}{1+2\Delta\lambda}\tilde{w}_{r,\lambda}(\eta, 1-\Delta\lambda) + \frac{a(1-\Delta\lambda)^2\eta(2-\eta^2)}{2(1+2\Delta\lambda)}\tilde{w}_{r,\eta}(\eta, 1-\Delta\lambda) \\
& + \frac{a\eta(1-\Delta\lambda)^3(2-\eta^2)}{4(1+2\Delta\lambda)}\tilde{w}_{r,\lambda\eta}(\eta, 1-\Delta\lambda) \\
& - \frac{a(1-\Delta\lambda)^2(-3\eta^4+6\eta^2-2)}{4(1+2\Delta\lambda)\eta(2-\eta^2)^{\frac{1}{2}}}\tilde{w}_\theta(\eta, 1-\Delta\lambda) \\
& + \frac{a(1-\Delta\lambda)^2(2-\eta^2)^{\frac{1}{2}}(6-7\eta^2)}{8(1+2\Delta\lambda)}\tilde{w}_{\theta,\eta}(\eta, 1-\Delta\lambda) \\
& + \frac{a(1-\Delta\lambda)^2\eta(2-\eta^2)^{\frac{3}{2}}}{8(1+2\Delta\lambda)}\tilde{w}_{\theta,\eta\eta}(\eta, 1-\Delta\lambda) = 0 \quad (5.41)
\end{aligned}$$

is the Woods boundary condition on the hemispherical boundary $\lambda = 1$ for the Stokes streamfunction ψ , expressed in terms of the velocity and vorticity perturbation functions.

5.3.6 Finite difference scheme

The system of equations (5.15), (5.16), (5.18), (5.19), (5.21) (and their corresponding boundary conditions) were next written in finite difference form on a uniform grid using the method discussed in chapter 4. That is to say the first derivatives were approximated using Leonard's [68] method and the second derivatives using central differences. The resulting system was then solved over a 11×11 grid (see figure 4.3, where the stability grid is shown by solid lines). Note that in this chapter the dependant variables are known on the boundaries $\eta = 0$ and $\lambda = 0$ and therefore these lines do not appear in the stability grid. Clearly the grid points used to solve the linear stability problem in the hemisphere with $m \geq 1$ coincide with points on the equally spaced 61×61 grid on which the underlying steady-state flow variables f , g and t have been calculated (see the grid of dotted lines in figure 4.3). As before any derivatives of the variables f , g or t were approximated by central differences using neighbouring points on the 61×61 mesh.

5.3.7 Method of solution

The solution method for the linear stability system for integers $m \geq 1$ is now summarised. The governing stability equations (5.15), (5.16), (5.18), (5.19) and (5.21) (and their corresponding boundary conditions), written in finite difference form, were expressed in terms of a matrix \mathbf{A} of coefficients and a vector \mathbf{x} of perturbation functions over the entire grid where the variable values are unknown, to give

$$\mathbf{Ax} = \mathbf{0}, \quad (5.42)$$

when σ_1 is set equal to zero. The vector \mathbf{x} consists of the unknown perturbation functions \tilde{v}_r , \tilde{v}_θ , \tilde{w}_r , \tilde{w}_θ and \tilde{T} at each grid point on the solid grid shown in figure 4.3. With σ_1 identically zero, equations (5.15), (5.16), (5.18), (5.19) and (5.21) were solved at each grid point (except for (5.16) on $\lambda = 1$) and the coefficients in front of each of the unknowns were evaluated from the values of f , g and t (and their derivatives) at that grid point calculated from the steady-state solution discussed in chapter 3. These coefficients produce the elements of matrix \mathbf{A} . The solution method for the system described by (5.42) is presented in the previous chapter.

5.4 Results and discussion

The stability system was solved at many closely spaced positions throughout the $(J, \partial\gamma/\partial T)$ parameter space in which the steady-state model converged. At each position the determinant of the matrix \mathbf{A} was calculated and stored. As the current was increased in small steps, for a fixed value of $\partial\gamma/\partial T$ between $\pm 3.5 \times 10^{-4} \text{Nm}^{-1}\text{K}^{-1}$, the calculated value for the determinant of \mathbf{A} varied smoothly, indicating that the eigenvalues associated with the system also vary smoothly. The size of the pool in the underlying steady-state model was chosen to be $2mm$.

The results obtained in this chapter cannot be compared with [7] since the condition Belgrove applied on the boundary $\lambda = 1$ has been changed, for the reasons discussed earlier, and therefore our results are different to those obtained by Belgrove.

Positive surface tension gradient, $\partial\gamma/\partial T > 0$

For $m = 1, 2$ and 3 , in turn, no change in the sign of $\det\mathbf{A}$ was observed, indicating that no marginal stability curves exist for any value of the current J over the entire range for which the underlying steady-state model converged. Consequently, assuming that instability initially occurs in the lower modes ($m = 1, 2$ and 3) of vibration, no instability is predicted in any of the upper modes of vibration ($m \geq 1$) when the surface tension gradient is positive.

Negative surface tension gradient, $\partial\gamma/\partial T < 0$

The stability characteristics of the system of equations when $m = 1$ and the surface tension gradient $\partial\gamma/\partial T$ is negative are shown in figure 5.1. The upper solid line (labelled 1) represents the current at which the underlying steady-state model failed to converge (therefore at current values above curve 1 no solution to the steady-state model could be obtained). When the current was increased and crossed the lower line of the closed region 2, the determinant of matrix \mathbf{A} changed sign, indicating a region of instability. As the current was increased further the determinant of \mathbf{A} changed sign once again as the upper line of region 2 was crossed. By increasing the current from zero along lines of constant $\partial\gamma/\partial T$ which do not intersect region 2, no changes in the sign of the determinant of \mathbf{A} were observed. This behaviour suggests that for the mode $m = 1$ azimuthal perturbations are stable where the steady-state model breaks down. For the modes $m = 2$ and 3 no marginal stability curves were found for any values of J in the parameter range over which the steady-state model converged. It is possible that the instability to mode $m = 1$ perturbations just prior to breakdown is related to the transition between a double-loop and a single-loop flow structure in the underlying steady state model which is known to occur at about these parameter values.

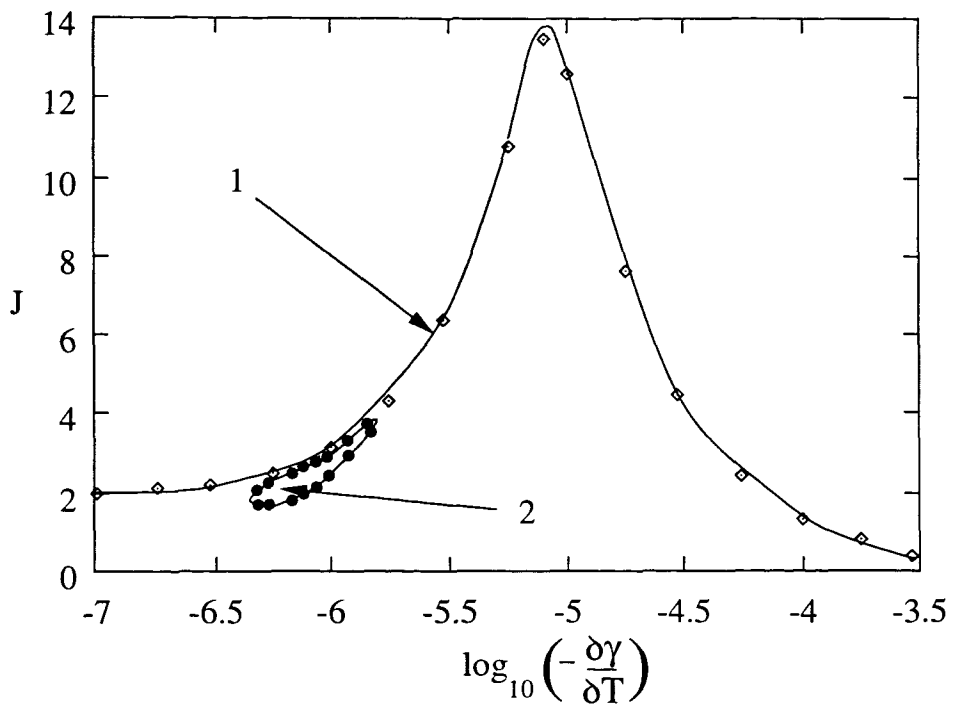


Figure 5.1: Stability and steady-state breakdown curves when $\partial\gamma/\partial T < 0$ and $m = 1$.

Chapter 6

Introduction to chapters 6 to 10 : Solidification models

One process which was not modelled in the welding problem considered in the first five chapters of this thesis was the unsteady growth of the pool of liquid metal. To model this effect the unsteady Navier-Stokes equations can be used together with an expression for the heat balance on the outer surface of the pool. Unlike the preceding chapters, however, the shape of the growing weld pool may not be spherical, especially when there is a strong Marangoni force on the free surface. Following a paper by Szekely and Stanek [121], Kroeger and Ostrach [62] modelled the continuous casting process of a pure metal or alloy solidifying along a plane freezing front. Convection in the liquid metal was caused by the introduction of feed metal with superheat, supplied to the liquid region through the top surface and this region was cooled from the side. The outer surface of the liquid pool was determined by the classical sharp interface latent heat (or Stefan) condition for the conservation of energy across the interface. Oreper and Szekely [79] considered a similar type of problem. They solved the coupled problem of an unsteady Navier-Stokes equation and a heat transfer equation. These authors introduced a mushy layer whenever the temperature was between typical solidus and liquidus temperatures for steel, and they insisted that the streamfunction was identically zero in these regions.

In chapters 6 to 10 of this thesis we consider a related problem which involves a non-isothermal phase change process with convection in the liquid phase. We model this process using the sharp and diffuse interface methods and compare the solutions as the thickness of the interface in the diffuse interface model is reduced to zero. In chapter 7 we develop a Stefan model [119] for the solidification of a growing solid sphere in an infinite bath of super-cooled liquid. This model assumes that the solid/liquid phase transition is sharp. The results of this model are formulated in a similar way to Schaefer and Glicksman [95], however in the

model derived in chapter 7 we allow for a disparity between the solid and liquid densities and therefore flow ensues in the liquid phase, an effect which is absent from [95]. This model is then compared to a recent phase-field model developed by Anderson, McFadden and Wheeler [2], outlined at the end of this introductory chapter. In chapter 8 we show that, under certain simplifications, a leading order asymptotic expansion of the model in [2] describes the sharp interface model in chapter 7. Finally, in chapter 9 we make a comparison in one-dimension between the numerical results of these two models as the thickness of the diffuse interface tends to zero.

Early in the nineteenth century Young, Laplace and Gauss considered the nature of the interface between two fluids. Generally they represented this interface as a sharp discontinuity in the phase of a material and other physical quantities such as density. Boundary conditions introduced at this ‘interface of zero thickness’ accounted for its physical properties. An important boundary condition at this interface involves surface tension, which accounts for capillarity effects (a term which derives its name from the rise in the level of fluid inside a tube above the surrounding fluid when the diameter of this tube is comparable to a hairs width (Latin:capillus)). By considering this phenomenon, Laplace obtained the equation

$$p^l - p^g = 2\sigma/R, \quad (6.1)$$

describing the difference between the pressure inside a spherical drop of liquid p^l and the pressure of the (in this case) gas outside, p^g , in terms of the curvature κ (given by $\kappa = 2/R$ where R denotes the radius of the spherical drop of liquid) and the surface tension σ . Equation (6.1) was later derived by Gibbs in [46] using thermodynamic arguments, and an outline of both derivations can be found in [93]. Young [139], discussed in [93], went slightly further than Laplace. He considered the forces parallel to a solid surface and obtained an expression for the resulting angle of contact between a solid and liquid as

$$\sigma^{sg} = \sigma^{ls} + \sigma^{lg} \cos \theta,$$

where the surface tension (or energy) of the solid-gas, liquid-solid and liquid-gas interfaces are given by σ^{sg} , σ^{ls} and σ^{lg} respectively, and the contact angle between the liquid and solid phases is given by θ .

A boundary-value problem ([32]) occurs when the solution to a differential equation must satisfy certain conditions on the boundary of its domain (in this case the interface between two immiscible fluids). If in addition the position of the boundary must also be determined this is known as a ‘free boundary problem’ when the boundary is stationary and a steady-state solution exists; or a ‘moving boundary problem’ when the boundary is time dependent ([32], [63], [6]). In these problems the position of the interfacial boundary is required in addition to the solution of the differential equation at the interface. Suitable initial and fixed boundary

conditions are needed to obtain these two requirements. Moving boundary problems, such as these, are usually referred to as Stefan problems after J. Stefan, who modelled the melting of the polar ice cap in the late nineteenth century [119]. Essentially the condition derived by Stefan at the boundary between, in this case, the solid and liquid phases of water, can be easily obtained as

$$-K_1 \frac{\partial T_1}{\partial x} + K_2 \frac{\partial T_2}{\partial x} = L\rho \frac{dR}{dt} \quad (6.2)$$

by referring to figure 6.1. In equation (6.2) L denotes the latent heat, ρ the density, $R(t)$ the

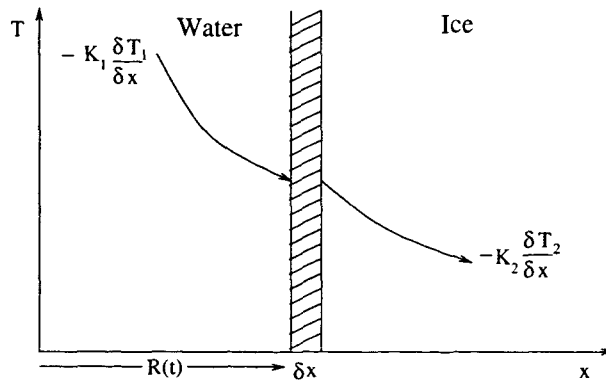


Figure 6.1: Latent heat boundary condition at a solid/liquid interface. A similar figure appears in [32].

position of the interface as a function of time, $T_i(x)$ the temperature of water (when $i = 1$) and ice (when $i = 2$) as a function of position x and K_i the heat conductivity of water (when $i = 1$) and ice (when $i = 2$). When there are no heat sources at the interface an amount of heat $L\rho\delta x$ is required to melt the shaded region in figure 6.1. In the absence of other sources this heat must be supplied by the difference between the heat entering the shaded element from the water phase, $-K_1\delta t\partial T_1/\partial x$, and the heat escaping into the ice, $-K_2\delta t\partial T_2/\partial x$.

Few exact solutions to these free-boundary problems can be obtained, those that can are variations of the solution of Neumann, who, in his classical problem, considered a semi-infinite medium of initially constant temperature in contact with a different constant temperature at its face. These exact solutions are functions of $x/t^{\frac{1}{2}}$ and are known as similarity solutions. Many such solutions can be found in text books on this subject, two good examples are by Carslaw and Jaeger [23] and John Crank [32].

The simple one-dimensional, two-phase Stefan problem can be described as the heat flow in the solid and liquid phases of a two-phase system which initially has its solid phase below the melting temperature. It is then required that the solution to the system supplies the variables $T_1(x, t)$ and $T_2(x, t)$ throughout the solution space, and $x = R(t)$, the position of the interface. In its simplest form a plane interfacial surface is considered with its temperature

fixed at the melting temperature, and the conductivities and densities of the solid and liquid phases equal, thereby assuming negligible volume change on solidification. There have been many generalisations to this problem including non-linear heat parameters and ‘mushy region’ development, density change and convection in the liquid phase, ablation (continuous or immediate removal of the surface of a melting solid or evaporating liquid), inverse problems (where $R(t)$ is known but $T(x = R(t))$ is unknown), multiphase problems, diffusion and heat flow in alloys, solution in two or three spatial dimensions and various implicit boundary conditions to name but a few. Extensive discussions on all these problems can be found in [32], and [94] presents a systematic development of the Stefan problem. Numerical methods in solving various types of ‘moving boundary’ problems (including an alternative enthalpy approach, an example of which can be found in [52]) are discussed in [80].

In the remainder of this thesis we restrict ourselves to the situation where a sphere of super-cooled pure material is growing into its super-cooled melt. The term ‘super-cooled’ refers to the temperature of the liquid phase which is below the equilibrium melting temperature of the material. We also allow for a disparity between the density of the solid and liquid phases. In general, energy, momentum and mass must be conserved during any phase change, therefore when the density of the solid phase is not equal to the density of the liquid phase, conservation of mass requires fluid flow in the liquid phase. To include the effect of such a density change at the sharp interface Dankwerts [33] introduced coordinates at rest in the two phases which are then in relative bodily motion along an axis perpendicular to the interface when the two phases are free from convection currents. He showed that, with respect to the interface, relative motion can exist between these two phases and he also considered several physical situations. In particular, he obtained a similarity solution to the problem of progressive freezing of a liquid when the plane interface was maintained at a constant temperature. He noted that when the disparity between the densities was removed his solution reduced to the classical similarity solution found by Carslaw and Jaeger in [23]. Chambré [25] analysed the dynamics of growth of the solid phase in a super-cooled, semi-infinite two-phase system of unequal densities with either a plane, cylindrical or spherical boundary starting from initially negligible dimensions. He assumed that the solid phase remained at a constant surface temperature, a condition which implied that the conductivity was infinite in this phase, and that the velocity of the liquid phase was zero at infinity. To determine the velocity in the liquid phase he used the equation of motion with a constant pressure field, instead of the continuity equation and by using an appropriate coordinate transformation he was then able to obtain similarity solutions to this problem. A Neumann type solution to a similar problem with a plane interface was obtained by Carslaw and Jaeger (and reported by Crank [32]). They considered the example of the freezing of a semi-infinite region when $\rho_S > \rho_L$ and both phases are incompressible, and applying slightly different boundary conditions in the solid

and liquid phases they obtained a similarity solution. Later Horvay [54] produced alternative similarity solutions to Chambré [25] by considering the effect of a varying pressure field on the equation of motion and using the continuity equation to account for conservation of mass in each volume element of the fluid. In an extensive later paper [55] Horvay modelled one-dimensional freezing of highly super-cooled Nickel, from a finite initial embryo, studying the flow velocities, temperatures and pressures in the liquid phase.

He assumed that the fluid was incompressible, obtained a profile of the pressure field from Euler's equation and an expression for the temperature at the interface from the pressure differences. This formulation resulted in a variant of the classical Gibbs-Thompson equation at the interface. Under certain conditions Horvay found that his asymptotic solution became indistinguishable from the classical solution (in [23] and [32]) which does not account for pressure changes. Rubinstein [94] derived a similarity solution to the problem including a density change on solidification, considered by Carslaw and Jaeger, but took the liquid phase to be incompressible. Wilson [134], reported by Crank [32], considered a planar problem where several phases of different densities occupy a (finite) slab of material.

More exact solutions to the Stefan problem have been produced by Tao. In [123] he obtained a convergent analytical exact solution to the planar Stefan problem with arbitrary initial and boundary conditions in the solid and liquid phases, but without a volume change on solidification, and gave infinite series solutions for the temperature and position of the interface. In [124] he further investigated the density change, planar solidification problem subject to similar arbitrary initial and boundary conditions in the solid and liquid phases, again obtaining convergent, exact, series solutions for this problem by using a new variable $y = (x + \epsilon S(t))/(1 + \epsilon)$ where $S(t)$ is the position of the interface and $\epsilon = (\rho_L - \rho_S)/\rho_L$ denotes the non-dimensional difference between the density of the solid and liquid phases.

With the exception of Horvay [55] all the papers discussed so far fix the temperature of the solid phase and/or the sharp interface. However an accurate description of the temperature for the solidification of a super-cooled liquid requires special attention, especially for an embryo of solid which necessarily has a large curvature. As mentioned in reference to Horvay's paper [55], an equation which accounts for the effect of the solid/liquid interface curvature on the equilibrium temperature is the 'Gibbs-Thompson' equation. Interface attachment kinetics (i.e. requiring that the rate of solidification (dR/dt) is related to the difference between the interfacial temperature and the equilibrium temperature (ΔT)) is another process which should be taken into consideration at the solid-liquid interface. A discussion of this effect and consideration of the nucleation process and microscopic heat flow at the interface can be found in Chalmers textbook on solidification processes [24]. In this book he describes the relationship between the process of molecular attachment at the solidifying front and the subsequent dependency on the interfacial super-cooling ΔT . He comments that when

all atomic sites are equivalent the velocity of the interface, dR/dt , is proportional to ΔT . Therefore appending the interface velocity of a growing spherical crystal by a linear kinetic function of ΔT is reasonable and should be included with the Gibbs-Thompson equation at the interface. This condition, including the linear kinetic function, was incorporated into the Stefan problem and solved using a Greens function technique in a useful paper by Schaefer and Glicksman [95]. These authors used physical values for white phosphorus to produce results for the growth rate and surface temperature of a super-cooled system comprising of a growing spherical crystal embryo in its melt. They initiated growth of the embryo by setting the initial radius of the solid phase 0.1% larger than the radius of a solid embryo which is in equilibrium with its super-cooled melt. At this so-called critical radius the effect of the pressure difference (given by equation (6.1)) on the free energy is just compensated for by ΔT , the departure of the interfacial temperature from the equilibrium temperature. By assuming incompressibility in the solid phase, and thereby equating the pressure difference with the difference in the free energy between the solid and liquid phases at a temperature $T - \Delta T$, Chalmers [24] obtained an expression for the equilibrium radius r^* (used in [95]) which is given by

$$r^* = \frac{2\sigma T_E}{L\Delta T},$$

where T_E denotes the equilibrium, or melting temperature. In this paper, however, Schaefer and Glicksman [95] did not account for a volume change on solidification due to a difference in the density of the solid and liquid phases.

In chapter 7 we obtain a numerical solution to a problem similar to [95], but in addition we account for volume changes on solidification. We solve this problem using a finite difference method and compare our solutions favourably with [95] in the limiting case $\rho_S = \rho_L$.

An important aspect of the work of Young, Laplace and Gauss and the subsequent Stefan models discussed above was first pointed out by Poisson in 1816. Namely that, in reality, the density changes continuously when passing from a solid to a liquid state (or equivalently from a liquid state to a gas) rather than as a step function. He suggested that the discontinuous density should be replaced with a continuous function $\rho(x)$, where x is the position variable. Working with a suggestion that the density function shares some of the properties of the Van der Waals equation of state, Rayleigh [88] obtained an equation for the surface tension in terms of the density gradients. Van der Waals [127] also developed this theory, which he based upon the local free-energy density. He noted that the excess free-energy density, which is caused by the presence of the interface, is equal to the surface tension σ and the free energy density $f(\rho, T)$ can be expressed by a double-well function which is shown schematically in figure 6.2. The distance of this curve above the dotted tangent line describes a double well with respect to the density with minima at ρ_S and ρ_L . To account for the surface tension at the interface Van der Waals added the term $(K/2)|\nabla\rho(x)|^2$ to the free-energy double-well,

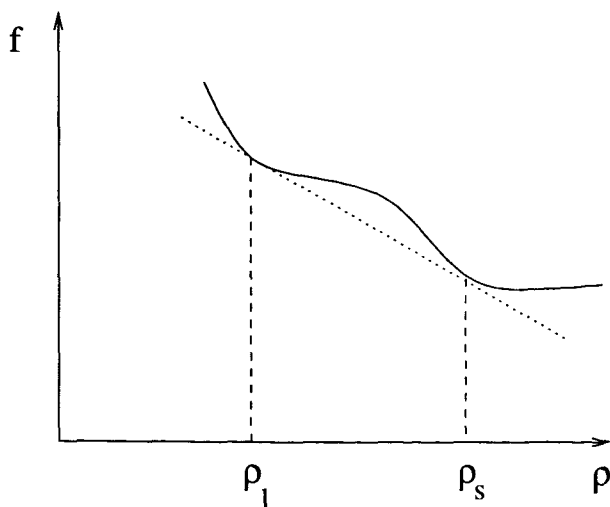


Figure 6.2: Thermodynamic free-energy density $f(\rho, T)$ as a function of ρ for a fixed temperature T in a region traversing two phases. ρ_L denotes the density of the liquid phase and ρ_S the density of the solid phase. A similar figure appears in [93].

where K is a gradient energy coefficient (related to the second moment of the intermolecular potential). This term is necessarily large when the density gradient is large and without such a term in the excess free-energy density the surface tension would vanish. The integral of the excess free-energy density is then given by

$$\sigma = K \int_{-\infty}^{\infty} \left(\frac{d\rho}{dx} \right)^2 dx,$$

when the gradient energy coefficient K is assumed to be a constant. Anisotropy can be introduced to the system by making K a function of the density gradient. Further details of this theory can be found in Rowlinson and Widom [93]. In the formulation of Van der Waals the density ρ can be described as an ‘order parameter’, since it distinguishes between the solid and liquid phases and the interface between them. This theory was reformulated later by Cahn and Hilliard [22] who expressed the free energy of the system in terms of a scalar quantity c . They make the comment that this quantity could be either composition (in the case of a binary fluid) or density. Like Van der Waals before them, they found that the thickness of the interface increased in the vicinity of the critical temperature T_c where it became infinite. If we consider the phase change of a pure material with negligible change in the density on solidification then neither the composition nor the density can play the role of an order parameter. In this case a so-called ‘phase field variable’ $\phi(\mathbf{x}, t)$ can be introduced to distinguish between the two phases. ϕ is usually constant in the bulk phases, with a larger constant value in one of the phases. (In [82] the authors make the comment that for ϕ to be an ‘order parameter’ rather than a ‘disorder parameter’ it should have a larger constant value in the phase with the lower energy. In the literature, however, this is not always the

case.) The quantity ϕ varies smoothly between the two bulk values across the diffuse interface and when the solid and liquid phases are represented by $\phi = 1$ and $\phi = 0$ for example, the interface is located at the level set $\phi = 1/2$. Using this definition for the phase-field variable the Van der Waals free-energy density can be expressed in terms of the function

$$\mathcal{F} = \int_{\Omega} \left[f(\phi, T) + \frac{1}{2} K |\nabla \phi|^2 \right] dV \quad (6.3)$$

where Ω is the fixed region of space occupied by the system and $f(\phi, T)$ is the local Helmholtz free-energy density which has a double well structure with respect to ϕ (instead of ρ as shown in figure 6.2). Langer [66] adapted ‘Model C’ by Halperin *et al.* [50], to obtain a phase-field model to describe the phase change of a pure substance and independently Collins and Levine [28] introduced a similar model. Both of these models can be made to account for different interfacial effects including the Gibbs-Thompson equation at the solid-liquid interface in the solidification problem, as we shall see later. These authors proposed the governing equation

$$M \frac{\partial \phi}{\partial t} = - \frac{\partial \mathcal{F}}{\partial \phi} = K \nabla^2 \phi - \frac{\partial f}{\partial \phi}, \quad (6.4)$$

for the phase-field variable, where M is the relaxation time to equilibrium (where ϕ minimises \mathcal{F}) and $1/M$ is called the mobility. Equation (6.4) was obtained from the free energy functional described by equation (6.3), and in Langer’s model K is replaced with ϵ^2 where ϵ is proportional to the thickness of the interface. This equation is coupled to the modified unsteady temperature diffusion equation

$$c \frac{\partial T}{\partial t} = k \nabla^2 T + L \frac{\partial \phi}{\partial t}, \quad (6.5)$$

where c is the thermal heat capacity, k the thermal conductivity, and L the latent heat per unit volume of the material. The final term of equation (6.5) acts as a source of latent heat when $\dot{\phi} \neq 0$, i.e., at the moving interface. Away from the critical point the interface thickness decreases and approaches a sharp interface, the approximation used in the Stefan model. To show that the diffuse-interface models (described by equations similar to (6.4) and (6.5)) are justified away from the critical temperature it has been shown by Caginalp and co-workers in [16], [17], [18] and [19] that these equations asymptotically approach various free boundary problems, including the model of solidification described by Schaefer and Glicksman in [95]. In particular, in [16] Caginalp shows, using detailed asymptotic analyses, that various sharp-interface models can arise from different scalings of the parameters in equations (6.4) and (6.5) as ϵ , the interfacial thickness parameter, is reduced to zero. Fife and Gill [42] examined the one-dimensional solutions of the phase field model described in [19] using a computer simulation under conditions which lead to the presence of mushy zones. They justified these mushy zones by commenting that they can occur in a pure material which experiences rapid internal heating, and in a binary alloy which is rapidly quenched. To

describe a material which is not in any distinct phase they applied smooth initial data and removed all source terms from their phase-field model. They observed that this situation contained oscillatory instabilities which, when applied to the solution, evolved by gradually increasing their dominant wavelength. Eventually these oscillations died out leaving a solution which was divided into a separate solid and liquid phase. They suggested that this effect could be interpreted as a fine-grained coarsening process, as in the solidification of alloys. Later, [43], these same authors considered the formation and disappearance of mushy regions in a material undergoing internal heating. Here they made a connection between fine-grain coarsening and spinodal decomposition, the phenomenon of spontaneous phase separation into a free-grained mixture. Above a certain critical value of internal heating, however, they observed that the coarsening process was curtailed and even eliminated.

Penrose and Fife [82] identified a drawback in the class of phase-field descriptions originally derived by Langer [66] and Collins and Levine [28]. Namely that the phase-field equation (6.4) is based on a free-energy functional which is considered to be isothermal, however the expression for the temperature field, given by equation (6.5), is then derived by allowing the temperature to vary and applying a term proportional to $\partial\phi/\partial t$, to account for the latent heat. To avoid this *ad hoc* approach these authors derived a class of thermodynamically consistent models, which include the phase-field model described above, from an entropy rather than a free energy functional. In [129] Wang *et al.*, following the method described in [82], derived a class of phase-field models for the solidification of a pure material in its own melt. These authors showed that by making specific choices for the functions and parameters their approach could be made to describe the models of Langer [66], Collins and Levine [28] and others.

Until recently numerical methods for computation of these type of solidification problems have been restricted by the limitations of computing power. An early numerical solution was obtained by Smith in [109]. He used a finite element method to produce results in two-spatial dimensions. This approach was based on a weak formulation of the single-domain method which gave the interfacial conditions implicitly (as in the phase-field model). However, to accurately approximate the temperature profile near the interface he uses a front tracking method which (like the sharp-interface Stefan model) calculated the interfacial position explicitly. Later, however, Caginalp and Socolovsky [21] applied the single-domain method alone, avoiding explicit front tracking by using a finely spaced finite-difference grid over the entire co-ordinate range. They adopted the perspective that equations (6.4) and (6.5) are essentially a means of approximating the sharp interface Stefan problems described previously, and showed that, provided the non-dimensional interfacial thickness parameter ϵ was small, an increase or decrease in its magnitude did not affect the accuracy of their results. They compared these results to the classical exact solution to the plane-interface Stefan model and

found close agreement when ϵ was small. They also observed a numerical restriction on the ratio $\epsilon/\Delta r$, where Δr is the mesh spacing. If this ratio was too small significant numerical oscillations occurred which caused the solution method to break down and the most suitable range for this ratio was $0.75 < \epsilon/\Delta r < 1.1$. A similar result was later observed independently by Wheeler *et al.* in [133] and is verified in chapter 9 of this thesis.

In nature solidification occurs by the formation of dendrites at the surface of a growing crystal (snowflakes for example display a variety of fascinating dendritic shapes). This process of crystal formation is often seen in many solidification problems. A dendrite tip of freely growing succinonitrile is shown in figure 6.3, which has been taken from a paper by Glicksman, Schaefer and Ayers [47]. In this paper they carefully obtain experimental results and compare

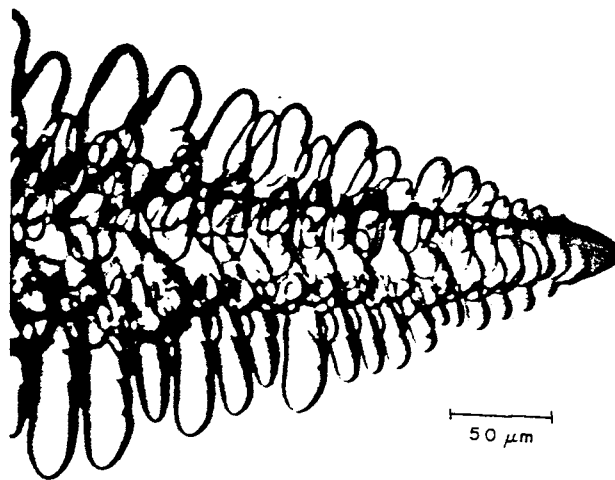


Figure 6.3: Micro-morphology of a freely growing dendrite of succinonitrile, from [47].

these results with the velocity of a growing dendrite as predicted by various different crystal growth theories. The dendrite in figure 6.3 displays a main stem with a smooth parabola-like tip followed by small perturbations which grow to form side branches that eventually become perpendicular to the main-stem.

To obtain these complex shapes from theoretical models requires a numerical solution to the solidification problem in at least two spatial dimensions. An early numerical solidification model which was based on an equation of motion for the heat content per unit area of the surface was developed by Ben-Jacob, Goldenfield and Langer *et al.* [8]. In this model these authors incorporated the Gibbs-Thompson and Cahn-Hilliard conditions and used a thermal boundary layer approach to approximate the diffuse interface, ignoring heat diffusion in the solid phase. They solved this model numerically by tracking the interface and showed that introducing anisotropy to the description of the interface triggered model instabilities and

dendritic behaviour which they qualitatively compared to snowflake patterns.

Later Kobayashi [61] performed a series of numerical calculations in 2 spatial dimensions which showed the formation of dendritic patterns using the phase-field approach. He was critical of the earlier numerical method of Ben-Jacob [8] and others [60], [107] since these papers keep the interfacial data explicitly and move the position of the interface according to the interfacial equation of motion. Instead he solved the phase-field equations directly by using a simple explicit numerical method for an equation similar to (6.4) and an implicit numerical method for an equation similar to (6.5), since these equations express the interfacial conditions implicitly. He introduced anisotropy by assuming that the small parameter ϵ depended on the direction of the normal to the interface, and produced results for directional solidification and the growth of the solid phase after nucleation.

Wheeler *et al.* [133] solved the model developed in [129] in both one- and two-dimensions. These authors were critical of Kobayashi's numerical work [61] as he did not address the issues of numerical accuracy, the relation to classical solidification problems (such as the Stefan problem discussed above) or the comparison of his results with experimental evidence. To address these issues Wheeler *et al.* [133] compared the one dimensional numerical results of the model in [129] to the results of Schaefer and Glicksman [95], as the interfacial thickness parameter of the model was reduced. In this paper the authors obtained excellent agreement between these two methods in the sharp interface limit when $\epsilon \leq 0.01$, however larger values of ϵ were less accurate. In two-dimensions they produced quantitative and qualitative numerical results which compare favourably with dendrite formation in the growth of a super-cooled melt.

Recently there have been a few papers which consider hydrodynamic flow effects in the liquid phase when deriving a phase-field model. In [20] Caginalp and Jones derived a phase-field model with flow in the liquid phase to describe the phase-change process of a pure material. They chose an order parameter which was not fixed in either phase but varied linearly with the position variable \mathbf{x} . These authors made a formulation of the phase-field equations using the continuity equation and Euler's equation to determine the specific gravity and the pressure. They considered briefly the sharp interface limit of this model, to obtain a generalisation of the Gibbs-Thompson equation, and the planar geometrical situation.

In [3], a recent review paper by Anderson *et al.*, a thermodynamic model is outlined in which convection in the liquid phase is included. This model involves a gradient internal energy coefficient and it leads to a set of equations which, together with an equation of state, describe a phase-field model for viscous, compressible, non-isothermal flow. In this paper ([3]) and references therein, various other diffuse interface models and their applications are discussed. Some of these applications for a single component fluid include shear flows in near-critical fluids, moving contact lines (see [97] for example, where a diffuse interface model is

used to determine equations for a viscous flow near a plane wall), nucleation of droplets, instabilities of planar jets and spinodal decomposition with hydro-dynamic effects. Binary fluid models and their application are also considered.

Tönhardt and Amberg [126] used a phase-field model to study the effect of a shear flow in the liquid phase on a solid nucleus attached to a solid wall and growing into the melt. These authors produced numerical results in two spatial dimensions and found that the shear flow significantly affected the shape of the growing dendrite and the local heat transfer. More specifically, growth of the dendritic side branches of the vertical main-stem were enlarged on the up-stream side and reduced on the down-stream side. They also noted that a change in the orientation of the main-stem occurred when the shear flow was significant, whereas decreasing the under-cooling reduced the radius of the dendrite tip and therefore the velocity and growth of the side branches also decreased.

Very recently Anderson, McFadden and Wheeler [2] have developed a phase-field model which allows for convection in the liquid phase. To extend previously existing phase-field models to include convection these authors base their model upon a non-conserved order parameter, $\phi(\mathbf{x}, t)$ which denotes the liquid and solid phases by $\phi(\mathbf{x}, t) = 0$ and $\phi(\mathbf{x}, t) = 1$ respectively. This model is unusual because it treats both the solid and liquid phases as Newtonian fluids, where the viscosity (which is dependent upon ϕ) of the solid phase is much larger than the liquid phase. The density is not treated as an independent variable but is prescribed as a function of ϕ only and therefore the density of the bulk solid and liquid phases are uniform in the spatial variable. Also these authors allow for a non-standard (in a fluid-fluid system) interfacial anisotropic surface energy. Following Penrose and Fife [82] and Wang *et al.* [129], governing equations are developed from gradient entropy and internal energy functionals.

Since this thesis deals with the model described in [2] we end this chapter by briefly outlining the functionals and physical balance laws which lead to the model obtained therein.

The total entropy of the system is given by

$$\mathcal{S} = \int_{\Omega(t)} \left[\rho s - \frac{1}{2} \epsilon_S^2 \Gamma^2(\nabla \phi) \right] dV, \quad (6.6)$$

where ρs is the classical entropy density per unit volume and the non-classical term involving spatial phase-field gradients contains a gradient entropy coefficient ϵ_S which is assumed to be a constant for simplicity. $\Omega(t)$ is a material volume and the homogeneous degree one function $\Gamma(\nabla \phi)$ allows for a diffuse interface with an anisotropic surface energy (if $\Gamma(\nabla \phi) = |\nabla \phi|$ is chosen, the surface energy of the interface becomes isotropic). Then the total mass \mathcal{M} , linear momentum $\vec{\mathcal{P}}$ and internal energy \mathcal{E} which incorporates the non-classical phase-field gradient

term with a gradient energy coefficient ϵ_E , are

$$\mathcal{M} = \int_{\Omega(t)} \rho \, dV, \quad (6.7)$$

$$\vec{\mathcal{P}} = \int_{\Omega(t)} \rho \vec{u} \, dV \quad (6.8)$$

and

$$\mathcal{E} = \int_{\Omega(t)} \left[\rho e + \frac{1}{2} \rho |\vec{u}|^2 + \frac{1}{2} \epsilon_E^2 \Gamma^2(\nabla \phi) \right] dV \quad (6.9)$$

respectively where \vec{u} denotes velocity and e the internal energy density per unit mass.

The physical balance law for entropy is given by

$$\frac{d\mathcal{S}}{dt} + \int_{\delta\Omega(t)} \vec{q}_S \cdot \hat{n} \, dA = \int_{\Omega(t)} \dot{s}^{prod} \, dV \quad (6.10)$$

where \vec{q}_S denotes the entropy flux and \dot{s}^{prod} is the local rate of entropy production, which by the second law of thermodynamics must not be negative. The remaining physical balance laws for mass, momentum and energy are

$$\frac{d\mathcal{M}}{dt} = 0, \quad (6.11)$$

$$\frac{d\vec{\mathcal{P}}}{dt} = \int_{\delta\Omega(t)} \hat{n} \cdot \mathbf{m} \, dA \quad (6.12)$$

and

$$\frac{d\mathcal{E}}{dt} + \int_{\delta\Omega(t)} \vec{q}_E \cdot \hat{n} \, dA = \int_{\delta\Omega(t)} \hat{n} \cdot \mathbf{m} \cdot \vec{u} \, dA \quad (6.13)$$

respectively, where \mathbf{m} is the stress tensor, \vec{q}_E the internal energy flux and \hat{n} is the outward unit normal to $\delta\Omega(t)$.

The local entropy production can now be expressed in terms of \mathbf{m} , \vec{q}_E , \vec{q}_S and $D\phi/Dt$ by writing equations (6.6) to (6.13) as differential equations. Forms for these terms are then chosen by using the second law of thermodynamics which requires that \dot{s}^{prod} cannot be negative. Further details of this procedure can be found in [2]. Resulting equations of motion for mass, momentum, the phase-field variable and internal energy can then be written as

$$\frac{D\rho}{Dt} = -\rho \nabla \cdot \vec{u}, \quad (6.14)$$

$$\rho \frac{D\vec{u}}{Dt} = \nabla \cdot \left[\left(-p + \frac{1}{2} \epsilon_F^2 |\Delta \phi|^2 \right) \mathbf{I} - \epsilon_F^2 \nabla \phi \otimes \nabla \phi + \boldsymbol{\tau} \right], \quad (6.15)$$

$$M \frac{D\phi}{Dt} = \epsilon_F^2 \nabla \cdot (\nabla \phi) - \rho \frac{\partial e}{\partial \phi} \quad (6.16)$$

and

$$\rho \frac{De}{Dt} = \nabla \cdot [k \nabla t] + \epsilon_E^2 \nabla \cdot (\nabla \phi) \frac{D\phi}{Dt} + \left[\left(-p + \frac{1}{2} T \epsilon_S^2 |\nabla \phi|^2 \right) \mathbf{I} - T \epsilon_S^2 \nabla \phi \otimes \nabla \phi + \boldsymbol{\tau} \right] : \nabla \vec{u} \quad (6.17)$$

respectively where the thermal conductivity k is constant, the gradient free energy Helmholtz coefficient $\epsilon_F^2 = \epsilon_E^2 + T\epsilon_S^2$, the viscous stress tensor $\boldsymbol{\tau} = \mu(\nabla\vec{u} + \nabla\vec{u}^T) + \lambda(\nabla \cdot \vec{u})\mathbf{I}$ where μ , λ are viscosity coefficients and \mathbf{I} is the unit tensor, and M is a constant (positive) mobility coefficient. The matrix identity $\mathbf{a} : \nabla\vec{u} = a_{kj}\partial u_j/\partial x_k$, with summation over the repeated indices k and j , and in equations (6.14) to (6.17) we have assumed that the surface energy is isotropic by substituting $|\nabla\phi|$ for $\Gamma(\nabla\phi)$.

To study situations in which the density is constant in the solid and liquid phases, which implies therefore that these bulk phases are incompressible, the density was not chosen to be an independent variable as in the quasi-incompressible formulation, described in [72]. Accordingly, therefore, the pressure and temperature are chosen as independent variables and the internal energy per unit mass is expressed as

$$e = g(T, p, \phi) + Ts(T, p, \phi) - \frac{p}{\rho(T, p, \phi)} \quad (6.18)$$

where $g(T, p, \phi)$ is the Gibbs free energy per unit mass and the following thermodynamic relationships hold:

$$\frac{1}{\rho(T, p, \phi)} = \left. \frac{\partial g}{\partial p} \right|_{T, \phi}, \quad s(T, p, \phi) = - \left. \frac{\partial g}{\partial T} \right|_{p, \phi} \quad \text{and} \quad \left. \frac{\partial e}{\partial \phi} \right|_{s, p} = \left. \frac{\partial g}{\partial \phi} \right|_{p, T}. \quad (6.19)$$

The density is described in terms of the phase-field variable ϕ alone by

$$\rho(\phi) = \rho_S r(\phi) + \rho_L [1 - r(\phi)] \quad (6.20)$$

where ρ_S and ρ_L denote constant solid and liquid densities respectively and $r(\phi)$ is given by $r(\phi) = \phi^2(3 - 2\phi)$, a smooth monotonic function satisfying $r(0) = 0$ and $r(1) = 1$. The equation (6.19)₁ can be integrated and the Gibbs free energy expressed as

$$g(T, p, \phi) = g_0(T, \phi) + \frac{p - p_0}{\rho(\phi)} \quad (6.21)$$

where p_0 is a reference pressure and in [2] they let

$$g_0(T, \phi) = \left[e_0 - cT_M - r(\phi)L + \frac{1}{4a_S}H(\phi) \right] \left(1 - \frac{T}{T_M} \right) - cT \ln \left(\frac{T}{T_M} \right) + \frac{1}{4a}H(\phi). \quad (6.22)$$

This expression for the free energy gives the following corresponding expressions for the entropy as

$$s = \frac{1}{T_M} \left[e_0 - r(\phi)L + \frac{1}{4a_S}H(\phi) \right] + c \ln \left(\frac{T}{T_M} \right) \quad (6.23)$$

and internal energy as

$$e = e_0 + c(T - T_M) - r(\phi)L + \left[\frac{1}{4a_S} + \frac{1}{4a} \right] H(\phi) - \frac{p_0}{\rho(\phi)}. \quad (6.24)$$

In equations (6.22) to (6.24) the symbols e_0 , c , L , T_M , a_S and a are assumed to be constant terms and they denote respectively the reference energy, the heat capacity per unit mass, the

latent heat per unit mass, the melting point at the reference pressure, and entropy and free energy coefficients. $H(\phi)$ is a double well potential which is given by $H(\phi) = \phi^2(1 - \phi)^2$. In [2] the authors justify their choice of g_0 , shown in equation (6.22), by commenting that it leads to an energy density in the liquid phase which is a linear function of the temperature. This assumption was made in equation (31) of an earlier paper by Wang *et al.* [129], who argued that in solidification problems heat conduction occurs mostly in the liquid phase.

The model outlined above has been used in chapters 8 and 9 of this thesis where we show its asymptotic and numerical relationship to the sharp interface Stefan model of chapter 7 in the sharp interface limit as ε_S , a non-dimensional parameter related to the interfacial thickness, tends to 0.

Chapter 7

Sharp interface Stefan model with flow

7.1 Introduction

In this chapter we derive a one-dimensional sharp interface Stefan model in spherical polar co-ordinates for the growth of a solid sphere into a super-cooled melt. Allowance is made for a flow velocity caused by a change in volume on solidification due to a difference in the density between the solid phase and the liquid phase. We formulate this problem in such a way that it may be directly compared to the numerical Green's function solution of a similar problem without flow described by Schaefer and Glicksman in [95]. The problem in this chapter, however, is solved numerically in one spatial direction by using finite differences.

7.2 Derivation

The problem of a growing solid phase inside a liquid phase can be characterised by a set of partial differential equations within the solid and liquid phases coupled by a set of boundary conditions at the interface between the two phases.

7.2.1 Liquid phase

The equation for temperature describing heat transfer due to convection and diffusion in a liquid phase is given by

$$\frac{\partial T}{\partial t} + \mathbf{u} \cdot \nabla T = \kappa_L \nabla^2 T \quad (7.1)$$

where T , t , \mathbf{u} and κ denote temperature, time, velocity and thermal diffusivity respectively.

In a spherically symmetric geometry, equation (7.1) becomes

$$\frac{\partial T_L}{\partial t} + u_L \frac{\partial T_L}{\partial r} = \kappa \left(\frac{\partial^2 T_L}{\partial r^2} + \frac{2}{r} \frac{\partial T_L}{\partial r} \right) \quad (7.2)$$

where the subscript l denotes the liquid phase and r is the radial position vector from a point at the centre of the growing sphere.

The equation describing conservation of momentum takes the form

$$\rho \frac{D\mathbf{u}}{Dt} = \rho \mathbf{F} + \nabla \cdot \boldsymbol{\sigma} \quad (7.3)$$

where \mathbf{F} is a vector describing the volume body forces per unit mass of fluid, and $\boldsymbol{\sigma}$ is the stress tensor which is given in tensor form by

$$\sigma_{i,j} = \mu \left(\frac{\partial u_i}{\partial x_j} + \frac{\partial u_j}{\partial x_i} \right) - p \delta_{ij} \quad (7.4)$$

where p and μ denote pressure and viscosity.

In a spherically symmetric geometry this equation becomes

$$\rho_L \frac{Du_L}{Dt} = \rho_L \left[(u_L)_t + u_L (u_L)_r \right] = - (p_L)_r + \mu_L \left[(u_L)_{rr} + \frac{2}{r} (u_L)_r \right] \quad (7.5)$$

where we have assumed no body forces (such as gravity) are acting and the radial component of velocity, pressure, viscosity and density in the liquid phase are given by u_L , p_L , μ_L and ρ_L respectively.

Incompressibility in the liquid phase requires that

$$\nabla \cdot \mathbf{u} = 0. \quad (7.6)$$

Integrating (7.6) with respect to r gives

$$u_L = \frac{C_u(t)}{r^2}, \quad (7.7)$$

where the term C_u is a function of time.

7.2.2 Solid phase

The temperature equation in the solid phase is identical to equation (7.1), however since the velocity is identically zero it simplifies to

$$\frac{\partial T_S}{\partial t} = \kappa_S \left(\frac{\partial^2 T_S}{\partial r^2} + \frac{2}{r} \frac{\partial T_S}{\partial r} \right) \quad (7.8)$$

where the subscript s denotes the solid phase. Since $u_S = 0$, equation (7.3), which describes conservation of momentum in the solid phase, becomes

$$\frac{\partial}{\partial r} (-p_S) = 0, \quad (7.9)$$

which indicates that the pressure is constant in the solid phase.

7.2.3 Interfacial boundary conditions

Across the moving boundary the mass must be conserved. Consider the freezing sphere in

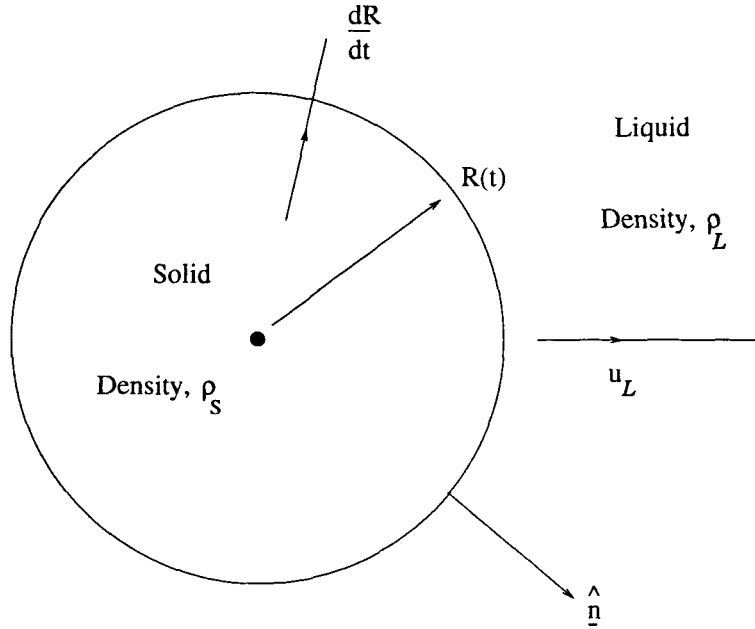


Figure 7.1: A freezing sphere.

figure 7.1 which has a radius $R(t)$, a solid density ρ_S and a liquid density ρ_L . Assuming spherical symmetry, on the liquid side of the interface the velocity of the fluid u_L acts only in a direction normal to the sphere since the no slip condition on the boundary requires that there is no tangential component.

In one-dimension the mass of the solid enclosed by the surface at any instant is

$$\frac{4}{3}\pi R^3 \rho_S.$$

The net velocity at which fluid flows towards the interface is

$$\frac{dR}{dt} - u_L,$$

and the net rate at which mass flows towards the interface is given by

$$4\pi R^2 \rho_L \left(\frac{dR}{dt} - u_L \right).$$

Therefore conservation of mass in one-dimension implies that

$$\frac{d}{dt} \left(\frac{4}{3}\pi R^3 \rho_S \right) - 4\pi R^2 \rho_L \left(\frac{dR}{dt} - u_L \right) = 0$$

which simplifies to

$$\frac{dR}{dt} = \frac{u_L}{\epsilon} \tag{7.10}$$

where

$$\epsilon = (\rho_L - \rho_S)/\rho_L \quad (7.11)$$

and u_L denotes the normal velocity at the interface where $r = R(t)$. Equation (7.10) gives a relationship between the velocity of the interface (dR/dt) and the velocity in the liquid at the interface (u_L). Therefore using equation (7.7) we can write (7.10) as

$$\frac{dR}{dt} = \frac{1}{\epsilon} \frac{C_u(t)}{R^2}. \quad (7.12)$$

Next we consider the latent heat condition to describe conservation of heat at the interface. When the temperature of the solid phase is greater than the liquid phase, therefore, heat will be conducted towards the interface from the solid and away into the cooler liquid. The difference between the heat conducted towards and away from the interface is equal to the latent heat of solidification. A schematic representation of this is shown in figure 7.2.

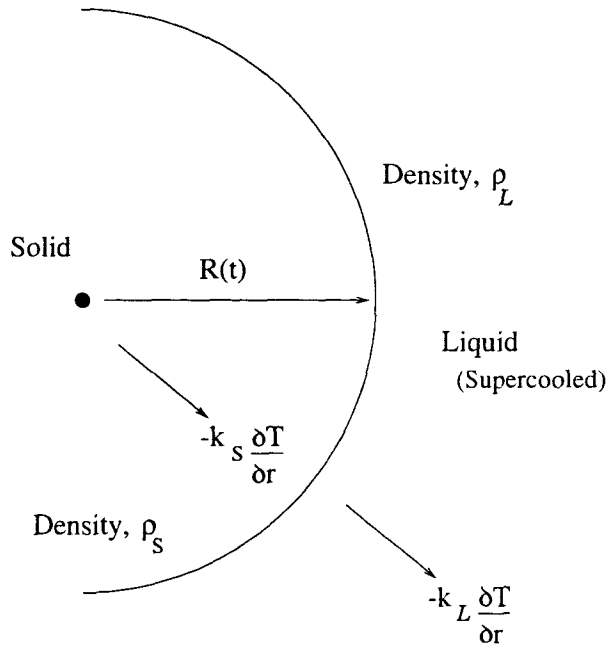


Figure 7.2: Heat transfer at the boundary of a freezing sphere.

In the situation where the specific heat c is a constant the latent heat boundary condition can be written as

$$k_S \frac{\partial T_S}{\partial r} - k_L \frac{\partial T_L}{\partial r} = L\rho_S \frac{dR}{dt} \quad (7.13)$$

where k_S and k_L are the thermal conductivities in the solid and liquid phases respectively.

Following [95] the effect of the interface curvature is included in an expression for the equilibrium temperature; this is known as the Gibbs-Thompson effect. We also require that the rate of motion of the interface is a function of the deviation of the interface temperature from the local equilibrium temperature of the bath. This effect is known as interface attachment

kinetics. The effect of the curvature on the equilibrium temperature will be very pronounced for a spherical crystal whose radius is very small. For an interface of radius $R(t)$, surface energy γ and a planar interface melting temperature given by T_m , the Gibbs-Thompson relationship in spherical polar co-ordinates describes the local equilibrium temperature T as

$$T = T_m - \frac{A L}{R c}$$

where $A = 2\gamma T_m c / L^2$, L is the latent heat of fusion per unit volume and c the specific heat of the super-cooled liquid per unit volume. For some small radius of curvature $R^* = A / \Delta\theta$, where $\Delta\theta$ is the normalised bath super-cooling defined by $\Delta\theta = c\Delta T / L$, the local equilibrium temperature will be reduced to the temperature of the super-cooled bath of liquid. We now introduce attachment kinetics into this equation. Defining the surface temperature of the growing sphere as T_{st} , then the rate of motion of the interface is assumed to be a function of the difference between T_{st} and the local equilibrium temperature of the curved interface of radius $R(t)$. This function will depend upon the molecular attachment process at the interface. For a solid phase which remains spherical as it grows, a reasonable choice is to assume this function is linear. The surface temperature of the interface is then given by

$$T_{st} = T_m - \frac{A L}{R c} - \frac{1}{\mu} \frac{dR}{dt}. \quad (7.14)$$

where μ cm/sec $^{\circ}C$ is the linear kinetic coefficient.

Finally it is required that the temperature at the interface is continuous since a discontinuity in the temperature profile would clearly be unrealistic. Therefore at $r = R(t)$ we require that

$$\lim_{r \rightarrow R(t)^-} T = T_{st} = \lim_{r \rightarrow R(t)^+} T \quad (7.15)$$

where $R(t)^-$ and $R(t)^+$ denote the limit as $r \rightarrow R(t)$ from the solid and liquid sides of the interface respectively.

7.3 Non-dimensionalisation

Equations (7.2), (7.5), (7.8), (7.12), (7.13) and (7.14) can be solved numerically. To compare the numerical results to those obtained in [95], however, it is convenient to first non-dimensionalise the variables in a similar way. Therefore we let

$$\bar{r} = \frac{r}{R^*}, \quad (7.16)$$

$$\tau = \frac{4\kappa_{SL}}{(R^*)^2} t, \quad (7.17)$$

$$T = \frac{L}{c} \theta, \quad (7.18)$$

$$\frac{dR}{dt} = \frac{4\kappa_{SL}}{R^*} \frac{d\bar{R}}{d\tau}, \quad (7.19)$$

and in addition the spatial constant of integration C_u in equation (7.7), which was introduced by integrating the incompressibility condition (7.6), is non-dimensionalised by

$$C_u(\tau) = \kappa_{SL} R^* \bar{C}_v(\tau). \quad (7.20)$$

R^* denotes the radius of a spherical solid crystal in equilibrium with the super-cooled bath and κ_{SL} is the average thermal diffusivity, defined as

$$\kappa_{SL} = \frac{1}{2} (\kappa_S + \kappa_L).$$

Similarly the average density ρ_{SL} is defined by

$$\rho_{SL} = \frac{1}{2} (\rho_S + \rho_L).$$

Finally we define the normalised temperature variable $\bar{\theta}$ via

$$\theta = \theta_m + \Delta\theta\bar{\theta}, \quad (7.21)$$

which describes the temperature in terms of the under-cooling $\Delta\theta$. Initially with $\bar{\theta} = -1$ everywhere the super-cooling is $\Delta\theta$, and $\bar{\theta} = 0$ corresponds to zero super-cooling (i.e. the non-dimensional temperature θ is equal to the melting temperature θ_m).

Applying non-dimensionalisations (7.16) to (7.21) to the system of equations (7.2), (7.8), (7.12), (7.13) and (7.14) leaves

$$4 \frac{\kappa_{SL}}{\kappa_L} (\bar{\theta}_L)_\tau + \frac{\kappa_{SL}}{\kappa_L} \left(\frac{\bar{C}_v}{\bar{r}^2} \right) (\bar{\theta}_L)_{\bar{r}} = (\bar{\theta}_L)_{\bar{r}\bar{r}} + \frac{2}{\bar{r}} (\bar{\theta}_L)_{\bar{r}} \quad (7.22)$$

$$4 \frac{\kappa_{SL}}{\kappa_S} (\bar{\theta}_S)_\tau = (\bar{\theta}_S)_{\bar{r}\bar{r}} + \frac{2}{\bar{r}} (\bar{\theta}_S)_{\bar{r}} \quad (7.23)$$

$$\bar{R}_\tau = \frac{1}{4\epsilon} \frac{\bar{C}_v}{\bar{R}^2} \quad (7.24)$$

$$-\frac{\kappa_S \rho_S}{\kappa_{SL}} (\bar{\theta}_S)_{\bar{r}} \Big|_{\bar{r}=\bar{R}} + \frac{\kappa_L \rho_L}{\kappa_{SL}} (\bar{\theta}_L)_{\bar{r}} \Big|_{\bar{r}=\bar{R}} = -4 \left(\frac{\rho_S}{\Delta\theta} \right) \bar{R}_\tau \quad (7.25)$$

$$\frac{d\bar{R}}{d\tau} = -\xi \left[\bar{\theta} \Big|_{\bar{r}=\bar{R}} + \frac{1}{\bar{R}} \right] \quad (7.26)$$

where $\xi = AL\mu/4\kappa_{SL}c$. The system of equations (7.22) to (7.26) can be solved without reference to the pressure. The pressure will vary throughout the liquid phase, especially

when flow is induced in the liquid by a density difference between the two phases. This flow will also affect the pressure in the solid phase according to the *vapour recoil effect*. The effect of the change in pressure on the melting temperature will be small, however, since the latent heat coefficient L is large. We have used the Gibbs-Thompson equation (7.14) to obtain an expression for the interfacial temperature and the pressure term is absent from (7.14) and consequently (7.26). Therefore, since we do not need to evaluate the pressure in either phase the momentum equation (7.5) and the pressure are not considered any further.

7.4 Tracking of the interface

To solve equations (7.22) to (7.26) the position of the interface is tracked as it grows into the liquid phase. Introducing the variable $\bar{\zeta}$ where

$$\bar{\zeta} = \frac{1}{2} \left(\frac{\bar{r} - \bar{R}}{\bar{r} + \bar{R}} + 1 \right) \quad (7.27)$$

ensures that:

- the interface is always at $\bar{\zeta} = 1/2$,
- in the limit as $\bar{r} \rightarrow \infty$ then $\bar{\zeta} \rightarrow 1$,
- in the limit as $\bar{r} \rightarrow 0$ then $\bar{\zeta} \rightarrow 0$.

The change of variable from \bar{r} to $\bar{\zeta}$ transforms the non-dimensional equations outlined in the previous section since

$$\bar{r} = \frac{\bar{R}\bar{\zeta}}{(1-\bar{\zeta})}, \quad (7.28)$$

$$\frac{\partial}{\partial \bar{r}} = \frac{\partial \bar{\zeta}}{\partial \bar{r}} \frac{\partial}{\partial \bar{\zeta}} = \frac{\bar{R}}{(\bar{r} + \bar{R})^2} \frac{\partial}{\partial \bar{\zeta}} = \frac{(1-\bar{\zeta})^2}{\bar{R}} \frac{\partial}{\partial \bar{\zeta}}, \quad (7.29)$$

$$\frac{\partial^2}{\partial \bar{r}^2} = \frac{\bar{R}^2}{(\bar{r} + \bar{R})^4} \frac{\partial^2}{\partial \bar{\zeta}^2} - \frac{2\bar{R}}{(\bar{r} + \bar{R})^3} \frac{\partial}{\partial \bar{\zeta}} = \frac{(1-\bar{\zeta})^4}{\bar{R}^2} \frac{\partial^2}{\partial \bar{\zeta}^2} - \frac{2(1-\bar{\zeta})^3}{\bar{R}^2} \frac{\partial}{\partial \bar{\zeta}} \quad (7.30)$$

and

$$\frac{\partial}{\partial \tau} = -\frac{\bar{r}\bar{R}_\tau}{(\bar{r} + \bar{R})^2} \frac{\partial}{\partial \bar{\zeta}} + \frac{\partial}{\partial \tau} = -\left[\frac{\bar{\zeta}(1-\bar{\zeta})\bar{R}_\tau}{\bar{R}} \right] \frac{\partial}{\partial \bar{\zeta}} + \frac{\partial}{\partial \tau}. \quad (7.31)$$

Unfortunately these transformations significantly complicate the system. On application of conditions (7.27) to (7.31) equations (7.22) and (7.23) become

$$4 \frac{\kappa_{SL}}{\kappa_L} (\bar{\theta}_L)_\tau = \frac{(1-\bar{\zeta})^4}{\bar{R}^2} (\bar{\theta}_L)_{\bar{\zeta}\bar{\zeta}} - 4 \frac{\kappa_{SL}}{\kappa_L} \frac{(1-\bar{\zeta})}{\bar{R}} \left[\epsilon \frac{(1-\bar{\zeta})^3}{4\bar{\zeta}^2} - \bar{\zeta} \right] \bar{R}_\tau (\bar{\theta}_L)_{\bar{\zeta}} + \left[\frac{2(1-\bar{\zeta})^3}{\bar{\zeta}\bar{R}^2} - \frac{2(1-\bar{\zeta})^3}{\bar{R}^2} \right] (\bar{\theta}_L)_{\bar{\zeta}}, \quad (7.32)$$

and

$$4 \frac{\kappa_{SL}}{\kappa_S} (\bar{\theta}_S)_\tau = \frac{(1 - \bar{\zeta})^4}{\bar{R}^2} (\bar{\theta}_S)_{\bar{\zeta}\bar{\zeta}} + 4 \frac{\kappa_{SL}}{\kappa_S} \frac{\bar{\zeta}(1 - \bar{\zeta})}{\bar{R}} \bar{R}_\tau (\bar{\theta}_S)_{\bar{\zeta}} - \frac{2(1 - \bar{\zeta})^3}{\bar{R}^2} (\bar{\theta}_S)_{\bar{\zeta}} + \frac{2(1 - \bar{\zeta})^3}{\bar{\zeta}\bar{R}^2} (\bar{\theta}_S)_{\bar{\zeta}}. \quad (7.33)$$

Combining equations (7.24) and (7.25) gives

$$\bar{C}_v = \epsilon \bar{R} \Delta \bar{\theta} (1 - \bar{\zeta})^2 \left[-\frac{\kappa_{L\rho L}}{\kappa_{SL\rho S}} \frac{\partial \bar{\theta}_L}{\partial \bar{\zeta}} \Big|_{\bar{\zeta}=\frac{1}{2}^+} + \frac{\kappa_S}{\kappa_{SL}} \frac{\partial \bar{\theta}_S}{\partial \bar{\zeta}} \Big|_{\bar{\zeta}=\frac{1}{2}^-} \right]; \quad (7.34)$$

equations (7.25) and (7.26) together yield

$$4\xi \left[\bar{R} \bar{\theta} + 1 \right] = \Delta \bar{\theta} (1 - \bar{\zeta})^2 \left[\frac{\kappa_{L\rho L}}{\kappa_{SL\rho S}} \frac{\partial \bar{\theta}_L}{\partial \bar{\zeta}} \Big|_{\bar{\zeta}=\frac{1}{2}^+} - \frac{\kappa_S}{\kappa_{SL}} \frac{\partial \bar{\theta}_S}{\partial \bar{\zeta}} \Big|_{\bar{\zeta}=\frac{1}{2}^-} \right]. \quad (7.35)$$

Equation (7.26) remains unchanged. Equation (7.32) is used to evaluate the non-dimensional temperature $\bar{\theta}$ at every grid point in the liquid phase using forward time and central space finite differences. Similarly, equation (7.33) is used to evaluate $\bar{\theta}$ at every grid point in the solid phase again using forward time and central space finite differences. Equations (7.26), (7.34) and (7.35) are evaluated at the interface where $\bar{\zeta} = 1/2$. Equation (7.26) can be used to evaluate \bar{R} at $t + \delta t$, the new time level, by using forward differencing for the time derivative and evaluating the right hand side at the previous time step in the usual way. It is possible to obtain values for \bar{C}_v and $\bar{\theta}$ on $\bar{\zeta} = 1/2$ at $t + \delta t$ directly from equations (7.24) and (7.25), however these equations must be evaluated at the new time step and therefore a finite difference approximation for \bar{R}_τ is required at $t + \delta t$. From the combination of (7.24) and (7.25) however, we obtain equation (7.34), which contains no time derivatives and therefore can simply be evaluated at $t + \delta t$. A similar combination of (7.25) and (7.26) yields equation (7.35) which can also be simply evaluated at $t + \delta t$.

7.5 Finite differences

Equations (7.26), (7.32), (7.33), (7.34) and (7.35) were initially discretised by using Crank-Nicolson's method [108] which averages over the new and previous time step. Due to the initial non-equilibrium data imposed upon the system, however, persistent numerical oscillations were produced. These oscillations did not decay with time despite changing the size of the time and/or position steps. Obtaining results using this method was found to be impossible since the system proved to be sensitive to small oscillations at the interface. Therefore the Crank-Nicolson approach was dropped in favour of the simpler forward time, central space approximation. Dropping the bars the finite difference approximations of equations (7.26), (7.32), (7.33), (7.34) and (7.35) are outlined below.

Temperature equation (7.33) in the solid phase:

$$0 = -4 \frac{\kappa_{SL}}{\kappa_S} \left(\frac{\theta_\zeta^{\tau+d\tau} - \theta_\zeta^\tau}{d\tau} \right) + \frac{(1 - \zeta)^4}{(R^\tau)^2} \frac{(\theta_{\zeta+d\zeta}^\tau - 2\theta_\zeta^\tau + \theta_{\zeta-d\zeta}^\tau)}{(d\zeta)^2} \quad (7.36)$$

$$+ \left[-\frac{2(1-\zeta)^3}{(R^\tau)^2} + \frac{2(1-\zeta)^3}{\zeta(R^\tau)^2} + \frac{\kappa_{SL}}{\kappa_S} \frac{4(1-\zeta)\zeta}{R^\tau} \left(\frac{R^{\tau+d\tau} - R^\tau}{d\tau} \right) \right] \frac{(\theta_{\zeta+d\zeta}^\tau - \theta_{\zeta-d\zeta}^\tau)}{2d\zeta}.$$

Temperature equation (7.32) in the liquid phase:

$$\begin{aligned} 0 = & -4 \frac{\kappa_{SL}}{\kappa_L} \left(\frac{\theta_{\zeta+d\tau}^\tau - \theta_{\zeta}^\tau}{d\tau} \right) + \frac{(1-\zeta)^4}{(R^\tau)^2} \frac{(\theta_{\zeta+d\zeta}^\tau - 2\theta_{\zeta}^\tau + \theta_{\zeta-d\zeta}^\tau)}{d\zeta^2} \\ & + \frac{(\theta_{\zeta+d\zeta}^\tau - \theta_{\zeta-d\zeta}^\tau)}{2d\zeta} \left[-\frac{2(1-\zeta)^3}{(R^\tau)^2} + \frac{2(1-\zeta)^3}{\zeta(R^\tau)^2} \right] \\ & - \frac{\kappa_{SL}}{\kappa_L} \frac{4(1-\zeta)}{R^\tau} \left[\epsilon \frac{(1-\zeta)^3}{4\zeta^2} - \zeta \right] \left(\frac{R^{\tau+d\tau} - R^\tau}{d\tau} \right) \frac{(\theta_{\zeta+d\zeta}^2 - \theta_{\zeta-d\zeta}^\tau)}{2d\zeta}. \end{aligned} \quad (7.37)$$

Incompressibility condition (7.34) evaluated at the new time step:

$$0 = C^{\tau+d\tau} - \epsilon R^{\tau+d\tau} \Delta\theta (1-\zeta)^2 \left[\frac{\kappa_S}{\kappa_{SL}} \frac{\partial(\theta_S)_R^{\tau+d\tau}}{\partial\zeta} \Big|_{\zeta=\frac{1}{2}^-} - \frac{\kappa_L \rho_L}{\kappa_{SL} \rho_S} \frac{\partial(\theta_L)_R^{\tau+d\tau}}{\partial\zeta} \Big|_{\zeta=\frac{1}{2}^+} \right]. \quad (7.38)$$

Boundary condition (7.35) evaluated at the new time step:

$$0 = 4\xi \left(R^{\tau+d\tau} \theta_R^{\tau+d\tau} + 1 \right) + \Delta\theta (1-\zeta)^2 \left[\frac{\kappa_S}{\kappa_{SL}} \frac{\partial(\theta_S)_R^{\tau+d\tau}}{\partial\zeta} \Big|_{\zeta=\frac{1}{2}^-} - \frac{\kappa_L \rho_L}{\kappa_{SL} \rho_S} \frac{\partial(\theta_L)_R^{\tau+d\tau}}{\partial\zeta} \Big|_{\zeta=\frac{1}{2}^+} \right]. \quad (7.39)$$

The Gibbs Thompson condition (7.26):

$$0 = \frac{R^{\tau+d\tau} - R^\tau}{d\tau} + \xi \left(\theta_R^\tau + \frac{1}{R^\tau} \right). \quad (7.40)$$

In the boundary equations (7.39) and (7.40) a one-sided derivative of $\partial\theta/\partial\zeta$ must be used in both the solid phase and the liquid phase. The standard up-wind and down-wind differencing approximations for the first derivative (see [108]) introduce large discretisation errors (i.e. $O(\Delta\zeta)$). Since the surface boundary conditions are sensitive to small changes (as observed by the failure of the Crank-Nicholson method discussed above), a non-standard one-sided finite difference approximation for $\partial\theta/\partial\zeta$ has been derived which has a smaller discretisation error. We can obtain a second order accurate one-sided finite difference scheme to approximate $\partial\theta/\partial\zeta$ by considering a three term Taylor series expansion in θ . Specifically

$$\frac{\partial(\theta_S)_\zeta^{\tau+d\tau}}{\partial\zeta} \Big|_{\zeta=\frac{1}{2}} = \frac{3\theta_{\frac{1}{2}}^{\tau+d\tau} - 4\theta_{\frac{1}{2}-d\zeta}^{\tau+d\tau} + \theta_{\frac{1}{2}-2d\zeta}^{\tau+d\tau}}{2d\zeta} + O([d\zeta]^2), \quad (7.41)$$

and

$$\frac{\partial(\theta_L)_\zeta^{\tau+d\tau}}{\partial\zeta} \Big|_{\zeta=\frac{1}{2}} = \frac{-3\theta_{\frac{1}{2}}^{\tau+d\tau} + 4\theta_{\frac{1}{2}+d\zeta}^{\tau+d\tau} - \theta_{\frac{1}{2}+2d\zeta}^{\tau+d\tau}}{2d\zeta} + O([d\zeta]^2). \quad (7.42)$$

Equations (7.41) and (7.42) are used in the discretisation of the interfacial boundary conditions (7.38) and (7.39).

7.6 Boundary conditions

The temperature equations (7.36) and (7.37) must be solved on the boundaries $\zeta = 0$ and $\zeta = 1$ respectively. At the origin and in the far field, the Neumann boundary conditions

$$\lim_{\zeta \rightarrow 0} \frac{\partial \theta}{\partial \zeta} = 0 \quad \text{and} \quad \lim_{\zeta \rightarrow \infty} \frac{\partial \theta}{\partial \zeta} = 0,$$

are used. When evaluating equation (7.33) at the origin where $\bar{\zeta} = 0$ special treatment is required for the final term on the right hand side. Since the numerator and denominator both vanish on $\bar{\zeta} = 0$, L'Hôpital's rule can be used to write

$$\frac{2(1-\zeta)^3}{(R)^2\zeta} (\theta_S)_\zeta \quad \text{on} \quad \zeta = 0,$$

as

$$\frac{4}{(R^\tau)^2} \frac{\theta_{d\zeta}^\tau - \theta_0^\tau}{(d\zeta)^2}.$$

Therefore on $\zeta = 0$ equation (7.33) becomes

$$0 = -4 \frac{\kappa_{SL}}{\kappa_S} \left(\frac{\theta_0^{\tau+d\tau} - \theta_0^\tau}{d\tau} \right) + \frac{6}{(R^\tau)^2} \frac{\theta_{d\zeta}^\tau - \theta_0^\tau}{(d\zeta)^2}, \quad (7.43)$$

where fictitious points have been removed using the central difference approximation for the Neumann derivative boundary condition on $\zeta = 0$.

No special treatment is required to evaluate equation (7.32) on $\zeta = 1$, which yields

$$-4 \frac{\kappa_{SL}}{\kappa_L} \left(\frac{\theta_1^{\tau+d\tau} - \theta_1^\tau}{d\tau} \right) = 0. \quad (7.44)$$

7.7 Method of solution

The system of equations (7.36), (7.37), (7.38), (7.39) and (7.40) with boundary conditions (7.43) and (7.44) cannot be solved using an explicit method since there is no order in which the system of equations can be solved explicitly at each new time step. Therefore an implicit solution method was adopted, using Newton iteration [29] at each time step.

Firstly the normalised non-dimensional temperature $\bar{\theta}$ was everywhere set equal to -1 , corresponding to a non-dimensional super-cooling of $\Delta\theta$. Growth was initiated by setting the initial position of the interface $\bar{R}(0)$ to $1 + \delta$ where $\delta \ll 1$ (i.e. $R(0) = (1 + \delta) \times R^*$) and the velocity to zero by letting the unknown flow parameter $\bar{C}(0) = 0$. To solve the system (7.36), (7.37), (7.38), (7.39) and (7.40) with boundary conditions (7.43) and (7.44) using Newton's method it was written in terms of an $(n + 3)$ -vector ζ satisfying the system

$$\mathbf{F}(\zeta) = \mathbf{0} \quad (7.45)$$

where n denotes the number of grid points in ζ between 0 and 1.

In equation (7.45) $F_i(\zeta)$ denotes:

i	Equation
1	the temperature equation (7.43) on $r = 0$ (when $\zeta = 0$)
2 ... $n/2$	the temperature equation (7.36) in the solid phase when $\zeta = (i - 1)\Delta\zeta$
$n/2 + 1$	the latent heat - Gibbs-Thompson boundary condition (7.39) when $\zeta = (n/2) \times \Delta\zeta = 1/2$
$n/2 + 2$... $n - 1$	the temperature equation (7.37) in the liquid phase when $\zeta = (i - 1)\Delta\zeta$
n	the temperature equation (7.44) as $r \rightarrow \infty$ (when $\zeta = 1$)
$n + 2$	the Gibbs-Thompson boundary condition (7.40) when $\zeta = (n/2) \times \Delta\zeta = 1/2$
$n + 3$	the mass balance - latent heat boundary condition (7.38) when $\zeta = (n/2) \times \Delta\zeta = 1/2$

From the Taylor expansion [120] of \mathbf{F} the i th component function F_i satisfies

$$F_i(\mathbf{x} + \mathbf{h}) = F_i(\mathbf{x}) + \left[\nabla F_i(\mathbf{x}) \right]^T \mathbf{h} + O(|\mathbf{h}|^2)$$

when F_i has continuous first and second partial derivatives. Therefore

$$\mathbf{F}(\mathbf{x} + \mathbf{h}) = \mathbf{F}(\mathbf{x}) + \mathbf{J}(\mathbf{x})\mathbf{h} + O(|\mathbf{h}|^2)$$

where $\mathbf{J}(\mathbf{x})$ is the Jacobian matrix of \mathbf{F} at \mathbf{x} which is given by

$$\mathbf{J}(\mathbf{x}) = \left(\frac{\partial F_i}{\partial x_j} \right)_{i,j=1}^n.$$

Now the linearised equation for the correction vector \mathbf{h} can be solved from

$$\mathbf{J}(\mathbf{x})\mathbf{h} = \mathbf{F}(\mathbf{x} + \mathbf{h}) - \mathbf{F}(\mathbf{x})$$

using Gaussian elimination. The new approximation to the vector ζ is then given as

$$\mathbf{x}^{\text{new}} = \mathbf{x} + \alpha\mathbf{h}$$

where α is a relaxation parameter. For the problem considered in this chapter the Newton method did not require relaxation and therefore $\alpha = 1$. This procedure was repeated until the 2-norm of $\mathbf{F}(\mathbf{x})$ was less than a specified tolerance of 10^{-7} . The Jacobian was re-calculated at each stage since the number of row operations required to solve the system by Gaussian elimination was minimal.

To make an accurate guess of each variable at every position step at the next time level, a spline was fitted over the previous time steps. A quadratic spline was found to obtain more than sufficient accuracy.

Despite the use of an implicit solution method the explicit forward time, centre space finite difference scheme required that the usual time step constraint for an explicit scheme was adopted, namely

$$\Delta\tau = \beta(\Delta\zeta)^2, \quad (7.46)$$

where $\beta \leq 1$ is the relaxation coefficient. Solutions could be obtained for values of β close to 1 and $\beta = 0.75$ was used to evaluate the results in the following section.

7.8 Results and discussion

The parameter values for white phosphorus were used and are shown in Table 1.1. The coefficients for white phosphorus (P_4) and water shown in this table are given in [69] and [95].

<i>substance :</i>		P_4	H_2O
$L\rho/c$	$^{\circ}C$	25.4	80
$A \left(= 2\sigma T_m c / (L\rho)^2 \right)$	cm	5.5×10^{-7}	6.5×10^{-8}
κ	cm^2/sec	1.5×10^{-3}	1.35×10^{-3}
ξ/μ	$sec-^{\circ}C/cm$	2.3×10^{-3}	9.7×10^{-4}
T_m	$^{\circ}C$	44.31	0

Table 1: Values of relevant physical constants given in [69] and [95].

The results obtained for the normalised growth rate-time curves, using the model described in this chapter were compared to the results in [95] by equating the densities of the solid and liquid phases. Growth was initiated by setting $R(0) = (1 + \delta)R^*$ where $\delta = 0.001$ (i.e. a 0.1% increment on the critical radius) as in [95]. However, the temperature profiles were obtained by initially setting $\delta = 0.1$.

The accuracy of the results obtained from the model described in this chapter is dependent on the number of grid points (n) used in the position variable ζ . Results could be achieved with less than $n = 50$ points, and figure 7.3 displays the maximum percentage change between equivalent temperature profiles when n is increased from 50 to 100, 100 to 150 and 150 to 200. These results were obtained for the three data sets: $\Delta\theta = 0.1$, $\rho_S = \rho_L = 1.823 \text{ g/cm}^3$, and

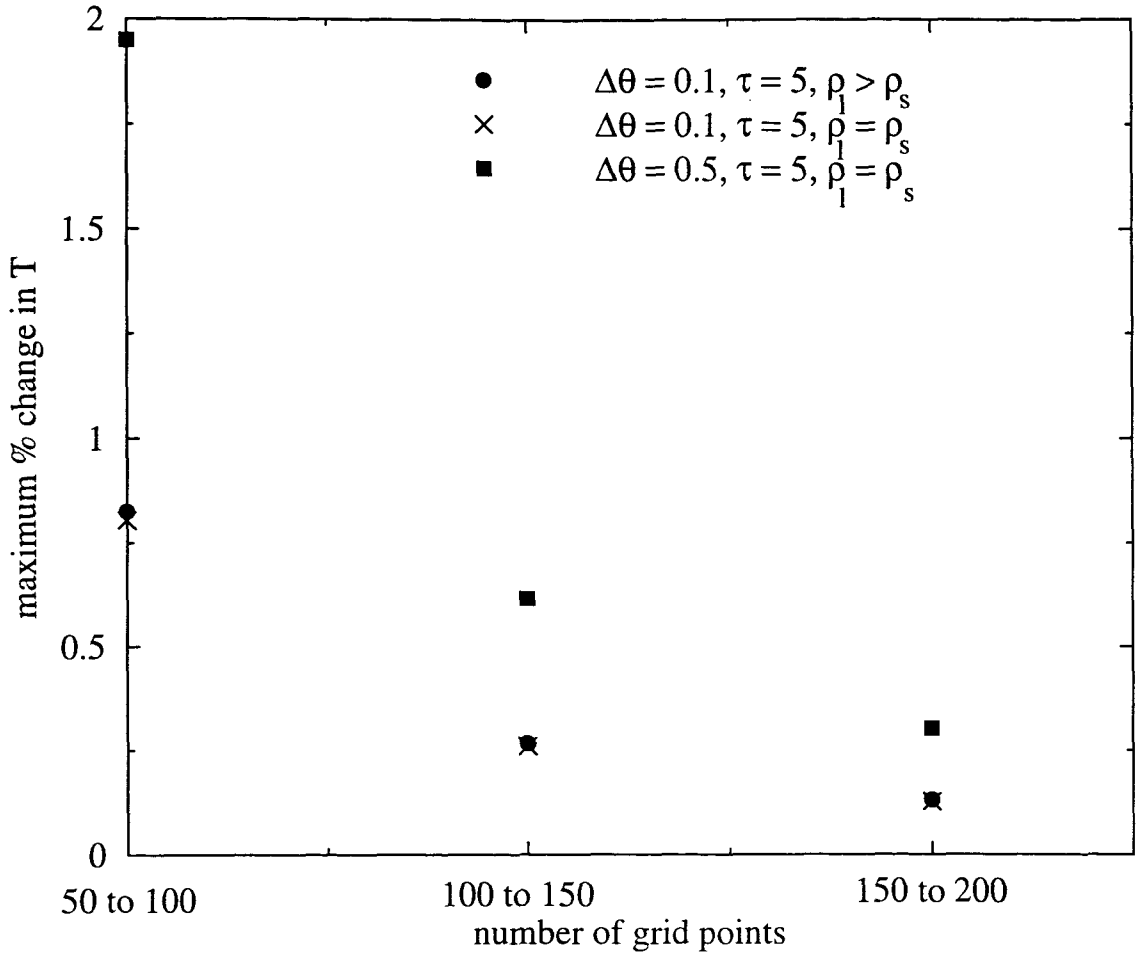


Figure 7.3: Maximum percentage change in the temperature profiles at time $\tau = 5$ and $\mu = 500 \text{ cm/sec } ^\circ\text{C}$ when n , the number of grid points in ζ , is increased, for the three data sets: $\Delta\theta = 0.1, \rho_S = \rho_L = 1.823 \text{ g/cm}^3$, and $\Delta\theta = 0.1, \rho_S = 1.823 \text{ g/cm}^3, \rho_L = 2.026 \text{ g/cm}^3$, and $\Delta\theta = 0.5, \rho_S = \rho_L = 1.823 \text{ g/cm}^3$.

$\Delta\theta = 0.1$, $\rho_S = 1.823 \text{ g/cm}^3$, $\rho_L = 2.026 \text{ g/cm}^3$, and $\Delta\theta = 0.5$, $\rho_S = \rho_L = 1.823 \text{ g/cm}^3$ when time $\tau = 5$ and $\mu = 500 \text{ cm/sec } ^\circ\text{C}$.

Figure 7.3 clearly shows that at time $\tau = 5$ and $\mu = 500 \text{ cm/sec } ^\circ\text{C}$ the maximum percentage change reduces with the number of grid points and the super-cooling $\Delta\theta$. The maximum percentage change for all three data sets at any point in the temperature profile is less than 0.5% when the number of grid points is increased from $n = 150$ to $n = 200$. If we assume that the exact solution is obtained when $n = 200$, then

$$T_n^i = T_{200}^i + A \left(\frac{1}{n}\right)^\alpha \quad (7.47)$$

where T_n^i is the temperature at $\zeta = i\Delta\zeta$ using a grid of $n < 200$ points, T_{200}^i is the temperature at $\zeta = i\Delta\zeta$ using a grid of $n = 200$ points, A is a constant and α is the order of the discretisation error. A value of $\alpha \approx 2$ is expected, since we have used forward time (with a time step restriction given by equation (7.46)) and central space finite differences. Taking the natural log of (7.47) yields

$$\ln(T_n^i - T_{200}^i) = \ln A + \alpha \ln\left(\frac{1}{n}\right) \quad (7.48)$$

which we can evaluate point-wise or by using the 2-norm via

$$\ln \left\{ \left[\sum_{i=1}^n (T_n^i - T_{200}^i)^2 \right]^{\frac{1}{2}} \right\} = \ln A + \alpha \ln\left(\frac{1}{n}\right) \quad (7.49)$$

at $n = 50, 100$ and 150 . Figure 7.4 displays equation (7.49) evaluated at these three points. The solid line in the figure is a linear regression curve which was fitted using the plotting package XMGR. From this curve values of $\alpha = 1.995$ and $\ln A = 4.798$ were obtained. As expected the error of the discrete finite difference scheme, outlined in section 7.5, is approximately second order in $\Delta\zeta$. Therefore using $n = 200$ the discretisation error estimate in the temperature profile is $O(10^{-3})$. (Evaluating equation (7.48) point-wise, thereby evaluating three values of α^i at every coincident grid point, and averaging these values gave $\alpha_{\text{average}} = 2.33$.) All the results displayed in the remaining figures in this chapter use $n = 200$ grid points in ζ .

Figure 7.5 displays growth rate curves, as functions of time, of a spherical nucleus growing into a melt with super-cooling $\Delta\theta = 0.5$, when the linear kinetic coefficient $\mu = 500, 200, 100$ and $50 \text{ cm/sec } ^\circ\text{C}$ and $\rho_S = \rho_L$. The dots, crosses, pluses and squares on this figure denote values of the Green's-function solution discussed in [95] when $\mu = 500, 200, 100$ and $50 \text{ cm/sec } ^\circ\text{C}$ respectively. These points were obtained from an enlargement of a graph shown in [95] and are therefore not exact. However figure 7.5 clearly shows close agreement with the corresponding figure in [95]. After passing through a maximum the growth rate decays, and at large time resembles $t^{-1/2}$, the similarity solution behaviour (observed in [23]) when kinetic and curvature effects are not important.

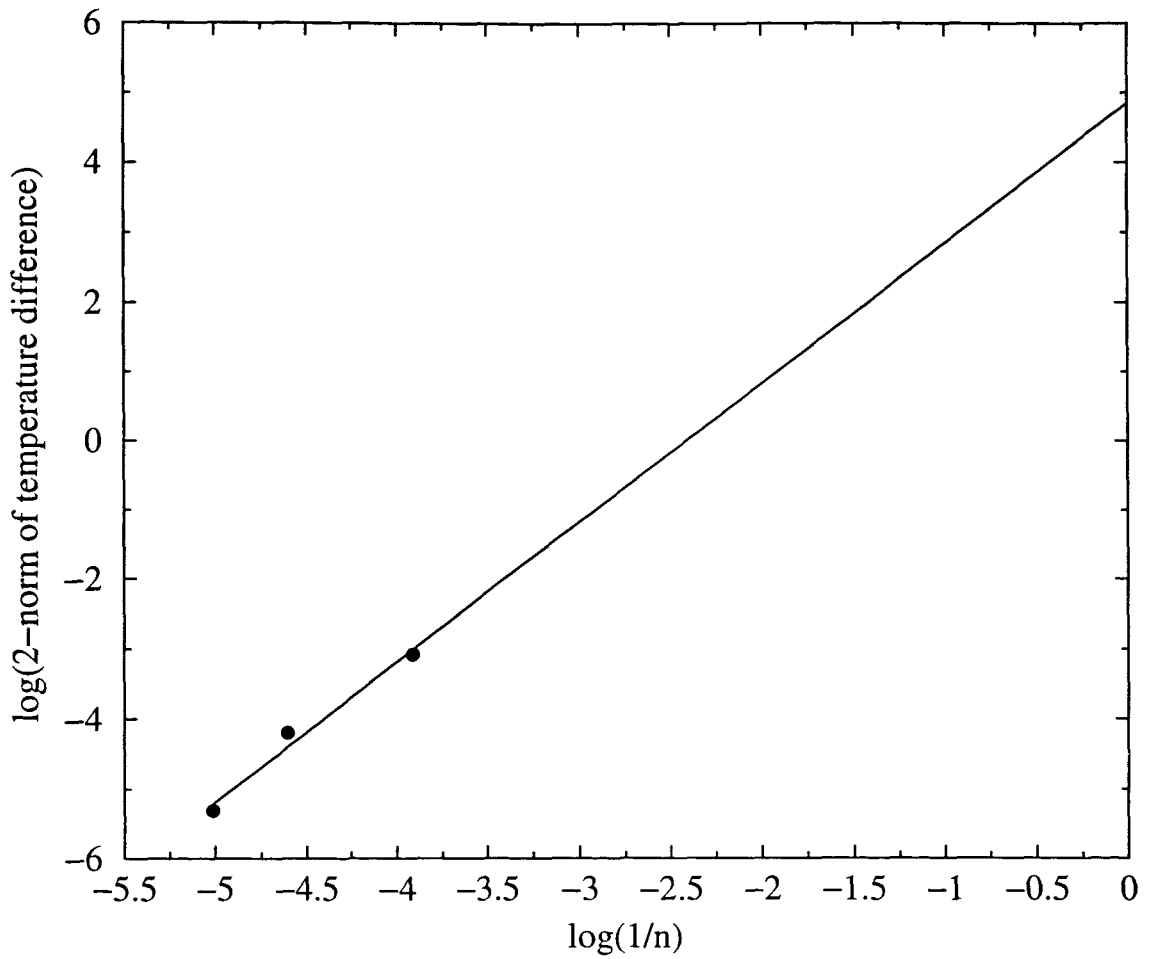


Figure 7.4: A linear regression curve is fitted to the data points obtained using equation (7.49) with $n = 50, 100$ and 150 to find an estimate for the order of the error in the discrete finite difference scheme when $\tau = 5$, $\mu = 500 \text{ cm/sec } ^\circ\text{C}$, $\rho_S = \rho_L = 1.823 \text{ g/cm}^3$ and $\Delta\theta = 0.5$.

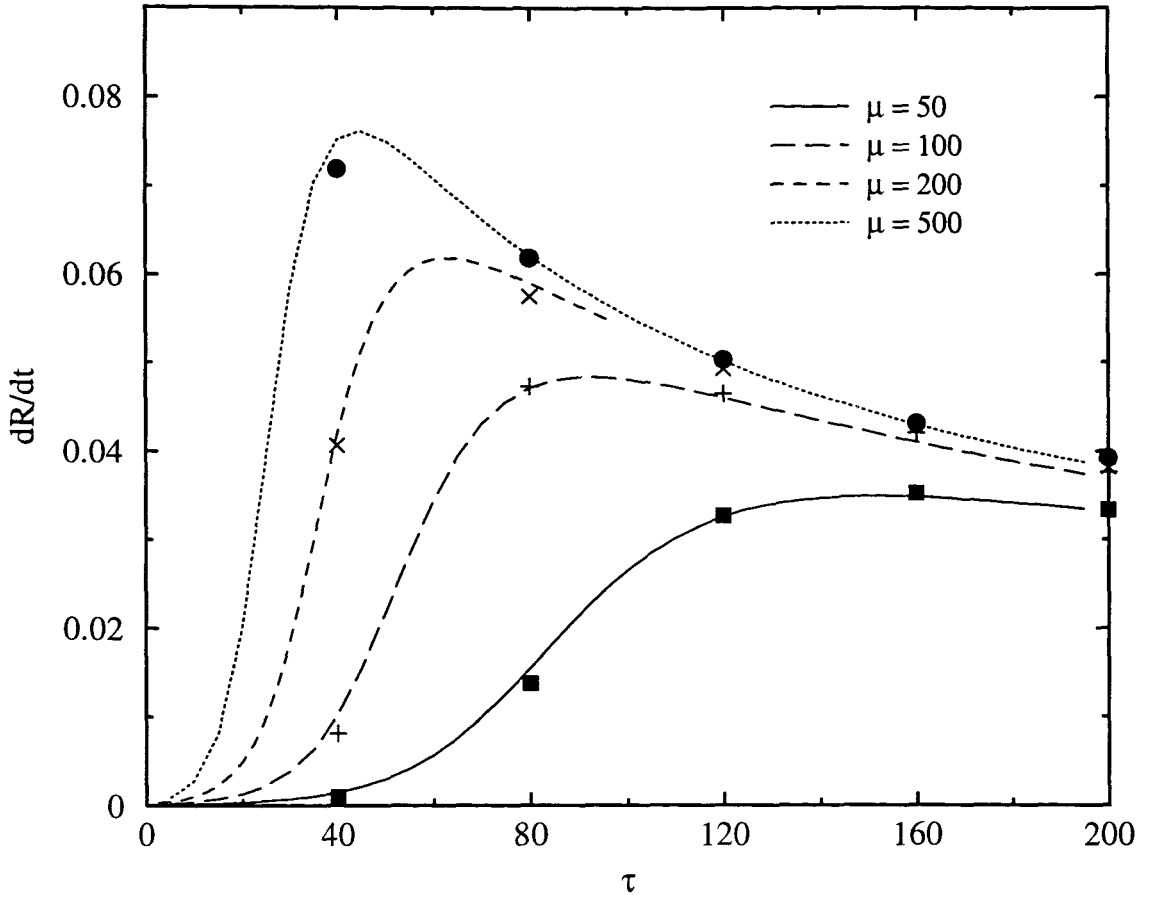


Figure 7.5: Normalised growth rate-time curves for bath with super-cooling $\Delta\theta = 0.5$ when $\mu = 500, 200, 100$ and $50 \text{ cm/sec } ^\circ\text{C}$. The corresponding values of the Green's-function solution in [95] are denoted by \bullet , \times , $+$ and \blacksquare respectively. The initial radius $R(0) = 1.001R^*$.

Flow is introduced into the problem by setting $\rho_S \neq \rho_L$. Since this problem is driven by the interfacial boundary conditions, the effect of the hydrodynamics on the system is difficult to compare with figure 7.5 (where the velocity in the liquid phase is zero) if the thermal conductivities k_L and k_S change with the density. This can be clearly seen by inspection of the coefficients in front of the temperature derivatives on the left hand side of the latent heat boundary condition (7.13). Also, and more importantly, in chapter 9 the model described in this chapter will be compared with a phase-field model which assumes that the thermal conductivity remains constant. The density, thermal diffusivity and thermal conductivity are linked via the relation

$$k = \kappa \rho c$$

where c is the specific heat (which is assumed constant). It follows that if k is kept fixed as ρ is changed, then κ must also change. Therefore, we proceed to rescale κ_S and κ_L by adopting the following two conditions:

- the average thermal diffusivity remains constant,
where $\kappa_{SL} = \frac{1}{2}(\kappa_S + \kappa_L) = 1.5 \times 10^{-3} \text{ cm}^2/\text{sec}$ (the value of κ given in table 1),
- $k_S = \kappa_S \rho_S c = \kappa_L \rho_L c = k_L$.

These two conditions require that

$$\kappa_L = 2\kappa_{SL} \frac{\rho_S}{\rho_L + \rho_S} \quad \text{and} \quad \kappa_S = 2\kappa_{SL} \frac{\rho_L}{\rho_L + \rho_S}$$

where the constant average thermal diffusivity κ_{SL} is given above. Figure 7.6 shows the comparison between growth rates of spherical nuclei growing in a melt with super-cooling $\Delta\theta = 0.5$ when the linear kinetic coefficient $\mu = 500 \text{ cm}/\text{sec} \text{ } ^\circ\text{C}$ and $\mu = 50 \text{ cm}/\text{sec} \text{ } ^\circ\text{C}$. Again growth was initiated by setting the initial radius to 0.1% above the critical radius. Figure 7.7 shows the equivalent growth rates with a smaller super-cooling of $\Delta\theta = 0.1$. The solid lines in figures 7.6 and 7.7 show the case described in figure 7.5 where $\rho_L = \rho_S = 1.823 \text{ g}/\text{cm}^3$ (the density of (solid) white phosphorus given in [69]) and therefore from (7.11) $\epsilon = (\rho_L - \rho_S)/\rho_L = 0$. The upper dashed lines show the case where $\rho_L = 2.026 \text{ g}/\text{cm}^3$ and $\rho_S = 1.823 \text{ g}/\text{cm}^3$ and therefore $\epsilon = (\rho_L - \rho_S)/\rho_L = 0.1$. The lower dashed lines show the case where $\rho_L = 1.657 \text{ g}/\text{cm}^3$ and $\rho_S = 1.823 \text{ g}/\text{cm}^3$ and therefore $\epsilon = (\rho_L - \rho_S)/\rho_L = -0.1$. As expected, in figures 7.6 and 7.7 the velocity of the interface is reduced when ϵ is negative, since the flow in the liquid is inwards towards the solid phase when the density of the solid is less than the density of the liquid and consequently heat transfer from the interface is also reduced. On the other hand when ϵ is positive (as for water) the liquid phase is flowing away from the solid phase and the velocity of the interface increases. Note that the disparity between the density of the solid phase and the density of the liquid phase must be large to obtain a significant difference between the velocity of the interface when $\epsilon \neq 0$ and the corresponding velocity when $\epsilon = 0$. Comparing figures 7.6 and 7.7 we observe that the

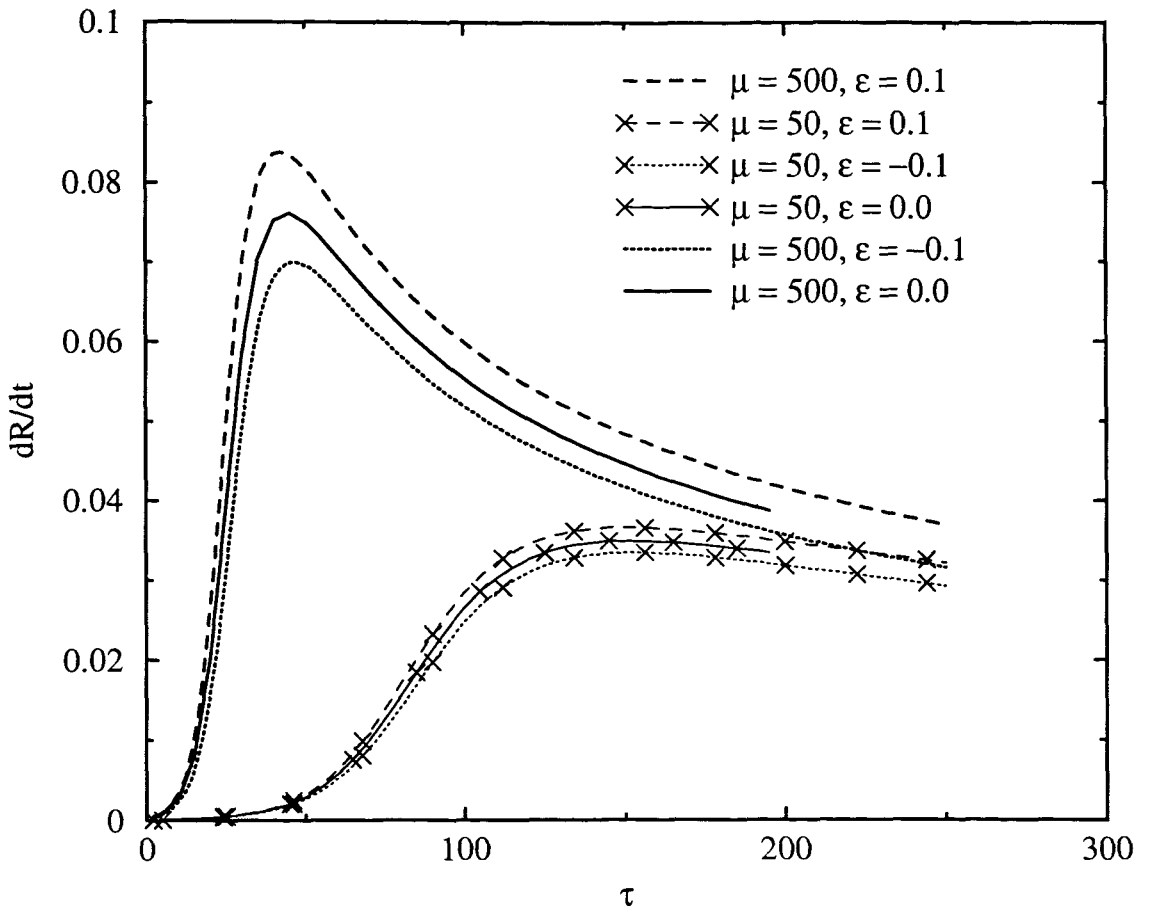


Figure 7.6: Normalised growth rate-time curves for bath with super-cooling $\Delta\theta = 0.5$, $\mu = 50$ and $500 \text{ cm/sec } ^\circ\text{C}$, and $R(0) = 1.001 \times R^*$, when $\epsilon = -0.1, 0.0$ and 0.1 .

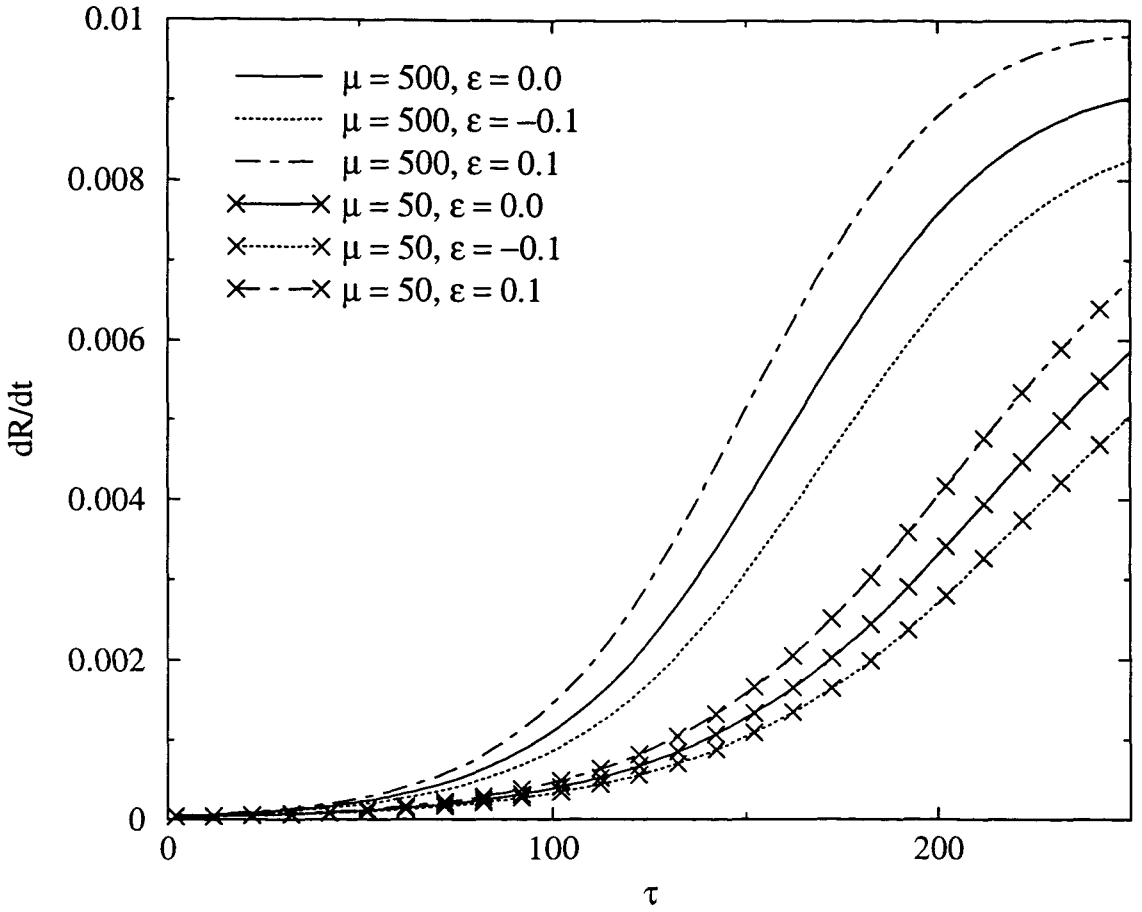


Figure 7.7: Normalised growth rate-time curves for bath with super-cooling $\Delta\theta = 0.1$, $\mu = 50$ and $500 \text{ cm/sec } ^\circ\text{C}$, and $R(0) = 1.001 \times R^*$, when $\epsilon = -0.1, 0.0$ and 0.1 .

velocity of the interface is greatly reduced when the super-cooling is small. In figure 7.7 dR/dt reaches a maximum at a much later time τ than the maximum value reached in figure 7.6 (when $\tau \approx 45$). Further, the maximum value of dR/dt and the difference between the velocity of the interface when $\epsilon = \pm 0.1$ and $\epsilon = 0.0$ is smaller in figure 7.7, when $\Delta\theta = 0.1$, than in figure 7.6, when $\Delta\theta = 0.5$.

We now consider the temperature profiles at successive time levels when $\Delta\theta = 0.5$ and $\Delta\theta = 0.1$. Figure 7.8 shows the temperature profiles when $\epsilon = -0.1, 0.0$ and 0.1 as a function of the radial co-ordinate r , when the super-cooling $\Delta\theta = 0.5$ and the linear kinetic coefficient $\mu = 500 \text{ cm/sec } ^\circ\text{C}$ at times $\tau = 5, 10, 15, 20, 25, 30, 35$ and 40 . Figure 7.9 shows the corresponding temperature profiles when the super-cooling $\Delta\theta = 0.1$. Initially the normalised non-dimensional temperature $\bar{\theta} = -1$ everywhere, corresponding to an initial super-cooling, $\Delta\theta$, of 0.5 in figure 7.8 and 0.1 in figure 7.9. In these figures growth was initiated by setting the radius at $\tau = 0$ to 10% above the critical radius (i.e. $R(0) = (1 + \delta) \times R^*$ where $\delta = 0.1$). Increasing the initial radius of the solid phase will increase the velocity of the interface obtained in figures 7.6 and 7.7 when $\delta = 0.001$. Consequently the difference between the temperature profiles with and without flow will increase.

The upper dashed lines in figures 7.8 and 7.7 show the temperature profiles when $\rho_L = 2.026 \text{ g/cm}^3$ and $\rho_S = 1.823 \text{ g/cm}^3$ and therefore $\epsilon = 0.1$. The lower dotted lines show the temperature profiles at successive time levels when $\rho_L = 1.657 \text{ g/cm}^3$ and $\rho_S = 1.823 \text{ g/cm}^3$ and therefore $\epsilon = -0.1$. As we discussed previously, when $\epsilon < 0$ the velocity in the liquid phase is inward (i.e. towards the solid phase) and the temperature profiles are lower, and when $\epsilon > 0$ the velocity in the liquid phase is outward (i.e. away from the solid phase) and the temperature profiles are therefore higher.

The difference between the temperature profiles in figures 7.8 and 7.9 when $\epsilon = -0.1, 0$ and 0.1 is small when τ is small. This is expected however since, from equation (7.10), the flow in the liquid phase is given by $\epsilon \times dR/dt$ and figure 7.5 shows that when τ is small dR/dt is vanishingly small, even when (as in this case) the linear kinetic coefficient μ is unrealistically large. (In their paper [95] Schaefer and Glicksman commented that an approximate realistic value for μ is $17 \text{ cm/sec } ^\circ\text{C}$.) As expected the difference between the temperature profiles when $\epsilon = -0.1, 0.0$ and 0.1 in figure 7.9, where $\Delta\theta = 0.1$, is greatly reduced when compared to the difference between these profiles shown in figure 7.8, where $\Delta\theta = 0.5$.

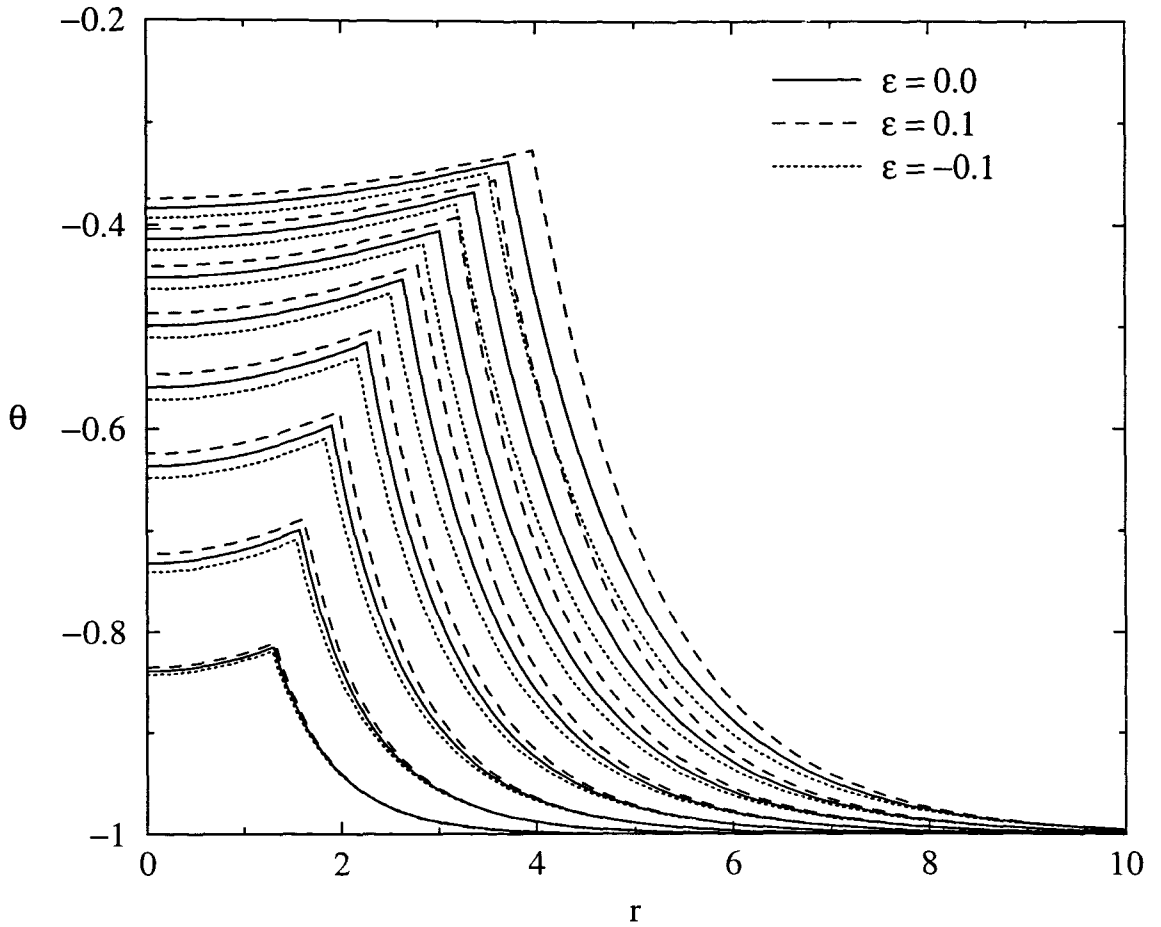


Figure 7.8: Temperature profiles with and without flow at times $\tau = 5, 10, 15, 20, 25, 30, 35$ and 40 , as a function of the radial co-ordinate r when the super-cooling $\Delta\theta = 0.5$, $\mu = 500 \text{ cm/sec } ^\circ\text{C}$ and $R(0) = 1.1 \times R^*$ for different values of ϵ .

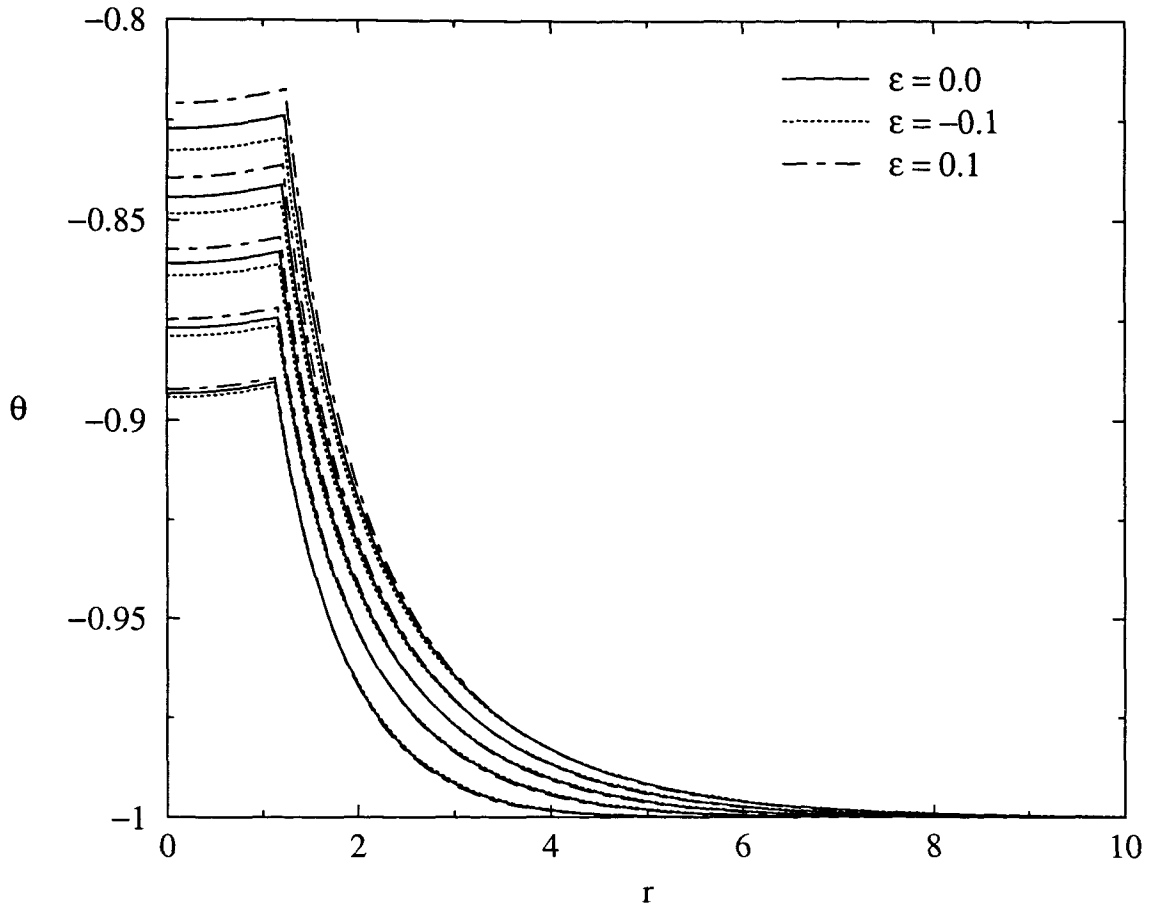


Figure 7.9: Temperature profiles with and without flow at times $\tau = 5, 10, 15, 20$ and 25 , as a function of the radial co-ordinate r when the super-cooling $\Delta\theta = 0.1$, $\mu = 500 \text{ cm/sec } ^\circ\text{C}$ and $R(0) = 1.1 \times R^*$ when $\epsilon = 0.1, 0.0$ and -0.1 .

Chapter 8

Sharp interface limit of the phase-field equations due to Anderson, McFadden and Wheeler

8.1 Introduction

In this chapter we consider the sharp interface limit of the phase-field model recently devised by Anderson, McFadden and Wheeler [2], which includes convection in the liquid phase. This model combines the thermodynamically-consistent framework in a previous paper by Wang *et al.* [129] with the phase-field approach devised by Langer, Collins and Levine and others [66]. We compare the one-dimensional form of this model to the sharp interface limit including flow described in chapter 7 (an extension to the work of Schaefer and Glicksman in [95]). In this chapter, however, we initially dispense with the density difference between the solid and liquid phases (and thereby convection in the liquid phase) before considering the one-dimensional form of the complete phase-field system ([2]). In this thesis the surface energy in the model described in [2] is assumed to be isotropic since we are considering growth of a spherical solid crystal. First, the appropriate non-dimensionalisations of Schaefer and Glicksman [95] are used to compare this model with the sharp-interface Stefan model described in the previous chapter. Then, using the method of Caginalp [16], the model described in this chapter is shown to be equivalent to the sharp interface model in the sharp interface limit. Once the non-dimensional parameters associated with the no-flow case of [2] have been determined in terms of the material parameters, a sharp interface analysis of the full model of Anderson, McFadden and Wheeler [2] is considered.

8.2 Asymptotic limit of phase-field equations without flow

The simplified form of the one-dimensional phase-field equations of Anderson, McFadden and Wheeler [2], with the gradient energy coefficient ϵ_E set to zero (i.e. $\epsilon_F^2 = T\epsilon_S^2$ rather than $\epsilon_F^2 = T\epsilon_S^2 + \epsilon_E^2$), equal solid and liquid densities and an isotropic surface free energy are

$$M\phi_t = \epsilon_F^2 \nabla^2 \phi - \rho e_\phi \quad (8.1)$$

and

$$\rho e_t = k \nabla^2 T, \quad (8.2)$$

where $T, \phi, t, \epsilon_F, \rho, k$ and e denote temperature, phase-field variable, time, gradient free energy Helmholtz coefficient, density, thermal conductivity and internal energy density respectively. The constant M is related to the mobility. The phase field variable ϕ is given by $\phi = 0$ in the liquid phase and $\phi = 1$ in the solid phase.

The internal energy density (per unit mass), e , is assumed to have the form

$$e = e_0 + c(T - T_m) - r(\phi)L + \frac{1}{4} \left[\frac{1}{a_S} + \frac{1}{a} \right] H(\phi) - \frac{p_0}{\rho}, \quad (8.3)$$

where e_0, c, L, T_m and p_0 denote a reference energy, heat capacity, latent heat (all per unit mass), melting temperature and pressure. The quantities a_S and a are positive constants; $1/a_S$ and $1/a$ represent the height of the entropy and the free energy double well potentials respectively. The function $r(\phi)$ is a smooth monotonic function which satisfies $r(0) = 0$ and $r(1) = 1$ and in [2] Anderson, McFadden and Wheeler assume it to have the form

$$r(\phi) = \phi^2(3 - 2\phi). \quad (8.4)$$

The function $H(\phi)$ is the double-well potential given in [2] by

$$H(\phi) = \phi^2(1 - \phi)^2 \quad (8.5)$$

and it is also noted from [2] that

$$\left. \frac{\partial e}{\partial \phi} \right|_{s,\rho} = \left. \frac{\partial g}{\partial \phi} \right|_{p,T},$$

where

$$g(T, p, \phi) = g_0(T, \phi) + \frac{(p - p_0)}{\rho},$$

and

$$g_0(T, \phi) = \left[e_0 - cT_m - r(\phi)L + \frac{1}{4a_S} H(\phi) \right] \left(1 - \frac{T}{T_m} \right) - cT \ln \left(\frac{T}{T_m} \right) + \frac{1}{4a} H(\phi).$$

Hence (8.1) can be written as

$$M\phi_t = \epsilon_F^2 \nabla^2 \phi - \rho g_\phi. \quad (8.6)$$

Now, it can be clearly seen from the corresponding equation in Wang *et al.* [129] that

$$\rho g_\phi = -TQ(T)p'(\phi) + TG'(\phi), \quad (8.7)$$

where

$$Q(T) = \int_{T_m}^T \frac{L}{\zeta^2} d\zeta = \frac{L(T - T_m)}{TT_m}. \quad (8.8)$$

Since ρg_ϕ can be written as

$$\rho \frac{\partial g}{\partial \phi} \Big|_{p,T} = \rho \left\{ \left[-r'(\phi)L + \frac{H'(\phi)}{4a_S} \right] \left(1 - \frac{T}{T_m} \right) + \frac{1}{4a} H'(\phi) \right\}, \quad (8.9)$$

the functions $p'(\phi)$ and $G'(\phi)$ can be found by comparing equations (8.8) and (8.9) to equation (8.7). Therefore

$$G'(\phi) = \rho \frac{H'(\phi)}{4aT_m}, \quad (8.10)$$

and

$$p'(\phi) = \rho \left\{ -r'(\phi) + \frac{1}{4L} \left(\frac{1}{a_S} + \frac{1}{a} \right) H'(\phi) \right\}. \quad (8.11)$$

Consequently, equation (8.6) can now be written in a similar form to that of Wang *et al.* [129] as

$$\frac{M}{T} \phi_t = \epsilon_S^2 \nabla^2 \phi + Q(T)p'(\phi) - G'(\phi), \quad (8.12)$$

where $\epsilon_F^2 = T\epsilon_S^2$.

Substituting the form of $e(T, \phi, t)$ given in (8.3) into equation (8.2) gives

$$cT_t + \left[\frac{1}{4} \left(\frac{1}{a} + \frac{1}{a_S} \right) H'(\phi) - r'(\phi)L \right] \phi_t = \frac{k}{\rho} \nabla^2 T, \quad (8.13)$$

and further substitution for the functions $H'(\phi)$ and $r'(\phi)$ yields

$$cT_t + \frac{L}{\rho} p'(\phi) \phi_t = \frac{k}{\rho} \nabla^2 T. \quad (8.14)$$

The parameters a and ϵ_S can be related to the thickness of the interface δ and the surface energy σ by considering the steady one-dimensional planar solution to equation (8.12) under equilibrium temperature conditions $T = T_m$. Using these conditions, in one spatial dimension x , equation (8.12) becomes

$$\epsilon_S^2 \frac{d^2 \phi}{dx^2} = G'(\phi), \quad (8.15)$$

with boundary conditions $\phi \rightarrow 0$ in the liquid as $x \rightarrow \infty$ and $\phi \rightarrow 1$ as $x \rightarrow -\infty$ in the solid. The solution to equation (8.15) is

$$\phi(x) = \frac{1}{2} \left[1 - \tanh \left(\frac{x}{2\epsilon_S} \sqrt{\frac{\rho}{2aT_m}} \right) \right], \quad (8.16)$$

and from this solution it is clear that the interface has characteristic thickness

$$\delta = \epsilon_S \sqrt{\frac{aT_m}{\rho}}. \quad (8.17)$$

The surface free energy associated with this one-dimensional solution is calculated from the Helmholtz free energy functional \mathcal{F} [3] at the melting temperature T_m which is given by

$$\mathcal{F} = \mathcal{E} - T_m \mathcal{S} = \int \left[f_v(T_m, \phi) + \frac{1}{2} \epsilon_S^2 T_m \left(\frac{d\phi}{dx} \right)^2 \right] dx \quad (8.18)$$

where $f_v = e_v - s_v T$ defines the Helmholtz free energy density f_v in terms of the internal energy density e_v and the entropy density s_v . Since the form for the internal energy per unit mass, as given in [2], is

$$e(T, p, \phi) = g(T, p, \phi) + T s(T, p, \phi) - \frac{p}{\rho(T, p, \phi)}$$

then

$$\left. \frac{\partial f_v}{\partial \phi} \right|_{p,T} = \left. \frac{\partial}{\partial \phi} (e_v - s_v T) \right|_{p,T} = \left. \frac{\partial}{\partial \phi} (g_v - p) \right|_{p,T} = \left. \frac{\partial g_v}{\partial \phi} \right|_{p,T} = T[Q(T)p'(\phi) + G'(\phi)],$$

and using (8.8) it is clear that $Q(T_m) = 0$ and consequently

$$f_v(T_m, p, \phi) = T_m G(\phi). \quad (8.19)$$

Integrating equation (8.15) with respect to ϕ and then using equation (8.19) gives

$$f_v(T_m, p, \phi) = T_m G(\phi) = \frac{1}{2} T_m \epsilon_S^2 \left(\frac{d\phi}{dx} \right)^2. \quad (8.20)$$

Therefore using equation (8.20) to substitute for f_v in equation (8.18) the corresponding surface free energy per unit area, which is a surface excess quantity because $f(T_m, \phi) = 0$ in the bulk, is given by

$$\sigma = \int_{-\infty}^{+\infty} \epsilon_S^2 T_m \left(\frac{d\phi}{dx} \right)^2 dx, \quad (8.21)$$

since the tangential components are ignored in one dimension. By using equation (8.16) and transforming the range of integration, equation (8.21) can be written as

$$\sigma = \int_0^1 \epsilon_S \phi(1 - \phi) \sqrt{\frac{T_m \rho}{2a}} d\phi,$$

from which it follows that

$$\sigma = \frac{\sqrt{2}\delta\rho}{12a} \quad (8.22)$$

relates the constant a to the thickness of the interface δ and the parameters of the material.

8.2.1 Non-dimensionalisations

Schaefer and Glicksman [95] used the following non-dimensionalisations:

$$\bar{r} = \frac{r}{R^*}, \quad \tau = \frac{4\kappa}{(R^*)^2}t, \quad T = \frac{L\theta}{c}, \quad \frac{d\bar{r}}{d\tau} = \frac{R^*}{4\kappa} \frac{dR}{dt}$$

where R^* and κ denote the radius of a spherical particle which is in equilibrium with the super-cooled melt and the thermal diffusivity respectively. Under these transformations equations (8.12) and (8.14) become

$$\left[\frac{4MT_m a \kappa}{T(R^*)^2 \rho} \right] \phi_\tau = \left[\frac{aT_m \epsilon_S^2}{(R^*)^2 \rho} \right] \bar{\nabla}^2 \phi + aT_m Q(T) \bar{p}'(\phi) - \frac{1}{4} H'(\phi), \quad (8.23)$$

and

$$4[\theta_\tau + \bar{p}'(\phi)\phi_\tau] = \bar{\nabla}^2 \theta, \quad (8.24)$$

where $k = \kappa \rho c$ and $\bar{p}'(\phi) = p'(\phi)/\rho$ is the dimensionless form of the derivative of the function $p(\phi)$. For brevity we have introduced in (8.23) and (8.24) the ordinary differential operator

$$\bar{\nabla}^2 = \partial^2 / \partial \bar{r}^2 + (2/\bar{r}) \partial / \partial \bar{r} \quad (8.25)$$

which we will use subsequently.

It is clear from [16] and [129] that the sharp interface limit can be achieved from the first order perturbation expansion of the phase field model only if the coefficient of the term on the left hand side and the coefficient of the first term on the right hand side of equation (8.23) are both order ϵ_S^2 , whilst the coefficient of $p'(\phi)$ is of order ϵ_S , where ϵ_S is the non-dimensional thickness of the interface. In this chapter ϵ_S is given by

$$\epsilon_S^2 = \frac{\delta^2}{(R^*)^2} = \frac{aT_m \epsilon_S^2}{(R^*)^2 \rho}, \quad (8.26)$$

and consequently the first term on the right hand side of equation (8.23) is clearly of order ϵ_S^2 as required. This equation can now be written as

$$\frac{\epsilon_S^2}{X} \phi_\tau = \epsilon_S^2 \bar{\nabla}^2 \phi + \epsilon_S Y \bar{p}'(\phi) - \frac{1}{4} H'(\phi) \quad (8.27)$$

with

$$X = \frac{\theta \delta^2 \rho}{4M \theta_m a \kappa} \quad (8.28)$$

and

$$Y = \frac{R^* a L (\theta - \theta_m)}{\delta \theta}, \quad (8.29)$$

where θ_m is the non-dimensional melting temperature and both X and Y are assumed¹ to be $O(1)$ as $\epsilon_S \rightarrow 0$. Both X and Y are dependent on the non-dimensional temperature θ and

¹In chapter 9 it will be shown that this assumption is not unreasonable when using the parameter values for white phosphorus shown in chapter 7.

can be written as

$$Y = \bar{Y} \left(\frac{\theta - \theta_m}{\theta} \right) \quad \text{and} \quad X = \bar{X} \frac{\theta}{\theta_m},$$

where

$$\bar{Y} = \frac{R^* a L}{\delta} \quad \text{and} \quad \bar{X} = \frac{\delta^2 \rho}{4 M a \kappa}.$$

The non-dimensional temperature θ is similar in magnitude to the non-dimensional melting temperature θ_m and can therefore be approximated by $\theta = \theta_m(1 + \delta)$ where δ is small. Consequently,

$$\frac{(\theta - \theta_m)}{\theta} \simeq \delta - \delta^2 + \delta^3 - \dots \quad \text{and} \quad \frac{\theta}{\theta_m} = 1 + \delta.$$

So to first order in δ

$$\frac{(\theta - \theta_m)}{\theta} \simeq \frac{1}{\theta_m} (\theta - \theta_m) \tag{8.30}$$

and to leading order in δ

$$\frac{\theta}{\theta_m} = 1.$$

These approximations simplify the asymptotic expansions in the following sections. Without using these simplifications additional terms appear in the Gibbs-Thompson equation.

8.2.2 Perturbation expansion

An asymptotic perturbation expansion of equations (8.24) and (8.27) can now be carried out in the style of Caginalp [16]. Below, the inner and outer expansions are considered separately in one spatial dimension. In the phase field model the mean position of the interface may be specified as

$$\Gamma(t) = \{\bar{r} \in \Omega : \phi(t, \bar{r}) = \frac{1}{2}\}$$

where the material, which can be in either of two phases (namely solid or liquid) occupies a region $\Omega \subset \mathfrak{R}^N$ in space and Γ is regular provided the initial and boundary conditions are smooth. For a sufficiently small neighbourhood around $\Gamma(t)$ we define $r(x, t)$ to be the distance from x to $\Gamma(t)$, r being positive in the liquid, and negative in the solid. Further, in the neighbourhood of Γ

$$|\nabla r| = 1 \quad \text{and} \quad \nabla^2 r = \kappa_c,$$

where κ_c denotes the curvature. Now formally expanding the variables in their original coordinates, the *outer expansion* can be written as

$$\theta(\bar{r}, \tau, \varepsilon_S) = \vartheta^0(r, \tau) + \varepsilon_S \vartheta^1(r, \tau) + \varepsilon_S^2 \vartheta^2(r, \tau) + \dots, \tag{8.31}$$

$$\phi(\bar{r}, \tau, \varepsilon_S) = \varphi^0(r, \tau) + \varepsilon_S \varphi^1(r, \tau) + \varepsilon_S^2 \varphi^2(r, \tau) + \dots, \tag{8.32}$$

where these terms may be discontinuous at $r = 0$ but are smooth for $r \neq 0$. By “stretching out” [128] the r variable, a new variable Z , can be defined as

$$\varepsilon_S Z = r = (\bar{r} - r_I) \quad (8.33)$$

where r_I denotes the position $r_I(\tau) = \bar{r}$ of the solid-liquid interface $\Gamma(t)$. The *inner expansion* can then be written as

$$\theta(\bar{r}, \tau, \varepsilon_S) = \Theta^0(Z, \tau) + \varepsilon_S \Theta^1(Z, \tau) + \varepsilon_S^2 \Theta^2(Z, \tau) + \dots, \quad (8.34)$$

$$\phi(\bar{r}, \tau, \varepsilon_S) = \Phi^0(Z, \tau) + \varepsilon_S \Phi^1(Z, \tau) + \varepsilon_S^2 \Phi^2(Z, \tau) + \dots. \quad (8.35)$$

8.2.3 Outer expansion

Substituting equations (8.31) and (8.32) into the non-dimensionalised phase-field equations (8.24) and (8.27) gives,

$$\begin{aligned} \frac{\varepsilon_S^2}{X} \left(\varphi_\tau^0 + \varepsilon_S \varphi_\tau^1 + \varepsilon_S^2 \varphi_\tau^2 \right) &= \varepsilon_S^2 \left(\bar{\nabla}^2 \varphi^0 + \varepsilon_S \bar{\nabla}^2 \varphi^1 + \varepsilon_S^2 \bar{\nabla}^2 \varphi^2 \right) \\ &+ \varepsilon_S \bar{Y} \frac{1}{\vartheta_m} (\vartheta^0 + \varepsilon_S \vartheta^1 + \varepsilon_S^2 \vartheta^2 - \vartheta_m) \\ &\times \left[\bar{p}'(\varphi^0) + (\varepsilon_S \varphi^1 + \varepsilon_S^2 \varphi^2) \bar{p}''(\varphi^0) + \frac{1}{2} (\varepsilon_S \varphi^1)^2 \bar{p}'''(\varphi^0) \right] \\ &- \frac{1}{4} \left[H'(\varphi^0) + (\varepsilon_S \varphi^1 + \varepsilon_S^2 \varphi^2) H''(\varphi^0) + \frac{1}{2} (\varepsilon_S \varphi^1)^2 H'''(\varphi^0) \right] \\ &+ O(\varepsilon_S^3), \end{aligned} \quad (8.36)$$

and

$$\begin{aligned} \vartheta_\tau^0 + \varepsilon_S \vartheta_\tau^1 + \varepsilon_S^2 \vartheta_\tau^2 \\ + \left[\bar{p}'(\varphi^0) + (\varepsilon_S \varphi^1 + \varepsilon_S^2 \varphi^2) \bar{p}''(\varphi^0) + \frac{1}{2} (\varepsilon_S \varphi^1)^2 \bar{p}'''(\varphi^0) \right] \left(\varphi_\tau^0 + \varepsilon_S \varphi_\tau^1 + \varepsilon_S^2 \varphi_\tau^2 \right) \\ = \frac{1}{4} \left(\bar{\nabla}^2 \vartheta^0 + \varepsilon_S \bar{\nabla}^2 \vartheta^1 + \varepsilon_S^2 \bar{\nabla}^2 \vartheta^2 \right) + O(\varepsilon_S^3), \end{aligned} \quad (8.37)$$

where, in general, the phase-field equation (8.36) will depend on the forms of M and $\bar{p}(\phi)$. At each order of ε_S we find:

$O(1)$:

$$0 = -\frac{1}{4} H'(\varphi^0), \quad (8.38)$$

$$4 \left[\vartheta_\tau^0 + \bar{p}'(\varphi^0) \varphi_\tau^0 \right] = \bar{\nabla}^2 \vartheta^0. \quad (8.39)$$

$O(\varepsilon_S)$:

$$0 = \bar{Y} \left(\frac{\vartheta^0 - \vartheta_m}{\vartheta_m} \right) \bar{p}'(\varphi^0) - \frac{1}{4} \varphi^1 H''(\varphi^0), \quad (8.40)$$

$$4 \left[\vartheta_\tau^1 + \bar{p}'(\varphi^0) \varphi_\tau^1 + \varphi^1 \varphi_\tau^0 \bar{p}''(\varphi^0) \right] = \bar{\nabla}^2 \vartheta^1. \quad (8.41)$$

$O(\varepsilon_S^2)$:

$$\frac{1}{\bar{X}} \varphi_\tau^0 = \bar{\nabla}^2 \varphi^0 + \bar{Y} \left(\frac{\vartheta^0 - \vartheta_m}{\vartheta_m} \right) \varphi^1 \bar{p}''(\varphi^0) + \bar{Y} \frac{\vartheta^1}{\vartheta_m} \bar{p}'(\varphi^0) - \frac{1}{4} \left[\varphi^2 H''(\varphi^0) + \frac{(\varphi^1)^2}{2} H'''(\varphi^0) \right], \quad (8.42)$$

$$4 \left\{ \vartheta_\tau^2 + \bar{p}'(\varphi^0) \varphi_\tau^2 + \bar{p}''(\varphi^0) \varphi^1 \varphi_\tau^1 + \left[\varphi^2 \bar{p}''(\varphi^0) + \frac{(\varphi^1)^2}{2} \bar{p}'''(\varphi^0) \right] \varphi_\tau^0 \right\} = \bar{\nabla}^2 \vartheta^2. \quad (8.43)$$

From the $O(1)$ balance, equation (8.38) implies that $\varphi^0 = 0, 1$ or $1/2$, however $\phi = 1/2$ is unphysical in this context since it is an unstable solution, therefore equation (8.39) reduces to

$$4\vartheta_\tau^0 = \bar{\nabla}^2 \vartheta^0 \quad (8.44)$$

and when re-dimensionalised equation (8.44) becomes the heat diffusion equation

$$T_t^0 = \kappa \nabla^2 T^0. \quad (8.45)$$

8.2.4 Inner expansion

Using the inner stretched coordinate, Z , the Laplacian is given by

$$\bar{\nabla}^2 \theta = \Theta_{\bar{r}\bar{r}} + \bar{\nabla}^2 \bar{r} \Theta_{\bar{r}} = \frac{1}{\varepsilon_S^2} \Theta_{ZZ} + \frac{1}{\varepsilon_S} \bar{\nabla}^2 \bar{r} \Theta_Z + O(1),$$

where $\bar{\nabla}^2$ is given by (8.25) and the time derivative, θ_τ as

$$\theta_\tau = \Theta_\tau - \frac{1}{\varepsilon_S} (r_I)_\tau \Theta_Z.$$

Then substituting equations (8.34) and (8.84) into equations (8.24) and (8.27) gives

$$\begin{aligned} \frac{\varepsilon_S^2}{\bar{X}} \left[\Phi_\tau^0 - \frac{(r_I)_\tau}{\varepsilon_S} \Phi_Z^0 - (r_I)_\tau \Phi_\tau^1 \right] &= \varepsilon_S^2 \left[\frac{\Phi_{ZZ}^0}{\varepsilon_S^2} + \frac{\Phi_{ZZ}^1}{\varepsilon_S} + \Phi_{ZZ}^2 + \frac{\bar{\nabla}^2 r}{\varepsilon_S} \Phi_Z^0 + \bar{\nabla}^2 r \Phi_Z^1 \right] \\ &+ \varepsilon_S \bar{Y} \frac{1}{\Theta_m} (\Theta^0 + \varepsilon_S \Theta^1 + \varepsilon_S^2 \Theta^2 - \Theta_m) \left[\bar{p}'(\Phi^0) + (\varepsilon_S \Phi^1 + \varepsilon_S^2 \Phi^2) \bar{p}''(\Phi^0) \right] \\ &- \frac{1}{4} \left[H'(\Phi^0) + (\varepsilon_S \Phi^1 + \varepsilon_S^2 \Phi^2) H''(\Phi^0) + \frac{1}{2} \varepsilon_S^2 (\Phi^1)^2 H'''(\Phi^0) \right] + O(\varepsilon_S^3) \end{aligned} \quad (8.46)$$

and

$$\begin{aligned} \varepsilon_S^2 \left[\Theta_\tau^0 - \frac{(r_I)_\tau}{\varepsilon_S} \Theta_Z^0 + \varepsilon_S \Theta_\tau^1 - (r_I)_\tau \Theta_Z^1 + \varepsilon_S^2 \Theta_\tau^2 \varepsilon_S (r_I)_\tau \Theta_Z^2 \right] \\ + \varepsilon_S^2 \left[\bar{p}'(\Phi^0) + (\varepsilon_S \Phi^1 + \varepsilon_S^2 \Phi^2) \bar{p}''(\Phi^0) + \frac{1}{2} \varepsilon_S^2 (\Phi^1)^2 \bar{p}'''(\Phi^0) \right] \\ \times \left[\Phi_\tau^0 + \varepsilon_S \Phi_\tau^1 + \varepsilon_S^2 \Phi_\tau^2 - \frac{(r_I)_\tau}{\varepsilon_S} \Phi_Z^0 - (r_I)_\tau \Phi_Z^1 - \varepsilon_S (r_I)_\tau \Phi_Z^2 \right] \\ = \frac{\varepsilon_S^2}{4} \left[\frac{\Theta_{ZZ}^0}{\varepsilon_S^2} + \frac{\Theta_{ZZ}^1}{\varepsilon_S} + \Theta_{ZZ}^2 + \frac{\bar{\nabla}^2 r}{\varepsilon_S} \Theta_Z^0 + \bar{\nabla}^2 r \Theta_Z^1 + \varepsilon_S \bar{\nabla}^2 r \Theta_Z^2 \right] + O(\varepsilon_S^5). \end{aligned} \quad (8.47)$$

At each order of ε_S we obtain

$O(1)$:

$$0 = -\frac{1}{4}H'(\Phi^0) + \Phi_{ZZ}^0, \quad (8.48)$$

$$\Theta_{ZZ}^0 = 0. \quad (8.49)$$

$O(\varepsilon_S)$:

$$-\frac{(r_I)_\tau}{\bar{X}}\Phi_Z^0 = \Phi_{ZZ}^1 + \bar{\nabla}^2 r \Phi_Z^0 + \bar{Y} \left(\frac{\Theta^0 - \Theta_m}{\Theta_m} \right) \bar{p}'(\Phi^0) - \frac{H''(\Phi^0)}{4}\Phi^1, \quad (8.50)$$

$$-4(r_I)_\tau \Theta_Z^0 - 4\bar{p}'(\Phi^0)(r_I)_\tau \Phi_Z^0 = \Theta_{ZZ}^1 + \bar{\nabla}^2 r \Theta_Z^0. \quad (8.51)$$

The general solution to equation (8.49) is

$$\Theta^0 = C_0(\tau)Z + C_1(\tau) \quad (8.52)$$

where C_0 and C_1 are functions of time.

8.2.5 Matching

We require the inner and outer solutions to match for $\varepsilon_S \rightarrow 0$. We first consider the outer and inner expansions of the non-dimensional temperature variable which are given by (8.31) and (8.34) as

$$\theta(\bar{r}, \tau, \varepsilon_S) = \vartheta^0(\bar{r}, \tau) + \varepsilon_S \vartheta^1(\bar{r}, \tau) + \varepsilon_S^2 \vartheta^2(\bar{r}, \tau) + \dots$$

and

$$\Theta(Z, \tau, \varepsilon_S) = \Theta^0(Z, \tau) + \varepsilon_S \Theta^1(Z, \tau) + \varepsilon_S^2 \Theta^2(Z, \tau) + \dots$$

The Van Dyke matching principle [128] states that

$$\begin{aligned} &\text{the } m \text{ term inner expansion (} n \text{ term outer expansion)} = \\ &\text{the } n \text{ term outer expansion (} m \text{ term inner expansion)}. \end{aligned}$$

Therefore taking $m = n = 2$ the 2-term inner expansion is

$$\Theta(Z, \tau, \varepsilon_S) = \Theta^0(Z, \tau) + \varepsilon_S \Theta^1(Z, \tau)$$

and the 2-term outer expansion is

$$\theta(\bar{r}, \tau, \varepsilon_S) = \vartheta^0(\bar{r}, \tau) + \varepsilon_S \vartheta^1(\bar{r}, \tau).$$

Therefore the 2-term inner expansion of the 2-term outer expansion is

$$\begin{aligned} \theta(\bar{r}, \tau, \varepsilon_S) &= \vartheta^0(r_I + \varepsilon_S Z, \tau) + \varepsilon_S \vartheta^1(r_I + \varepsilon_S Z, \tau) \\ &= \left[\vartheta^0(r_I, \tau) + \varepsilon_S Z \frac{\partial \vartheta^0}{\partial \bar{r}}(r_I, \tau) \right] + \varepsilon_S \left[\vartheta^1(r_I, \tau) + \varepsilon_S Z \frac{\partial \vartheta^1}{\partial \bar{r}}(r_I, \tau) \right] \end{aligned}$$

and the 2-term outer expansion of the 2-term inner expansion is

$$\Theta(Z, \tau, \varepsilon_S) = \Theta^0\left(\frac{\bar{r} - r_I}{\varepsilon_S}, \tau\right) + \varepsilon_S \Theta^1\left(\frac{\bar{r} - r_I}{\varepsilon_S}, \tau\right)$$

Therefore we require

$$\begin{aligned} \Theta^0\left(\frac{\bar{r} - r_I}{\varepsilon_S}, \tau\right) + \varepsilon_S \Theta^1\left(\frac{\bar{r} - r_I}{\varepsilon_S}, \tau\right) &= \left[\vartheta^0(r_I, \tau) + \varepsilon_S Z \frac{\partial \vartheta^0}{\partial \bar{r}}(r_I, \tau) \right] \\ &+ \varepsilon_S \left[\vartheta^1(r_I, \tau) + \varepsilon_S Z \frac{\partial \vartheta^1}{\partial \bar{r}}(r_I, \tau) \right], \end{aligned} \quad (8.53)$$

and the first two matching conditions of equation (8.53) are

$O(1)$:

$$\Theta^0(Z, \tau) = \vartheta^0(r_I, \tau) \quad (8.54)$$

$O(\varepsilon_S)$:

$$\Theta^1(Z, \tau) = \vartheta^1(r_I, \tau) + Z \frac{\partial \vartheta^0}{\partial \bar{r}}(r_I, \tau). \quad (8.55)$$

Clearly equation (8.54) shows that the leading order inner and outer solutions must be equal and independent of Z and r as $\varepsilon_S \rightarrow 0$. This condition is only satisfied if $C_0 \equiv 0$ in equation (8.52), hence

$$\Theta^0 = C_1(\tau).$$

A similar matching procedure for the ϕ variable requires that

$$\Phi(\pm\infty, \tau) = \phi(r_I^\pm, \tau) = \begin{cases} 0, & r \rightarrow +\infty \\ 1, & r \rightarrow -\infty, \end{cases}$$

and because Γ is defined by $\phi(0, \tau) = 1/2$ then $\varphi^0(0, \tau) = 1/2$ and $\Phi^0(Z, \tau) = \Phi^0(Z)$. Since $C_0 \equiv 0$ equation (8.51) becomes

$$-4\bar{p}'(\Phi^0)(r_I^0)_\tau \Phi_Z^0 = \Theta_{ZZ}^1$$

which can be integrated to yield

$$\Theta_Z^1 = -4\bar{p}'(\Phi^0)(r_I^0)_\tau + C_2(\tau), \quad (8.56)$$

where C_2 is a function of time. Differentiating equation (8.55) with respect to Z leaves

$$\lim_{Z \rightarrow \infty} \Theta_Z^1(Z, \tau) = \vartheta_r^0(r_I, \tau).$$

Consequently taking the limit of equation (8.56) as $Z \rightarrow 0$ from the liquidus side denoted by Γ_+ , leaves

$$\vartheta_r^0 \Big|_{\Gamma_+} = C_2(\tau) \quad (8.57)$$

and taking the limit of equation (8.56) as $Z \rightarrow 0$ from the solidus side denoted by Γ_- , leaves

$$\vartheta_r^0 \Big|_{\Gamma_-} = 4(r_I)_\tau^0 + C_2(\tau). \quad (8.58)$$

Noting that the dimensionless normal velocity is given by $(r_I)_\tau = \bar{v}^0$ and subtracting equation (8.58) from equation (8.57) leaves

$$\left[\vartheta_r^0 \right] \Big|_{\Gamma_\pm} = -4\bar{v}^0. \quad (8.59)$$

By re-dimensionalising equation (8.59) we obtain

$$k_S(T_S^0)_r - k_L(T_L^0)_r = L\rho \frac{dR}{dt}, \quad (8.60)$$

the well known latent heat condition, described in chapter 7, for the sharp interface Stefan model. Finally we need to obtain an expression for the modified Gibbs-Thompson condition [16] from the phase-field model.

The $O(\varepsilon_S)$ equation (8.50) can be written in the form

$$\mathcal{L}\Phi^1 \equiv \Phi_{ZZ}^1 - \frac{1}{4}H''(\Phi^0)\Phi^1 = -\frac{\bar{v}^0}{\bar{X}}\Phi_Z^0 - \bar{\kappa}_c^0\Phi_Z^0 - \bar{Y}\frac{\Theta^0 - \Theta_m}{\Theta_m}\bar{p}'(\Phi^0).$$

where $\bar{\kappa}_c^0 = \bar{\nabla}^2 r^0$ is the leading order curvature. By considering the theory of adjoint systems (see, amongst others, Boyce and DiPrima [14]) it can be shown that for a solution Φ^1 to exist

$$\int_{-\infty}^{+\infty} \Phi_Z^0 \left[-\bar{Y}\frac{\Theta^0 - \Theta_m}{\Theta_m}\bar{p}'(\Phi^0) - \bar{\kappa}_c^0\Phi_Z^0 - \frac{\bar{v}^0}{\bar{X}}\Phi_Z^0 \right] dZ = 0 \quad (8.61)$$

from which it follows that

$$\frac{\bar{Y}}{\Theta_m}(\Theta^0 - \Theta_m) \left[p(\Phi^0) \right]_{Z=-\infty}^{Z=+\infty} = -\left(\bar{\kappa}_c^0 + \frac{\bar{v}^0}{\bar{X}} \right) \int_{-\infty}^{+\infty} (\Phi_Z^0)^2 dZ, \quad (8.62)$$

where

$$\left[p(\Phi^0) \right]_{Z=-\infty}^{Z=+\infty} = \left[p(\Phi^0) \right]_{\Phi=1}^{\Phi=0} = 1. \quad (8.63)$$

Equation (8.21) states that

$$\sigma = \int_{-\infty}^{+\infty} \epsilon_S^2 T_m(\phi_x)^2 dx,$$

which may be expressed in terms of the inner stretched coordinate as

$$\sigma = \frac{\epsilon_S^2 T_m}{R^* \varepsilon_S} \int_{-\infty}^{+\infty} (\Phi_Z)^2 dZ.$$

We now employ the identity (8.26)

$$\varepsilon_S^2 = \frac{\delta^2}{(R^*)^2} = \frac{aT_m \epsilon_S^2}{(R^*)^2 \rho},$$

and define the quantity σ^0 as the leading order approximation for σ by

$$\sigma^0 = \frac{\epsilon_S^2 T_m}{R^* \epsilon_S} \int_{-\infty}^{+\infty} (\Phi_Z^0)^2 dZ.$$

Therefore, the integral on the right hand side of equation (8.62) may be expressed as

$$\int_{-\infty}^{+\infty} (\Phi_Z^0)^2 dZ = \frac{\sigma^0 a}{\delta \rho} \quad (8.64)$$

and from equations (8.62), (8.63) and (8.64) we obtain

$$\Theta^0 = \Theta_m - \frac{\sigma^0 \Theta_m}{\rho R^* L} \left(\bar{\kappa}_c^0 + \frac{\bar{v}^0}{\bar{X}} \right),$$

which in its dimensional form becomes

$$T = T_m - \left(\frac{\sigma^0 T_m}{\rho L} \right) \kappa_c^0 - \left(\frac{\sigma^0 T_m}{4 \kappa \rho L} \right) \frac{v^0}{\bar{X}}. \quad (8.65)$$

The usual form of the Gibbs-Thompson equation with attachment kinetics [95] is

$$T = T_m - \left(\frac{\sigma T_m}{\rho L} \right) \kappa_c - \left(\frac{1}{\mu} \right) v, \quad (8.66)$$

therefore by comparing equations (8.65) and (8.66) we require that

$$\bar{X} = \frac{\sigma T_m \mu}{4 \kappa \rho L} \quad (8.67)$$

where, from its definition,

$$\begin{aligned} \sigma &= \frac{\epsilon_S^2 T_m}{R^* \epsilon_S} \int_{-\infty}^{+\infty} (\Phi_Z)^2 dZ \\ &= \frac{\epsilon_S^2 T_m}{R^* \epsilon_S} \int_{-\infty}^{+\infty} (\Phi_Z^0)^2 dZ + \frac{\epsilon_S^2 T_m}{R^*} \int_{-\infty}^{+\infty} 2\Phi_Z^0 \Phi_Z^1 dZ + \dots \\ &= \sigma^0 + O(\epsilon_S) \end{aligned}$$

and so to leading order $\sigma = \sigma^0$. Using equation (8.28) the relationship described by equation (8.67) serves to define M in terms of the material parameters.

The first order phase-field problem has now been shown to be equivalent to the sharp interface Modified Stefan Model ² without flow (characterised by the dimensional equations (8.45), (8.60) and (8.65)) in the sharp interface limit. Also the unknown constants in the phase field model of Anderson, McFadden and Wheeler [2] without flow have been related to the sharp interface Stefan model [132] without flow by using the non-dimensionalisations of Schaefer and Glicksman in [95].

²so called by Caginalp in [16].

8.3 Asymptotic limit of phase-field equations with flow

In this section we consider the sharp interface limit of the complete phase-field model of Anderson, McFadden and Wheeler [2] by taking the asymptotic limit of the phase-field equations in one-dimension. The leading order expression of the asymptotic analysis of this model, which includes convection in the liquid phase, is then compared to the sharp interface Modified Stefan Model with flow, which is an extension of the work by Schaefer and Glicksman in [95] (as described in chapter 7). The surface energy in the model described in this chapter is assumed to be isotropic and we use the non-dimensionalisations of Schaefer and Glicksman [95] to compare this model to the sharp-interface Modified Stefan Model with flow which is described in chapter 7.

The simplified form of the one-dimensional phase-field equations of Anderson, McFadden and Wheeler [2], with the gradient energy coefficient ϵ_E set to zero (i.e. $\epsilon_F^2 = T\epsilon_S^2$ rather than $\epsilon_F^2 = T\epsilon_S^2 + \epsilon_E^2$) and an isotropic surface free energy are given by

$$\frac{\partial \rho}{\partial t} + u \frac{\partial \rho}{\partial r} = -\rho \left(\frac{\partial u}{\partial r} + \frac{2}{r} u \right), \quad (8.68)$$

$$\begin{aligned} \rho \left[\frac{\partial u}{\partial t} + u \frac{\partial u}{\partial r} \right] &= -\frac{\partial p}{\partial r} - \frac{\epsilon_F^2}{2} \left\{ \frac{\partial}{\partial r} \left[\left(\frac{\partial \phi}{\partial r} \right)^2 \right] + \frac{2}{r} \left(\frac{\partial \phi}{\partial r} \right)^2 \right\} \\ &+ \frac{\partial}{\partial r} \left\{ 2\mu \frac{\partial u}{\partial r} + \lambda \left(\frac{\partial u}{\partial r} + \frac{2}{r} u \right) \right\} + \frac{2}{r} \left\{ 2\mu \frac{\partial u}{\partial r} + \lambda \left(\frac{\partial u}{\partial r} + \frac{2}{r} u \right) \right\}, \end{aligned} \quad (8.69)$$

$$M \left[\phi_t + u \phi_r \right] = \epsilon_F^2 \left(\frac{\partial^2 \phi}{\partial r^2} + \frac{2}{r} \frac{\partial \phi}{\partial r} \right) - \rho e_\phi \quad (8.70)$$

and

$$\rho [e_t + u e_r] = k \left(\frac{\partial^2 T}{\partial r^2} + \frac{2}{r} \frac{\partial T}{\partial r} \right) + \left[-p - \frac{\epsilon_F^2}{2} \left(\frac{\partial \phi}{\partial r} \right)^2 + 2\mu \frac{\partial u}{\partial r} + \lambda \left(\frac{\partial u}{\partial r} + \frac{2}{r} u \right) \right] \frac{\partial u}{\partial r}, \quad (8.71)$$

where $t, \epsilon_F, \rho, k, p, \mu, \lambda$ and e denote time, gradient free energy Helmholtz coefficient, density, thermal conductivity, pressure, viscosity coefficients and internal energy density respectively, all per unit mass. The temperature and the phase-field variables are denoted by T and ϕ respectively and the quantity M is related to the interface mobility using equations (8.28) and (8.67).

To simplify the problem the term denoting the viscous heating in the energy equation (8.71) namely

$$\left[-p - \frac{\epsilon_F^2}{2} \left(\frac{\partial \phi}{\partial r} \right)^2 + 2\mu \frac{\partial u}{\partial r} + \lambda \left(\frac{\partial u}{\partial r} + \frac{2}{r} u \right) \right] \frac{\partial u}{\partial r}$$

is henceforth ignored, as in many situations its contribution to the heat balance is small. The internal energy density (per unit mass) e is given by (8.3) as

$$e = e_0 + c(T - T_m) - r(\phi)L + \frac{1}{4} \left[\frac{1}{a_S} + \frac{1}{a} \right] H(\phi) - \frac{p_0}{\rho(\phi)},$$

where $r(\phi)$ and $H(\phi)$ are defined by (8.4) and (8.5). The density and dynamic viscosities will be assumed to have the forms

$$\rho(\phi) = \rho_S r(\phi) + \rho_L [1 - r(\phi)] \quad \text{and} \quad \mu(\phi) = \mu_S r(\phi) + \mu_L [1 - r(\phi)],$$

respectively. Anderson, McFadden and Wheeler [2] state that

$$\left. \frac{\partial e}{\partial \phi} \right|_{s,\rho} = \left. \frac{\partial g}{\partial \phi} \right|_{p,T}$$

where

$$g(T, p, \phi) = g_0(T, \phi) + \frac{(p - p_0)}{\rho(\phi)}$$

and

$$g_0(T, \phi) = \left[e_0 - cT_m - r(\phi)L + \frac{1}{4a_S} H(\phi) \right] \left(1 - \frac{T}{T_m} \right) - cT \ln \left(\frac{T}{T_m} \right) + \frac{1}{4a} H(\phi).$$

As we discussed in section 8.2, the phase-field equation (8.70) can be expressed in terms of the functions $p'(\phi)$ and $G'(\phi)$ if we let

$$\begin{aligned} \rho(\phi)g_\phi &= \rho(\phi) \left[-r'(\phi)L + \frac{1}{4a_S} H'(\phi) \right] \left(1 - \frac{T}{T_m} \right) + \frac{1}{4a} \rho(\phi) H'(\phi) - (p - p_0) \frac{\rho'(\phi)}{\rho(\phi)} \\ &= -TQ(T)p'(\phi) + TG'(\phi), \end{aligned} \quad (8.72)$$

where

$$\begin{aligned} Q(T) &= \int_{T_m}^T \frac{L}{\zeta^2} d\zeta = \frac{L(T - T_m)}{TT_m}, \\ p'(\phi) &= -r'(\phi)\rho(\phi) + \frac{\rho(\phi)}{4L} \left(\frac{1}{a_S} + \frac{1}{a} \right) H'(\phi) - (p - p_0) \frac{\rho'(\phi)}{L\rho(\phi)}. \end{aligned} \quad (8.73)$$

and

$$G'(\phi) = \frac{H'(\phi)\rho(\phi)}{4aT_m} - (p - p_0) \frac{\rho'(\phi)}{T_m\rho(\phi)}.$$

The functions $p'(\phi)$ and $G'(\phi)$ are not unique in this context, however by expressing the phase-field equation (8.70) in terms of these functions we can formulate the larger system of equations in this section in a similar way to the simplified equations discussed in section 8.2. However we first non-dimensionalise equations (8.68) to (8.71) using the non-dimensionalisations of Schaefer and Glicksman [95], which are

$$\bar{r} = \frac{r}{R^*}, \quad \tau = \frac{4\kappa_{SL}}{(R^*)^2} t, \quad T = \frac{L\theta}{c}, \quad \frac{d\bar{R}}{d\tau} = \frac{R^*}{4\kappa_{SL}} \frac{dR}{dt}$$

where κ_{SL} is an average thermal diffusivity given by

$$\kappa_{SL} = \frac{\kappa_S + \kappa_L}{2}.$$

Additionally the density, dynamic viscosities and pressure are non-dimensionalised via

$$\rho(\phi) = \rho_{SL}\bar{\rho}(\phi), \quad \mu(\phi) = \nu_{SL}\bar{\mu}(\phi), \quad \lambda(\phi) = \nu_{SL}\bar{\lambda}(\phi), \quad p = \rho_{SL}\left(\frac{4\kappa_{SL}}{R^*}\right)^2 \bar{p}$$

where the parameters ρ_{SL} and ν_{SL} are averages given by

$$\rho_{SL} = \frac{\rho_S + \rho_L}{2} \quad \text{and} \quad \nu_{SL} = \frac{1}{2} \left[\frac{(\lambda_L + \lambda_S)}{2} + \frac{(\mu_S + \mu_L)}{2} \right].$$

Therefore equations (8.68) and (8.69) become

$$\bar{\rho}_\tau(\phi) + \bar{u}\bar{\rho}_\tau(\phi) = -\bar{\rho}(\phi) \left(\frac{\partial \bar{u}}{\partial \bar{r}} + \frac{2}{\bar{r}}\bar{u} \right) \quad (8.74)$$

and

$$\begin{aligned} \bar{\rho}(\phi)[\bar{u}_\tau + \bar{u}\bar{u}_\tau] = & - \frac{\partial \bar{p}}{\partial \bar{r}} - \epsilon_S^2 C_{M1} \left\{ \frac{\partial}{\partial \bar{r}} \left[\left(\frac{\partial \phi}{\partial \bar{r}} \right)^2 \right] + \frac{2}{\bar{r}} \left(\frac{\partial \phi}{\partial \bar{r}} \right)^2 \right\} \\ & + C_{M2} \left\{ \frac{\partial}{\partial \bar{r}} \left[2\bar{\mu}(\phi) \frac{\partial \bar{u}}{\partial \bar{r}} + \bar{\lambda}(\phi) \left(\frac{\partial \bar{u}}{\partial \bar{r}} + \frac{2}{\bar{r}}\bar{u} \right) \right] \right. \\ & \left. + \frac{2}{\bar{r}} \left[2\bar{\mu}(\phi) \frac{\partial \bar{u}}{\partial \bar{r}} + \bar{\lambda}(\phi) \left(\frac{\partial \bar{u}}{\partial \bar{r}} + \frac{2}{\bar{r}}\bar{u} \right) \right] \right\}, \quad (8.75) \end{aligned}$$

where C_{M1} and C_{M2} are given by

$$C_{M1} = \frac{\epsilon_S^2 L \theta}{(4\kappa_{SL})^2 2c\rho_{SL}\epsilon_S^2} = \frac{(R^*)^2 \theta}{2a(4\kappa_{SL})^2 \theta_m}$$

and

$$C_{M2} = \frac{\nu_{SL}}{\rho_{SL} 4\kappa_{SL}}.$$

Using (8.72) and (8.73) equation (8.70) can be written as

$$\begin{aligned} \frac{\epsilon_S^2}{X} [\phi_\tau + \bar{u}\phi_{\bar{r}}] & = \epsilon_S^2 \bar{\nabla}^2 \phi - \frac{aT_m}{T} \bar{\rho}(\phi) g_\phi \\ & = \epsilon_S^2 \bar{\nabla}^2 \phi + Y\epsilon_S \bar{p}'(\phi) + C_P(\bar{p} - \bar{p}_0) \frac{\bar{p}'(\phi)}{\bar{\rho}(\phi)} - \frac{1}{4} H'(\phi) \bar{\rho}(\phi) \end{aligned} \quad (8.76)$$

where

$$C_P = a \left(\frac{4\kappa_{SL}}{R^*} \right)^2, \quad X = \frac{\delta^2 \theta \rho_{SL}}{4\kappa_{SL} M a \theta_m}, \quad Y = \frac{aL(\theta - \theta_m)R^*}{\theta \delta}$$

and³

$$\bar{p}'(\phi) = -r'(\phi)\bar{\rho}(\phi) + \frac{\bar{\rho}(\phi)}{4L} \left(\frac{1}{a} + \frac{1}{a_S} \right) H'(\phi) - \frac{1}{L} \left(\frac{4\kappa_{SL}}{R^*} \right)^2 (\bar{p} - \bar{p}_0) \frac{\bar{p}'(\phi)}{\bar{\rho}(\phi)}.$$

³where we have used the non-dimensionalisation $p'(\phi) = \rho_{SL}\bar{p}'(\phi)$

Finally, by dropping the viscous heating term equation (8.71) becomes

$$\bar{\rho}(\phi) \left[\bar{e}_\tau + \bar{u} \bar{e}_{\bar{r}} \right] = \frac{1}{4} \left\{ \frac{\partial^2 \theta}{\partial \bar{r}^2} + \frac{2}{\bar{r}} \frac{\partial \theta}{\partial \bar{r}} \right\} \quad (8.77)$$

where

$$\begin{aligned} \bar{e}_\tau &= \theta_\tau + \left[-r'(\phi) + \frac{1}{4L} \left(\frac{1}{a_S} + \frac{1}{a} \right) H'(\phi) + C_E \bar{\rho}_0 \frac{\bar{\rho}'(\phi)}{[\bar{\rho}(\phi)]^2} \right] \phi_\tau, \\ \bar{e}_{\bar{r}} &= \theta_{\bar{r}} + \left[-r'(\phi) + \frac{1}{4L} \left(\frac{1}{a_S} + \frac{1}{a} \right) H'(\phi) + C_E \bar{\rho}_0 \frac{\bar{\rho}'(\phi)}{[\bar{\rho}(\phi)]^2} \right] \phi_{\bar{r}}. \end{aligned}$$

and $k = \kappa_{SL} \rho_{SL} c$ has been used to relate the thermal conductivity k , to the thermal diffusivity κ . The energy equation coefficient C_E is given by

$$C_E = \frac{(4\kappa_{SL})^2}{L(R^*)^2}.$$

Writing $\theta = \theta_m(1 + \delta)$, to leading order in δ the coefficients X, Y and C_{M1} become

$$X = \bar{X} = \frac{\delta^2 \rho_{SL}}{4\kappa_{SL} M a}, \quad Y = \bar{Y} \frac{\theta - \theta_m}{\theta_m} \quad \text{where} \quad \bar{Y} = \frac{aLR^*}{\delta} \quad \text{and} \quad C_{M1} = \bar{C}_{M1} = \frac{(R^*)^2}{2a(4\kappa_{SL})^2}.$$

The coefficients C_E, C_P, \bar{C}_{M1} and C_{M2} are all assumed to be approximately $O(1)$ in the following sections of this chapter. This assumption, however, will clearly not be valid for the parameter values of every fluid.

8.3.1 Perturbation expansion

An asymptotic perturbation expansion of equations (8.74), (8.75), (8.76) and (8.77) can now be carried out in the style of Caginalp [16]. By formally expanding the variables in their original coordinates the *outer expansions* can be written as

$$\theta(\bar{r}, \tau, \varepsilon_S) = \vartheta^0(r, \tau) + \varepsilon_S \vartheta^1(r, \tau) + \varepsilon_S^2 \vartheta^2(r, \tau) + \dots, \quad (8.78)$$

$$\phi(\bar{r}, \tau, \varepsilon_S) = \varphi^0(r, \tau) + \varepsilon_S \varphi^1(r, \tau) + \varepsilon_S^2 \varphi^2(r, \tau) + \dots, \quad (8.79)$$

$$\bar{u}(\bar{r}, \tau, \varepsilon_S) = \dot{r}_I + \hat{u}^0(r, \tau) + \varepsilon_S \hat{u}^1(r, \tau) + \varepsilon_S^2 \hat{u}^2(r, \tau) + \dots, \quad (8.80)$$

$$\bar{p}(\bar{r}, \tau, \varepsilon_S) = \bar{p}^0(r, \tau) + \varepsilon_S \bar{p}^1(r, \tau) + \varepsilon_S^2 \bar{p}^2(r, \tau) + \dots, \quad (8.81)$$

where the relative velocity \hat{u} is defined by

$$\hat{u} = \bar{u} - \dot{r}_I, \quad (8.82)$$

with the speed of the interface denoted by \dot{r}_I . These terms may be discontinuous at $r = 0$ but are smooth for $r \neq 0$.

A new variable Z is defined by equation (8.33) by “stretching out” the r variable and the position of the interface is illustrated in figure 8.1.

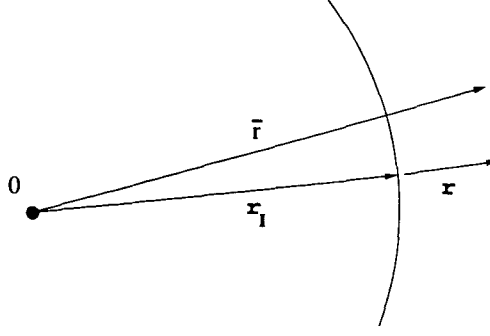


Figure 8.1: Position of the moving interface.

The *inner expansions* for the temperature, phase-field, velocity and pressure variables can be written as

$$\Theta(\bar{r}, \tau, \varepsilon_S) = \Theta^0(Z, \tau) + \varepsilon_S \Theta^1(Z, \tau) + \varepsilon_S^2 \Theta^2(Z, \tau) + \dots, \quad (8.83)$$

$$\Phi(\bar{r}, \tau, \varepsilon_S) = \Phi^0(Z, \tau) + \varepsilon_S \Phi^1(Z, \tau) + \varepsilon_S^2 \Phi^2(Z, \tau) + \dots, \quad (8.84)$$

$$\bar{U}(\bar{r}, \tau, \varepsilon_S) = \bar{U}^0(Z, \tau) + \varepsilon_S \bar{U}^1(Z, \tau) + \varepsilon_S^2 \bar{U}^2(Z, \tau) + \dots \quad (8.85)$$

and

$$\bar{P}(\bar{r}, \tau, \varepsilon_S) = \bar{P}^0(Z, \tau) + \varepsilon_S \bar{P}^1(Z, \tau) + \varepsilon_S^2 \bar{P}^2(Z, \tau) + \dots. \quad (8.86)$$

Differentiating with respect to time requires care. By using equation (8.82) we obtain the expression

$$\frac{\partial \bar{u}}{\partial \tau} = \ddot{r}_I + \frac{\partial \hat{u}}{\partial \tau} - \dot{r}_I \frac{\partial \hat{u}}{\partial r}$$

which relates $\partial \bar{u} / \partial \tau$ (the time differential of the velocity in the stationary frame) with $\partial \hat{u} / \partial \tau$ (the time differential in the moving frame) since

$$\frac{\partial r}{\partial \tau} = \frac{\partial}{\partial \tau}(\bar{r} - r_I) = -\dot{r}_I.$$

From this expression it follows that the total differential

$$\frac{D\bar{u}}{D\tau} = \frac{\partial \bar{u}}{\partial \tau} + \bar{u} \frac{\partial \bar{u}}{\partial \bar{r}} = \ddot{r}_I + \frac{\partial \hat{u}}{\partial \tau} + \hat{u} \frac{\partial \hat{u}}{\partial r},$$

and similarly

$$\frac{\partial \phi}{\partial \tau} = \frac{\partial \phi}{\partial \tau} + \frac{\partial r}{\partial \tau} \frac{\partial \phi}{\partial r} = \phi_\tau - \dot{r}_I \phi_r$$

relates the time differential of the phase-field variable in the stationary frame with its time differential in the moving frame. It follows that the total time differential $D\phi / D\tau$ is therefore given as

$$\frac{D\phi}{D\tau} = \frac{\partial \phi}{\partial \tau} + \hat{u} \frac{\partial \phi}{\partial r}$$

in the moving frame of reference.

8.3.2 Scaling of the pressure and viscosities

In the model of Anderson, McFadden and Wheeler [2] the Clausius-Clapeyron condition instead of the Gibbs-Thompson condition with kinetics is sought at the interface. The Clausius-Clapeyron equation accounts for the pressure on one side of the interface as well as the interfacial curvature. Therefore to obtain this condition in an asymptotic analysis it is required that in the *inner asymptotic expansion* of equations (8.74), (8.75), (8.76) and (8.77) (i.e. in the interfacial region) the pressure should vary. To satisfy this condition we consider a variety of scalings for the non-dimensional viscosities and pressure $\bar{\mu}(\Phi)$, $\bar{\lambda}(\Phi)$ and \bar{P} . To this end we express these variables as

$$\bar{\mu}(\Phi) = \varepsilon_S^\alpha \left\{ \bar{\mu}(\Phi^0) + (\varepsilon_S \Phi^1 + \varepsilon_S^2 \Phi^2 + \dots) \bar{\mu}'(\Phi^0) + (\varepsilon_S \Phi^1 + \varepsilon_S^2 \Phi^2 + \dots)^2 \bar{\mu}''(\Phi^0) + \dots \right\},$$

$$\bar{\lambda}(\Phi) = \varepsilon_S^\alpha \left\{ \bar{\lambda}(\Phi^0) + (\varepsilon_S \Phi^1 + \varepsilon_S^2 \Phi^2 + \dots) \bar{\lambda}'(\Phi^0) + (\varepsilon_S \Phi^1 + \varepsilon_S^2 \Phi^2 + \dots)^2 \bar{\lambda}''(\Phi^0) + \dots \right\}$$

and

$$\bar{P} = \varepsilon_S^\beta \left\{ \bar{P}^0 + \varepsilon_S \bar{P}^1 + \varepsilon_S^2 \bar{P}^2 + \dots \right\}$$

respectively, where the coefficients α and β must now be determined. Using equations (8.83) to (8.86) we obtain the *inner expansion* of the momentum equation (8.75) which is given by

$$\begin{aligned} & \left[\bar{\rho}(\Phi^0) + \varepsilon_S \Phi^1 \bar{\rho}'(\Phi^0) \right] \left[(\hat{U}_\tau^0 + \bar{r}_I) + \varepsilon_S \hat{U}_\tau^1 + \frac{1}{\varepsilon_S} (\hat{U}^0 + \varepsilon_S \hat{U}^1) (\hat{U}_Z^0 + \varepsilon_S \hat{U}_Z^1) \right] = \\ & \frac{1}{\varepsilon_S} \frac{\partial}{\partial Z} \left[-\varepsilon_S^\beta (\bar{P}^0 + \varepsilon_S \bar{P}^1) - \bar{C}_{M1} (\Phi_Z^0 + \varepsilon_S \Phi_Z^1)^2 \right. \\ & + \varepsilon_S^{\alpha-1} C_{M2} \left\{ [\bar{\mu}(\Phi^0) + \varepsilon_S \Phi^1 \bar{\mu}'(\Phi^0)] [\hat{U}_Z^0 + \varepsilon_S \hat{U}_Z^1] + [\bar{\lambda}(\Phi^0) + \varepsilon_S \Phi^1 \bar{\lambda}'(\Phi^0)] \right. \\ & \left. \left. \left(\hat{U}_Z^0 + \varepsilon_S \hat{U}_Z^1 + \varepsilon_S \left[\frac{2}{r_I} - \varepsilon_S \frac{2Z}{(r_I)^2} \right] [(\dot{r}_I + \hat{U}^0) + \varepsilon_S \hat{U}^1] \right) \right\} \right] \\ & + \left[\frac{2}{r_I} - \varepsilon_S \frac{2Z}{(r_I)^2} \right] \left[-\bar{C}_{M1} (\Phi_Z^0 + \varepsilon_S \Phi_Z^1)^2 \right. \\ & + \varepsilon_S^{\alpha-1} C_{M2} \left\{ [\bar{\mu}(\Phi^0) + \varepsilon_S \Phi^1 \bar{\mu}'(\Phi^0)] [\hat{U}_Z^0 + \varepsilon_S \hat{U}_Z^1] + [\bar{\lambda}(\Phi^0) + \varepsilon_S \Phi^1 \bar{\lambda}'(\Phi^0)] \right. \\ & \left. \left. \left(\hat{U}_Z^0 + \varepsilon_S \hat{U}_Z^1 + \varepsilon_S \left[\frac{2}{r_I} - \varepsilon_S \frac{2Z}{(r_I)^2} \right] [(\dot{r}_I + \hat{U}^0) + \varepsilon_S \hat{U}^1] \right) \right\} \right] \end{aligned} \quad (8.87)$$

and to leading order in ε_S we obtain

$$\varepsilon_S^{-1} \bar{\rho}(\Phi^0) \hat{U}^0 \hat{U}_Z^0 = -\varepsilon_S^{\beta-1} \bar{P}_Z^0 - C_{M1} \varepsilon_S^{-1} \frac{\partial}{\partial Z} \left[(\Phi_Z^0)^2 \right] + \varepsilon_S^{\alpha-2} C_{M2} \frac{\partial}{\partial Z} [\bar{\mu}(\Phi^0) \hat{U}_Z^0 + \bar{\lambda}(\Phi^0) \hat{U}_Z^0]. \quad (8.88)$$

To retain as many terms as possible in this equation we choose $\alpha - 2 = \beta - 1 = -1$ (i.e. $\beta = 0$ and $\alpha = 1$), the scaling which is required to balance all four of the terms in equation (8.88). Then at order ε_S^{-1} equation (8.87) gives

$$\bar{\rho}(\Phi^0)\hat{U}^0\hat{U}_Z^0 = -\frac{\partial\bar{P}^0}{\partial Z} - \bar{C}_{M1}\frac{\partial}{\partial Z}(\Phi^0)^2 + C_{M2}\frac{\partial}{\partial Z}\left\{\hat{U}_Z^0[\bar{\lambda}(\Phi^0) + \bar{\mu}(\Phi^0)]\right\}.$$

The viscosity and pressure scaling $\beta = 0$ and $\alpha = 1$ are used throughout the remainder of this chapter.

8.3.3 Outer expansion

Substituting equations (8.78), (8.79), (8.80) and (8.81) into the non-dimensionalised phase-field equations (8.74), (8.75), (8.76) and (8.77) we obtain the expansions shown in section A.1 of appendix A. From these asymptotic expansions at leading order in ε_S we obtain to leading order:

$$\bar{\rho}'(\varphi^0)\varphi_\tau^0 - \dot{r}_I\varphi_\tau^0\bar{\rho}'(\varphi^0) + (\hat{u}^0 + \dot{r}_I)\bar{\rho}'(\varphi^0)\varphi_\tau^0 = -\bar{\rho}(\varphi^0)\left(\frac{\partial\hat{u}^0}{\partial r} + \frac{2}{r}\hat{u}^0\right), \quad (8.89)$$

$$\bar{\rho}(\varphi^0)\left[\hat{u}_\tau^0 + \dot{r}_I + \hat{u}_\tau^0\hat{u}^0\right] = -\frac{\partial\bar{p}^0}{\partial r}, \quad (8.90)$$

$$0 = C_P(\bar{p}^0 - \bar{p}_0)\frac{\bar{\rho}'(\varphi^0)}{\bar{\rho}(\varphi^0)} - \frac{1}{4}H'(\Phi^0)\bar{\rho}(\Phi^0), \quad (8.91)$$

$$\begin{aligned} & \left[\frac{1}{4L}\left(\frac{1}{a} + \frac{1}{a_S}\right)H'(\varphi^0)\bar{\rho}(\varphi^0) - r'(\varphi^0)\bar{\rho}(\varphi^0) + C_E\bar{p}^0\frac{\bar{\rho}'(\varphi^0)}{\bar{\rho}(\varphi^0)}\right]\left[\varphi_\tau^0 - \dot{r}_I\varphi_\tau^0\right] \\ & + \left[\vartheta_\tau^0\bar{\rho}(\varphi^0) + \frac{1}{4L}\left(\frac{1}{a} + \frac{1}{a_S}\right)H'(\varphi^0)\varphi_\tau^0\bar{\rho}(\varphi^0) - r'(\varphi^0)\varphi_\tau^0\bar{\rho}(\varphi^0) + C_E\bar{p}^0\frac{\bar{\rho}'(\varphi^0)}{\bar{\rho}(\varphi^0)}\varphi_\tau^0\right] \\ & \times \left[\dot{r}_I + \hat{u}^0\right] + \bar{\rho}(\varphi^0)\left(-\dot{r}_I\vartheta_\tau^0 + \vartheta_\tau^0\right) = \frac{1}{4}\left\{\frac{\partial^2\vartheta^0}{\partial r^2} + \frac{2}{r}\frac{\partial\vartheta^0}{\partial r}\right\}. \end{aligned} \quad (8.92)$$

Equation (8.91) implies that

$$0 = 2\varphi^0(1 - \varphi^0)\left\{3C_P(\bar{p}^0 - \bar{p}_0)(\bar{\rho}_S - \bar{\rho}_L) - \frac{1}{4}(1 - 2\varphi^0)[(\bar{\rho}_S - \bar{\rho}_L)r(\varphi^0) + \bar{\rho}_L]\right\},$$

which admits three solutions, two of these are stable, namely

$$\varphi^0 = 0 \quad \text{and} \quad \varphi^0 = 1.$$

Therefore incorporating these into the leading order conservation of mass equation (8.89) implies that

$$\bar{\nabla} \cdot \hat{u}^0 = 0. \quad (8.93)$$

This leading order relationship is the incompressibility condition ([6]) which was given by equation (7.6) in chapter 7. Since there is no flow in the solid, \bar{u}^0 , and all its derivatives with respect to \bar{r} are identically zero, and

$$\hat{u}_S^0 = -\dot{r}_I.$$

Applying this condition to equation (8.92) in the solid, where $\varphi^0 = 1$, yields

$$\bar{\rho}_S \left(-\dot{r}_I \vartheta_r^0 + \vartheta_\tau^0 \right) = \frac{1}{4} \left\{ \frac{\partial^2 \vartheta^0}{\partial r^2} + \frac{2}{r} \frac{\partial \vartheta^0}{\partial r} \right\},$$

or equivalently

$$\bar{\rho}_S \vartheta_\tau^0 = \frac{1}{4} \left\{ \frac{\partial^2 \vartheta^0}{\partial r^2} + \frac{2}{r} \frac{\partial \vartheta^0}{\partial r} \right\} \quad (8.94)$$

in a non-moving frame. Re-dimensionalising equation (8.94) leaves

$$\frac{\partial T^0}{\partial t} = \frac{\kappa_{SL}}{\bar{\rho}_S} \left\{ \frac{\partial^2 T^0}{\partial r^2} + \frac{2}{r} \frac{\partial T^0}{\partial r} \right\}. \quad (8.95)$$

In chapter 7 the values of κ_L and κ_S were arranged so that k remains constant assuming c is constant, therefore since

$$k = \kappa_{SL} \rho_{SL} c = \kappa_L \rho_L c = \kappa_S \rho_S c$$

then

$$\frac{\kappa_{SL}}{\bar{\rho}_S} = \frac{\kappa_{SL} \rho_{SL}}{\rho_S} = \kappa_S$$

and equation (8.95) may be written as

$$T_t^0 = \kappa_S \left\{ \frac{\partial^2 T^0}{\partial r^2} + \frac{2}{r} \frac{\partial T^0}{\partial r} \right\}. \quad (8.96)$$

This is the sharp interface heat transfer equation in the solid phase [32] which was given by equation (7.8) in chapter 7.

We now consider equation (8.92) in the liquid phase where $\varphi^0 = 0$ and therefore

$$\vartheta_\tau^0 \bar{\rho}_L \left[\dot{r}_I + \hat{u}_L^0 \right] + \bar{\rho}_L \left[-\dot{r}_I \vartheta_r^0 + \vartheta_\tau^0 \right] = \frac{1}{4} \left\{ \frac{\partial^2 \vartheta^0}{\partial r^2} + \frac{2}{r} \frac{\partial \vartheta^0}{\partial r} \right\}.$$

Consequently

$$\bar{\rho}_L \left(\vartheta_\tau^0 + \bar{u}_L^0 \vartheta_r^0 \right) = \frac{1}{4} \left\{ \frac{\partial^2 \vartheta^0}{\partial r^2} + \frac{2}{r} \frac{\partial \vartheta^0}{\partial r} \right\}$$

in a non-moving frame of reference. Therefore upon re-dimensionalisation

$$T_t^0 + u_L^0 T_r^0 = \frac{\kappa_{SL}}{\bar{\rho}_L} \left\{ \frac{\partial^2 T^0}{\partial r^2} + \frac{2}{r} \frac{\partial T^0}{\partial r} \right\} = \kappa_L \left\{ \frac{\partial^2 T^0}{\partial r^2} + \frac{2}{r} \frac{\partial T^0}{\partial r} \right\} \quad (8.97)$$

where $\kappa_L = \kappa_{SL} / \bar{\rho}_L = k / \rho_L c$. This is the sharp interface heat transfer equation in the liquid phase [32] which was given by equation (7.2) in chapter 7.

Finally we consider equation (8.90) in the liquid phase where

$$\bar{\rho}_L \left[(\hat{u}_L^0)_\tau + \hat{u}_L^0 (\hat{u}_L^0)_r + \ddot{r}_I \right] = -\frac{\partial \bar{p}_L^0}{\partial r}. \quad (8.98)$$

Clearly since

$$\bar{u}_\tau^0 = \ddot{r}_I + \hat{u}_\tau^0 - \dot{r}_I \hat{u}_\tau^0,$$

where $\bar{u}^0 = \dot{r}_I + \hat{u}^0$, then

$$(\hat{u}_L^0)_\tau + \hat{u}_L^0 (\hat{u}_L^0)_r + \ddot{r}_I = \bar{u}_\tau^0 + \bar{u}^0 \bar{u}_\tau^0$$

and therefore on re-dimensionalisation equation (8.98) becomes

$$\rho_L \left[(u_L)_t + u_L (u_L)_r \right] = -\frac{\partial p_L}{\partial r}, \quad (8.99)$$

which is the Euler equation in the liquid phase [32] in spherical polar co-ordinates. This equation was given by (7.5) in chapter 7.

8.3.4 Inner expansion

Noting that the Laplacian in the inner region is given by

$$\bar{\nabla}^2 \theta = \frac{1}{\varepsilon_S^2} \Theta_{ZZ} + \frac{\bar{\nabla}^2 r}{\varepsilon_S} \Theta_Z,$$

the divergence operator as

$$\bar{\nabla} \cdot (\theta \mathbf{e}_r) = \frac{1}{\varepsilon_S} \Theta_Z + \frac{2}{r_I + \varepsilon_S Z} \Theta,$$

and the material time derivative Θ_τ as

$$\Theta_\tau = \Theta_\tau + \frac{\hat{U}}{\varepsilon_S} \Theta_Z,$$

equations (8.74) to (8.77) can be written in terms of the inner stretched coordinate as

$$\bar{\rho}'(\Phi) \left[\Phi_\tau + \frac{1}{\varepsilon_S} \hat{U} \Phi_Z \right] = -\bar{\rho}(\Phi) \left[\frac{1}{\varepsilon_S} \hat{U}_Z + \frac{2}{(r_I + \varepsilon_S Z)} (\hat{U} + \dot{r}_I) \right], \quad (8.100)$$

$$\begin{aligned} \bar{\rho}(\Phi) \left[\hat{U}_\tau + \ddot{r}_I + \frac{1}{\varepsilon_S} \hat{U} \hat{U}_Z \right] &= \frac{1}{\varepsilon_S} \frac{\partial}{\partial Z} \left\{ -\bar{P} - \bar{C}_{M1} (\Phi_Z)^2 \right. \\ &+ C_{M2} \left[2\bar{\mu}(\Phi) \hat{U}_Z + \bar{\lambda}(\Phi) \left\{ \hat{U}_Z + \frac{2\varepsilon_S}{(r_I + \varepsilon_S Z)} (\dot{r}_I + \hat{U}) \right\} \right] \left. \right\} \\ &+ \frac{2}{r_I + \varepsilon_S Z} \left\{ -\bar{C}_{M1} (\Phi_Z)^2 \right. \\ &\left. + C_{M2} \left[2\bar{\mu}(\Phi) \hat{U}_Z + \bar{\lambda}(\Phi) \left\{ \hat{U}_Z + \frac{2\varepsilon_S}{(r_I + \varepsilon_S Z)} (\dot{r}_I + \hat{U}) \right\} \right] \right\}, \end{aligned} \quad (8.101)$$

$$\frac{\varepsilon_S^2}{X} \left[\Phi_\tau + \frac{1}{\varepsilon_S} \hat{U} \Phi_Z \right] = \varepsilon_S^2 \left[\frac{\bar{\nabla}^2 r}{\varepsilon_S} \Phi_Z + \frac{1}{\varepsilon_S^2} \Phi_{ZZ} \right] + \varepsilon_S \bar{Y} \frac{\Theta - \Theta_m}{\Theta_m} \bar{p}'(\Phi) \quad (8.102)$$

$$- \frac{1}{4} H'(\Phi) \bar{\rho}(\Phi) + C_P [\bar{P} - \bar{P}_0] \frac{\bar{\rho}'(\Phi)}{\bar{\rho}(\Phi)}$$

$$\varepsilon_S^2 \bar{\rho}(\Phi) \Theta_\tau + \varepsilon_S^2 \Phi_\tau \left[-r'(\Phi) \bar{\rho}(\Phi) + \frac{1}{4L} \left(\frac{1}{a} + \frac{1}{a_S} \right) H'(\Phi) \bar{\rho}(\Phi) + C_E \bar{P}_0 \frac{\bar{\rho}'(\Phi)}{\bar{\rho}(\Phi)} \right]$$

$$+ \varepsilon_S \hat{U} \Theta_Z \bar{\rho}(\Phi) + \Phi_Z \hat{U} \varepsilon_S \left[-r'(\Phi) \bar{\rho}(\Phi) + \frac{1}{4L} \left(\frac{1}{a} + \frac{1}{a_S} \right) H'(\Phi) \bar{\rho}(\Phi) + C_E \bar{P}_0 \frac{\bar{\rho}'(\Phi)}{\bar{\rho}(\Phi)} \right]$$

$$= \frac{\varepsilon_S^2}{4} \left[\frac{1}{\varepsilon_S^2} \Theta_{ZZ} + \frac{\bar{\nabla}^2 r}{\varepsilon_S} \Theta_Z \right]. \quad (8.103)$$

The asymptotic expansions of equations (8.100) to (8.103) are derived in section A.2 of Appendix A. From these expansions at each order of ε_S we obtain:

$O(1)$:

$$\hat{U}^0 \bar{\rho}'(\Phi^0) \Phi_Z^0 = -\bar{\rho}(\Phi^0) \hat{U}_Z^0, \quad (8.104)$$

$$\bar{\rho}(\Phi^0) \hat{U}^0 \hat{U}_Z^0 = \frac{\partial}{\partial Z} \left[-\bar{P}^0 - \bar{C}_{M1} (\Phi_Z^0)^2 + C_{M2} \left\{ 2\bar{\mu}(\Phi^0) + \bar{\lambda}(\Phi^0) \right\} \hat{U}_Z^0 \right], \quad (8.105)$$

$$\Phi_{ZZ}^0 + C_P (\bar{P}^0 - \bar{P}_0) \frac{\bar{\rho}'(\Phi^0)}{\bar{\rho}(\Phi^0)} - \frac{1}{4} H'(\Phi^0) \bar{\rho}(\Phi^0) = 0 \quad (8.106)$$

and

$$\frac{1}{4} \Theta_{ZZ}^0 = 0. \quad (8.107)$$

$O(\varepsilon_S)$:

$$\left(\Phi_\tau^0 + \hat{U}^0 \Phi_Z^1 + \hat{U}^1 \Phi_Z^0 \right) \bar{\rho}'(\Phi^0) + \hat{U}^0 \Phi_Z^0 \bar{\rho}''(\Phi^0) \Phi^1 =$$

$$-\bar{\rho}(\Phi^0) \left[\hat{U}_Z^1 + \frac{2}{r_I} (\hat{U}^0 + \dot{r}_I) \right] - \bar{\rho}'(\Phi^0) \Phi^1 \hat{U}_Z^0, \quad (8.108)$$

$$\bar{\rho}(\Phi^0) \left[\hat{U}_\tau^0 + \dot{r}_I + \hat{U}^1 \hat{U}_Z^0 + \hat{U}^0 \hat{U}_Z^1 \right] + \Phi^1 \bar{\rho}'(\Phi^0) \hat{U}^0 \hat{U}_Z^0$$

$$= \frac{2}{r_I} \left[-\bar{C}_{M1} (\Phi_Z^0)^2 + C_{M2} \left\{ 2\bar{\mu}(\Phi^0) + \bar{\lambda}(\Phi^0) \right\} \hat{U}_Z^0 \right]$$

$$+ \frac{\partial}{\partial Z} \left[-\bar{P}^1 - 2\bar{C}_{M1} \Phi_Z^0 \Phi_Z^1 + C_{M2} \left\{ 2\bar{\mu}(\Phi^0) \hat{U}_Z^1 + 2\bar{\mu}'(\Phi^0) \Phi^1 \hat{U}_Z^0 \right. \right.$$

$$\left. \left. + \bar{\lambda}(\Phi^0) \left[\hat{U}_Z^1 + \frac{2}{r_I} (\dot{r}_I + \hat{U}^0) \right] + \bar{\lambda}'(\Phi^0) \Phi^1 \hat{U}_Z^0 \right\} \right], \quad (8.109)$$

$$\begin{aligned}
\frac{1}{\bar{X}}\hat{U}^0\Phi_Z^0 &= \Phi_{ZZ}^1 + \bar{\nabla}^2 r\Phi_Z^0 + \bar{Y}\left(\frac{\Theta^0 - \Theta_m}{\Theta_m}\right)\bar{\rho}'(\Phi^0) \\
&+ C_P(\bar{P}^0 - \bar{P}_0)\left[\frac{\bar{\rho}''(\Phi^0)}{\bar{\rho}(\Phi^0)} - \left(\frac{\bar{\rho}'(\Phi^0)}{\bar{\rho}(\Phi^0)}\right)^2\right]\Phi^1 \\
&- \frac{1}{4}\left[H'(\Phi^0)\bar{\rho}'(\Phi^0) + H''(\Phi^0)\bar{\rho}(\Phi^0)\right]\Phi^1 + C_P\bar{P}^1\frac{\bar{\rho}'(\Phi^0)}{\bar{\rho}(\Phi^0)} \quad (8.110)
\end{aligned}$$

and

$$\begin{aligned}
\left\{\frac{1}{4L}\left(\frac{1}{a} + \frac{1}{a_S}\right)H'(\Phi^0)\bar{\rho}(\Phi^0) - r'(\Phi^0)\bar{\rho}(\Phi^0) + C_E\bar{P}_0\frac{\bar{\rho}'(\Phi^0)}{\bar{\rho}(\Phi^0)}\right\}\Phi_Z^0\hat{U}^0 \\
+ \Theta_Z^0\bar{\rho}(\Phi^0)\hat{U}^0 = \frac{1}{4}\left[\Theta_{ZZ}^1 + \bar{\nabla}^2 r\Theta_Z^0\right]. \quad (8.111)
\end{aligned}$$

Integrating equation (8.104) with respect to Z leaves

$$\hat{U}^0\bar{\rho}(\Phi^0) = C_3(\tau), \quad (8.112)$$

where C_3 is a function of τ . Therefore in the solid limit as $Z \rightarrow -\infty$ (i.e. as $\Phi^0 \rightarrow 1$) equation (8.112) becomes

$$-\dot{r}_I\bar{\rho}_S = C_3(\tau), \quad (8.113)$$

since

$$0 = \bar{U}_S^0 = \dot{r}_I + \hat{U}_S^0.$$

Using equation (8.113) to substitute for $C_3(\tau)$ in (8.112) leaves

$$\hat{U}^0 = -\dot{r}_I\frac{\bar{\rho}_S}{\bar{\rho}(\Phi^0)}, \quad (8.114)$$

which gives

$$\bar{U}^0 = \dot{r}_I\left(1 - \frac{\bar{\rho}_S}{\bar{\rho}(\Phi^0)}\right) \quad (8.115)$$

as required. The general solution to equation (8.107) is

$$\Theta^0 = C_4(\tau)Z + C_5(\tau) \quad (8.116)$$

where $C_4(\tau)$ and $C_5(\tau)$ are functions of time τ . Following the Van Dyke matching procedure outlined in section 8.2.5 the first matching condition between the inner and outer temperature variable requires that

$$\Theta^0(Z, \tau) = \vartheta^0(r_I, \tau),$$

which clearly shows that the leading order inner and outer solutions must be equal as $\varepsilon_S \rightarrow 0^4$. This condition is only satisfied if $C_4 \equiv 0$, and therefore

$$\Theta^0 = C_5(\tau). \quad (8.117)$$

⁴A similar relationship was also derived in the appendix of Caginalp [16], citing Caginalp and Fife[19].

Consequently the temperature in the interfacial region is uniform at leading order and from the appropriate matching argument we obtain

$$\lim_{Z \rightarrow \infty} [\Theta^0] = \lim_{r \rightarrow r_I} [\vartheta^0] = \lim_{Z \rightarrow -\infty} [\Theta^0].$$

Therefore re-dimensionalising

$$T_L^0 = T^0 = T_S^0 \quad \text{on } \bar{r} = r_I \text{ (or equivalently when } r = 0), \quad (8.118)$$

which is the sharp interface boundary condition on the temperature given by equation (7.15) in chapter 7.

We now obtain the latent heat boundary condition from the first order energy equation (8.111). By integrating (8.111) with respect to Z and using equations (8.112), (8.117) and (8.118) we obtain

$$\bar{\rho}(\Phi^0) \hat{U}^0 \left\{ \frac{1}{4L} \left(\frac{1}{a} + \frac{1}{a_S} \right) H(\Phi^0) - r(\Phi^0) - C_E \bar{P}_0 \frac{1}{\bar{\rho}(\Phi^0)} \right\} = \frac{1}{4} \Theta_Z^1 + C_6(\tau), \quad (8.119)$$

where \bar{P}_0 denotes the constant reference pressure and C_6 is a function of τ . Taking the limit of equation (8.119) as $Z \rightarrow \infty$ (i.e., into the liquid) gives

$$\bar{\rho}_L \hat{U}_L^0 \left(-C_E \frac{\bar{P}_0}{\bar{\rho}_L} \right) = \frac{1}{4} (\Theta_Z^1)_L + C_6(\tau), \quad (8.120)$$

and taking the limit of equation (8.119) as $Z \rightarrow -\infty$ (i.e., into the solid) gives

$$\bar{\rho}_S \hat{U}_S^0 \left(-1 - C_E \frac{\bar{P}_0}{\bar{\rho}_S} \right) = \frac{1}{4} (\Theta_Z^1)_S + C_6(\tau). \quad (8.121)$$

Then subtracting equation (8.121) from equation (8.120) leaves

$$\bar{\rho}_S \hat{U}_S^0 = \frac{1}{4} \left[(\Theta_Z^1)_L - (\Theta_Z^1)_S \right] + C_E \bar{P}_0 \left[\hat{U}_L^0 - \hat{U}_S^0 \right] \quad (8.122)$$

and using equation (8.113) (which requires that $\hat{U}_S^0 = -\dot{r}_I$ and $\hat{U}_L^0 = -\dot{r}_I \rho_S / \rho_L$) equation (8.122) becomes

$$-\dot{r}_I \bar{\rho}_S = \frac{1}{4} \left[-(\Theta_Z^1)_S + (\Theta_Z^1)_L \right] - \dot{r}_I \bar{P}_0 C_E \left[\frac{\bar{\rho}_S}{\bar{\rho}_L} - 1 \right]. \quad (8.123)$$

By writing $\rho_L = \rho_S + \Delta$ where Δ / ρ_S is small, the last term on the right hand side of (8.123) can be expanded in terms of Δ / ρ_S to give

$$\dot{r}_I \bar{P}_0 \left\{ \frac{\bar{\rho}_S}{\bar{\rho}_L} - 1 \right\} = \left(\frac{\Delta}{\rho_S} \right) \dot{r}_I \bar{P}_0 \left[-1 + \frac{\Delta}{\rho_S} + O(\Delta^2) \right],$$

and since \dot{r}_I is small the latter term can be ignored. Using the derivative of equation (8.55) with respect to Z and non-dimensionalising equation (8.123) yields

$$L \rho_S \frac{dR}{dt} = k_S (T_S^0)_r - k_L (T_L^0)_r. \quad (8.124)$$

Equation (8.124) is the sharp interface latent heat boundary condition given by equation (7.13) in chapter 7, where k_S and k_L are the thermal conductivity coefficients in the solid and liquid phases respectively.

Finally, we require the Gibbs-Thompson equation with attachment kinetics at the solid-liquid interface. The Gibbs-Thompson equation does not account for changes in the pressure across the interface, however the model described in this chapter does account for these changes. Therefore the first order asymptotic expression for the phase-field equation at the interface, given by equation (8.110), should yield the Clausius-Clapeyron equation which accounts for pressure differences across the interface. Firstly, however, we consider the simpler case, namely by ignoring the pressure differences in equation (8.110) we can obtain the Gibbs-Thompson equation. Therefore equation (8.110) becomes

$$\begin{aligned} \frac{1}{\bar{X}} \hat{U}^0 \Phi_Z^0 &= \Phi_{ZZ}^1 + \bar{\nabla}^2 r^0 \Phi_Z^0 + \bar{Y} \left(\frac{\Theta^0 - \Theta_m}{\Theta_m} \right) \bar{p}'(\Phi^0) \\ &\quad - \frac{1}{4} [H'(\Phi^0) \bar{\rho}'(\Phi^0) + H''(\Phi^0) \bar{\rho}(\Phi^0)] \Phi^1, \end{aligned} \quad (8.125)$$

which can be written in the form

$$\begin{aligned} \mathcal{L}\Phi^1 &\equiv \Phi_{ZZ}^1 - \frac{1}{4} [H'(\Phi^0) \bar{\rho}'(\Phi^0) + H''(\Phi^0) \bar{\rho}(\Phi^0)] \Phi^1 \\ &= \frac{1}{\bar{X}} \hat{U}^0 \Phi_Z^0 - \bar{\kappa}_c^0 \Phi_Z^0 - \bar{Y} \left(\frac{\Theta^0 - \Theta_m}{\Theta_m} \right) \bar{p}'(\Phi^0) \end{aligned}$$

where $\bar{\kappa}_c^0 = \bar{\nabla}^2 r^0$ is the leading order curvature. By considering the theory of adjoint systems (see, amongst others Boyce and DiPrima [14]) it can be shown that for a solution Φ^1 to exist

$$\int_{-\infty}^{\infty} \Phi_Z^0 \left[\frac{1}{\bar{X}} \hat{U}^0 \Phi_Z^0 - \bar{\kappa}_c^0 \Phi_Z^0 - \bar{Y} \left(\frac{\Theta^0 - \Theta_m}{\Theta_m} \right) \bar{p}'(\Phi^0) \right] dZ = 0,$$

from which we obtain

$$\bar{Y} \left(\frac{\Theta^0 - \Theta_m}{\Theta_m} \right) \int_{-\infty}^{\infty} \bar{p}'(\Phi^0) \Phi_Z^0 dZ = - \int_{-\infty}^{\infty} \left[\bar{\kappa}_c^0 + \frac{\dot{r}_I}{\bar{X}} \left(\frac{\bar{\rho}_S}{\bar{\rho}(\Phi^0)} \right) \right] (\Phi_Z^0)^2 dZ$$

where

$$\bar{p}'(\Phi^0) = -r'(\Phi^0) \bar{\rho}(\Phi^0) + \frac{1}{4L} \left(\frac{1}{a} + \frac{1}{a_S} \right) \bar{\rho}(\Phi^0) H'(\Phi^0)$$

with the pressure terms removed. Therefore

$$\bar{Y} \left(\frac{\Theta^0 - \Theta_m}{\Theta_m} \right) = - \left[\bar{\kappa}_c^0 + \frac{\dot{r}_I}{\bar{X}} \right] \int_{-\infty}^{\infty} (\Phi_Z^0)^2 dZ + O \left(\frac{\Delta}{\rho_{SL}} \right)$$

and using (8.64)

$$\Theta^0 = \Theta_m - \frac{\sigma^0 \Theta_m}{\rho_{SL} R^* L} \left(\bar{\kappa}_c^0 + \frac{\dot{r}_I}{\bar{X}} \right) + O \left(\frac{\Delta}{\rho_{SL}} \right), \quad (8.126)$$

which yields

$$T^0 = T_m - \left(\frac{\sigma^0 T_m}{\rho_{SL} L} \right) \bar{\kappa}_c^0 - \left(\frac{\sigma^0 T_m}{4 \kappa_{SL} \rho_{SL} L} \right) \frac{\dot{r}_I}{\bar{X}} + O \left(\frac{\Delta}{\rho_{SL}} \right) \quad (8.127)$$

on re-dimensionalisation. This is the form of the Gibbs-Thompson condition given by equation (8.65) in section 8.2. It is clear that the coefficients in equation (8.127) are related to the corresponding coefficients in the Gibbs-Thompson equation, given in chapter 7, in an identical way to section 8.2.

Finally by accounting for pressure changes the Clausius-Clapeyron equation is required. The Clausius-Clapeyron equation is a relationship between the phase transition temperature and the pressure, for a non-planar, unsteady interface. Equating the bulk values of chemical potential by setting $g(p_\infty, T, 0) = g(p_\infty, T, 1)$ gives the jump in the bulk pressure for an equilibrium, planar interface as

$$(p'_\infty - p_0) \left[\frac{1}{\rho_S} - \frac{1}{\rho_L} \right] = L \left(1 - \frac{T}{T_m} \right).$$

This relationship denotes the Clausius-Clapeyron relation when the jump in the chemical potential is ignored. In [2] Anderson, McFadden and Wheeler derived a generalised version of the Clausius-Clapeyron equation for a steady, planar interface which accounts for a jump in the chemical potential in addition to the jump in the bulk pressure. The effect of pressure on the melting point is thereby altered by the rate of solidification. In one dimension Anderson, McFadden and Wheeler [2] found that the jump in the chemical potential for a moving planar interface is given by

$$g_L^\infty - g_S^\infty = M \rho_S V \int_{-\infty}^{\infty} \frac{1}{[\rho(\phi)]^2} (\phi_z)^2 dz - \frac{V^2}{2} \left[\left(\frac{\rho_S}{\rho_L} \right)^2 - 1 \right] + \frac{1}{V \rho_S} \int_{-\infty}^{\infty} [2\mu(\phi) + \lambda(\phi)] (u_z)^2 dz \quad (8.128)$$

where, in the notation of [2] V is the velocity of the interface. Expanding the variables in a power series in terms of the small parameter ϵ_F which was used by Anderson, McFadden and Wheeler in [2] and scaling the z variable by ϵ_F to consider the inner asymptotic expansion, equation (8.128) becomes

$$\begin{aligned} g_L^\infty - g_S^\infty &= \left\{ \frac{1}{V \rho_S} \int_{-\infty}^{\infty} [2\bar{\mu}(\Phi^0) + \bar{\lambda}(\Phi^0)] (u_Z^0)^2 dZ - \frac{V^2}{2} \left[\left(\frac{\rho_S}{\rho_L} \right)^2 - 1 \right] \right\} \\ &+ \epsilon_F \left\{ \tilde{M} \rho_S V \int_{-\infty}^{\infty} \frac{1}{[\rho(\Phi^0)]^2} (\Phi_Z^0)^2 dZ \right. \\ &\quad + \frac{1}{V \rho_S} \int_{-\infty}^{\infty} \Phi^1 [2\bar{\mu}'(\Phi^0) + \bar{\lambda}'(\Phi^0)] (u_Z^0)^2 dZ \\ &\quad \left. + \frac{1}{V \rho_S} \int_{-\infty}^{\infty} [2\bar{\mu}(\Phi^0) + \bar{\lambda}(\Phi^0)] 2u_Z^0 u_Z^1 dZ \right\} + O(\epsilon_F^2). \end{aligned} \quad (8.129)$$

The mobility M and the viscosities μ and λ have been scaled by $M = \epsilon_F^2 \tilde{M}$, $\mu(\Phi^0) = \epsilon_F \bar{\mu}(\Phi^0)$ and $\lambda(\Phi^0) = \epsilon_F \bar{\lambda}(\Phi^0)$, which are consistent with the scalings discussed in section

8.3.2. Equation (8.129) will prove useful despite the significant differences between the non-dimensionalisation in [2] compared with those in this chapter since this equation expresses the asymptotic form of the Clausius-Clapeyron relationship in the absence of curvature, time dependency and thermal effects. The derivation of the generalised Clausius-Clapeyron relationship is long and complicated, therefore it has been placed in section B.1 of appendix B where equation (B.31) gives the jump in the chemical potential for a moving, non-planar, time dependent non-equilibrium interface as

$$\begin{aligned}
g_L - g_S &= \left(\frac{4\kappa_{SL}}{R^*}\right)^2 \left\{ -\frac{(\dot{r}_I)^2}{2} \left[\left(\frac{\bar{\rho}_S}{\bar{\rho}_L}\right)^2 - 1 \right] + \frac{C_{M2}}{\dot{r}_I \bar{\rho}_S} \int_{-\infty}^{\infty} [2\bar{\mu}(\Phi^0) + \bar{\lambda}(\Phi^0)] (\hat{U}_Z^0)^2 dZ \right\} \\
&+ \epsilon_S \left\{ \frac{1}{a\bar{X}} \dot{r}_I \bar{\rho}_S \int_{-\infty}^{\infty} \frac{1}{[\bar{\rho}(\Phi^0)]^2} (\Phi_Z^0)^2 dZ \right. \\
&\quad + \left(\frac{4\kappa_{SL}}{R^*}\right)^2 \frac{C_{M2}}{\bar{\rho}_S \dot{r}_I} \int_{-\infty}^{\infty} \left(2[2\bar{\mu}(\Phi^0) + \bar{\lambda}(\Phi^0)] \hat{U}_Z^0 \hat{U}_Z^1 \right. \\
&\quad \left. \left. + [2\bar{\mu}'(\Phi^0) + \bar{\lambda}'(\Phi^0)] \Phi^1 (\hat{U}_Z^0)^2 \right) dZ + \left(\frac{2}{r_I}\right) I_1 + I_2 - I_3 \right\} + O(\epsilon_S^2)
\end{aligned} \tag{8.130}$$

where the functions I_1 , I_2 and I_3 are collections of the terms related to curvature, time dependence and thermal variation respectively. They are defined as

$$\begin{aligned}
I_1 &= \left(\frac{4\kappa_{SL}}{R^*}\right)^2 \int_{-\infty}^{\infty} \frac{1}{\bar{\rho}(\Phi^0)} \left\{ C_7 + \bar{\rho}(\Phi^0) (\hat{U}^0)^2 + \bar{P}^0 + C_{M2} \frac{\partial}{\partial Z} [\bar{\lambda}(\Phi^0) (\hat{U}^0 + \dot{r}_I)] \right\} dZ \\
&- \left(\frac{4\kappa_{SL}}{R^*}\right)^2 \frac{C_{M2}}{\dot{r}_I \bar{\rho}_S} \int_{-\infty}^{\infty} \delta_\kappa \frac{\partial}{\partial Z} \left\{ [2\bar{\mu}(\Phi^0) + \bar{\lambda}(\Phi^0)] \hat{U}_Z^0 \right\} dZ \\
&+ \int_{-\infty}^{\infty} \frac{1}{a\bar{\rho}(\Phi^0)} (\Phi_Z^0)^2 dZ + \left(\frac{4\kappa_{SL}}{R^*}\right)^2 [\hat{U}^0 \delta_\kappa]_{-\infty}^{\infty} + \frac{C_{M2}}{\dot{r}_I \bar{\rho}_S} \hat{U}_L^0 [2\bar{\mu}_L + \bar{\lambda}_L],
\end{aligned} \tag{8.131}$$

$$I_2 = -\left(\frac{4\kappa_{SL}}{R^*}\right)^2 \int_{-\infty}^{\infty} \left(\hat{U}_\tau^0 + \dot{r}_I \right) + \frac{C_{M2}}{\dot{r}_I \bar{\rho}_S} \delta_\tau \frac{\partial}{\partial Z} \left\{ [2\bar{\mu}(\Phi^0) + \bar{\lambda}(\Phi^0)] \hat{U}_Z^0 \right\} dZ + \left(\frac{4\kappa_{SL}}{R^*}\right)^2 [\hat{U}^0 \delta_\tau]_{-\infty}^{\infty} \tag{8.132}$$

and

$$I_3 = \left[\frac{e_0}{\Theta_m} + \frac{L}{\Theta_m} \ln \left(\frac{\Theta^0}{\Theta_m} \right) \right] \left[\Theta_L^1 - \Theta_S^1 \right] + \frac{1}{\Theta_m} \int_{-\infty}^{\infty} \Theta_Z^1 \left[-Lr(\Phi^0) + \frac{1}{4a_S} H(\Phi^0) \right] dZ, \tag{8.133}$$

where δ_τ denotes an unsteady term given by

$$\delta_\tau = \frac{1}{\bar{\rho}(\Phi^0)} \int \Phi_\tau^0 \bar{\rho}'(\Phi^0) dZ$$

and δ_κ denotes a curvature term given by

$$\delta_\kappa = \frac{1}{\bar{\rho}(\Phi^0)} \int \bar{\rho}(\Phi^0) (\hat{U}^0 + \dot{r}_I) dZ.$$

The integral function I_1 which is defined by equation (8.131), is multiplied by the leading order curvature term $2/r_I$. The integral function I_2 contains all the unsteady terms, namely \hat{U}_τ^0 , \ddot{r}_I and δ_τ and the integral function I_3 contains all the non-equilibrium thermal terms. Clearly in the limit as $r_I \rightarrow \infty$ the curvature terms vanish, which is the required condition for a planar interface. Further, making the steady assumption removes the terms \hat{U}_τ^0 , \ddot{r}_I and δ_τ which implies that $I_2 = 0$ and applying thermal equilibrium requires that $\Theta_L^1 = \Theta_S^1$ and $\Theta_Z^1 = 0$ which implies that $I_3 = 0$.

Using these conditions equation (8.130) reduces to a form which is similar to equation (8.129), the Clausius-Clapeyron relationship for a planar, steady, temperature invariant interface (as considered in [2]). These last three effects are described by I_1 , I_2 and I_3 respectively in the more general system described by equation (8.130). The differences in the coefficients between equations (8.130) and (8.129) are due to the non-dimensionalisations used in this chapter.

Further it is shown in section B.2 of appendix B that when the density in the liquid phase is written as $\rho_L = \rho_S + \Delta$, where Δ/ρ_S is small, the leading order expansion in Δ/ρ_S of equation (8.130) is equivalent to the Gibbs-Thompson condition described by equation (8.65) in the previous section and (7.14) in chapter 7. To obtain this expression we use an asymptotic expansion to leading and first order in ε_S to express the difference between the Gibbs free energy (given by equation (B.36) in appendix B) in the solid and liquid phases. Then we equate the resulting expression with an asymptotic expansion of (8.130) to leading and first order in Δ/ρ_S . Using this approach we obtain

$$\begin{aligned}
\Theta^0 = & \Theta_m - \frac{\Theta_m \sigma^0}{R^* L \rho_{SL}} \bar{\kappa}_c^0 - \frac{\sigma^0 \Theta_m}{\bar{X} R^* L \rho_{SL}} \dot{r}_I \\
& - \left(\frac{\Delta}{\rho_S} \right) \left\{ \left(\frac{4\kappa_{SL}}{R^*} \right)^2 \frac{\Theta_m}{L} (\bar{P}_0 - \bar{P}_L^0) - \left(\frac{\Theta_m \sigma^0}{LR^* \rho_{SL}} \right) \bar{\kappa}_c^0 - \left(\frac{2\Theta_m \sigma^0}{LR^* \rho_{SL}} \right) \frac{\dot{r}_I}{\bar{X}} \right\} \\
& - \varepsilon_S \left\{ -\Theta_m [\Theta_L^1 - \Theta_S^1] + \Theta_S^1 - \int_{-\infty}^{\infty} \Theta_Z^1 [-r(\Phi^0) + \frac{1}{4a_S L} H(\Phi^0)] dZ \right\} \\
& - \varepsilon_S \left(\frac{\Delta}{\rho_S} \right) \left\{ \left(\frac{4\kappa_{SL}}{R^*} \right)^2 \frac{\Theta_m}{L} [\bar{P}_S^1 - r(\Phi^0) \bar{P}_L^1] + \frac{\Theta_m}{aL} \int_{-\infty}^{\infty} r(\Phi^0) \frac{\partial}{\partial Z} (\Phi_Z^0 \Phi_Z^1) dZ \right. \\
& \quad \left. + \left(\frac{\Theta_m \bar{\kappa}_c^0}{La} + \frac{2\Theta_m \dot{r}_I}{La\bar{X}} \right) \int_{-\infty}^{\infty} r(\Phi^0) (\Phi_Z^0)^2 dZ \right. \\
& \quad \left. + \frac{\Theta_m}{L} \left(\frac{4\kappa_{SL}}{R^*} \right)^2 \int_{-\infty}^{\infty} r(\Phi^0) \bar{P}_Z^1 dZ \right\} + O\left(\left[\frac{\Delta}{\rho_S}\right]^2\right), \tag{8.134}
\end{aligned}$$

to leading and first order in ε_S . The integrands $r(\Phi^0)(\Phi_Z^0)^2$, $r(\Phi^0)(\Phi_Z^1 \Phi_Z^0)_Z$ and $r(\Phi^0) \bar{P}_Z^1$ cannot be directly integrated with respect to Z . However if $r(\Phi^0)$ is approximated by a

constant average value, given as α say, then these three integrals may be expressed as

$$\int_{-\infty}^{\infty} r(\Phi^0) \frac{\partial}{\partial Z} (\Phi_Z^0 \Phi_Z^1) dZ \approx \alpha [\Phi_Z^0 \Phi_Z^1]_{-\infty}^{\infty} = 0, \quad \int_{-\infty}^{\infty} r(\Phi^0) (\Phi_Z^0)^2 dZ \approx \alpha \left(\frac{\sigma^0 a}{\delta \rho_{SL}} \right)$$

and

$$\int_{-\infty}^{\infty} r(\Phi^0) \bar{P}_Z^1 dZ \approx \alpha [\bar{P}_L^1 - \bar{P}_S^1].$$

Therefore re-dimensionalising equation (8.134) and ignoring all terms which are first or higher order in ε_S we obtain

$$\begin{aligned} T^0 = & T_m - \left(\frac{\sigma^0 T_m}{\rho_{SL} L} \right) \kappa_c^0 - \left(\frac{\sigma^0 T_m}{4\kappa_{SL} \bar{X} L \rho_{SL}} \right) \frac{dR}{dt} \\ & + \left(\frac{\Delta}{\rho_S} \right) \left\{ \frac{T_m}{\rho_S L} (P_0 - P_L^0) - (1 - \alpha) \left(\frac{\sigma^0 T_m}{\rho_{SL} L} \right) \kappa_c^0 - (1 - \alpha) \left(\frac{2\sigma^0 T_m}{4\kappa_{SL} \bar{X} L \rho_{SL}} \right) \frac{dR}{dt} \right\} \end{aligned} \quad (8.135)$$

which, to leading order in Δ/ρ_S is clearly equivalent to the Gibbs-Thompson condition given by equation (8.65) in this chapter and equation (7.14) in chapter 7. The first order term in Δ/ρ_S is small if the latent heat term L is large or if α is $O(1)$.

8.3.5 Problem statement

To leading order in ε_S the phase-field problem with flow described by equations (8.68) to (8.71) has been shown to be equivalent to the sharp interface Modified Stefan Model with flow described in chapter 7 when $\rho_L = \rho_S + \Delta$ where Δ/ρ_S is small. In summary therefore as $\varepsilon_S \rightarrow 0$ the leading order asymptotic expansion of the phase-field model described in this chapter is given by a set of equations in the solid and liquid phases:

$$\begin{aligned} \bar{\nabla} \cdot \hat{u}^0 &= 0, \\ T_t^0 &= \kappa_S \nabla^2 T^0, \\ T_t^0 + u^0 T_r^0 &= \kappa_L \nabla^2 T^0, \\ \rho_L [(u_L)_t + u_L (u_L)_r] &= -\nabla \cdot p_L, \end{aligned}$$

and boundary conditions on $r = R$:

$$\begin{aligned} T_L^0 &= T^0 = T_S^0 \\ L\rho_S \frac{dR}{dt} &= k_S (T_S^0)_r - k_L (T_L^0)_r \end{aligned}$$

and

$$g_L - g_S = \left(\frac{4\kappa_{SL}}{R^*} \right)^2 \left\{ -\frac{(\dot{r}_I)^2}{2} \left[\left(\frac{\bar{\rho}_S}{\bar{\rho}_L} \right)^2 - 1 \right] + \frac{C_{M2}}{\dot{r}_I \bar{\rho}_S} \int_{-\infty}^{\infty} [2\bar{\mu}(\Phi^0) + \bar{\lambda}(\Phi^0)] (\hat{U}_Z^0)^2 dZ \right\}$$

$$\begin{aligned}
& + \varepsilon_S \left\{ \frac{1}{aX} \dot{r}_I \bar{\rho}_S \int_{-\infty}^{\infty} \frac{1}{[\bar{\rho}(\Phi^0)]^2} (\Phi_Z^0)^2 dZ \right. \\
& \quad + \left(\frac{4\kappa_{SL}}{R^*} \right)^2 \frac{C_{M2}}{\bar{\rho}_S \dot{r}_I} \int_{-\infty}^{\infty} \left[2 \left[2\bar{\mu}(\Phi^0) + \bar{\lambda}(\Phi^0) \right] \hat{U}_Z^0 \hat{U}_Z^1 \right. \\
& \quad \left. \left. + \left[2\bar{\mu}'(\Phi^0) + \bar{\lambda}'(\Phi^0) \right] \Phi^1 (\hat{u}_Z^0)^2 \right] dZ + \left(\frac{2}{r_I} \right) I_1 + I_2 - I_3 \right\} + O(\varepsilon_S^2)
\end{aligned}$$

where I_1, I_2 and I_3 are given by equations (B.28), (B.29) and (B.30) respectively. This final equation may be expressed as

$$T^0 = T_m - \left(\frac{\sigma^0 T_m}{\rho_{SL} L} \right) \kappa_c^0 - \left(\frac{\sigma^0 T_m}{4\kappa_{SL} \bar{X} L \rho_{SL}} \right) \frac{dR}{dt} + O\left(\frac{\Delta}{\rho_S}\right)$$

by expanding the equation above in a power series in Δ/ρ_S .

The equations above denote the incompressibility condition in the liquid phase (8.93), the heat transfer equation in the solid phase (8.96), the heat transfer equation in the liquid phase (8.97), the momentum equation in the liquid phase (8.99), the interfacial temperature boundary condition (8.118), the latent heat boundary condition (8.124) and finally the generalised Clausius-Clapeyron relationship (8.130) respectively. All of these equations have been obtained by using an asymptotic expansion of the phase-field equations. Also the unknown constants in the phase-field model of Anderson, McFadden and Wheeler [2] have now been related to the model described in chapter 7 via [16], [19] and [129] using the non-dimensionalisations of Schaefer and Glicksman in [95].

Chapter 9

Numerical results

9.1 Introduction

In this chapter we solve numerically the phase-field model described in chapter 8. The results are then compared with the sharp interface Stefan model described in chapter 7 as the non-dimensional interface thickness parameter $\varepsilon_S \rightarrow 0$.

9.2 Phase-field equations without flow

First we consider the case without flow, where the non-dimensional phase-field equations reduce to a simpler form which is similar to the problem considered in [133]. The non-dimensional phase-field equations (8.24) and (8.27) without flow are given by

$$\frac{\varepsilon_S^2}{X} \phi_\tau = \varepsilon_S^2 \bar{\nabla}^2 \phi + \varepsilon_S Y \bar{p}'(\phi) - \frac{1}{4} H'(\phi) \quad (9.1)$$

and

$$4(\theta_\tau + \bar{p}'(\phi)\phi_\tau) = \bar{\nabla}^2 \theta \quad (9.2)$$

where

$$X = \frac{\sigma T_m \mu}{4\kappa \rho L}, \quad Y = \frac{R^* a L}{\delta} \left(\frac{\theta - \theta_m}{\theta} \right) \quad (9.3)$$

and $\bar{p}(\phi)$, $H(\phi)$ and $r(\phi)$ are given by

$$\bar{p}'(\phi) = -r'(\phi) + \frac{1}{4L} \left(\frac{1}{a} + \frac{1}{a_S} \right) H'(\phi), \quad (9.4)$$

$$H(\phi) = \phi^2(1 - \phi)^2 \quad \text{and} \quad r(\phi) = \phi^2(3 - 2\phi) \quad (9.5)$$

respectively.

Following the non-dimensionalisations used in chapter 7 the normalised temperature θ can be rescaled in terms of the normalised super-cooling $\Delta\theta$ where

$$\theta = \theta_m + \Delta\theta\bar{\theta} \quad (9.6)$$

and θ_m is the normalised melting temperature of the planar interface. Initially the system is super-cooled to $\Delta\theta$ everywhere and therefore $\bar{\theta}$ is set equal to -1. A value of $\bar{\theta} = 0$ corresponds to zero super-cooling (i.e. $T = T_m =$ melting temperature).

To compare the results obtained in this chapter with the results obtained in chapter 7 the coefficients (9.3), (9.4) and (9.5) in the system described by equations (9.1) and (9.2) must be related to the coefficients for white phosphorus (P_4) given in chapter 7, and shown again in table 1.

<i>substance</i>		P_4	H_2O
L/c	$^{\circ}C$	25.4	80
$A \left(= 2\sigma T_m c / L^2 \rho \right)$	cm	5.5×10^{-7}	6.5×10^{-8}
κ	cm^2/sec	1.5×10^{-3}	1.35×10^{-3}
$\xi/\mu \left(= \sigma T_m / 2\kappa_{SL} L \rho \right)$	$sec^{\circ}C / cm$	2.3×10^{-3}	9.7×10^{-4}
T_m	$^{\circ}C$	44.31	0

Table 1: Values of relevant physical constants from [95] and [69].

From equation (8.22) in the previous chapter

$$\frac{a}{\delta} = \frac{\sqrt{2}\rho}{12\sigma}, \quad (9.7)$$

therefore from (9.3)

$$\begin{aligned} Y &= R^* L \frac{a}{\delta} \frac{\theta - \theta_m}{\theta} \\ &= R^* L \frac{\sqrt{2}\rho}{12\sigma} \frac{\theta - \theta_m}{\theta} \\ &= \frac{R^*(L\rho)}{6\sqrt{2}\sigma} \frac{\Delta\theta\bar{\theta}}{\theta} \end{aligned}$$

where (9.6) has been used to write the difference between the normalised temperature θ and the melting temperature θ_m in terms of the normalised super-cooling $\Delta\theta$. Writing $T_m = L\theta_m/c$, from table 1

$$A = \frac{2\sigma\theta_m}{L\rho}$$

and consequently

$$Y = \frac{R^*}{6\sqrt{2}} \frac{2\theta_m}{A} \frac{\Delta\theta\bar{\theta}}{\theta} = \frac{\bar{\theta}}{3\sqrt{2}} \frac{\theta_m}{\theta}$$

since $A = R^*\Delta\theta$. As described in chapter 8 we use the non-dimensional temperature approximation $\theta = \theta_m(1 + \delta_\theta)$ where δ_θ is small, to express Y as

$$Y = \frac{\bar{\theta}}{3\sqrt{2}}.$$

Similarly from (9.3) X can be expressed as

$$X = \frac{\sigma T_m}{2\kappa_{SL}L\rho} \frac{\mu}{2} = \left(\frac{\xi}{\mu}\right) \frac{\mu}{2}$$

where the coefficient (ξ/μ) is found in table 1.

It remains to find $1/aL$, the coefficient of $H'(\phi)$ in expression (9.4). Using (9.7), $\delta = \varepsilon_S R^*$ and $A = R^*\Delta\theta$ implies that this coefficient becomes

$$\begin{aligned} \frac{1}{4aL} &= \frac{1}{4L} \frac{12\sigma}{\sqrt{2}\rho\varepsilon_S R^*} = \frac{3}{\sqrt{2}\varepsilon_S R^*} \frac{A}{2\theta_m} \\ &= \frac{3\Delta\theta}{2\sqrt{2}\varepsilon_S\theta_m}. \end{aligned}$$

The coefficient a_S which determines the height of the entropy double-well is undetermined. By adopting the condition $a_S = -a$ the double-well potential is removed from the expression for the internal energy and in this system $\bar{p}'(\phi_r^\tau)$ simply becomes $-r'(\phi_r^\tau)$.

9.2.1 Finite differences

The discrete system, comprising equations (9.1) and (9.2), can be solved explicitly when the derivatives are approximated by forward time and central space finite differences. Therefore equations (9.1) and (9.2) become

$$\frac{\phi_r^{\tau+d\tau} - \phi_r^\tau}{d\tau} = X \left\{ \frac{\phi_{r+dr}^\tau - 2\phi_r^\tau + \phi_{r-dr}^\tau}{(dr)^2} + \frac{2}{r} \frac{\phi_{r+dr}^\tau - \phi_{r-dr}^\tau}{2dr} \right\} + \frac{XY}{\varepsilon_S} \bar{p}'(\phi_r^\tau) - \frac{X}{4\varepsilon_S^2} H'(\phi_r^\tau) \quad (9.8)$$

and

$$\frac{\bar{\theta}_r^{\tau+d\tau} - \bar{\theta}_r^\tau}{d\tau} = \frac{1}{4} \left\{ \frac{\bar{\theta}_{r+dr}^\tau - 2\bar{\theta}_r^\tau + \bar{\theta}_{r-dr}^\tau}{(dr)^2} + \frac{2}{r} \frac{\bar{\theta}_{r+dr}^\tau - \bar{\theta}_{r-dr}^\tau}{2dr} \right\} - \frac{1}{\Delta\theta} \bar{p}'(\phi_r^\tau) \frac{\phi_r^{\tau+d\tau} - \phi_r^\tau}{d\tau} \quad (9.9)$$

where

$$X = \left(\frac{\xi}{\mu}\right) \frac{\mu}{2}, \quad Y = \frac{\bar{\theta}_r^\tau}{3\sqrt{2}}$$

and $\bar{p}(\phi)$, $H(\phi)$ and $r(\phi)$ are given by

$$\bar{p}'(\phi_r^\tau) = -r'(\phi_r^\tau) + \frac{1}{4L} \left(\frac{1}{a} + \frac{1}{a_S} \right) H'(\phi_r^\tau),$$

$$H'(\phi_r^\tau) = 2\phi_r^\tau(1 - \phi_r^\tau)(1 - 2\phi_r^\tau) \quad \text{and} \quad r'(\phi_r^\tau) = 6(\phi_r^\tau)^2(1 - \phi_r^\tau).$$

The explicit forward time and centre space finite difference discretisation was used for simplicity, however the explicit nature of the calculation requires a severe restriction on the time step $d\tau$. It was observed that for the method to be convergent when $\varepsilon_S = dr = 0.01$, the time step restriction on the explicit formulation, namely

$$d\tau = \alpha(dr)^2 \quad \text{where} \quad \alpha < 1.0$$

requires that

$$\max(\alpha) \approx 0.875.$$

A further stability restriction on the size of the time step was observed, namely when $dr > \varepsilon_S$ the system of phase-field equations was unstable and solutions could not be obtained. This numerical stability restriction was also noted in [133] and confirms the suggestion in [21] that the numerical solution of the phase-field equations by a finite difference method on a uniform mesh could break down for $\varepsilon_S < dr$. Stable results were produced however when $dr = \varepsilon_S$, and this condition was used to evaluate the results in this chapter.

As expected the code was sensitive to initial data and a sharp discontinuity in the phase field profile at the interface was not adequate. Therefore the hyperbolic tangent solution

$$\phi(\bar{r}) = \frac{1}{2} \left[1 - \tanh \left(\frac{\bar{r}}{2\sqrt{2}\varepsilon_S} \right) \right] \quad (9.10)$$

to the isothermal, steady phase-field equation with a planar interface, given by

$$0 = \varepsilon_S^2 \phi_{rr} - \frac{1}{4} H'(\phi) \quad (9.11)$$

was used as an initial phase-field profile.

9.2.2 Boundary conditions

Solving this system on the boundary $\bar{r} = 0$ requires special treatment to avoid the coordinate singularity in the Laplacian operator. In chapter 7 the Neumann boundary conditions

$$\lim_{r \rightarrow 0} \left(\frac{\partial \phi}{\partial r} \right) = 0 \quad \text{and} \quad \lim_{r \rightarrow 0} \left(\frac{\partial \bar{\theta}}{\partial r} \right) = 0$$

were used at the origin. Consequently we use the same conditions here and therefore the central finite difference approximation to the second spatial derivatives in ϕ and $\bar{\theta}$ at the origin become

$$\left(\phi_0^\tau \right)_{rr} = 2 \left[\frac{\phi_{dr}^\tau - \phi_0^\tau}{(dr)^2} \right] \quad \text{and} \quad \left(\bar{\theta}_0^\tau \right)_{rr} = 2 \left[\frac{\bar{\theta}_{dr}^\tau - \bar{\theta}_0^\tau}{(dr)^2} \right]$$

respectively. Then using L'Hôpital's rule

$$\lim_{r \rightarrow 0} \left(\frac{2}{r} \frac{\partial \phi}{\partial r} \right) = \lim_{r \rightarrow 0} \left(2 \frac{\partial^2 \phi}{\partial r^2} \right) \quad \text{and} \quad \lim_{r \rightarrow 0} \left(\frac{2}{r} \frac{\partial \bar{\theta}}{\partial r} \right) = \lim_{r \rightarrow 0} \left(2 \frac{\partial^2 \bar{\theta}}{\partial r^2} \right),$$

and therefore on $\bar{r} = 0$ equations (9.1) and (9.2) become

$$\frac{\phi_0^{\tau+d\tau} - \phi_0^\tau}{d\tau} = 2X \frac{\phi_{dr}^\tau - \phi_0^\tau}{(dr)^2} + \frac{XY}{\varepsilon_S} \bar{p}'(\phi_0^\tau) - \frac{X}{4\varepsilon_S^2} H'(\phi_0^\tau) \quad (9.12)$$

and

$$\frac{\bar{\theta}_0^{\tau+d\tau} - \bar{\theta}_0^\tau}{d\tau} = \frac{1}{2} \frac{\bar{\theta}_{dr}^\tau - \bar{\theta}_0^\tau}{(dr)^2} - \frac{1}{\Delta\theta} \bar{p}'(\phi_0^\tau) \frac{\phi_0^{\tau+d\tau} - \phi_0^\tau}{d\tau}. \quad (9.13)$$

The far field is made to correspond to a value of $\bar{r} = R = 10$ and the boundary conditions in the far field were then chosen to be

$$\frac{\partial \bar{\theta}_R^\tau}{\partial r} + \frac{\bar{\theta}_R^\tau + 1}{R} = 0 \quad \text{and} \quad \frac{\partial \phi_R^\tau}{\partial r} = 0. \quad (9.14)$$

These conditions are consistent with assuming unity in the phase field equation and a quasi-static approximation for the heat diffusion equation in the far field. Therefore on $\bar{r} = R$ equations (9.1) and (9.2) become

$$\frac{\phi_R^{\tau+d\tau} - \phi_R^\tau}{d\tau} = 2X \frac{\phi_{R-dr}^\tau - \phi_R^\tau}{(dr)^2} + \frac{XY}{\varepsilon_S} \bar{p}'(\phi_R^\tau) - \frac{X}{4\varepsilon_S^2} H'(\phi_R^\tau) \quad (9.15)$$

and

$$\frac{\bar{\theta}_R^{\tau+d\tau} - \bar{\theta}_R^\tau}{d\tau} = -\frac{1}{\Delta\theta} \bar{p}'(\phi_R^\tau) \left(\frac{\phi_R^{\tau+d\tau} - \phi_R^\tau}{d\tau} \right) \quad (9.16)$$

since

$$\frac{\partial \bar{\theta}_R^\tau}{\partial r} = -\frac{\bar{\theta}_R^\tau + 1}{R}, \quad \frac{\partial^2 \bar{\theta}_R^\tau}{\partial r^2} = 2 \frac{\bar{\theta}_R^\tau + 1}{R^2} \quad \text{and} \quad \frac{\partial^2 \phi_R^\tau}{\partial r^2} = 2 \left[\frac{\phi_{R-dr}^\tau - \phi_R^\tau}{(dr)^2} \right].$$

9.2.3 Solution method

Equations (9.8) and (9.9) were solved subject to boundary conditions (9.12), (9.13), (9.15) and (9.16). Initially the parameters μ , ε_S and $R(0)$ were set and then:

- equation (9.8) was evaluated at every position step, calculating $\phi_r^{\tau+d\tau}$
for all $0 \leq \bar{r} \leq R$
- and then equation (9.9) was evaluated at every position step, calculating $\bar{\theta}_r^{\tau+d\tau}$
for all $0 \leq \bar{r} \leq R$.

Finally results were recorded at prescribed time steps defined by the user.

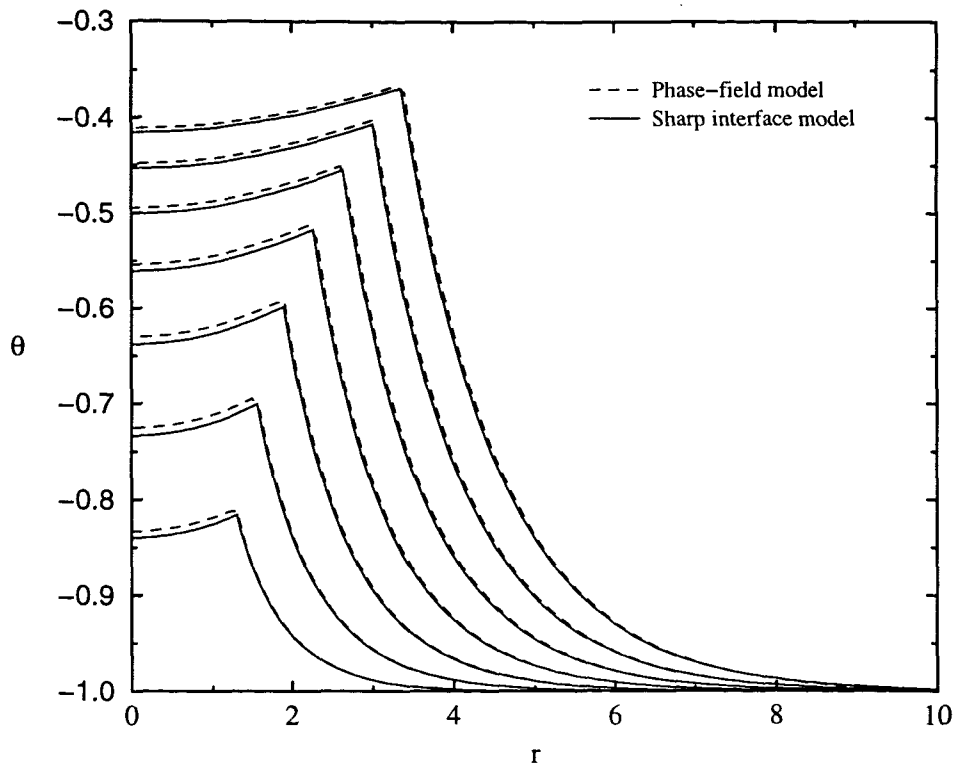


Figure 9.1: Comparison between the temperature profiles when $\tau = 5, 10, \dots, 30$ and 35 produced by the phase-field model with $\epsilon_S = 0.01$, $dr = 0.01$, $\Delta\theta = 0.5$ and $\xi = 1.0$ (i.e. $\mu = 434.78 \text{ cm/sec } ^\circ\text{C}$ for P_4) and the corresponding Stefan model from chapter 7.

9.2.4 Results and discussion

Figure 9.1 shows the temperature profiles of the sharp interface Stefan model described in chapter 7 and the phase field model described in this chapter. The normalised super-cooling $\Delta\theta$ was set to 0.5 and the parameter ξ to 1.0 (which requires that the mobility μ takes the value $\mu = 434.78 \text{ cm/sec } ^\circ\text{C}$ when using the material parameter values for P_4). Growth was initiated by setting the initial radius 10% above the critical radius (i.e. $\phi = 1/2$ when $\bar{r} = (1 + \delta_r)$ where $\delta_r = 0.1$) and the non-dimensional interface thickness parameter ε_S was set to 0.01. As briefly discussed in section 9.2.1 a mesh size of $dr = \varepsilon_S (= 0.01)$ was used since it was found to be the largest value of dr , for a given value of ε_S , for which the numerical scheme remained stable. Almost identical results were obtained by using smaller values of the position step dr when $\varepsilon_S = 0.01$. However the restriction on the mesh size ($dr \leq \varepsilon_S$) in conjunction with the explicit time stepping restriction ($dt < dr^2$) was a significant limiting constraint and therefore we chose the largest stable mesh size $dr = \varepsilon_S$. Figure 9.1 clearly shows relatively small differences between the phase-field model when $\varepsilon_S = 0.01$ and the sharp interface Stefan model. Furthermore these differences are similar in magnitude to the discretisation error in the finite difference approximation. With such a small value for ε_S we expect close agreement between the two methods.

Figure 9.2 shows the temperature profiles of the sharp interface Stefan model and the phase-field model when all the parameters are identical to those in figure 9.1 except for ε_S which is 0.005. As expected the figure shows excellent agreement between the two models.

Due to the restrictions on dr and dt however it took approximately one week of continuous running time on a Pentium II desktop machine to complete figure 9.2, and for this reason further reductions in ε_S were impractical using this explicit finite difference method.

The agreement between the sharp interface model and the phase-field model depends strongly on the value of ε_S . This is shown by figure 9.3 in which all the parameters are identical to those in figure 9.1 except that $\varepsilon_S = dr = 0.1$. The disparity between the numerical solution to the phase-field and sharp-interface models was observed to increase monotonically with both ε_S and τ . Figure 9.3 does not indicate a sharp discontinuity in the temperature profile at the interface which in the phase-field model is positioned at approximately $\phi = 1/2$. The smooth nature of this figure close to $\phi = 1/2$ indicates the diffuse nature of the interface. It should also be observed that although the sharp interface solution at each time level is not coincident with the corresponding phase-field solution when $\varepsilon_S = 0.1$ the position of the interface is approximately coincident with the sharp-interface solution. This can be clearly seen by the dashed line in figure 9.3 which displays the position of $\phi = 1/2$ in the solution to the phase-field model. This curve is almost coincident with the discontinuities in the temperature profile of the sharp-interface Stefan model which denote the position of the interface

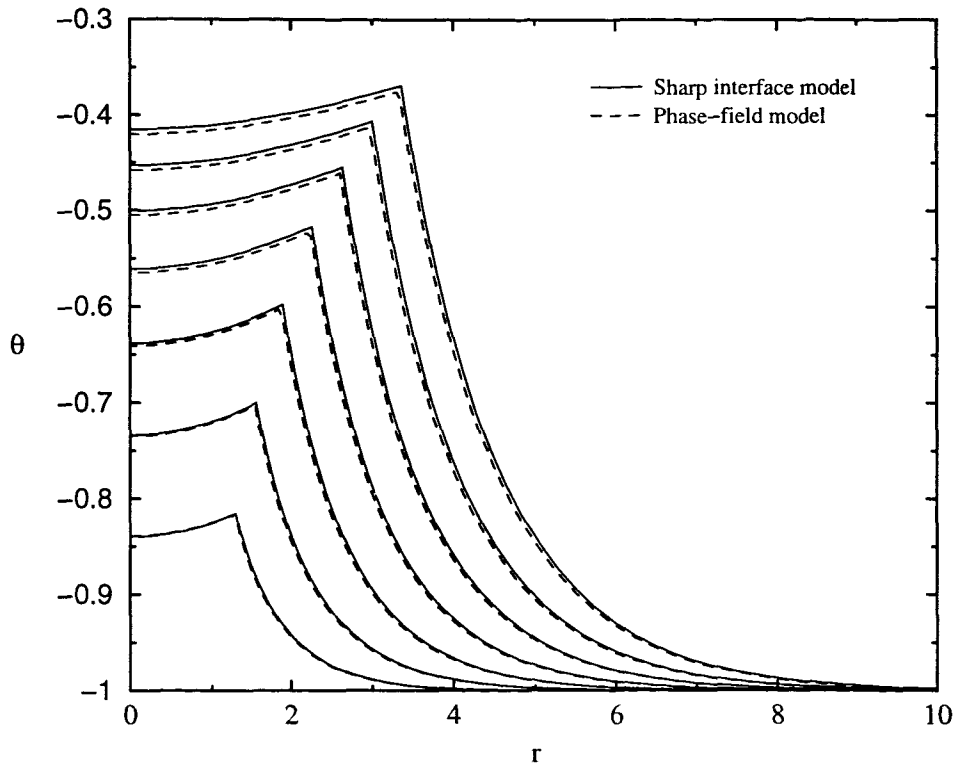


Figure 9.2: Comparison between the temperature profiles when $\tau = 5, 10, \dots, 30$ and 35 produced by the phase-field model with $\epsilon_S = 0.005$, $dr = 0.005$, $\Delta\theta = 0.5$ and $\xi = 1.0$ (i.e. $\mu = 434.78 \text{ cm/sec}^0C$ for P_4) and the corresponding Stefan model from chapter 7.

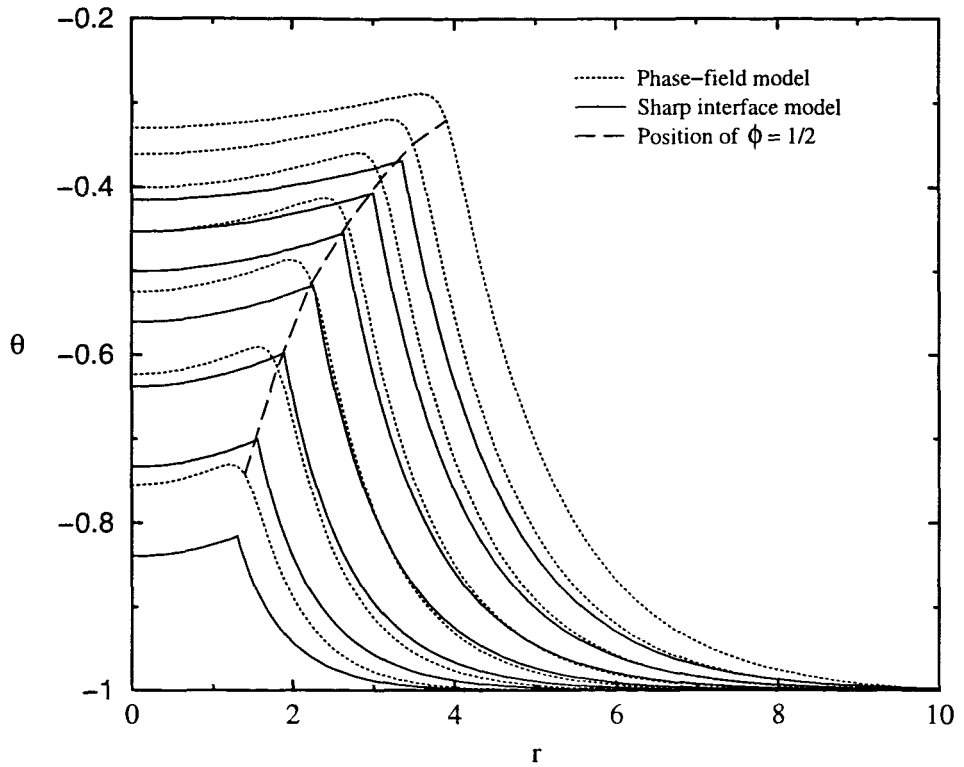


Figure 9.3: Comparison between the temperature profiles when $\tau = 5, 10, \dots, 30$ and 35 produced by the phase-field model with $\epsilon_S = 0.1$, $dr = 0.1$, $\Delta\theta = 0.5$ and $\xi = 1.0$ (i.e. $\mu = 434.78 \text{ cm/sec } ^\circ\text{C}$ for P_4) and the corresponding Stefan model.

at successive time levels.

9.3 Phase-field equations with flow

We now consider the non-dimensionalised phase-field equations (8.68), (8.69), (8.70) and (8.71) which include flow due to a change in density on solidification. As presented in the previous chapter this system of equations is given by

$$\bar{\rho}_\tau(\phi) + \bar{u}\bar{\rho}_{\bar{R}}(\phi) = -\bar{\rho}(\phi) \left(\frac{\partial \bar{u}}{\partial \bar{R}} + \frac{2}{\bar{R}}\bar{u} \right), \quad (9.17)$$

$$\frac{\varepsilon_S^2}{X} [\phi_\tau + \bar{u}\phi_{\bar{R}}] = \varepsilon_S^2 \bar{\nabla}^2 \phi + Y \varepsilon_S \bar{p}'(\phi) + C_{pf}(\bar{p} - \bar{p}_0) \frac{\bar{p}'(\phi)}{\bar{\rho}(\phi)} - \frac{1}{4} H'(\phi) \bar{\rho}(\phi), \quad (9.18)$$

$$\begin{aligned} \bar{\rho}(\phi)[\bar{u}_\tau + \bar{u}\bar{u}_{\bar{R}}] &= -\frac{\partial \bar{p}}{\partial \bar{R}} - \varepsilon_S^2 C_{M1} \left\{ \frac{\partial}{\partial \bar{R}} \left[\left(\frac{\partial \phi}{\partial \bar{R}} \right)^2 \right] + \frac{2}{\bar{R}} \left(\frac{\partial \phi}{\partial \bar{R}} \right)^2 \right\} \\ &\quad + \varepsilon_S C_{M2} \left\{ \frac{\partial}{\partial \bar{R}} \left[\bar{\mu}(\phi) \frac{\partial \bar{u}}{\partial \bar{R}} + \bar{\lambda}(\phi) \left(\frac{\partial \bar{u}}{\partial \bar{R}} + \frac{2}{\bar{R}}\bar{u} \right) \right] \right. \\ &\quad \left. + \frac{2}{\bar{R}} \left[2\bar{\mu}(\phi) \frac{\partial \bar{u}}{\partial \bar{R}} + \bar{\lambda}(\phi) \left(\frac{\partial \bar{u}}{\partial \bar{R}} + \frac{2}{\bar{R}}\bar{u} \right) \right] \right\} \end{aligned} \quad (9.19)$$

and

$$\bar{\rho}(\phi) [\bar{e}_\tau + \bar{u}\bar{e}_{\bar{R}}] = \frac{1}{4} \left\{ \frac{\partial^2 \theta}{\partial \bar{R}^2} + \frac{2}{\bar{R}} \frac{\partial \theta}{\partial \bar{R}} \right\}, \quad (9.20)$$

where \bar{e}_τ and $\bar{e}_{\bar{R}}$ are

$$\bar{e}_\tau = \theta_\tau + \left[-r'(\phi) + \frac{1}{4L} \left(\frac{1}{a_S} + \frac{1}{a} \right) H'(\phi) + C_{T3} \bar{p}_0 \frac{\bar{p}'(\phi)}{[\bar{\rho}(\phi)]^2} \right] \phi_\tau$$

and

$$\bar{e}_{\bar{R}} = \theta_{\bar{R}} + \left[-r'(\phi) + \frac{1}{4L} \left(\frac{1}{a_S} + \frac{1}{a} \right) H'(\phi) + C_{T3} \bar{p}_0 \frac{\bar{p}'(\phi)}{[\bar{\rho}(\phi)]^2} \right] \phi_{\bar{R}}.$$

The coefficients X , Y , C_{M1} , C_{M2} , C_{pf} and C_{T1} are given by

$$\begin{aligned} X &= \frac{\delta^2 \theta \rho_{SL}}{4\kappa_{SL} M a \theta_m}, & Y &= \frac{aL(\theta - \theta_m)R^*}{\theta \delta}, \\ C_{M1} &= \frac{(R^*)^2 \theta}{2a\theta_m (4\kappa_{SL})^2}, & C_{M2} &= \frac{\nu_{SL}}{\varepsilon_S \rho_{SL} 4\kappa_{SL}} \\ C_{pf} &= a \left(\frac{4\kappa_{SL}}{R^*} \right)^2 & \text{and} & \quad C_{T1} = \frac{\theta}{2aL\theta_m}. \end{aligned}$$

Using the approximation $\theta = \theta_m(1 + \delta_\theta)$, described in section 9.2, to leading order in δ_θ we can express X , Y , C_{M1} and C_{T1} as

$$X = \frac{\delta^2 \rho_{SL}}{4\kappa_{SL} M a}, \quad Y = \frac{\bar{\theta}}{3\sqrt{2}}, \quad C_{M1} = \frac{(R^*)^2}{2a(4\kappa_{SL})^2}$$

and

$$C_{T1} = \frac{1}{2aL}.$$

The pressure, however, is not considered in the sharp interface Stefan model discussed in chapter 7. Therefore we remove the pressure variable from the system of equations (9.17), (9.18), (9.19) and (9.20) by assuming that the pressure \bar{p} does not significantly change from the constant reference pressure \bar{p}_0 , i.e. we assume that there is a constant pressure field (the assumption made by Chambré in [25]). In this case therefore, the term $\bar{p} - \bar{p}_0$ is removed from equation (9.18), $\partial\bar{p}/\partial\bar{R}$ from equation (9.19) and \bar{p}_0 from (9.20). Since the pressure variable has now been removed from the system we no longer need to evaluate the momentum equation (9.19), so the simplified system of equations become

$$\bar{\rho}_\tau(\phi) + \bar{u}\bar{\rho}_{\bar{R}}(\phi) = -\bar{\rho}(\phi) \left(\frac{\partial\bar{u}}{\partial\bar{R}} + \frac{2}{\bar{R}}\bar{u} \right), \quad (9.21)$$

$$\frac{\varepsilon_S^2}{X} [\phi_\tau + \bar{u}\phi_{\bar{R}}] = \varepsilon_S^2 \bar{\nabla}^2 \phi + Y\varepsilon_S \bar{p}'(\phi) - \frac{1}{4} H'(\phi) \bar{\rho}(\phi) \quad (9.22)$$

and

$$\bar{\rho}(\phi) \left\{ \bar{\theta}_\tau + \bar{u}\bar{\theta}_{\bar{R}} - \frac{r'(\phi)}{\Delta\theta} [\phi_\tau + \bar{u}\phi_{\bar{R}}] \right\} = \frac{1}{4} \left\{ \frac{\partial^2\bar{\theta}}{\partial\bar{R}^2} + \frac{2}{\bar{R}} \frac{\partial\bar{\theta}}{\partial\bar{R}} \right\} \quad (9.23)$$

where for simplicity we apply the condition $a_S = -a$ and the temperature $\bar{\theta}$ has been rescaled in terms of the super-cooling $\Delta\theta$ according to (9.6).

9.3.1 Finite differences

The system of equations (9.21), (9.22) and (9.23) can be solved explicitly. The first and second derivatives in equations (9.22) and (9.23) are approximated by forward time and central space finite differences except for the terms $\bar{u}\phi_{\bar{R}}$ and $\bar{u}\bar{\theta}_{\bar{R}}$. These derivatives are approximated by up-wind and down-wind differences depending on the sign of their velocity coefficient \bar{u} .

Therefore equation (9.22) becomes

$$\begin{aligned} \frac{\varepsilon_S^2}{X} \left[\frac{\phi_r^{\tau+d\tau} - \phi_r^\tau}{d\tau} + \bar{u} \frac{\partial\phi}{\partial\bar{R}} \right] &= \varepsilon_S^2 \left(\frac{\phi_{r+d}^\tau - 2\phi_r^\tau + \phi_{r-d}^\tau}{(dr)^2} + \frac{2}{r} \frac{\phi_{r+d}^\tau - \phi_{r-d}^\tau}{2dr} \right) \\ &+ Y\varepsilon_S \bar{p}'(\phi_r^\tau) - \frac{1}{4} H'(\phi_r^\tau) \bar{\rho}(\phi_r^\tau) \end{aligned} \quad (9.24)$$

where the non-standard one-sided finite difference approximations (7.42) and (7.41), which were derived in chapter 7, have been used to approximate $\partial\phi/\partial\bar{R}$. Specifically

$$\bar{u} \frac{\partial\phi}{\partial\bar{R}} = \bar{u}_r^\tau \frac{3\phi_r^\tau - 4\phi_{r-d}^\tau + \phi_{r-2d}^\tau}{2dr} \quad \text{if } \bar{u} > 0 \quad (9.25)$$

and

$$\bar{u} \frac{\partial\phi}{\partial\bar{R}} = \bar{u}_r^\tau \frac{-3\phi_r^\tau + 4\phi_{r+d}^\tau - \phi_{r+2d}^\tau}{2dr} \quad \text{if } \bar{u} < 0. \quad (9.26)$$

Similarly (9.23) becomes

$$\begin{aligned} \bar{\rho}(\phi_r^\tau) \left[\frac{\bar{\theta}_r^{\tau+d\tau} - \bar{\theta}_r^\tau}{d\tau} + \bar{u} \frac{\partial \bar{\theta}}{\partial \bar{R}} - r'(\phi_r^\tau) \left(\frac{\phi_r^{\tau+d\tau} - \phi_r^\tau}{d\tau} + \bar{u} \frac{\partial \phi}{\partial \bar{R}} \right) \right] \\ = \frac{1}{4} \left[\frac{\bar{\theta}_{r+d\tau}^{\tau+d\tau} - 2\bar{\theta}_r^{\tau+d\tau} + \bar{\theta}_{r-d\tau}^{\tau+d\tau}}{(dr)^2} + \frac{2}{r} \frac{\bar{\theta}_{r+d\tau}^{\tau+d\tau} - \bar{\theta}_{r-d\tau}^{\tau+d\tau}}{2dr} \right] \end{aligned} \quad (9.27)$$

and the one-sided finite difference approximations (9.25) and (9.26) have been used to approximate $\bar{u}\partial\phi/\partial\bar{R}$ and $\bar{u}\partial\bar{\theta}/\partial\bar{R}$ (by replacing ϕ with θ in equations (9.25) and (9.26)). Equation (9.21) denotes conservation of mass in terms of the phase-field variable. Obtaining a solution to this equation requires special treatment since it does not contain a time derivative in the non-dimensional velocity \bar{u} , the remaining unknown variable at the new time step. Many finite difference formulations were attempted to solve this equation. By this stage in the numerical solution $\bar{\theta}_r^{\tau+d\tau}$ and $\phi_r^{\tau+d\tau}$ are known at all spatial grid points and therefore it is possible to employ a Crank-Nicolson formulation explicitly, however this approach produced highly unstable numerical oscillations and no convergent averaging method could be found.

A leapfrog method evaluated at the new time-step, which approximates (9.21) by

$$\bar{\rho}'(\phi_r^{\tau+d\tau}) \left[\frac{\phi_r^{\tau+d\tau} - \phi_r^\tau}{d\tau} + \bar{u}^{\tau+d\tau} \frac{\phi_r^{\tau+d\tau} - \phi_{r-d\tau}^{\tau+d\tau}}{2dr} \right] = -\bar{\rho}(\phi_r^{\tau+d\tau}) \left(\frac{\bar{u}_r^{\tau+d\tau} - \bar{u}_{r-d\tau}^{\tau+d\tau}}{2dr} + \frac{2}{r} \bar{u}_r^{\tau+d\tau} \right)$$

produced solutions if the first n time steps (where $n \geq 100$) were linearly smoothed in the updating procedure. However solutions at large τ were extremely difficult to obtain due to the instability of this method.

Attempts were also made to integrate equation (9.21) directly and find $\bar{u}^{\tau+d\tau}$ using numerical quadrature via NAG routine D01GAF. However no sensible solutions could be obtained using this approach. A convergent, stable integration technique was eventually found by substituting (9.22) into equation (9.21) to give

$$\begin{aligned} \bar{\rho}'(\phi) \left(\frac{\partial \phi}{\partial \tau} + \bar{u} \frac{\partial \phi}{\partial r} \right) &= \bar{\rho}'(\phi) \left[X \left(\frac{\partial^2 \phi}{\partial r^2} + \frac{2}{r} \frac{\partial \phi}{\partial r} \right) + \frac{XY}{\epsilon_S} \bar{p}'(\phi) - \frac{X}{4\epsilon_S^2} H'(\phi) \bar{\rho}(\phi) \right] \\ &= -\bar{\rho}(\phi) \frac{1}{r^2} \frac{\partial}{\partial r} (r^2 \bar{u}). \end{aligned} \quad (9.28)$$

Subsequently integrating (9.28) leaves

$$\begin{aligned} \bar{u}_r^{\tau+d\tau} &= \frac{1}{r^2} \int_0^r r^2 \frac{\bar{\rho}'(\phi_r^{\tau+d\tau})}{\bar{\rho}(\phi_r^{\tau+d\tau})} \left[X \left(\frac{\partial^2 \phi_r^{\tau+d\tau}}{\partial r^2} + \frac{2}{r} \frac{\partial \phi_r^{\tau+d\tau}}{\partial r} \right) \right. \\ &\quad \left. + \frac{XY}{\epsilon_S} \bar{p}'(\phi_r^{\tau+d\tau}) - \frac{X}{4\epsilon_S^2} H'(\phi_r^{\tau+d\tau}) \bar{\rho}(\phi_r^{\tau+d\tau}) \right] dr \end{aligned} \quad (9.29)$$

and using $\phi_r^{\tau+d\tau}$ and $\bar{\theta}_r^{\tau+d\tau}$, which are known at every position step in \bar{r} , equation (9.29) can be discretised by

$$\bar{u}_r^{\tau+d\tau} = \frac{1}{r^2} \int_0^r r^2 \frac{\bar{\rho}'(\phi_r^{\tau+d\tau})}{\bar{\rho}(\phi_r^{\tau+d\tau})} \left[X \left(\frac{\phi_r^{\tau+d\tau} - 2\phi_r^{\tau+d\tau} + \phi_{r-d\tau}^{\tau+d\tau}}{(dr)^2} + \frac{2}{r} \frac{\phi_{r+d\tau}^{\tau+d\tau} - \phi_{r-d\tau}^{\tau+d\tau}}{2dr} \right) \right]$$

$$+ \frac{XY}{\varepsilon_S} \bar{p}'(\phi_r^{\tau+d\tau}) - \frac{X}{4\varepsilon_S^2} H'(\phi_r^{\tau+d\tau}) \bar{\rho}(\phi_r^{\tau+d\tau}) \Big] dr \quad (9.30)$$

which is evaluated explicitly at the new time step using the trapezoidal rule [131].

An initial phase-field profile was obtained from the hyperbolic tangent solution (9.10) to the steady, isothermal phase-field equation without flow described by equation (9.11) and the stability restriction $d\tau \leq \varepsilon_S$ was observed.

9.3.2 Boundary conditions

The boundary conditions at $\bar{r} = 0$ and $\bar{r} = R$ (where R denotes the radius which is taken to represent the far-field) are identical to those imposed on the no-flow case discussed in the previous section. The velocity $\bar{u} = 0$ on $\bar{r} = 0$ is the only additional boundary condition.

Therefore on $\bar{r} = 0$ equations (9.21), (9.22) and (9.23) become

$$\bar{u} = 0, \quad (9.31)$$

$$\frac{\phi_0^{\tau+d\tau} - \phi_0^\tau}{d\tau} = 2X \frac{\phi_{dr}^\tau - \phi_0^\tau}{(dr)^2} + \frac{XY}{\varepsilon_S} \bar{p}'(\phi_0^\tau) - \frac{X}{4\varepsilon_S^2} H'(\phi_0^\tau) \quad (9.32)$$

and

$$\frac{\bar{\theta}_0^{\tau+d\tau} - \bar{\theta}_0^\tau}{d\tau} = \frac{1}{2} \frac{\bar{\theta}_{dr}^\tau - \bar{\theta}_0^\tau}{(dr)^2} - \frac{1}{\Delta\theta} \bar{p}'(\phi_0^\tau) \frac{\phi_0^{\tau+d\tau} - \phi_0^\tau}{d\tau}. \quad (9.33)$$

In the far field (which we have taken to be $\bar{r} = R = 10$) equations (9.21), (9.22) and (9.23) become

$$\begin{aligned} \bar{u}_R^{\tau+d\tau} = & \frac{1}{R^2} \int_0^R r^2 \frac{\bar{p}'(\phi_r^{\tau+d\tau})}{\bar{\rho}(\phi_r^{\tau+d\tau})} \left[2X \frac{\phi_{R-dr}^{\tau+d\tau} - \phi_R^{\tau+d\tau}}{(dr)^2} \right. \\ & \left. + \frac{XY}{\varepsilon_S} \bar{p}'(\phi_R^{\tau+d\tau}) - \frac{X}{4\varepsilon_S^2} H'(\phi_R^{\tau+d\tau}) \bar{\rho}(\phi_R^{\tau+d\tau}) \right] dr, \quad (9.34) \end{aligned}$$

$$\frac{\phi_R^{\tau+d\tau} - \phi_R^\tau}{d\tau} = 2X \frac{\phi_{R-dr}^\tau - \phi_R^\tau}{(dr)^2} + \frac{XY}{\varepsilon_S} \bar{p}'(\phi_R^\tau) - \frac{X}{4\varepsilon_S^2} H'(\phi_R^\tau) \quad (9.35)$$

and

$$\frac{\bar{\theta}_R^{\tau+d\tau} - \bar{\theta}_R^{\tau+d\tau}}{d\tau} = \bar{u}_R^\tau \frac{\bar{\theta}_R^\tau + 1}{R} - \frac{1}{\Delta\theta} \bar{p}'(\phi_R^\tau) \left(\frac{\phi_R^{\tau+d\tau} - \phi_R^\tau}{d\tau} \right) \quad (9.36)$$

where we have used boundary conditions (9.14) for the spatial derivatives.

9.3.3 Solution method

Equations (9.24), (9.27) and (9.30) were solved subject to boundary conditions (9.31) to (9.36). We initially set the parameters μ , ε_S , $R(0)$, ρ_S and ρ_L and then:

- equation (9.24) was evaluated at every position step, calculating $\phi_r^{\tau+d\tau}$ for all $0 \leq \bar{r} \leq R$

- next equation (9.27) was evaluated at every position step, calculating $\bar{\theta}_r^{\tau+d\tau}$ for all $0 \leq \bar{r} \leq R$
- and finally the integral in equation (9.30) was evaluated at every position step, and using the trapezoidal rule $\bar{u}_r^{\tau+d\tau}$ was calculated for all $0 \leq \bar{r} \leq R$.

Finally results were recorded at specific time steps.

9.3.4 Results and discussion

After extensive testing and developing of this program we were unable to obtain results which could be compared to the sharp-interface Stefan model with flow described in chapter 7 when the expression for the density in equations (9.22) and (9.23) was dependent on the phase-field variable ϕ . A small difference between the density of the solid and liquid phases caused a large velocity in the liquid phase which significantly affected the numerical solution to the temperature profiles. This situation is shown in figure 9.4 where the phase-field solution is obtained by using the leapfrog method and the non-dimensional interface thickness $\varepsilon_S = 0.01$, $dr = 0.0025$ and the difference between the density of the solid and liquid phases was 0.02 g/cm^3 . The mobility of the interface μ was set to $434.78 \text{ cm/sec } ^\circ\text{C}$ which is the required value for the non-dimensional parameter ξ to be 1.0, and the results are shown at times $\tau = 0.5, 1.0$ and 1.5 . The upper dashed lines display results obtained when $\rho_L = 1.823 \text{ g/cm}^3$, $\rho_S = 1.803 \text{ g/cm}^3$ and therefore $\epsilon = (\rho_L - \rho_S)/\rho_L = 0.011$. The lower dotted lines display results obtained when $\rho_L = 1.803 \text{ g/cm}^3$, $\rho_S = 1.823 \text{ g/cm}^3$ and therefore $\epsilon = -0.011$. The sharp interface solution without flow is shown by the dots on the figure. However the sharp interface solution with flow is not displayed since the density differences used in the phase-field model in this figure made no appreciable difference to the temperature profiles obtained by the sharp interface model.

The asymptotic analysis in chapter 8 shows that the interfacial boundary condition which was obtained from the phase-field model in the sharp interface limit contained leading order errors which were proportional to the difference between the solid and liquid densities. We observed in chapter 7 that the equations at the solid/liquid interface were sensitive to small changes in the initial conditions and the finite difference method which was used to evaluate them. In [21] Caginalp and Socolovsky work with the ansatz that the phase-field model is more sensitive to small changes in the surface tension σ than the interfacial thickness ε_S . The surface tension term appears only in the interfacial Gibbs-Thompson equation in the sharp interface model described in chapter 7. If, therefore, the leading order error in the Gibbs-Thompson equation in the sharp-interface limit of the phase-field model is interpreted as a small change in the surface tension gradient then figure 9.4 indicates the validity of Caginalp and Socolovsky's ansatz [21]. To reduce the leading order difference between the

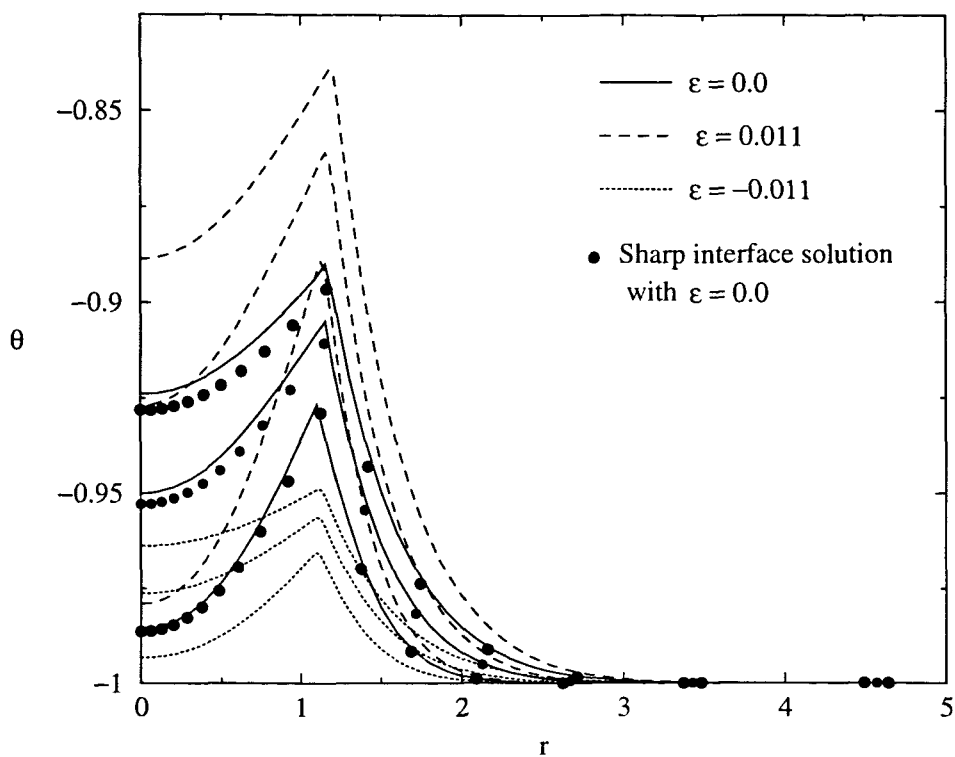


Figure 9.4: Comparison between the temperature profiles when $\tau = 0.5, 1.0$ and 1.5 produced by the phase-field model with flow when $\epsilon_S = 0.01$, $dr = 0.0025$, $\Delta\theta = 0.5$, $\xi = 1.0$ (i.e. $\mu = 434.78 \text{ cm/sec } ^\circ\text{C}$ for P_4) and $\epsilon = -0.011, 0.0$ and 0.011 and the corresponding Stefan model from chapter 7.

Gibbs-Thompson equation and the equation obtained from the sharp interface limit of the phase-field model the density, which can be written as

$$\bar{\rho}(\phi) = 1.0 + \epsilon r(\phi)$$

where $\epsilon = (\rho_L - \rho_S)/\rho_L$ (replacing ρ_{SL} with ρ_L for simplicity) can be replaced with $\bar{\rho}(\phi) = 1.0$, to leading order in ϵ , in equations (9.22) and (9.23). Using this density approximation the temperature profiles of the phase-field model with flow at $\tau = 5$ and 10 when the normalised super-cooling $\Delta\theta = 0.5$ and $\xi = 1.0$ are shown in figure 9.5. Growth was initiated by setting the initial radius 10% above the critical radius (i.e. $\phi = 1/2$ when $\bar{r} = (1 + \delta_r)$ where $\delta_r = 0.1$) and the non-dimensional interface thickness parameter ϵ_S and mesh spacing Δr , were set to 0.02 .

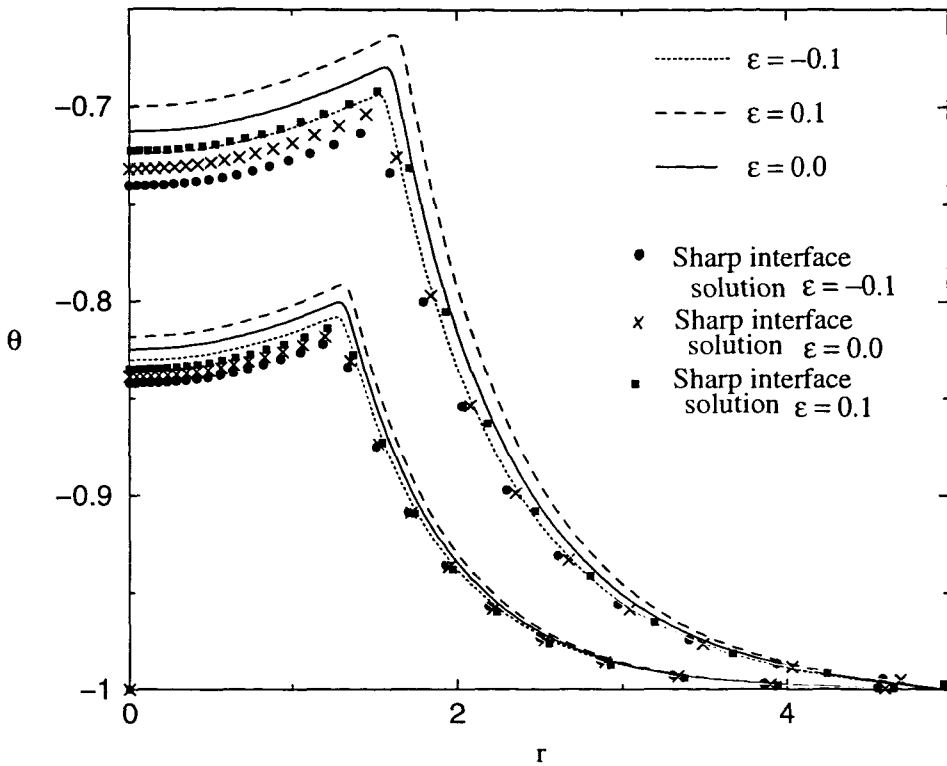


Figure 9.5: Comparison between the temperature profiles when $\tau = 5.0$ and 10.0 produced by the phase-field model with $\epsilon_S = 0.02$, $dr = 0.02$, $\Delta\theta = 0.5$ and $\xi = 1.0$ (i.e. $\mu = 434.78 \text{ cm/sec}^0\text{C}$ for P_4) when $\epsilon = 0.1, 0.0$ and -0.1 .

The upper dashed lines show the temperature profiles for $\rho_L = 2.026 \text{ g/cm}^3$ and $\rho_S = 1.823 \text{ g/cm}^3$ (when $\epsilon = (\rho_L - \rho_S)/\rho_L = 0.1$). The lower dotted lines show the temperature profiles for $\rho_L = 1.657 \text{ g/cm}^3$ and $\rho_S = 1.823 \text{ g/cm}^3$ (when $\epsilon = -0.1$) and the solid lines show the temperature profiles for $\rho_L = \rho_S = 1.823 \text{ g/cm}^3$ (when $\epsilon = 0.0$). The dots, crosses and squares show the solutions to the equivalent sharp-interface model (at $\tau = 5.0$ and 10.0)

when $\epsilon = -0.1, 0.0$ and 0.1 respectively. Clearly, with reference to the figures in section 9.2.4, a small yet significant disparity is expected between the temperature profiles obtained using these two methods when the interface thickness $\epsilon_S = 0.02$. This difference can be seen clearly on figure 9.5. However, even with ϵ_S two times larger than the value in figure 9.4, the disparity between these two methods is greatly reduced.

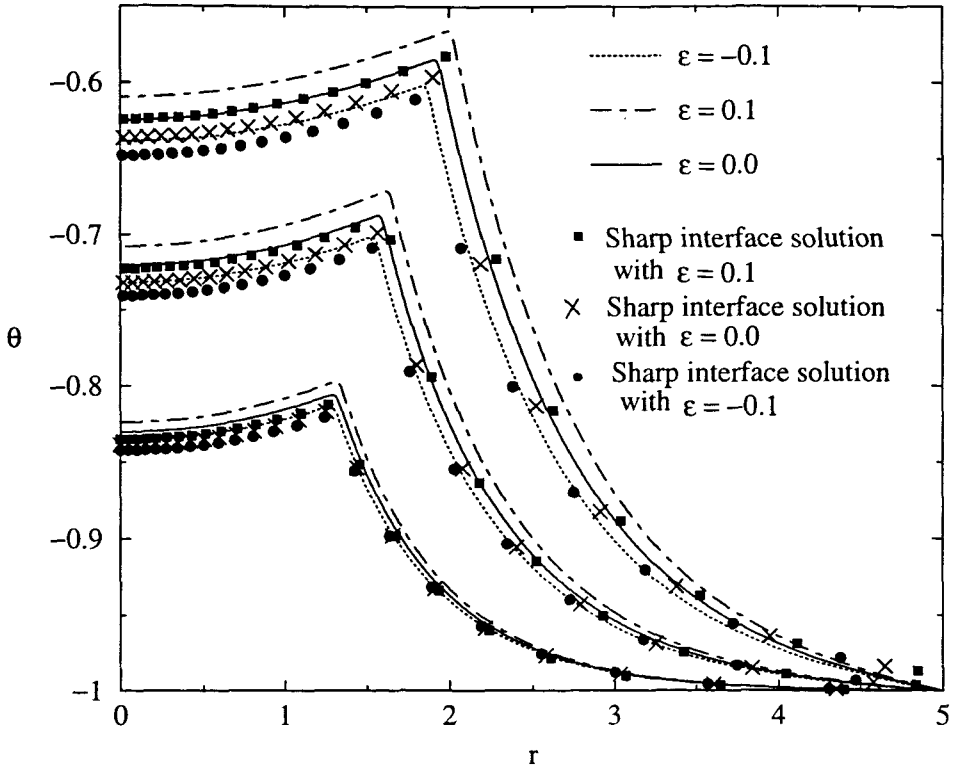


Figure 9.6: Comparison between the temperature profiles when $\tau = 5.0, 10.0$ and 15.0 produced by the phase-field model with $\epsilon_S = 0.01, dr = 0.01, \Delta\theta = 0.5$ and $\xi = 1.0$ (i.e. $\mu = 434.78 \text{ cm/sec}^{\circ}\text{C}$ for P_4) when $\epsilon = 0.1, 0.0$ and -0.1 .

Figure 9.6 shows a comparison between the temperature profiles when $\tau = 5.0, 10.0$ and 15.0 produced by the phase-field model with $\epsilon_S = 0.01, dr = 0.01, \Delta\theta = 0.5$ and $\xi = 1.0$. The dots, crosses and squares show the corresponding solutions to the equivalent sharp-interface model (at $\tau = 5.0, 10.0$ and 15.0) when $\epsilon = -0.1, 0.0$ and 0.1 respectively. Clearly with $\epsilon_S = 0.01$ a small disparity persists between the temperature profiles obtained using these two methods (as expected from figure 9.1 in section 9.2.4). However, the difference between the temperature profiles obtained using the Stefan model with flow and the phase-field model when $\epsilon_S = 0.01$, shown in figure 9.6 is significantly smaller than in figure 9.5 when the phase-field model was evaluated with $\epsilon_S = 0.02$. Unfortunately it required two weeks continuous running time on three Pentium II desktop machines to obtain figure 9.6. Therefore reducing ϵ_S any further is not practical using this explicit method. However it is clear from figures 9.7,

9.5 and 9.6 that the disparity between the temperature profiles obtained via these methods is decreasing with ϵ_S in an identical way to the section 9.2. Therefore we expect very close agreement if the non-dimensional interface thickness is reduced further.

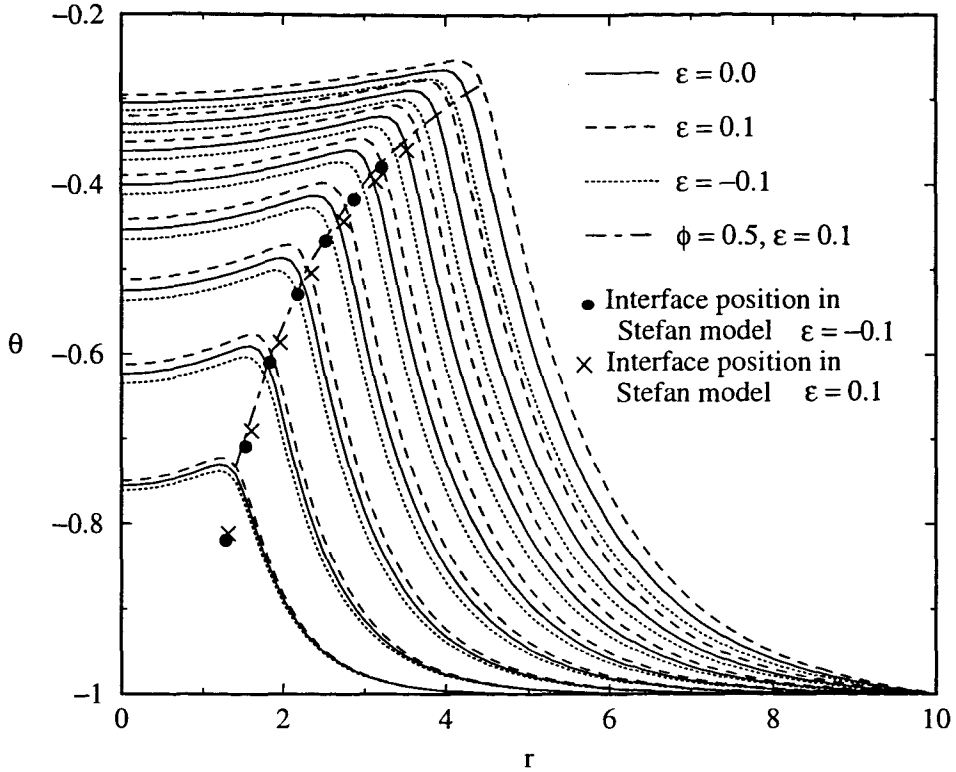


Figure 9.7: Comparison between the temperature profiles when $\tau = 5, 10, \dots, 35$ and 40 produced by the phase-field model with $\epsilon_S = 0.1$, $dr = 0.1$, $\Delta\theta = 0.5$ and $\xi = 1.0$ (i.e. $\mu = 434.78 \text{ cm/sec } ^\circ\text{C}$ for P_4) when $\epsilon = 0.1, 0.0$ and -0.1 .

Figure 9.7 shows the temperature profiles of the phase-field model with flow at $\tau = 5, 10, \dots, 35$ and 40 when the normalised super-cooling $\Delta\theta = 0.5$, $\xi = 1.0$ and $\epsilon_S = \Delta r = 0.1$. The density differences are identical to figure 9.6. The smooth temperature profile near $\phi = 1/2$ indicates the diffuse nature of the interface. A significant disparity exists between the temperature profiles obtained using these models since the disparity between the sharp interface and phase-field models is strongly dependent on ϵ_S . Therefore with $\epsilon_S = 0.1$ However the qualitative forms of the phase-field solutions with flow strongly resemble the sharp interface solutions with flow displayed in figure 7.8 in chapter 7. The dot-dashed line displays the temperature and position of $\phi = 1/2$ in the phase-field model when $\epsilon = 0.1$. The equivalent curve obtained when $\epsilon = -0.1$ is not displayed since it was almost identical to the curve shown in the figure. This suggests that the presence of flow in the system does not affect the temperature-position curve followed by the interface, only the velocity and subsequently temperature of the interface at any given time level. (Note that the line $\phi = 1/2$, $\epsilon = 0.1$

has been obtained by linear interpolation between data points in the phase-field model and therefore is slightly inaccurate). The crosses and dots display the position of the interface (shown as a discontinuity in the temperature profiles of figure 7.8) in the sharp interface Stefan model when $\epsilon = 0.1$ and -0.1 respectively. These points correspond to the position of the interface at $\tau = 5, 10, \dots, 30$ and 35 . It is clear, by inspection, that these points are almost coincident with the phase-field curve.

Chapter 10

Conclusions

A variety of problems have been considered in this thesis. In the first five chapters the solution and stability of flows in liquid steel driven by Lorentz, Marangoni and buoyancy forces were investigated. In the remainder of the thesis a diffuse interface phase-field model with flow, recently derived by Anderson *et al.* [2], was investigated for a freezing sphere.

In chapter 2 the numerical similarity solution for the steady flow induced by a point source of current and heat on the free surface of a semi-infinite region of ITEV fluid was described. This model was derived recently by Belgrove and Craine in [7] and [30]. An asymptotic solution for their model was obtained, to leading and first orders, when the surface tension gradient, $\partial\gamma/\partial T$, was negative and $O(10^{-4})$. The latter value represents the largest magnitude that occurs in practical situations in welding (see [59]). A narrow viscous shear layer was required near the free surface and it was shown that all the coefficients of the leading and first order expressions in the composite asymptotic expression for the temperature distribution and the streamfunction were dependent on $\partial\gamma/\partial T$. Excellent agreement between the asymptotic solution and the numerical similarity solution was obtained for a surprisingly large range of values of current J and negative $\partial\gamma/\partial T$. Using this asymptotic solution we obtained an analytical expression which indicated when the transition between one-loop and two-loop flow occurred. The results confirmed the numerical solutions in [7] and [30] and demonstrated the strong effect of the thermocapillary (Marangoni) force on the free surface. They also demonstrated how the Marangoni force opposes the Lorentz force and therefore increases the value of the current at which the semi-infinite point source model breaks down (i.e. when the velocity develops singularities on the axis of symmetry).

In chapter 3 we described a two-dimensional, stationary, steady-state model, presented first in [7], for the flow of ITEV fluid in a hemisphere induced by a point source of current and heat on the free surface. The model included the Lorentz force, the thermocapillary (Marangoni) force on the free surface and the buoyancy force, and was solved numerically

using finite difference methods. The results showed that the breakdown current depended strongly on the value of $\partial\gamma/\partial T$.

In chapter 4 a linear stability analysis for the azimuthal mode $m = 0$ was performed on the solution for the flow and temperature distributions in the hemisphere, obtained numerically using the model in chapter 3. This stability analysis allowed for the possibility of bifurcation to a rotating flow, an effect which was absent from the hemisphere solution described in chapter 3. The equation governing the linear stability of the rotating motion was observed to decouple from the poloidal stability equations, and hence both systems were considered separately using finite difference methods. The results indicated that the two-dimensional steady-state poloidal flow became unstable to azimuthal and poloidal perturbations at almost identical current values when $\partial\gamma/\partial T \approx -10^{-6}$. As the magnitude of the negative surface tension gradient was increased, i.e. $\partial\gamma/\partial T < -10^{-6}$, the steady-state solution in the hemisphere became unstable to azimuthal and poloidal perturbations at progressively smaller current values. On the other hand when $|\partial\gamma/\partial T| < 10^{-6}$ no azimuthal instability was detected at any value of the current J below that at which the steady-state model broke down. However, at these magnitudes of the surface tension gradient the underlying steady-state model remained unstable to poloidal perturbations at critical current values, J_{crit} , which were dependent on the magnitude of $\partial\gamma/\partial T$. When $\partial\gamma/\partial T > 10^{-6}$ no azimuthal or poloidal instability was detected at any current value. An investigation of the eigenvectors at the onset of instability revealed that the flow became unstable at a position close to the point source of heat and current in both the azimuthal and poloidal stability systems. It can be conjectured, therefore, that the stationary steady-state model of ITEV fluid in a hemisphere became unstable to azimuthal and/or poloidal disturbances of mode $m = 0$ near to the point source of heat and current.

The upper modes of stability $m = 1, 2$ and 3 were considered in chapter 5. For these modes it was shown that, unlike the $m = 0$ case, the azimuthal and poloidal stability systems did not now de-couple. However, when $m = 1, 2$ and 3 the steady-state model did not become unstable for any parameter values for which the underlying steady-state model converged, apart from a very small region in which $\partial\gamma/\partial T \approx -O(10^{-6})$, $m = 1$ and the current was just below the breakdown current.

Clearly the stability of the stationary, steady-state model is dependent on the flow in the hemisphere in a non-trivial way.

There are many possible extensions to the welding models considered in this thesis, some of these are outlined below:

- The welding problem could be extended by introducing a distributed source of heat and current on the free surface and then performing a stability analysis similar to the one

described in this thesis. The literature on analogous problems suggests that, in this case, the model would converge for a much larger range of current values and moreover the eigenvectors found in chapter 4 indicate a secondary flow which is strongest near to the point source. Therefore the point source may be the cause of the instability of the model at unrealistically low current values and a significant difference in the stability results might then arise if we use a distributed source of heat and current.

- At certain parameter values, such as those which correspond to the presence of a large Marangoni force on the free surface, the isotherms are not spherical and in this case the pool of liquid metal would also be aspherical. It would be instructive therefore to consider the stability of the steady-state flow in a spheroid, the shape of which can be determined from the isotherms of the semi-infinite model, as a first approximation to solving the fully coupled problem.
- The effect of a back emf on the steady-state welding model is not considered in this thesis. This exclusion relies upon the anzatz that the velocity of the liquid metal in the pool is small. However the velocity of the steady-state model described in this thesis is not small when the current is close to the critical value at which break down occurs. Including a back electro-magnetic force, therefore, could change the solution and/or the stability characteristics of the steady-state model.
- The material parameters, such as density and viscosity, are taken to be fixed average values in the welding models described in this thesis. Significant changes to the steady-state solutions might occur if the values of these material parameters were made temperature dependent.
- Although experimental evidence suggests that the free surface of the weld pool is flat at low current values it remains to be proven that this assumption is true for the model described in this thesis.
- For certain values of $\partial\gamma/\partial T$ the Reynolds number is large at current values where the steady-state model fails to converge. This may indicate turbulent flow, which could also be considered in the model.

By introducing some or all of the above extensions the velocity and/or temperature distributions of the steady-state model and their associated stability characteristics may be significantly altered.

In chapters 6 to 9 a different problem was considered, namely the solidification of a growing sphere of solid in a super-cooled melt with a density change on solidification. In chapter 7 a sharp-interface Stefan model, which describes the solidification process of an initial embryo

of solid with a disparity between the density of the solid and liquid phases, was derived and then solved numerically using a finite difference method. In this model the temperature of the interface was defined by the Gibbs-Thompson equation, with linear interface attachment kinetics, and the velocity of the interface by the latent heat equation, obtained through conservation of energy. When there is no density change on solidification the results agreed closely with the model of Schaefer and Glicksman [95]. When a density change was included, the temperature profiles obtained in chapter 7 were lower than the no-flow case when the flow was directed toward the solid phase, whereas the opposite is true for flow directed away from the growing solid phase. This effect is not unexpected since incoming super-cooled liquid will reduce the temperature of the solid/liquid boundary, whereas the temperature profiles will naturally rise when there is excess warmer fluid flowing away from the interface.

In chapter 8 an asymptotic analysis of the diffuse interface phase-field model with flow derived by Anderson *et al.* [2] was performed, when the thickness of this interface was vanishingly small, the so-called *sharp interface limit*. The one-dimensional isotropic case was considered and this reproduced, with one exception, the leading order asymptotic expressions for the Stefan model with flow derived in chapter 7. The equation which determined the temperature of the interface in this phase-field model was given by the non-planar, unsteady, temperature dependent Clausius-Clapeyron condition rather than the Gibbs-Thompson condition with linear interface attachment kinetics. However, it was shown in appendix B, that when the non-dimensional solid/liquid density difference, $\Delta(= \rho_l - \rho_s)/\rho_s$, is small the Clausius-Clapeyron relationship can be approximated, to leading order in Δ/ρ_s , by the modified Gibbs-Thompson condition.

Finally in chapter 9 the isotropic diffuse interface model of Anderson, McFadden and Wheeler [2] was solved numerically in one-dimension, and the numerical results were compared with those calculated in chapter 7. Firstly the case was considered where no difference exists between the density of the two phases. At consecutive time levels very close agreement was obtained between the temperature profiles produced with these two methods when the dimensionless interface thickness ε_S was chosen to be 0.01 in the diffuse interface model, and excellent agreement was obtained when ε_S equalled 0.005. By solving the phase-field model with flow in a constant pressure field and altering the phase-field equations so that density was kept fixed in the phase-field equation, the Clausius-Clapeyron relation given by the leading order expression in the sharp interface asymptotic limit could be replaced by the Gibbs-Thompson equation in this limit. Using this method solutions were obtained and compared with the numerical solution to the sharp interface Stefan model with flow, described in chapter 7. Close agreement was obtained between these models when the dimensionless interface thickness ε_S had the value 0.01.

A severe limiting restriction was observed on the numerical stability of the phase-field

model, namely that the numerical procedure used to obtain solutions to the diffuse-interface model became unstable near the interface when the grid spacing $\Delta r > \varepsilon_S$. A more efficient numerical procedure would involve using fine spacing close to the interface only and then a coarser grid everywhere else. The increased efficiency of this modified method must be balanced, however, against the requirement that the position of the interface would be needed in advance and, therefore, the numerical procedure would be significantly more complicated.

The phase-field model described in this thesis warrants further investigation. In the numerical work the effect of removing the constant pressure field restriction or the isotropic surface energy should be investigated and the numerical analysis could be extended to two-dimensions where dendritic shapes would be obtained. Extensions of the simpler case of planar geometry could also be investigated, by including for instance shear flows in the liquid phase, internal heat sources and confined geometries. An interesting approach to the welding problem considered in chapters 1 to 5 would be to use a diffuse-interface phase-field model with flow to describe the unsteady growth of a weld-pool for different interface thicknesses. The effects of surface tension, buoyancy and the Lorentz force could all be included in this approach and the results could then be compared with other models in the literature which employ a mushy layer (such as [79] or [86]).

Appendix A

Outer and inner asymptotic expansions of the phase-field equations with flow

A.1 Outer expansion

Substituting equations (8.78), (8.79), (8.80) and (8.81) into the non-dimensionalised phase-field equations (8.74), (8.75), (8.76) and (8.77) yields

$$\begin{aligned}
 & \left(\varphi_r^0 + \varepsilon_S \varphi_r^1 - \dot{r}_I \{ \varphi_r^0 + \varepsilon_S \varphi_r^1 \} \right) \left[\bar{\rho}'(\varphi^0) + \varepsilon_S \varphi^1 \bar{\rho}''(\varphi^0) \right] \\
 & + \left[\dot{r}_I + \hat{u}^0 + \varepsilon_S \hat{u}^1 \right] \left[\varphi_r^0 + \varepsilon_S \varphi_r^1 \right] \left[\bar{\rho}'(\varphi^0) + \varepsilon_S \varphi^1 \bar{\rho}''(\varphi^0) \right] \\
 & = - \left[\bar{\rho}(\varphi^0) + \varepsilon_S \varphi^1 \bar{\rho}'(\varphi^0) \right] \left[\left(\hat{u}_r^0 + \varepsilon_S \hat{u}_r^1 \right) + \frac{2}{r} \left(\hat{u}^0 + \varepsilon_S \hat{u}^1 \right) \right], \tag{A.1}
 \end{aligned}$$

$$\begin{aligned}
 & \left[\bar{\rho}(\varphi^0) + \varepsilon_S \varphi^1 \bar{\rho}'(\varphi^0) \right] \left[\left(\hat{u}_r^0 + \ddot{r}_I \right) + \varepsilon_S \hat{u}_r^1 + \left(\hat{u}^0 + \varepsilon_S \hat{u}^1 \right) \left(\hat{u}_r^0 + \varepsilon_S \hat{u}_r^1 \right) \right] \\
 & = - \left(\bar{p}_r^0 + \varepsilon_S \bar{p}_r^1 \right) - \varepsilon_S^2 \bar{C}_{M1} \left\{ \frac{\partial}{\partial r} \left(\varphi_r^0 + \varepsilon_S \varphi_r^1 \right)^2 + \frac{2}{r} \left(\varphi_r^0 + \varepsilon_S \varphi_r^1 \right)^2 \right\} \\
 & + \varepsilon_S C_{M2} \left\{ \frac{\partial}{\partial r} \left(2 \left[\bar{\mu}(\varphi^0) + \varepsilon_S \varphi^1 \bar{\mu}'(\varphi^0) \right] \left[\hat{u}_r^0 + \varepsilon_S \hat{u}_r^1 \right] \right. \right. \\
 & + \left. \left. \left[\bar{\lambda}(\varphi^0) + \varepsilon_S \varphi^1 \bar{\lambda}'(\varphi^0) \right] \left[\left(\hat{u}_r^0 + \varepsilon_S \hat{u}_r^1 \right) + \frac{2}{r} \left(\hat{u}^0 + \varepsilon_S \hat{u}^1 \right) \right] \right) \right. \\
 & + \frac{2}{r} \left(2 \left[\bar{\mu}(\varphi^0) + \varepsilon_S \varphi^1 \bar{\mu}'(\varphi^0) \right] \left[\hat{u}_r^0 + \varepsilon_S \hat{u}_r^1 \right] \right. \\
 & \left. \left. + \left[\bar{\lambda}(\varphi^0) + \varepsilon_S \varphi^1 \bar{\lambda}'(\varphi^0) \right] \left[\left(\hat{u}_r^0 + \varepsilon_S \hat{u}_r^1 \right) + \frac{2}{r} \left(\hat{u}^0 + \varepsilon_S \hat{u}^1 \right) \right] \right) \right\}, \tag{A.2}
 \end{aligned}$$

$$\begin{aligned}
& \frac{\varepsilon_S^2}{\bar{X}} \left[\varphi_\tau^0 + \varepsilon_S \varphi_\tau^1 - \dot{r}_I (\varphi_\tau^0 + \varepsilon_S \varphi_\tau^1) + (\hat{u}^0 + \varepsilon_S \hat{u}^1 + \dot{r}_I) (\varphi_\tau^0 + \varepsilon_S \varphi_\tau^1) \right] \\
&= \varepsilon_S^2 \left(\varphi_{\tau\tau}^0 + \frac{2}{r} \varphi_\tau^0 + \varepsilon_S \varphi_{\tau\tau}^1 + \frac{2}{r} \varepsilon_S \varphi_\tau^1 \right) + C_P \left[(\bar{p}^0 + \bar{p}_0) + \varepsilon_S \bar{p}^1 \right] \\
&\quad \left\{ \frac{\bar{\rho}'(\varphi^0)}{\bar{\rho}(\varphi^0)} + \varepsilon_S \left[\frac{\bar{\rho}''(\varphi^0)}{\bar{\rho}(\varphi^0)} - \left(\frac{\bar{\rho}'(\varphi^0)}{\bar{\rho}(\varphi^0)} \right)^2 \right] \varphi^1 \right\} \\
&\quad + \bar{Y} \left[\frac{1}{\theta_m} (\vartheta^0 + \varepsilon_S \vartheta^1 - \theta_m) \right] \varepsilon_S \left[\bar{p}'(\varphi^0) + \varepsilon_S \varphi^1 \bar{p}''(\varphi^0) \right] \\
&\quad - \frac{1}{4} \left[H'(\varphi^0) + \varepsilon_S \varphi^1 H''(\varphi^0) \right] \left[\bar{\rho}(\varphi^0) + \varepsilon_S \varphi^1 \bar{\rho}'(\varphi^0) \right], \tag{A.3}
\end{aligned}$$

$$\begin{aligned}
& \left[(\hat{u}^0 + \varepsilon_S \hat{u}^1) (\vartheta_\tau^0 + \varepsilon_S \vartheta_\tau^1) + \vartheta_\tau^0 + \varepsilon_S \vartheta_\tau^1 \right] \left[\bar{\rho}(\varphi^0) + \varepsilon_S \varphi^1 \bar{\rho}'(\varphi^0) \right] \\
&+ \left[\varphi_\tau^0 + \varepsilon_S \varphi_\tau^1 + (\hat{u}^0 + \varepsilon_S \hat{u}^1) (\varphi_\tau^0 + \varepsilon_S \varphi_\tau^1) \right] \left\{ \frac{1}{4L} \left(\frac{1}{a} + \frac{1}{a_S} \right) \right. \\
&\quad \times \left[H'(\varphi^0) + \varepsilon_S \varphi^1 H''(\varphi^0) \right] \left[\bar{\rho}(\varphi^0) + \varepsilon_S \varphi^1 \bar{\rho}'(\varphi^0) \right] \\
&\quad - \left[r'(\varphi^0) + \varepsilon_S \varphi^1 r''(\varphi^0) \right] \left[\bar{\rho}(\varphi^0) + \varepsilon_S \varphi^1 \bar{\rho}'(\varphi^0) \right] \\
&\quad \left. + C_E \bar{p}_0 \left[\frac{\bar{\rho}'(\varphi^0)}{\bar{\rho}(\varphi^0)} + \varepsilon_S \left\{ \frac{\bar{\rho}''(\varphi^0)}{\bar{\rho}(\varphi^0)} - \left(\frac{\bar{\rho}'(\varphi^0)}{\bar{\rho}(\varphi^0)} \right)^2 \right\} \varphi^1 \right] \right\} \\
&= \frac{1}{4} \left[\vartheta_{\tau\tau}^0 + \frac{2}{r} \vartheta_\tau^0 + \varepsilon_S \left(\vartheta_{\tau\tau}^1 + \frac{2}{r} \vartheta_\tau^1 \right) \right], \tag{A.4}
\end{aligned}$$

where

$$\begin{aligned}
\bar{C}_{M1} &= \frac{(R^*)^2}{2a(4\kappa_{SL})^2}, \quad C_{M2} = \frac{\nu_{SL}}{4\kappa_{SL}\rho_{SL}}, \quad \bar{X} = \frac{\delta^2 \rho_{SL}}{4\kappa_{SL} M a}, \quad \bar{Y} = \frac{a L R^*}{\delta}, \\
C_P &= a \left(\frac{4\kappa_{SL}}{R^*} \right)^2, \quad C_E = \frac{(4\kappa_{SL})^2}{L(R^*)^2}
\end{aligned}$$

and \bar{p}_0 denotes the constant non-dimensional reference pressure.

From these asymptotic expansions at each order of ε_S we obtain

O(1):

$$\bar{\rho}'(\varphi^0) \varphi_\tau^0 - \dot{r}_I \varphi^0 \bar{\rho}'(\varphi^0) + (\hat{u}^0 + \dot{r}_I) \bar{\rho}'(\varphi^0) \varphi_\tau^0 = -\bar{\rho}(\varphi^0) \left(\hat{u}_\tau^0 + \frac{2}{r} \hat{u}_\tau^0 \right),$$

$$\bar{\rho}(\varphi^0) \left[\hat{u}_\tau^0 + \ddot{r}_I + \hat{u}_\tau^0 (\dot{r}_I + \hat{u}^0) \right] = -\bar{p}_\tau^0,$$

$$0 = C_P (\bar{p}^0 + \bar{p}_0) \frac{\bar{\rho}'(\varphi^0)}{\bar{\rho}(\varphi^0)} - \frac{1}{4} H'(\varphi^0) \bar{\rho}(\varphi^0),$$

$$\left[\frac{1}{4L} \left(\frac{1}{a} + \frac{1}{a_S} \right) H'(\varphi^0) \bar{\rho}(\varphi^0) - r'(\varphi^0) \bar{\rho}(\varphi^0) + C_E \bar{p}_0 \frac{\bar{\rho}'(\varphi^0)}{\bar{\rho}(\varphi^0)} \right] \left[\varphi_\tau^0 + \hat{u}^0 \varphi_r^0 \right] \\ + \bar{\rho}(\varphi^0) \left(-\hat{u}^0 v_\tau^0 + v_\tau^0 \right) = \frac{1}{4} \left(v_{rr}^0 + \frac{2}{r} v_r^0 \right),$$

$O(\varepsilon_S)$:

$$\bar{\rho}'(\varphi^0) \varphi^1 \left[\hat{u}_\tau^0 + \ddot{r}_I + \hat{u}^0 \hat{u}_\tau^0 \right] + \bar{\rho}(\varphi^0) \left[\hat{u}_\tau^1 + \hat{u}^1 \hat{u}_\tau^0 + \hat{u}^0 \hat{u}_\tau^1 \right] \\ = C_{M2} \left\{ \frac{\partial}{\partial r} \left[2\bar{\mu}(\varphi^0) \hat{u}_\tau^0 + \bar{\lambda}(\varphi^0) \left(\hat{u}_\tau^0 + \frac{2}{r} \hat{u}^0 \right) \right] \right. \\ \left. + \frac{2}{r} \left[2\bar{\mu}(\varphi^0) \hat{u}_\tau^0 + \bar{\lambda}(\varphi^0) \left(\hat{u}_\tau^0 + \frac{2}{r} \hat{u}^0 \right) \right] \right\} - \bar{p}_r^1 \quad \text{from (A.2).}$$

A.2 Inner expansion

Noting that the Laplacian in the inner region is given by

$$\bar{\nabla}^2 \theta = \frac{1}{\varepsilon_S^2} \Theta_{ZZ} + \frac{\bar{\nabla}^2 r}{\varepsilon_S} \Theta_Z + O(1),$$

the divergence operator as

$$\bar{\nabla} \cdot (\theta \mathbf{e}_r) = \frac{1}{\varepsilon_S} \Theta_Z + \frac{2}{r_I + \varepsilon_S Z} \Theta + O(\varepsilon_S),$$

and the material time derivative θ_τ as

$$\theta_\tau = \Theta_\tau + \frac{\hat{U}}{\varepsilon_S} \Theta_Z,$$

equations (8.74) to (8.77) can be written in terms of the inner stretched coordinate as

$$\bar{\rho}'(\Phi) \left[\Phi_\tau + \frac{1}{\varepsilon_S} \hat{U} \Phi_Z \right] = -\bar{\rho}(\Phi) \left[\frac{1}{\varepsilon_S} \hat{U}_Z + \frac{2}{(r_I + \varepsilon_S Z)} (\hat{U} + \dot{r}_I) \right], \quad (\text{A.5})$$

$$\bar{\rho}(\Phi) \left[\hat{U}_\tau + \ddot{r}_I + \frac{1}{\varepsilon_S} \hat{U} \hat{U}_Z \right] = \frac{1}{\varepsilon_S} \frac{\partial}{\partial Z} \left\{ -\bar{P} - \bar{C}_{M1}(\Phi_Z)^2 \right. \\ \left. + C_{M2} \left[2\bar{\mu}(\Phi) \hat{U}_Z + \bar{\lambda}(\Phi) \left\{ \hat{U}_Z + \frac{2\varepsilon_S}{(r_I + \varepsilon_S Z)} (\dot{r}_I + \hat{U}) \right\} \right] \right\} \\ + \frac{2}{r_I + \varepsilon_S Z} \left\{ -\bar{C}_{M1}(\Phi_Z)^2 \right. \\ \left. + C_{M2} \left[2\bar{\mu}(\Phi) \hat{U}_Z + \bar{\lambda}(\Phi) \left\{ \hat{U}_Z + \frac{2\varepsilon_S}{(r_I + \varepsilon_S Z)} (\dot{r}_I + \hat{U}) \right\} \right] \right\}, \quad (\text{A.6})$$

$$\begin{aligned} \frac{\varepsilon_S^2}{\bar{X}} \left[\Phi_\tau + \frac{1}{\varepsilon_S} \hat{U} \Phi_Z \right] &= \varepsilon_S^2 \left[\frac{\bar{\nabla}^2 r}{\varepsilon_S} \Phi_Z + \frac{1}{\varepsilon_S^2} \Phi_{ZZ} \right] + \varepsilon_S \bar{Y} \frac{\Theta - \Theta_m}{\Theta_m} \bar{p}'(\Phi) \\ &\quad - \frac{1}{4} H'(\Phi) \bar{\rho}(\Phi) + C_P [\bar{P} - \bar{P}_0] \frac{\bar{\rho}'(\Phi)}{\bar{\rho}(\Phi)}, \end{aligned} \quad (\text{A.7})$$

$$\begin{aligned} \bar{\rho}(\Phi) \Theta_\tau + \Phi_\tau \left[-r'(\Phi) \bar{\rho}(\Phi) \frac{1}{4L} \left(\frac{1}{a} + \frac{1}{a_S} \right) H'(\Phi) \bar{\rho}(\Phi) + C_E \bar{P}_0 \frac{\bar{\rho}'(\Phi)}{\bar{\rho}(\Phi)} \right] \\ + \frac{1}{\varepsilon_S} \hat{U} \Theta_Z \bar{\rho}(\Phi) + \frac{\Phi_Z \hat{U}}{\varepsilon_S} \left[-r'(\Phi) \bar{\rho}(\Phi) + \frac{1}{4L} \left(\frac{1}{a} + \frac{1}{a_S} \right) H'(\Phi) \bar{\rho}(\Phi) + C_E \bar{P}_0 \frac{\bar{\rho}'(\Phi)}{\bar{\rho}(\Phi)} \right] \\ = \frac{1}{4} \left[\frac{1}{\varepsilon_S^2} \Theta_{ZZ} + \frac{\bar{\nabla}^2 r}{\varepsilon_S} \Theta_Z \right]. \end{aligned} \quad (\text{A.8})$$

Then substituting equations (8.83) to (8.86) into the non-dimensionalised phase-field equations (A.5) to (A.8) yields

$$\begin{aligned} \left[\Phi_\tau^0 + \varepsilon_S \Phi_\tau^1 + \frac{1}{\varepsilon_S} (\hat{U}^0 + \varepsilon_S \hat{U}^1) (\Phi_Z^0 + \varepsilon_S \Phi_Z^1) \right] \left[\bar{\rho}'(\Phi^0) + \varepsilon_S \Phi^1 \bar{\rho}''(\Phi^0) \right] \\ = - \left[\bar{\rho}(\Phi^0) + \varepsilon_S \Phi^1 \bar{\rho}'(\Phi^0) \right] \left\{ \frac{1}{\varepsilon_S} [\hat{U}_Z^0 + \varepsilon_S \hat{U}_Z^1] + \left[\frac{2}{r_I} - \varepsilon_S \frac{2Z}{(r_I)^2} \right] [(\hat{U}^0 + \dot{r}_I) + \varepsilon_S \hat{U}^1] \right\}, \end{aligned} \quad (\text{A.9})$$

$$\begin{aligned} \left[\bar{\rho}(\Phi^0) + \varepsilon_S \Phi^1 \bar{\rho}'(\Phi^0) \right] \left[(\hat{U}_\tau^0 + \dot{r}_I) + \varepsilon_S \hat{U}_\tau^1 + \frac{1}{\varepsilon_S} (\hat{U}^0 + \varepsilon_S \hat{U}^1) (\hat{U}_Z^0 + \varepsilon_S \hat{U}_Z^1) \right] = \\ \frac{1}{\varepsilon_S} \frac{\partial}{\partial Z} \left[-(\bar{P}^0 + \varepsilon_S \bar{P}^1) - \bar{C}_{M1} (\Phi_Z^0 + \varepsilon_S \Phi_Z^1)^2 \right] \\ + C_{M2} \left\{ 2 [\bar{\mu}(\Phi^0) + \varepsilon_S \Phi^1 \bar{\mu}'(\Phi^0)] [\hat{U}_Z^0 + \varepsilon_S \hat{U}_Z^1] + [\bar{\lambda}(\Phi^0) + \varepsilon_S \Phi^1 \bar{\lambda}'(\Phi^0)] \right. \\ \left. \left(\hat{U}_Z^0 + \varepsilon_S \hat{U}_Z^1 + \varepsilon_S \left[\frac{2}{r_I} - \varepsilon_S \frac{2Z}{(r_I)^2} \right] [(\dot{r}_I + \hat{U}^0) + \varepsilon_S \hat{U}^1] \right) \right\} \\ + \left[\frac{2}{r_I} - \varepsilon_S \frac{2Z}{(r_I)^2} \right] \left[-\bar{C}_{M1} (\Phi_Z^0 + \varepsilon_S \Phi_Z^1)^2 \right. \\ \left. + C_{M2} \left\{ 2 [\bar{\mu}(\Phi^0) + \varepsilon_S \Phi^1 \bar{\mu}'(\Phi^0)] [\hat{U}_Z^0 + \varepsilon_S \hat{U}_Z^1] + [\bar{\lambda}(\Phi^0) + \varepsilon_S \Phi^1 \bar{\lambda}'(\Phi^0)] \right. \right. \\ \left. \left. \left(\hat{U}_Z^0 + \varepsilon_S \hat{U}_Z^1 + \varepsilon_S \left[\frac{2}{r_I} - \varepsilon_S \frac{2Z}{(r_I)^2} \right] [(\dot{r}_I + \hat{U}^0) + \varepsilon_S \hat{U}^1] \right) \right\} \right], \end{aligned} \quad (\text{A.10})$$

$$\begin{aligned} \frac{\varepsilon_S^2}{\bar{X}} \left[\Phi_\tau^0 + \varepsilon_S \Phi_\tau^1 + \frac{1}{\varepsilon_S} (\hat{U}^0 + \varepsilon_S \hat{U}^1) (\Phi_Z^0 + \varepsilon_S \Phi_Z^1) \right] \\ = \varepsilon_S^2 \left[\frac{\bar{\nabla}^2 r}{\varepsilon_S} (\Phi_Z^0 + \varepsilon_S \Phi_Z^1) + \frac{1}{\varepsilon_S^2} (\Phi_{ZZ}^0 + \varepsilon_S \Phi_{ZZ}^1) \right] \\ + \varepsilon_S \bar{Y} \left[\frac{1}{\Theta_m} (\Theta^0 + \varepsilon_S \Theta^1 - \Theta_m) \right] \left[\bar{p}'(\Phi^0) + \varepsilon_S \Phi^1 \bar{p}''(\Phi^0) \right] \end{aligned} \quad (\text{A.11})$$

$$\begin{aligned}
& -\frac{1}{4} \left[H'(\Phi^0) + \varepsilon_S \Phi^1 H''(\Phi^0) \right] \left[\bar{\rho}(\Phi^0) + \varepsilon_S \Phi^1 \bar{\rho}'(\Phi^0) \right] \\
& + C_P \left[(\bar{P}^0 - \bar{P}_0) + \varepsilon_S \bar{P}^1 \right] \left[\frac{\bar{\rho}'(\Phi^0)}{\bar{\rho}(\Phi^0)} + \varepsilon_S \left\{ \frac{\bar{\rho}''(\Phi^0)}{\bar{\rho}(\Phi^0)} - \left(\frac{\bar{\rho}'(\Phi^0)}{\bar{\rho}(\Phi^0)} \right)^2 \right\} \Phi^1 \right], \\
& \left[\bar{\rho}(\Phi^0) + \varepsilon_S \Phi^1 \bar{\rho}'(\Phi^0) \right] \left[\Theta_\tau^0 + \varepsilon_S \Theta_\tau^1 \right] \\
+ & \left\{ - \left[r'(\Phi^0) + \varepsilon_S \Phi^1 r''(\Phi^0) \right] \left[\bar{\rho}(\Phi^0) + \varepsilon_S \Phi^1 \bar{\rho}'(\Phi^0) \right] \right. \\
& + \frac{1}{4L} \left(\frac{1}{a} + \frac{1}{a_s} \right) \left[H'(\Phi^0) + \varepsilon_S \Phi^1 H''(\Phi^0) \right] \left[\bar{\rho}(\Phi^0) + \varepsilon_S \Phi^1 \bar{\rho}'(\Phi^0) \right] \\
& + C_E \bar{P}_0 \left[\frac{\bar{\rho}'(\Phi^0)}{\bar{\rho}(\Phi^0)} + \varepsilon_S \left\{ \frac{\bar{\rho}''(\Phi^0)}{\bar{\rho}(\Phi^0)} - \left(\frac{\bar{\rho}'(\Phi^0)}{\bar{\rho}(\Phi^0)} \right)^2 \right\} \Phi^1 \right] \left. \right\} \left(\Phi_\tau^0 + \varepsilon_S \Phi_\tau^1 \right) \\
+ & \frac{1}{\varepsilon_S} \left[\hat{U}^0 + \varepsilon_S \hat{U}^1 \right] \left[\Theta_Z^0 + \varepsilon_S \Theta_Z^1 \right] \left[\bar{\rho}(\Phi^0) + \varepsilon_S \Phi^1 \bar{\rho}'(\Phi^0) \right] \\
+ & \left\{ - \left[r'(\Phi^0) + \varepsilon_S \Phi^1 r''(\Phi^0) \right] \left[\bar{\rho}(\Phi^0) + \varepsilon_S \Phi^1 \bar{\rho}'(\Phi^0) \right] \right. \\
& + \frac{1}{4L} \left(\frac{1}{a} + \frac{1}{a_s} \right) \left[H'(\Phi^0) + \varepsilon_S \Phi^1 H''(\Phi^0) \right] \left[\bar{\rho}(\Phi^0) + \varepsilon_S \Phi^1 \bar{\rho}'(\Phi^0) \right] \\
& + C_E \bar{P}_0 \left[\frac{\bar{\rho}'(\Phi^0)}{\bar{\rho}(\Phi^0)} + \varepsilon_S \left\{ \frac{\bar{\rho}''(\Phi^0)}{\bar{\rho}(\Phi^0)} - \left(\frac{\bar{\rho}'(\Phi^0)}{\bar{\rho}(\Phi^0)} \right)^2 \right\} \Phi^1 \right] \left. \right\} \frac{1}{\varepsilon_S} \left[\Phi_Z^0 + \varepsilon_S \Phi_Z^1 \right] \left[\hat{U}^0 + \varepsilon_S \hat{U}^1 \right] \\
= & \frac{1}{4} \left[\frac{1}{\varepsilon_S^2} (\Theta_{ZZ}^0 + \varepsilon_S \Theta_{ZZ}^1) + \frac{\bar{\nabla}^2 r}{\varepsilon_S} (\Theta_Z^0 + \varepsilon_S \Theta_Z^1) \right], \tag{A.12}
\end{aligned}$$

where the constant coefficients \bar{C}_{M1} , C_{M2} , \bar{X} , \bar{Y} , C_P and C_E are defined in section A.1 of this appendix and \bar{P}_0 denotes the inner non-dimensional reference pressure.

From these asymptotic expressions at each order of ε_S we obtain

$O(\varepsilon_S^{-2})$:

$$\frac{1}{4} \Theta_{ZZ}^0 = 0, \quad \text{from (A.12)}$$

$O(\varepsilon_S^{-1})$:

$$\hat{U}^0 \bar{\rho}'(\Phi^0) \Phi_Z^0 = -\bar{\rho}(\Phi^0) \hat{U}_Z^0, \quad \text{from (A.9)}$$

$$\bar{\rho}(\Phi^0) \hat{U}^0 \hat{U}_Z^0 = \frac{\partial}{\partial Z} \left[-\bar{P}^0 - \bar{C}_{M1} (\Phi_Z^0)^2 + C_{M2} \left\{ 2\bar{\mu}(\Phi^0) + \bar{\lambda}(\Phi^0) \right\} \hat{U}_Z^0 \right], \quad \text{from (A.10)}$$

$$\begin{aligned}
& \left\{ \frac{1}{4L} \left(\frac{1}{a} + \frac{1}{a_s} \right) H'(\Phi^0) \bar{\rho}(\Phi^0) - r'(\Phi^0) \bar{\rho}(\Phi^0) + C_E \bar{P}_0 \frac{\bar{\rho}'(\Phi^0)}{\bar{\rho}(\Phi^0)} \right\} \Phi_Z^0 \hat{U}^0 \\
& + \Theta_Z^0 \bar{\rho}(\Phi^0) \hat{U}^0 = \frac{1}{4} \left[\Theta_{ZZ}^1 + \bar{\nabla}^2 r \Theta_Z^0 \right], \quad \text{from (A.12)}
\end{aligned}$$

$O(1)$:

$$\begin{aligned} (\Phi_\tau^0 + \hat{U}^0 \Phi_Z^1 + \hat{U}^1 \Phi_Z^0) \bar{\rho}'(\Phi^0) + \hat{U}^0 \Phi_Z^0 \bar{\rho}''(\Phi^0) \Phi^1 = \\ -\bar{\rho}(\Phi^0) \left[\hat{U}_Z^1 + \frac{2}{r_I} (\hat{U}^0 + \dot{r}_I) \right] - \bar{\rho}'(\Phi^0) \Phi^1 \hat{U}_Z^0, \quad \text{from (A.9)} \end{aligned}$$

$$\begin{aligned} \bar{\rho}(\Phi^0) \left[\hat{U}_\tau^0 + \dot{r}_I + \hat{U}^1 \hat{U}_Z^0 + \hat{U}^0 \hat{U}_Z^1 \right] + \Phi^1 \bar{\rho}'(\Phi^0) \hat{U}^0 \hat{U}_Z^0 \\ = \frac{2}{r_I} \left[-\bar{C}_{M1} (\Phi_Z^0)^2 + C_{M2} \left[2\bar{\mu}(\Phi^0) + \bar{\lambda}(\Phi^0) \right] \hat{U}_Z^0 \right] \\ + \frac{\partial}{\partial Z} \left[-\bar{P}^1 - \bar{C}_{M1} \Phi_Z^0 \Phi_Z^1 + C_{M2} \left\{ 2\bar{\mu}(\Phi^0) \hat{U}_Z^1 + 2\bar{\mu}'(\Phi^0) \Phi^1 \hat{U}_Z^0 \right. \right. \\ \left. \left. + \bar{\lambda}(\Phi^0) \left[\hat{U}_Z^1 + \frac{2}{r_I} (\dot{r}_I + \hat{U}^0) \right] + \bar{\lambda}'(\Phi^0) \Phi^1 \hat{U}_Z^0 \right\} \right], \quad \text{from (A.10)} \end{aligned}$$

$$\Phi_{ZZ}^0 + C_P (\bar{P}^0 - \bar{P}_0) \frac{\bar{\rho}'(\Phi^0)}{\bar{\rho}(\Phi^0)} - \frac{1}{4} H'(\Phi^0) \bar{\rho}(\Phi^0) = 0, \quad \text{from (A.11)}$$

$O(\varepsilon_S)$:

$$\begin{aligned} \frac{1}{\bar{X}} \hat{U}^0 \Phi_Z^0 &= \Phi_{ZZ}^1 + \bar{\nabla}^2 r \Phi_Z^0 + \bar{Y} \left(\frac{\Theta^0 - \Theta_m}{\Theta_m} \right) \bar{\rho}'(\Phi^0) \\ &+ C_P (\bar{P}^0 - \bar{P}_0) \left[\frac{\bar{\rho}''(\Phi^0)}{\bar{\rho}(\Phi^0)} - \left(\frac{\bar{\rho}'(\Phi^0)}{\bar{\rho}(\Phi^0)} \right)^2 \right] \Phi^1 \\ &- \frac{1}{4} \left[H'(\Phi^0) \Phi^1 \bar{\rho}'(\Phi^0) + H''(\Phi^0) \Phi^1 \bar{\rho}(\Phi^0) \right] \\ &+ C_P \bar{P}^1 \frac{\bar{\rho}'(\Phi^0)}{\bar{\rho}(\Phi^0)}, \quad \text{from (A.11)} \end{aligned}$$

respectively.

Appendix B

Derivation and asymptotic expansion of Clausius-Clapeyron relation

B.1 Derivation of Clausius-Clapeyron equation from phase-field equation

To obtain the general Clausius-Clapeyron relation we re-write the inner phase-field equation (8.102) in chapter 8 in terms of the free energy g , giving

$$\begin{aligned} \frac{\varepsilon_S^2}{\bar{X}} \left[\Phi_\tau^0 + \varepsilon_S \Phi_\tau^1 + \frac{1}{\varepsilon_S} (\hat{U}^0 + \varepsilon_S \hat{U}^1) (\Phi_Z^0 + \varepsilon_S \Phi_Z^1) \right] \\ = \varepsilon_S^2 \left[\frac{\bar{\nabla}^2 r}{\varepsilon_S} (\Phi_Z^0 + \varepsilon_S \Phi_Z^1) + \frac{1}{\varepsilon_S^2} (\Phi_{ZZ}^0 + \varepsilon_S \Phi_{ZZ}^1) \right] \\ - a \left[\bar{\rho}(\Phi^0) + \varepsilon_S \Phi^1 \bar{\rho}'(\Phi^0) \right] \left[g_\phi^0 + \varepsilon_S g_\phi^1 \right] \end{aligned} \quad (\text{B.1})$$

where, as discussed in chapter 8, we have written $\Theta = \Theta_m(1 + \delta)$ and made the approximation

$$a \frac{\Theta_m}{\Theta} = a$$

by retaining only the leading order term. Then we obtain at each order of ε_S :

$O(1)$:

$$\Phi_{ZZ}^0 - a \bar{\rho}(\Phi^0) g_\phi^0 = 0 \quad (\text{B.2})$$

$O(\varepsilon_S)$:

$$\frac{1}{\bar{X}} \hat{U}^0 \Phi_Z^0 = \bar{\nabla}^2 r \Phi_Z^0 + \Phi_{ZZ}^1 - a \left[\bar{\rho}(\Phi^0) g_\phi^1 + \Phi^1 \bar{\rho}'(\Phi^0) g_\phi^0 \right]. \quad (\text{B.3})$$

Equation (B.2) can be rearranged to yield

$$g_\phi^0 = \frac{1}{a \bar{\rho}(\Phi^0)} \Phi_{ZZ}^0 \quad (\text{B.4})$$

and from equation (B.3) we can subsequently obtain

$$g_\phi^1 = \frac{1}{a\bar{\rho}(\Phi^0)} \left[\bar{\nabla}^2 r \Phi_Z^0 + \Phi_{ZZ}^1 - \frac{\bar{\rho}'(\Phi^0)}{\bar{\rho}(\Phi^0)} \Phi^1 \Phi_{ZZ}^0 \right] - \frac{\hat{U}^0}{X a \bar{\rho}(\Phi^0)} \Phi_Z^0. \quad (\text{B.5})$$

The differential of the leading order free energy term with respect to the expanded inner position variable Z is given by

$$\frac{dg^0}{dZ} = g_\phi^0 \Phi_Z^0 + \rho_{SL} \left(\frac{4\kappa_{SL}}{R^*} \right)^2 g_P^0 \bar{P}_Z^0 + g_T^0 T_Z^0. \quad (\text{B.6})$$

From equation (8.118) in chapter 8 it is required that $T_Z^0 = 0$, however to compare equation (B.6) with the inner asymptotic expansion of the Clausius-Clapeyron equation given by equation (8.129) it is necessary to find appropriate expressions for g_P^0 and \bar{P}_Z^0 . Expanding g_P by a power series in ε_S gives

$$g_P = g_P^0 + \varepsilon_S g_P^1 + \dots = \frac{1}{\rho_{SL}} \left\{ \frac{1}{\bar{\rho}(\Phi^0)} - \varepsilon_S \Phi^1 \frac{\bar{\rho}'(\Phi^0)}{[\bar{\rho}(\Phi^0)]^2} + \dots \right\},$$

which implies that

$$g_P^0 = \frac{1}{\rho_{SL}} \frac{1}{\bar{\rho}(\Phi^0)} \quad (\text{B.7})$$

and

$$g_P^1 = -\frac{1}{\rho_{SL}} \frac{\bar{\rho}'(\Phi^0)}{[\bar{\rho}(\Phi^0)]^2} \Phi^1. \quad (\text{B.8})$$

\bar{P}_Z^0 is obtained by re-arranging the leading order inner momentum equation (8.105) in chapter 8 which gives

$$\begin{aligned} \bar{P}_Z^0 &= -\bar{\rho}(\Phi^0) \hat{U}^0 \hat{U}_Z^0 - \bar{C}_{M1} 2\Phi_Z^0 \Phi_{ZZ}^0 + C_{M2} \{2\bar{\mu}'(\Phi^0) + \bar{\lambda}'(\Phi^0)\} \hat{U}_Z^0 \Phi_Z^0 \\ &\quad + C_{M2} \{2\bar{\mu}(\Phi^0) + \bar{\lambda}(\Phi^0)\} \hat{U}_{ZZ}^0. \end{aligned} \quad (\text{B.9})$$

Similarly, \bar{P}_Z^1 is obtained by re-arranging the first order inner momentum equation (8.109) which gives

$$\begin{aligned} \bar{P}_Z^1 &= \frac{2}{r_I} \left[-\bar{C}_{M1} (\Phi_Z^0)^2 + C_{M2} \left[2\bar{\mu}(\Phi^0) + \bar{\lambda}(\Phi^0) \right] \hat{U}_Z^0 \right. \\ &\quad \left. + C_{M2} \frac{\partial}{\partial Z} \left\{ \bar{\lambda}(\Phi^0) (r_I + \hat{U}^0) \right\} \right] \\ &\quad - \bar{\rho}(\Phi^0) (\hat{U}_\tau^0 + \hat{r}_I) - \bar{\rho}(\Phi^0) \frac{\partial}{\partial Z} (\hat{U}^0 \hat{U}^1) - \Phi^1 \bar{\rho}'(\Phi^0) \hat{U}^0 \hat{U}_Z^0 \\ &\quad + \frac{\partial}{\partial Z} \left[-2\bar{C}_{M1} \Phi_Z^0 \Phi_Z^1 + C_{M2} \left\{ \left[2\bar{\mu}(\Phi^0) + \bar{\lambda}(\Phi^0) \right] \hat{U}_Z^1 \right. \right. \\ &\quad \left. \left. + \left[2\bar{\mu}'(\Phi^0) + \bar{\lambda}'(\Phi^0) \right] \Phi^1 \hat{U}_Z^0 \right\} \right]. \end{aligned} \quad (\text{B.10})$$

Substituting equations (B.4), (B.7) and (B.9) into equation (B.6) gives

$$\begin{aligned} \frac{dg^0}{dZ} = & \frac{1}{a\bar{\rho}(\Phi^0)}\Phi_{ZZ}^0\Phi_Z^0 - \left(\frac{4\kappa_{SL}}{R^*}\right)^2\hat{U}^0\hat{U}_Z^0 - \bar{C}_{M1}\left(\frac{4\kappa_{SL}}{R^*}\right)^2\frac{2}{\bar{\rho}(\Phi^0)}\Phi_{ZZ}^0\Phi_Z^0 \\ & + \left(\frac{4\kappa_{SL}}{R^*}\right)^2\frac{C_{M2}}{\bar{\rho}(\Phi^0)}\frac{\partial}{\partial Z}\left\{\left[2\bar{\mu}(\Phi^0) + \bar{\lambda}(\Phi^0)\right]\hat{U}_Z^0\right\} \end{aligned} \quad (\text{B.11})$$

and since

$$\left(\frac{4\kappa_{SL}}{R^*}\right)^2\bar{C}_{M1} = \frac{1}{2a}$$

the first term cancels with the third term on the right hand side of equation (B.11). Therefore integrating the resulting expression leaves

$$g_L^0 - g_S^0 = -\frac{1}{2}\left(\frac{4\kappa_{SL}}{R^*}\right)^2\left[(\hat{U}^0)^2\right]_{-\infty}^{\infty} + \left(\frac{4\kappa_{SL}}{R^*}\right)^2C_{M2}\int_{-\infty}^{\infty}\frac{1}{\bar{\rho}(\Phi^0)}\frac{\partial}{\partial Z}\left\{\left[2\bar{\mu}(\Phi^0) + \bar{\lambda}(\Phi^0)\right]\hat{U}_Z^0\right\}dZ, \quad (\text{B.12})$$

and using

$$\frac{\partial}{\partial Z}\left\{\left[2\bar{\mu}(\Phi^0) + \bar{\lambda}(\Phi^0)\right]\hat{U}_Z^0\hat{U}^0\right\} = \left[2\bar{\mu}(\Phi^0) + \bar{\lambda}(\Phi^0)\right](\hat{U}_Z^0)^2 + \hat{U}^0\frac{\partial}{\partial Z}\left\{\left[2\bar{\mu}(\Phi^0) + \bar{\lambda}(\Phi^0)\right]\hat{U}_Z^0\right\},$$

equation (B.12) becomes

$$g_L^0 - g_S^0 = \left(\frac{4\kappa_{SL}}{R^*}\right)^2\left\{-\frac{(\dot{r}_I)^2}{2}\left[\left(\frac{\bar{\rho}_S}{\bar{\rho}_L}\right)^2 - 1\right] + \frac{C_{M2}}{\dot{r}_I\bar{\rho}_S}\int_{-\infty}^{\infty}\left[2\bar{\mu}(\Phi^0) + \bar{\lambda}(\Phi^0)\right](\hat{U}_Z^0)^2dZ\right\}, \quad (\text{B.13})$$

since $\lim_{Z \rightarrow \pm\infty} \hat{U}_Z^0 = 0$, by differentiating equation (8.114) with respect to Z . Equation (B.13) is equivalent to the leading order term of the inner asymptotic expansion of the Clausius-Clapeyron equation (8.129) where \dot{r}_I has replaced V and the non-dimensionalisations used in chapter 8 result in the coefficients $(4\kappa_{SL}/R^*)^2$ and C_{M2} .

In equation (8.129) the first order term in ϵ_F may be obtained from the differential with respect to Z of the first order free energy term, namely

$$\frac{dg^1}{dZ} = g_\phi^0\Phi_Z^1 + g_\phi^1\Phi_Z^0 + \rho_{SL}\left(\frac{4\kappa_{SL}}{R^*}\right)^2\left(g_P^0\bar{P}_Z^1 + g_P^1\bar{P}_Z^0\right) + g_T^0T_Z^1 + g_T^1T_Z^0. \quad (\text{B.14})$$

As we noted above $T_Z^0 = 0$, however $T_Z^1 \neq 0$ inside the interfacial region and therefore it is necessary to find an appropriate expression for g_T^0 to compare equation (B.14) with equation (8.129). The differential with respect to temperature of the leading order free energy term inside the inner region (from [2]), is given by

$$g_T^0\Big|_{P,\Phi} = -s^0(T, P, \Phi) = -\frac{1}{T_m}\left\{e_0 - r(\Phi^0)L + \frac{1}{4a_S}H(\Phi^0)\right\} - c\ln\left(\frac{T^0}{T_m}\right). \quad (\text{B.15})$$

Therefore using equations (B.7) and (B.8) to express g_P^0 and g_P^1 , (B.4) and (B.5) to express g_ϕ^0 and g_ϕ^1 , and (B.9) and (B.15) to express \bar{P}_Z^0 and g_T^0 , equation (B.14) becomes

$$\begin{aligned}
\frac{dg^1}{dZ} &= \frac{1}{a\bar{\rho}(\Phi^0)}\Phi_{ZZ}^0\Phi_Z^1 + \frac{\Phi_Z^0}{a\bar{\rho}(\Phi^0)}\left[\bar{\nabla}^2 r\Phi_Z^0 + \Phi_{ZZ}^1 - \frac{\bar{\rho}'(\Phi^0)}{\bar{\rho}(\Phi^0)}\Phi^1\Phi_{ZZ}^0\right] \\
&- \frac{\hat{U}^0}{\bar{X}a\bar{\rho}(\Phi^0)}(\Phi_Z^0)^2 + \left(\frac{4\kappa_{SL}}{R^*}\right)^2\left\{\frac{1}{\bar{\rho}(\Phi^0)}\bar{P}_Z^1 - \frac{\bar{\rho}'(\Phi^0)}{[\bar{\rho}(\Phi^0)]^2}\Phi^1\left(-\bar{\rho}(\Phi^0)\hat{U}^0\hat{U}_Z^0\right.\right. \\
&- \left.\left.2\bar{C}_{M1}\Phi_Z^0\Phi_{ZZ}^0 + C_{M2}[2\bar{\mu}'(\Phi^0) + \bar{\lambda}'(\Phi^0)]\hat{U}_Z^0\Phi_Z^0 + C_{M2}[2\bar{\mu}(\Phi^0) + \bar{\lambda}(\Phi^0)]\hat{U}_{ZZ}^0\right)\right\} \\
&- \frac{\Theta_Z^1}{\Theta_m}\{e_0 - r(\Phi^0)L + \frac{1}{4a_S}H(\Phi^0)\} - L\Theta_Z^1\ln\left(\frac{\Theta^0}{\Theta_m}\right). \tag{B.16}
\end{aligned}$$

The leading order inner expansion of the momentum equation given in chapter 8 by (8.105) can be integrated with respect to Z using equation (8.112) (which states that $\bar{\rho}(\Phi^0)\hat{U}^0 = C_3(\tau)$) to give

$$C_7(\tau) + \bar{\rho}(\Phi^0)(\hat{U}^0)^2 = -\bar{P}^0 - \bar{C}_{M1}(\Phi_Z^0)^2 + C_{M2}[2\bar{\mu}(\Phi^0) + \bar{\lambda}(\Phi^0)]\hat{U}_Z^0 \tag{B.17}$$

where C_7 is a function of τ introduced by the integration. This expression can be used in equation (B.10) to replace the term $C_{M2}[2\bar{\mu}(\Phi^0) + \bar{\lambda}(\Phi^0)]\hat{U}_Z^0$. The resulting expression can then be substituted for \bar{P}_Z^1 in equation (B.16) to leave

$$\begin{aligned}
\frac{dg^1}{dZ} &= \bar{\nabla}^2 r\frac{1}{a\bar{\rho}(\Phi^0)}(\Phi_Z^0)^2 - \frac{1}{a\bar{X}}\frac{1}{\bar{\rho}(\Phi^0)}\hat{U}^0(\Phi_Z^0)^2 + \left(\frac{4\kappa_{SL}}{R^*}\right)^2\left[-(\hat{U}_\tau^0 + \ddot{r}_I)\right. \\
&\quad \left. + \frac{2}{r_I}\frac{1}{\bar{\rho}(\Phi^0)}\left[C_7(\tau) + \bar{\rho}(\Phi^0)(\hat{U}^0)^2 + \bar{P}^0 + C_{M2}\frac{\partial}{\partial Z}\left\{\bar{\lambda}(\Phi^0)(\dot{r}_I + \hat{U}^0)\right\}\right]\right] \\
&+ C_{M2}\frac{1}{\bar{\rho}(\Phi^0)}\frac{\partial}{\partial Z}\left\{\left[2\bar{\mu}(\Phi^0) + \bar{\lambda}(\Phi^0)\right]\hat{U}_Z^1 + \left[2\bar{\mu}'(\Phi^0) + \bar{\lambda}'(\Phi^0)\right]\Phi^1\hat{U}_Z^0\right\} \\
&- C_{M2}\frac{\bar{\rho}'(\Phi^0)}{[\bar{\rho}(\Phi^0)]^2}\Phi^1\frac{\partial}{\partial Z}\left\{\left[2\bar{\mu}(\Phi^0) + \bar{\lambda}(\Phi^0)\right]\hat{U}_Z^0\right\} - \frac{\partial}{\partial Z}(\hat{U}^0\hat{U}^1) \\
&- \frac{\Theta_Z^1}{\Theta_m}\left[e_0 - Lr(\Phi^0) + \frac{1}{4a_S}H(\Phi^0)\right] - L\Theta_Z^1\ln\left(\frac{\Theta^0}{\Theta_m}\right). \tag{B.18}
\end{aligned}$$

Evaluating equation (B.17) in the liquid and solid limit (i.e. as $Z \rightarrow \infty$ and $Z \rightarrow -\infty$ respectively) gives two expressions for the constant of integration $C_7(\tau)$, namely

$$C_7(\tau) = -\bar{P}_S^0 - \bar{\rho}_S(\hat{U}_S^0)^2 = -\bar{P}_L^0 - \bar{\rho}_L(\hat{U}_L^0)^2. \tag{B.19}$$

Equation (B.19) gives the jump in the leading order pressure \bar{P}^0 across the interface, known as the *vapour recoil* effect. To obtain the form of the first order term in ϵ_F in equation (8.129) we must express $\left(\bar{\rho}'(\Phi^0)/[\bar{\rho}(\Phi^0)]^2\right)\Phi^1$ in terms of the first order inner velocity \hat{U}^1 . Therefore integrating equation (8.108) with respect to Z gives

$$\hat{U}^1 = \dot{r}_I\bar{\rho}_S\Phi^1\frac{\bar{\rho}'(\Phi^0)}{[\bar{\rho}(\Phi^0)]^2} - \delta_\tau - \left(\frac{2}{r_I}\right)\delta_\kappa \tag{B.20}$$

where δ_τ denotes an unsteady term given by

$$\delta_\tau = \frac{1}{\bar{\rho}(\Phi^0)} \int \Phi_\tau^0 \bar{\rho}'(\Phi^0) dZ, \quad (\text{B.21})$$

δ_κ denotes a curvature term given by

$$\delta_\kappa = \frac{1}{\bar{\rho}(\Phi^0)} \int \bar{\rho}(\Phi^0) (\hat{U}^0 + \dot{r}_I) dZ \quad (\text{B.22})$$

and we have used equations (8.112) and (8.113) to write $1/\bar{\rho}(\Phi^0)$ in terms of the leading order velocity \hat{U}^0 as

$$\frac{1}{\bar{\rho}(\Phi^0)} = -\frac{\hat{U}^0}{\dot{r}_I \bar{\rho}_S}. \quad (\text{B.23})$$

The viscous terms in equation (B.16) obey the differential relationships

$$\frac{\partial}{\partial Z} \left\{ [2\bar{\mu}(\Phi^0) + \bar{\lambda}(\Phi^0)] \hat{U}_Z^1 \hat{U}^0 \right\} = \hat{U}^0 \frac{\partial}{\partial Z} \left\{ [2\bar{\mu}(\Phi^0) + \bar{\lambda}(\Phi^0)] \hat{U}_Z^1 \right\} + [2\bar{\mu}(\Phi^0) + \bar{\lambda}(\Phi^0)] \hat{U}_Z^1 \hat{U}_Z^0, \quad (\text{B.24})$$

$$\frac{\partial}{\partial Z} \left\{ [2\bar{\mu}(\Phi^0) + \bar{\lambda}(\Phi^0)] \hat{U}^1 \hat{U}_Z^0 \right\} = \hat{U}^1 \frac{\partial}{\partial Z} \left\{ [2\bar{\mu}(\Phi^0) + \bar{\lambda}(\Phi^0)] \hat{U}_Z^0 \right\} + [2\bar{\mu}(\Phi^0) + \bar{\lambda}(\Phi^0)] \hat{U}_Z^1 \hat{U}_Z^0 \quad (\text{B.25})$$

and

$$\begin{aligned} \frac{\partial}{\partial Z} \left\{ [2\bar{\mu}'(\Phi^0) + \bar{\lambda}'(\Phi^0)] \Phi^1 \hat{U}_Z^0 \hat{U}^0 \right\} &= \hat{U}^0 \frac{\partial}{\partial Z} \left\{ [2\bar{\mu}'(\Phi^0) + \bar{\lambda}'(\Phi^0)] \Phi^1 \hat{U}_Z^0 \right\} \\ &\quad + [2\bar{\mu}'(\Phi^0) + \bar{\lambda}'(\Phi^0)] \Phi^1 (\hat{U}_Z^0)^2. \end{aligned} \quad (\text{B.26})$$

Therefore using equations (B.20), (B.23), (B.24), (B.25) and (B.26) and the conditions $\lim_{Z \rightarrow \pm\infty} \hat{U}_Z^0 = 0$ and $\lim_{Z \rightarrow \pm\infty} \hat{U}_Z^1 = -\left(2/r_I\right) \lim_{Z \rightarrow \pm\infty} (\hat{U}^0 + \dot{r}_I)$ (which require that the terms on the left hand side of equations (B.25) and (B.26) vanish under indefinite integration) the integral of equation (B.18) with respect to Z becomes

$$\begin{aligned} g_L^1 - g_S^1 &= \frac{1}{a\bar{X}} \dot{r}_I \bar{\rho}_S \int_{-\infty}^{\infty} \frac{1}{[\bar{\rho}(\Phi^0)]^2} (\Phi_Z^0)^2 dZ \\ &\quad + \frac{2C_{M2}}{\dot{r}_I \bar{\rho}_S} \left(\frac{4\kappa_{SL}}{R^*}\right)^2 \int_{-\infty}^{\infty} [2\bar{\mu}(\Phi^0) + \bar{\lambda}(\Phi^0)] \hat{U}_Z^0 \hat{U}_Z^1 dZ \\ &\quad + \frac{C_{M2}}{\dot{r}_I \bar{\rho}_S} \left(\frac{4\kappa_{SL}}{R^*}\right)^2 \int_{-\infty}^{\infty} [2\bar{\mu}'(\Phi^0) + \bar{\lambda}'(\Phi^0)] \Phi^1 (\hat{U}_Z^0)^2 dZ + \left(\frac{2}{r_I}\right) I_1 + I_2 - I_3. \end{aligned} \quad (\text{B.27})$$

The functions I_1 , I_2 and I_3 are collections of the terms related to curvature, time dependence and thermal variation respectively. They are defined as

$$I_1 = \left(\frac{4\kappa_{SL}}{R^*}\right)^2 \int_{-\infty}^{\infty} \frac{1}{\bar{\rho}(\Phi^0)} \left\{ C_7 + \bar{\rho}(\Phi^0) (\hat{U}^0)^2 + \bar{P}^0 + C_{M2} \frac{\partial}{\partial Z} \left[\bar{\lambda}(\Phi^0) (\hat{U}^0 + \dot{r}_I) \right] \right\} dZ$$

¹This expression has been obtained from the limit of equation (8.108) as $Z \rightarrow \pm\infty$.

$$\begin{aligned}
& -\left(\frac{4\kappa_{SL}}{R^*}\right)^2 \frac{C_{M2}}{\dot{r}_I \bar{\rho}_S} \int_{-\infty}^{\infty} \delta_{\kappa} \frac{\partial}{\partial Z} \left\{ \left[2\bar{\mu}(\Phi^0) + \bar{\lambda}(\Phi^0) \right] \hat{U}_Z^0 \right\} dZ \\
& + \int_{-\infty}^{\infty} \frac{1}{a\bar{\rho}(\Phi^0)} (\Phi_Z^0)^2 dZ + \left(\frac{4\kappa_{SL}}{R^*}\right)^2 \left[\hat{U}^0 \delta_{\kappa} \right]_{-\infty}^{\infty} + \frac{C_{M2}}{\dot{r}_I \bar{\rho}_S} \hat{U}_L^0 \left[2\bar{\mu}_L + \bar{\lambda}_L \right]
\end{aligned} \tag{B.28}$$

$$I_2 = -\left(\frac{4\kappa_{SL}}{R^*}\right)^2 \int_{-\infty}^{\infty} \left(\hat{U}_{\tau}^0 + \ddot{r}_I \right) + \frac{C_{M2}}{\dot{r}_I \bar{\rho}_S} \delta_{\tau} \frac{\partial}{\partial Z} \left\{ \left[2\bar{\mu}(\Phi^0) + \bar{\lambda}(\Phi^0) \right] \hat{U}_Z^0 \right\} dZ + \left(\frac{4\kappa_{SL}}{R^*}\right)^2 \left[\hat{U}^0 \delta_{\tau} \right]_{-\infty}^{\infty} \tag{B.29}$$

and

$$I_3 = \left[\frac{e_0}{\Theta_m} + \frac{L}{\Theta_m} \ln \left(\frac{\Theta^0}{\Theta_m} \right) \right] \left[\Theta_L^1 - \Theta_S^1 \right] + \frac{1}{\Theta_m} \int_{-\infty}^{\infty} \Theta_Z^1 \left[-Lr(\Phi^0) + \frac{1}{4a_S} H(\Phi^0) \right] dZ, \tag{B.30}$$

where δ_{τ} and δ_{κ} are defined by equations (B.21) and (B.22) respectively. The integral function I_1 defined by equation (B.28) is multiplied by the leading order curvature term $2/r_I$. The integral function I_2 contains all the unsteady terms, namely \hat{U}_{τ}^0 , \ddot{r}_I and δ_{τ} and the integral function I_3 contains all the non-equilibrium thermal terms.

Clearly in the limit as $r_I \rightarrow \infty$, the curvature term vanishes, which is the required condition for a planar interface. Further, making the steady assumption removes the terms \hat{U}_{τ}^0 , \ddot{r}_I and δ_{τ} which implies that $I_2 = 0$ and applying thermal equilibrium requires that $\Theta_L^1 = \Theta_S^1$ and $\Theta_Z^1 = 0$ which implies that $I_3 = 0$. Using these conditions equation (B.27) reduces to a form which is similar to the first order term in ϵ_F in equation (8.129).

Therefore combining equations (B.13) and (B.27), to leading and first order in ϵ_S the Clausius-Clapeyron relationship is given by

$$\begin{aligned}
g_L - g_S &= \left(\frac{4\kappa_{SL}}{R^*}\right)^2 \left\{ -\frac{(\dot{r}_I)^2}{2} \left[\left(\frac{\bar{\rho}_S}{\bar{\rho}_L} \right)^2 - 1 \right] + \frac{C_{M2}}{\dot{r}_I \bar{\rho}_S} \int_{-\infty}^{\infty} \left[2\bar{\mu}(\Phi^0) + \bar{\lambda}(\Phi^0) \right] (\hat{U}_Z^0)^2 dZ \right\} \\
&+ \epsilon_S \left\{ \frac{1}{a\bar{X}} \dot{r}_I \bar{\rho}_S \int_{-\infty}^{\infty} \frac{1}{[\bar{\rho}(\Phi^0)]^2} (\Phi_Z^0)^2 dZ \right. \\
&\quad + \left(\frac{4\kappa_{SL}}{R^*}\right)^2 \frac{C_{M2}}{\bar{\rho}_S \dot{r}_I} \int_{-\infty}^{\infty} \left(2 \left[2\bar{\mu}(\Phi^0) + \bar{\lambda}(\Phi^0) \right] \hat{U}_Z^0 \hat{U}_Z^1 \right. \\
&\quad \left. \left. + \left[2\bar{\mu}'(\Phi^0) + \bar{\lambda}'(\Phi^0) \right] \Phi^1 (\hat{U}_Z^0)^2 \right) dZ + \left(\frac{2}{r_I} \right) I_1 + I_2 - I_3 \right\} + O(\epsilon_S^2)
\end{aligned} \tag{B.31}$$

where I_1 , I_2 and I_3 are defined by equations (B.28), (B.29) and (B.30) respectively. Equation (B.31) is similar to equation (8.129) in chapter 8 which describes the Clausius-Clapeyron relationship for a planar, steady, temperature invariant interface. These last three effects are described in equation (B.31) by I_1 , I_2 and I_3 respectively. The differences between the coefficients in equations (B.31) and (8.129) result from the way in which our general system has been non-dimensionalised.

B.2 Expansion of Clausius-Clapeyron equation in Δ/ρ_S

Finally we show that when the density in the liquid phase is written as $\rho_L = \rho_S + \Delta$, where Δ/ρ_S is small, the leading order expansion in Δ of equation (B.31) is equivalent to the Gibbs-Thompson condition described by equation (8.65) in chapter 8 and (7.14) in chapter 7. Expressing the density in the form described in this paragraph allows us to express the non-dimensional density as

$$\bar{\rho}(\Phi^0) = 1 + \left(\frac{\Delta}{\rho_S}\right)[1 - r(\Phi^0)], \quad (\text{B.32})$$

where for simplicity we have taken $\rho_{SL} = \rho_S$. Therefore using equation (8.114) the leading order inner velocity can be written as

$$\begin{aligned} \hat{U}^0 &= -\dot{r}_I \left\{ 1 + \left(\frac{\Delta}{\rho_S}\right)[1 - r(\Phi^0)] \right\}^{-1} \\ &= -\dot{r}_I \left\{ 1 + \left(\frac{\Delta}{\rho_S}\right)(r(\Phi^0) - 1) \right\} + O\left(\left[\frac{\Delta}{\rho_S}\right]^2\right) \end{aligned}$$

and its derivative as

$$\hat{U}_Z^0 = -\left(\frac{\Delta}{\rho_S}\right)\dot{r}_I r'(\Phi^0)\Phi_Z^0 + O\left(\left[\frac{\Delta}{\rho_S}\right]^2\right).$$

Then using these expressions equation (B.13) becomes

$$\begin{aligned} g_L^0 - g_S^0 &= \left(\frac{4\kappa_{SL}}{R^*}\right)^2 \left\{ -\frac{(\dot{r}_I)^2}{2} \left[\left(\frac{\bar{\rho}_S}{\bar{\rho}_L}\right)^2 - 1 \right] \right. \\ &\quad \left. + \frac{C_{M2}}{\dot{r}_I \bar{\rho}_S} \int_{-\infty}^{\infty} [2\bar{\mu}(\Phi^0) + \bar{\lambda}(\Phi^0)] (\hat{U}_Z^0)^2 dZ \right\} \\ &= 0 + \left(\frac{\Delta}{\rho_S}\right) \left(\frac{4\kappa_{SL}}{R^*}\right)^2 \dot{r}_I^2 + O\left(\left[\frac{\Delta}{\rho_S}\right]^2\right). \quad (\text{B.33}) \end{aligned}$$

We consider the first order difference in the Gibbs free energy by integrating equation (B.16) directly to obtain

$$\begin{aligned} g_L^1 - g_S^1 &= \frac{1}{a} \left\{ \int_{-\infty}^{\infty} \left[1 + \left(\frac{\Delta}{\rho_S}\right)(r(\Phi^0) - 1) \right] \Phi_{ZZ}^0 \Phi_Z^1 dZ \right. \\ &\quad + \int_{-\infty}^{\infty} \bar{\nabla}^2 r \left[1 + \left(\frac{\Delta}{\rho_S}\right)(r(\Phi^0) - 1) \right] (\Phi_Z^0)^2 dZ \\ &\quad + \int_{-\infty}^{\infty} \left[1 + \left(\frac{\Delta}{\rho_S}\right)(r(\Phi^0) - 1) \right] \Phi_Z^0 \Phi_{ZZ}^1 dZ \\ &\quad - \int_{-\infty}^{\infty} \Phi_Z^0 \left[1 + \left(\frac{\Delta}{\rho_S}\right)(r(\Phi^0) - 1) \right]^2 \left[-\left(\frac{\Delta}{\rho_S}\right)r'(\Phi^0) \right] \Phi^1 \Phi_{ZZ}^0 dZ \\ &\quad \left. - \int_{-\infty}^{\infty} \frac{1}{\bar{X}} \hat{U}^0 \left[1 + \left(\frac{\Delta}{\rho_S}\right)(r(\Phi^0) - 1) \right] (\Phi_Z^0)^2 dZ \right\} \end{aligned}$$

$$\begin{aligned}
& + \left(\frac{4\kappa_{SL}}{R^*}\right)^2 \int_{-\infty}^{\infty} \left[1 + \left(\frac{\Delta}{\rho_S}\right)(r(\Phi^0) - 1)\right] \bar{P}_Z^1 dZ \\
& + \left(\frac{4\kappa_{SL}}{R^*}\right)^2 \int_{-\infty}^{\infty} \left\{ \left[1 + \left(\frac{\Delta}{\rho_S}\right)(r(\Phi^0) - 1)\right] \left[- \left(\frac{\Delta}{\rho_S}\right)r'(\Phi^0) \right] \Phi^1 \hat{U}^0 \hat{U}_Z^0 \right\} dZ \\
& + 2\bar{C}_{M1} \left(\frac{4\kappa_{SL}}{R^*}\right)^2 \int_{-\infty}^{\infty} \left\{ \left[1 + \left(\frac{\Delta}{\rho_S}\right)(r(\Phi^0) - 1)\right]^2 \right. \\
& \quad \left. \times \left[- \left(\frac{\Delta}{\rho_S}\right)r'(\Phi^0) \right] \Phi^1 \Phi_Z^0 \Phi_{ZZ}^0 \right\} dZ \\
& - C_{M2} \left(\frac{4\kappa_{SL}}{R^*}\right)^2 \int_{-\infty}^{\infty} \left\{ \left[1 + \left(\frac{\Delta}{\rho_S}\right)(r(\Phi^0) - 1)\right]^2 \left[- \left(\frac{\Delta}{\rho_S}\right)r'(\Phi^0) \right] \Phi^1 \right. \\
& \quad \left. \times \frac{\partial}{\partial Z} \left[\{2\bar{\mu}(\Phi^0) + \bar{\lambda}(\Phi^0)\} \hat{U}_Z^0 \right] \right\} dZ \\
& - \int_{-\infty}^{\infty} \left\{ \frac{\Theta_Z^1}{\Theta_m} \left\{ e_0 - r(\Phi^0)L + \frac{1}{4a_S} H(\Phi^0) \right\} + L\Theta_Z^1 \ln \left(\frac{\Theta^0}{\Theta_m} \right) \right\} dZ \\
& \quad + O\left(\left[\frac{\Delta}{\rho_S}\right]^2\right). \tag{B.34}
\end{aligned}$$

Equation (B.34) appears extremely complicated, however by considering only the leading order terms in Δ/ρ_S and ε_S the following simplifications can be made:

- The fourth and the eighth integrals in equation (B.34) cancel since

$$2\bar{C}_{M1} \left(\frac{4\kappa_{SL}}{R^*}\right)^2 = \frac{1}{a}.$$

- Because the first and second derivatives of the leading order inner velocity are expressed as

$$\hat{U}_Z^0 = - \left(\frac{\Delta}{\rho_S}\right) \dot{r}_I r'(\Phi^0) \Phi_Z^0 + O\left(\left[\frac{\Delta}{\rho_S}\right]^2\right)$$

and

$$\hat{U}_{ZZ}^0 = - \left(\frac{\Delta}{\rho_S}\right) \dot{r}_I \left[r'(\Phi^0) \Phi_{ZZ}^0 + r''(\Phi^0) \Phi_Z^0 \right] + O\left(\left[\frac{\Delta}{\rho_S}\right]^2\right)$$

the seventh and ninth integrals are both of order $\left(\Delta/\rho_S\right)^2$ and therefore they are ignored. Then noting that $\bar{\nabla}^2 r = \bar{\kappa}_c^0$, to leading order in ε_S equation (B.34) becomes

$$\begin{aligned}
g_L^1 - g_S^1 & = \frac{1}{a} \bar{\kappa}_c^0 \int_{-\infty}^{\infty} (\Phi_Z^0)^2 dZ \\
& + \frac{\dot{r}_I}{a\bar{X}} \int_{-\infty}^{\infty} (\Phi_Z^0)^2 dZ + \left(\frac{4\kappa_{SL}}{R^*}\right)^2 \left[\bar{P}_L^1 - \bar{P}_S^1 \right] \\
& - \int_{-\infty}^{\infty} \left\{ \frac{\Theta_Z^1}{\Theta_m} \left[e_0 - r(\Phi^0)L + \frac{1}{4a_S} H(\Phi^0) \right] + L\Theta_Z^1 \ln \left(\frac{\Theta^0}{\Theta_m} \right) \right\} dZ \\
& + \left(\frac{\Delta}{\rho_S}\right) \left\{ \frac{1}{a} \int_{-\infty}^{\infty} \left[(r(\Phi^0) - 1) \frac{\partial}{\partial Z} (\Phi_Z^0 \Phi_Z^1) \right] dZ \right.
\end{aligned}$$

$$\begin{aligned}
& + \left(\frac{\bar{\kappa}_c^0}{a} + \frac{2\dot{r}_I}{a\bar{X}} \right) \int_{-\infty}^{\infty} (r(\Phi^0) - 1) (\Phi_Z^0)^2 dZ \\
& + \left(\frac{4\kappa_{SL}}{R^*} \right)^2 \int_{-\infty}^{\infty} (r(\Phi^0) - 1) \bar{P}_Z^1 dZ \Big\} + O\left(\left[\frac{\Delta}{\rho_S}\right]^2\right). \quad (\text{B.35})
\end{aligned}$$

The Gibbs free energy is defined in chapter 8 as

$$g(T, p, \phi) = g_0(T, \phi) + \frac{p - p_0}{\rho(\phi)}$$

where from [2]

$$g_0(T, \phi) = \left[e_0 - cT_m - r(\phi)L + \frac{1}{4a_S}H(\phi) \right] \left(1 - \frac{T}{T_m} \right) - cT \ln \left(\frac{T}{T_m} \right) + \frac{1}{4a}H(\phi).$$

By non-dimensionalising this expression and using the inner asymptotic expansions for the variables T , p and ϕ in terms of the small parameter ε_S , to leading and first order the expression for the difference between the Gibbs free energy in the solid and liquid phases becomes

$$\begin{aligned}
g_L - g_S & = L \left(1 - \frac{\Theta^0}{\Theta_m} \right) + \left(\frac{4\kappa_{SL}}{R^*} \right)^2 (\bar{P}_L^0 - \bar{P}_0) - \left(\frac{4\kappa_{SL}}{R^*} \right)^2 \left(\frac{\bar{\rho}_S}{\bar{\rho}_L} \right) (\bar{P}_S^0 - \bar{P}_0) \\
& + \varepsilon_S \left\{ [e_0 - L\Theta_m] \left[\frac{\Theta_L^1 - \Theta_S^1}{\Theta_m} \right] + L \frac{\Theta_S^1}{\Theta_m} + L \ln \left[\frac{\Theta^0}{\Theta_m} \right] [\Theta_L^1 - \Theta_S^1] \right. \\
& \quad \left. + \left(\frac{4\kappa_{SL}}{R^*} \right)^2 \left[\bar{P}_S^1 - \bar{P}_L^1 - \left(\frac{\Delta}{\rho_S} \right) (r(\Phi^0) - 1) \bar{P}_L^1 \right] \right\} + O(\varepsilon_S^2). \quad (\text{B.36})
\end{aligned}$$

Therefore combining equations (B.33) and (B.35) and equating the resulting expression with equation (B.36) results in

$$\begin{aligned}
g_L - g_S & = L \left(1 - \frac{\Theta^0}{\Theta_m} \right) + \left(\frac{4\kappa_{SL}}{R^*} \right)^2 \left\{ (\bar{P}_L^0 - \bar{P}_S^0) - \left(\frac{\Delta}{\rho_S} \right) (\bar{P}_L^0 - \bar{P}_0) \right\} \\
& + \varepsilon_S \left\{ [e_0 - L\Theta_m] \left[\frac{\Theta_L^1 - \Theta_S^1}{\Theta_m} \right] + L \frac{\Theta_S^1}{\Theta_m} + L \ln \left[\frac{\Theta^0}{\Theta_m} \right] [\Theta_L^1 - \Theta_S^1] \right. \\
& \quad \left. + \left(\frac{4\kappa_{SL}}{R^*} \right)^2 \left[\bar{P}_S^1 - \bar{P}_L^1 - \left(\frac{\Delta}{\rho_S} \right) (r(\Phi^0) - 1) \bar{P}_L^1 \right] \right\} + O(\varepsilon_S^2) \\
& = \left(\frac{\Delta}{\rho_S} \right) \left(\frac{4\kappa_{SL}}{R^*} \right)^2 \dot{r}_I^2 + O\left(\left[\frac{\Delta}{\rho_S}\right]^2\right) \\
& + \varepsilon_S \left\{ \frac{\bar{\kappa}_c^0}{a} \frac{\sigma^0 a}{\delta \rho_{SL}} + \frac{\dot{r}_I}{a\bar{X}} \frac{\sigma^0 a}{\delta \rho_{SL}} + \left(\frac{4\kappa_{SL}}{R^*} \right)^2 \left[\bar{P}_L^1 - \bar{P}_S^1 \right] \right. \\
& \quad \left. - \int_{-\infty}^{\infty} \left[\frac{\Theta_Z^1}{\Theta_m} \left[e_0 - r(\Phi^0)L + \frac{1}{4a_S}H(\Phi^0) \right] - L\Theta_Z^1 \ln \left(\frac{\Theta^0}{\Theta_m} \right) \right] dZ \right\} \\
& + \varepsilon_S \left(\frac{\Delta}{\rho_S} \right) \left\{ \frac{1}{a} \int_{-\infty}^{\infty} \left[(r(\Phi^0) - 1) \frac{\partial}{\partial Z} (\Phi_Z^0 \Phi_Z^1) \right] dZ \right.
\end{aligned}$$

$$\begin{aligned}
& + \left(\frac{\bar{\kappa}_c^0}{a} + \frac{2\dot{r}_I}{a\bar{X}} \right) \int_{-\infty}^{\infty} [r(\Phi^0) - 1](\Phi_Z^0)^2 dZ \\
& + \left(\frac{4\kappa_{SL}}{R^*} \right)^2 \int_{-\infty}^{\infty} [r(\Phi^0) - 1] \bar{P}_Z^1 dZ \Big\} + O\left(\left[\frac{\Delta}{\rho_S}\right]^2\right), \quad (\text{B.37})
\end{aligned}$$

where²

$$\int_{-\infty}^{\infty} (\Phi_Z^0)^2 dZ = \frac{\sigma^0 a}{\delta \rho_{SL}}$$

has been used to transform the first two integrals in equation (B.35). Using equation (B.32) and expanding equation (B.19) in powers of (Δ/ρ_S) yields

$$\bar{P}_S^0 - \bar{P}_L^0 = -\dot{r}_I^2 \left(\frac{\Delta}{\rho_S} \right) + O\left(\left[\frac{\Delta}{\rho_S}\right]^2\right). \quad (\text{B.38})$$

Therefore the leading order pressure difference on the first line of (B.37) cancels with the first term on the right hand side of this equation. Finally, noting that $\delta = \varepsilon_S R^*$ then to first order in ε_S and (Δ/ρ_S) equation (B.37) becomes

$$\begin{aligned}
L \left(1 - \frac{\Theta^0}{\Theta_m} \right) & - \left(\frac{4\kappa_{SL}}{R^*} \right)^2 \left(\frac{\Delta}{\rho_S} \right) (\bar{P}_0 - \bar{P}_L^0) \\
- \varepsilon_S \Big\{ [e_0 & - L\Theta_m] \left[\frac{\Theta_L^1 - \Theta_S^1}{\Theta_m} \right] + L \frac{\Theta_S^1}{\Theta_m} + L \ln \left[\frac{\Theta^0}{\Theta_m} \right] [\Theta_L^1 - \Theta_S^1] \\
& + \left(\frac{4\kappa_{SL}}{R^*} \right)^2 \left[\bar{P}_S^1 - \bar{P}_L^1 - \left(\frac{\Delta}{\rho_S} \right) (r(\Phi^0) - 1) \bar{P}_L^1 \right] \Big\} + O(\varepsilon_S^2) \\
= \frac{\sigma^0 \bar{\kappa}_c^0}{R^* \rho_{SL}} & + \left(\frac{\sigma^0}{R^* \rho_{SL}} \right) \frac{\dot{r}_I}{\bar{X}} \\
+ \varepsilon_S \Big\{ - \int_{-\infty}^{\infty} & \left[\frac{\Theta_Z^1}{\Theta_m} \left[e_0 - r(\Phi^0)L + \frac{1}{4a_S} H(\Phi^0) \right] - L \Theta_Z^1 \ln \left(\frac{\Theta^0}{\Theta_m} \right) \right] dZ \\
& + \left(\frac{4\kappa_{SL}}{R^*} \right)^2 [\bar{P}_L^1 - \bar{P}_S^1] \Big\} \\
+ \varepsilon_S \left(\frac{\Delta}{\rho_S} \right) & \Big\{ - \left(\frac{\sigma^0}{R^* \varepsilon_S \rho_{SL}} \right) \bar{\kappa}_c^0 - \left(\frac{2\sigma^0}{\bar{X} R^* \varepsilon_S \rho_{SL}} \right) \dot{r}_I - \left(\frac{4\kappa_{SL}}{R^*} \right)^2 [\bar{P}_L^1 - \bar{P}_S^1] \\
+ \frac{1}{a} \int_{-\infty}^{\infty} & r(\Phi^0) \frac{\partial}{\partial Z} (\Phi_Z^0 \Phi_Z^1) dZ + \left(\frac{\bar{\kappa}_c^0}{a} + \frac{2\dot{r}_I}{a\bar{X}} \right) \int_{-\infty}^{\infty} r(\Phi^0) (\Phi_Z^0)^2 dZ \\
& + \left(\frac{4\kappa_{SL}}{R^*} \right)^2 \int_{-\infty}^{\infty} r(\Phi^0) \bar{P}_Z^1 dZ \Big\} + O(\varepsilon_S^2). \quad (\text{B.39})
\end{aligned}$$

Re-arranging equation (B.39) leaves

$$\Theta^0 = \Theta_m - \frac{\Theta_m \sigma^0}{R^* L \rho_{SL}} \bar{\kappa}_c^0 - \frac{\sigma^0 \Theta_m}{\bar{X} R^* L \rho_{SL}} \dot{r}_I$$

²This relationship was derived by equation (8.64) in chapter 8.

$$\begin{aligned}
& -\left(\frac{\Delta}{\rho_S}\right) \left\{ \left(\frac{4\kappa_{SL}}{R^*}\right)^2 \frac{\Theta_m}{L} (\bar{P}_0 - \bar{P}_L^0) - \left(\frac{\Theta_m \sigma^0}{LR^* \rho_{SL}}\right) \bar{\kappa}_c^0 - \left(\frac{2\Theta_m \sigma^0}{LR^* \rho_{SL}}\right) \frac{\dot{r}_I}{\bar{X}} \right\} \\
& -\varepsilon_S \left\{ -\Theta_m [\Theta_L^1 - \Theta_S^1] + \Theta_S^1 - \int_{-\infty}^{\infty} \Theta_Z^1 \left[-r(\Phi^0) + \frac{1}{4a_S L} H(\Phi^0) \right] dZ \right\} \\
& -\varepsilon_S \left(\frac{\Delta}{\rho_S}\right) \left\{ \left(\frac{4\kappa_{SL}}{R^*}\right)^2 \frac{\Theta_m}{L} [\bar{P}_S^1 - r(\Phi^0) \bar{P}_L^1] + \frac{\Theta_m}{aL} \int_{-\infty}^{\infty} r(\Phi^0) \frac{\partial}{\partial Z} (\Phi_Z^0 \Phi_Z^1) dZ \right. \\
& \quad + \left(\frac{\Theta_m \bar{\kappa}_c^0}{La} + \frac{2\Theta_m \dot{r}_I}{La \bar{X}}\right) \int_{-\infty}^{\infty} r(\Phi^0) (\Phi_Z^0)^2 dZ \\
& \quad \left. + \frac{\Theta_m}{L} \left(\frac{4\kappa_{SL}}{R^*}\right)^2 \int_{-\infty}^{\infty} r(\Phi^0) \bar{P}_Z^1 dZ \right\} + O\left[\left(\frac{\Delta}{\rho_S}\right)^2\right]. \tag{B.40}
\end{aligned}$$

The integrands $r(\Phi^0)(\Phi_Z^0)^2$, $r(\Phi^0)(\Phi_Z^1 \Phi_Z^0)_Z$ and $r(\Phi^0) \bar{P}_Z^1$ cannot be directly integrated with respect to Z . However if $r(\Phi^0)$ is approximated by a constant average value, given as α say, then these three integrals may be expressed as

$$\int_{-\infty}^{\infty} r(\Phi^0) \frac{\partial}{\partial Z} (\Phi_Z^0 \Phi_Z^1) dZ \approx \alpha [\Phi_Z^0 \Phi_Z^1]_{-\infty}^{\infty} = 0, \quad \int_{-\infty}^{\infty} r(\Phi^0) (\Phi_Z^0)^2 dZ \approx \alpha \left(\frac{\sigma^0 a}{\delta \rho_{SL}}\right)$$

and

$$\int_{-\infty}^{\infty} r(\Phi^0) \bar{P}_Z^1 dZ \approx \alpha [\bar{P}_L^1 - \bar{P}_S^1].$$

Therefore re-dimensionalising equation (B.40) and ignoring all terms which are first or higher order in ε_S we obtain

$$\begin{aligned}
T^0 &= T_m - \left(\frac{\sigma^0 T_m}{\rho_{SL} L}\right) \kappa_c^0 - \left(\frac{\sigma^0 T_m}{4\kappa_{SL} \bar{X} L \rho_{SL}}\right) \frac{dR}{dt} \\
&+ \left(\frac{\Delta}{\rho_S}\right) \left\{ \frac{T_m}{\rho_S L} (P_0 - P_L^0) - (1 - \alpha) \left(\frac{\sigma^0 T_m}{\rho_{SL} L}\right) \kappa_c^0 - (1 - \alpha) \left(\frac{2\sigma^0 T_m}{4\kappa_{SL} \bar{X} L \rho_{SL}}\right) \frac{dR}{dt} \right\}. \tag{B.41}
\end{aligned}$$

To leading order in Δ/ρ_S equation (B.41) is clearly equivalent to the Gibbs-Thompson condition shown in chapter 8 by equation (8.65) and equation (7.14) in chapter 7. The first order term in Δ/ρ_S is small if the latent heat term L is large or if α is $O(1)$.

Bibliography

- [1] O.O. Ajayi, C. Sozou, and W.M. Pickering. Nonlinear fluid motions in a container due to the discharge of an electric current. *J. Fluid Mech.*, 148:285–300, 1984.
- [2] D. M. Anderson, G.B. McFadden, and A. A. Wheeler. A phase-field model of solidification with convection. *Physica D*, 135:175–194, 2000.
- [3] D.M. Anderson, G.B. McFadden, and A.A. Wheeler. Diffuse-interface methods in fluid mechanics. *Annu. Rev. Fluid Mech.*, 30:139–65, 1998.
- [4] J.A. Andrews and R.E. Craine. Fluid flow in a hemisphere induced by a distributed source of current. *J. Fluid Mech.*, 84:281–290, 1978.
- [5] D.R. Atthey. A mathematical model for flow in a weld pool at high currents. *J. Fluid Mech.*, 98:787–802, 1980.
- [6] G.K. Batchelor. *An Introduction to Fluid Dynamics*. Cambridge University Press, 1985.
- [7] A. Belgrove. *Numerical Modelling and Stability Analysis of Convective Flows in Weld pools*. PhD thesis, Southampton University, 1996.
- [8] E. Ben-Jacob, N. Goldenfield, J.S. Langer, and G. Schon. Boundary layer model for pattern formation in solidification. *Phys. Rev. A*, 29:330–340, 1984.
- [9] V. Bojarevics. Magneto-hydrodynamic flows at an electric current point source. part i. *Magnitnaya Gidrodinamika*, 1:21–28, 1981.
- [10] V. Bojarevics. Magneto-hydrodynamic flows at an electric current point source. part ii. *Magnitnaya Gidrodinamika*, 2:41–44, 1981.
- [11] V. Bojarevics and R. Millere. Amplification of rotation of meridional electro-vortex flow in a hemisphere. *Magnitnaya Gidrodinamika*, 4:51–56, 1982.
- [12] V. Bojarevics and E.V. Shcherbinin. Azimuthal rotation in the axisymmetric meridional flow due to an electric current source. *J. Fluid Mech.*, 126:413–430, 1983.

- [13] V. Bojarevics, E.V. Shcherbinin, Ya. Freibergs, and E.L. Shilova. *Electrically induced vortical flows*. Kluwer Acad. Pub., 1989.
- [14] W.E. Boyce and R.C. DiPrima. *Elementary Differential Equations and Boundary Value Problems*. Wiley, 1992.
- [15] P. Burgardt and C.R. Heiple. Interaction between impurities and welding parameters in determining GTA weld shapes. *Welding J.*, 65:150s, 1986.
- [16] G. Caginalp. Stephan and Hele-Shaw type models as asymptotic limits of the phase-field equations. *Phys. Rev. A*, 39:5887–5896, 1989.
- [17] G. Caginalp and X. Chen. Phase-field equations in the singular limit of sharp interface problems. In M. E. Gurtin and G.B. McFadden, editors, *On the Evolution of Phase Boundaries.*, volume 43 of *The IMA Volumes in Mathematics and its Applications.*, chapter 1, pages 1–27. Springer-Verlag, 1992.
- [18] G. Caginalp and P.C. Fife. Phase-field methods for interfacial boundaries. *Phys. Rev. B*, 33:7792–7794, 1986.
- [19] G. Caginalp and P.C. Fife. Dynamics of layered interfaces arising from phase boundaries. *SIAM J. Appl. Math.*, 48:506–518, 1988.
- [20] G. Caginalp and J. Jones. A phase-field model: Derivation and new interface relations. In M. E. Gurtin and G.B. McFadden, editors, *On the Evolution of Phase Boundaries.*, volume 43, pages 29–47. Springer-Verlag, 1992.
- [21] G. Caginalp and E.A. Socolovsky. Computation of sharp phase boundaries by spreading: The planar and spherically symmetric cases. *J. Comput. Phys.*, 95:85–100, 1991.
- [22] J.W. Cahn and J.E. Hilliard. Free energy of a non-uniform system. i. interface free energy. *J. Chem. Phys.*, 28:258–267, 1958.
- [23] H.S. Carslaw and J.C. Jaeger. *Conduction of heat in solids*. Clarendon Press, Oxford, 1959.
- [24] B. Chalmers. *Principles of Solidification*. Wiley, 1964.
- [25] P.L. Chambre. On the dynamics of phase growth. *Quart. J. Mech. and Appl. Math.*, 9:224–233, 1956.
- [26] S. Chandrasaker. *Hydrodynamic and Hydromagnetic Stability*. Oxford University Press, 1968.

- [27] F. K. Chung and P.S. Wei. Mass, momentum, and energy transport in a molten pool when welding dissimilar metals. *Trans. ASME - J. Heat Trans.*, 121:451–461, 1999.
- [28] J.B. Collins and H. Levine. Diffuse interface model of diffusion-limited growth. *Phys. Rev. B*, 31:6119–6122, 1986.
- [29] S.D. Conte and C. de Boor. *Elementary Numerical Analysis*. McGraw-Hill, 1980.
- [30] R.E. Craine and A. Belgrove. *Submitted to J. Fluid Mech.*
- [31] R.E. Craine and N.P. Weatherill. Fluid flow in a hemispherical container induced by a distributed source of current and superimposed magnetic field. *J. Fluid Mech.*, 99:1–12, 1980.
- [32] J. Crank. *Free and Moving Boundary Problems*. Oxford Science Publications, 1984.
- [33] P.V. Dankwerts. Unsteady state diffusion or heat conduction with a moving boundary. *Trans. Faraday Soc.*, 46:701–712, 1950.
- [34] P.A. Davidson. Magnetohydrodynamics in materials processing. *Annu. Rev. Fluid Mech.*, 31:273–300, 1999.
- [35] P.A. Davidson, D. Kinnear, R.J. Lingwood, D.J. Short, and X. He. The role of Ekman pumping and the dominance of swirl in confined flows driven by Lorentz forces. *Eur. J. Mech. B- Fluids*, 18:693–711, 1999.
- [36] T. Debroy and S.A. David. Physical processes in fusion welding. *Rev. Modern Phys.*, 67:85–112, 1995.
- [37] P.G. Drazin. *Nonlinear systems*. Cambridge University Press, 1992.
- [38] P.G. Drazin and W.H. Reid. *Hydrodynamic Stability*. Cambridge University Press, 1981.
- [39] T.W. Eagar and N.-S. Tsai. Temperature fields produced by travelling distributed heat sources. *Welding J.*, 62:346s–355s, 1983.
- [40] C. Eddington. *The Internal Constitution of the Stars*. Cambridge University Press., 1926.
- [41] R. Fernandez-Feria, J.F. de la Mora, M. Perez-Saborid, and A. Barrero. Conically similar swirling flows at high Reynolds numbers. *Quart. J. Mech. and Appl. Math.*, 52:1–53, 1999.

- [42] P.C. Fife and G.S. Gill. The phase-field description of mushy zones. *Physica D*, 35:267–275, 1989.
- [43] P.C. Fife and G.S. Gill. Phase-transition mechanisms for the phase-field model under internal heating. *Phys. Rev. A*, 43:843–851, 1991.
- [44] C.A.J. Fletcher. *Computational Techniques for Fluid Dynamics*. Springer-Verlag, 1991.
- [45] R.W. Gardner, D.R. Douglass and S.A. Trogdon. Linear stability of natural convection in spherical annuli. *J. Fluid Mech.*, 221:105–129, 1990.
- [46] J.W. Gibbs. *Collected Works*. Yale University Press, New Haven, 1948.
- [47] R.J. Glicksman, M.E. Schaefer and J.D. Ayers. Dendritic growth - a test of theory. *Met. Trans. A*, 7A:1747–1759, 1976.
- [48] A.E. Guile. Arc-electrode phenomena. *IEE Proc.*, 118:1131–1154, 1971.
- [49] A.E. Guile. Electric arcs: their electrode processes and engineering applications. *IEE Proc. A*, 131:450–480, 1984.
- [50] B.I. Halperin, P.C. Hohenberg, and Ma Shang-keng. Renormalisation-group methods for critical dynamics: I. recursion relations and effects of energy conservation. *Phys. Rev. B*, 10:139–153, 1974.
- [51] C.R. Heiple and J.R. Roper. Effect of selenium on GTAW fusion zone geometry. *Welding J.*, 60:143s–145s, 1981.
- [52] N.C. Hibbert, S.E. Markatos and V.R. Voller. Computer simulation of moving-interface, convective, phase-change process. *Int. J. Heat Mass Trans.*, 31:1785–1795, 1988.
- [53] K. Hiraoka, A. Okada, and M. Inagaki. Effect of electrode geometry on maximum arc pressure in gas tungsten arc welding. *International Institute of Welding*, Doc 212-652-86, 1986.
- [54] G. Horvay. Freezing into an undercooled melt accompanied by density change. *Proc. 4th Natl. Cong. of Appl. Mech.*, 2:1315–1325, 1962.
- [55] G. Horvay. The tension field created by a spherical nucleus. *Int. J. Heat Mass Trans.*, 8:195–243, 1965.
- [56] Y.T. Hsieh, R.I. Pan and H.Y. Liou. The study of minor elements and shielding gas on penetration in TIG welding of type 304 stainless steel. *J. Mater. Eng. Perform.*, 8:68–74, 1999.

- [57] K. Ishizaki, S. Yokoya, T. Okada, and A. Matsunawa. Experimental studies on the various convectional flow in the weld pool. *International Institute of Welding*, Doc 212-656-86, 1986.
- [58] E. Kannatey-Asibu. Milestone developments in welding and joining processes. *J. Manufacturing Sci. Eng.*, 119:801–810, 1997.
- [59] B.J. Keene, K.C. Mills, and R.S. Brooks. Surface properties of liquid metals and their effects on weld ability. *Materials Science and Technology*, 1:568–571, 1985.
- [60] J. Kessler, D.A. Koplik and H. Levine. Geometrical models of interface evolution iii. theory of dendritic growth. *Phys. Rev. A*, 31:1712–1717, 1985.
- [61] R. Kobayashi. Modeling and numerical simulations of dendritic crystal growth. *Physica D*, 63:410–423, 1993.
- [62] P.G. Kroeger and S. Ostrach. The solution of a two-dimensional freezing problem including convection in the liquid region. *Int. J. Heat Mass Trans.*, 17:1191–1207, 1974.
- [63] H. Lamb. *Hydrodynamics*. Cambridge University Press, 1932.
- [64] J.F. Lancaster. The physics of fusion welding part 1: The electric arc in welding. *IEE Proc.*, 134:233–254, 1987.
- [65] J.F. Lancaster. The stability of meridional liquid flow induced by a gradient of surface tension or electro magnetic forces. *International Institute of Welding*, Doc 212-692-87, 1987.
- [66] J.S. Langer. Directions in condensed matter physics. *World Scientific, Singapore*, page 165, 1986.
- [67] P.N. Lee, P.D. Quisted and M. McLean. Modelling of Marangoni effects in electron beam melting. *Phil. Trans. Roy. Soc. London A*, 356:1027–1043, 1998.
- [68] B.P. Leonard. A stable and accurate convective modelling procedure based on quadratic upstream interpolation. *Computer methods in applied maths and engineering*, 19:59–98, 1979.
- [69] D. R. Lide. *Handbook of Chemistry and Physics*, volume 73. CRC press, 1992.
- [70] A. Lifschitz. On the instabilities of three-dimensional flows of an ideal incompressible fluid. *Phys. Letters A*, 167:465–474, 1992.

- [71] M.L. Lin and T.W. Eagar. Influence of arc pressure on weld pool geometry. *Welding J.*, 64:163s, 1985.
- [72] J. Lowengrub and J. Truskinovsky. Quasi-incompressible cahn-hillard fluids and topological transitions. *Proc. Roy. Soc. Ser. A*, 454:2617, 1998.
- [73] S. Lundquist. On the hydromagnetic viscous flow generated by a diverging electric current. *Arkiv. Fys.*, 40:89–95, 1969.
- [74] H. Maecker. Plasmastromungen in lichtebogen infolge elektromagnetischer kompression. *Z. Phys.*, 141:198–216, 1955.
- [75] S. Matsunawa, A. Yokoya and Y. Asako. Convection in the weld pool and its effect on penetration shape. *International Institute of Welding*, Doc 212-687-87, 1987.
- [76] G.S. Mills. Fundamental mechanisms of penetration in GTA welding. *Welding J.*, 58:21s–24s, 1979.
- [77] K.C. Mills, B.J. Keene, R.F. Brooks, and A. Shirali. Marangoni effects in welding. *Phil. Trans. Roy. Soc. London A*, 356:911–925, 1998.
- [78] P.E. Murray and A. Scotti. Depth of penetration in gas metal arc welding. *Sci. Technol. Weld. Join.*, 4:112–117, 1999.
- [79] G.M. Oreper and J. Szekely. Heat and fluid flow in weld pools. *J. Fluid Mech.*, 147:53–79, 1984.
- [80] S.V. Patankar. *Numerical Heat Transfer and Fluid Flow*. Series in Computational Methods in Mechanics and Thermal Sciences. McGraw-Hill, 1980.
- [81] C.E. Pearson. A computational method for viscous flow problems. *J. Fluid Mech.*, 21:611–622, 1965.
- [82] O. Penrose and P.C. Fife. Thermodynamically consistent models of phase-field type for the kinetics of phase transitions. *Physica D*, 43:44–62, 1990.
- [83] C-Y. Perng and R.L. Street. Three-dimensional unsteady flow simulations-alternative strategies for a volume averaged calculation. *Int. J. Numer. Methods Fluids*, 9:341–362, 1989.
- [84] P. Pierce, S.W. Burgardt and D.L. Olson. Thermocapillary and arc phenomena in stainless steel welding. *Welding J.*, 78:45s–52s, 1999.

- [85] J. Priede, A. Cramer, A. Bojarevics, A.Y. Gelfgat, P.Z. Barr-Yoseph, A.L. Yarin, and G. Gerbeth. Experimental and numerical study of anomalous thermocapillary convection in liquid gallium. *Phys. Fluids*, 11:3331–3339, 1999.
- [86] J. Ravindran, K. Srinivasan and A.G. Marathe. Finite element study on the role of convection in laser surface melting. *Num. Heat Trans. A*, 26:601–618, 1994.
- [87] Lord Rayleigh. On the stability, or instability of certain fluid motions. *Proc. Roy. Soc.*, 11:57–78, 1880.
- [88] Lord Rayleigh. On the theory of surface forces-ii. compressible fluids. *Phil. Mag.*, 33:209, 1892.
- [89] O. Reynolds. An experimental investigation of the circumstances which determine whether the motion of water shall be direct or sinuous, and of the law of resistance in parallel channels. *Phil. Trans. Roy. Soc.*, 174:935–982, 1883.
- [90] P.J. Roache. *Computational Fluid Dynamics*. Hermosa, Albuquerque, 1972.
- [91] S.I. Rokhlin. A study of arc force, pool depression and weld penetration during gas tungsten arc-welding. *Welding J.*, 72:381s–390s, 1993.
- [92] D. Rosenthal. Mathematical theory of heat distribution during welding and cutting. *Welding J.*, 20:220s, 1941.
- [93] J.S. Rowlinson and B. Widom. *Molecular Theory of Capillarity*. Oxford Science Publications, 1982.
- [94] L.I. Rubinstein. *The Stefan Problem.*, volume 27 of *Trans. Math. Monographs*. Am. Math. Soc., 1971.
- [95] R. J. Schaefer and M. E. Glicksman. Fully time-dependent theory for the growth of spherical crystal nuclei. *J. Crystal Growth*, 5:44–58, 1969.
- [96] R.F. Scheller, P.R. Brooks and K.C. Mills. Influence of sulfur and welding conditions on penetration in thin strip stainless steel. *Welding J.*, 74:69s–76s, 1995.
- [97] P. Seppecher. Moving contact lines in the Cahn-Hillard theory. *Int. J. Eng. Sci.*, 34:977–992, 1996.
- [98] J.A. Shercliff. *A Textbook of Magneto hydrodynamics*. Pergamon Press, 1965.
- [99] J.A. Shercliff. Fluid motions due to an electric current source. *J. Fluid Mech.*, 40:241–250, 1970.

- [100] A. Shirali and K.C. Mills. The effect of welding parameters on penetration in GTA welds. *Welding J.*, 72:347s–353s, 1993.
- [101] A. Shtern, V. Borissof and F. Hussain. Vortex sinks with axial flow: Solution and applications. *J. Fluid Mech.*, 9:2941–2959, 1997.
- [102] M. Shtern, V. Goldshtik and F. Hussain. Generation of swirl due to symmetry breaking. *Phys. Rev. E*, 49:2881–2886, 1994.
- [103] V. Shtern and A. Barrero. Bifurcation of swirl in liquid cones. *J. Fluid Mech.*, 300:169–205, 1995.
- [104] V. Shtern and F. Hussain. Azimuthal instability of divergent flows. *J. Fluid Mech.*, 256:535–560, 1993.
- [105] V. Shtern and F. Hussain. Instabilities of conical flows causing steady bifurcations. *J. Fluid Mech.*, 366:33–85, 1998.
- [106] V. Shtern and F. Hussain. Collapse, symmetry breaking and hysteresis in swirling flows. *Annu. Rev. Fluid Mech.*, 31:537–566, 1999.
- [107] G. Siato, Y. Goldbeck-Wood and H. Muller-Krumbhaar. Numerical simulation of dendritic growth. *Phys. Rev. A*, 38:2148–2157, 1988.
- [108] G.D. Smith. *Numerical Solutions of Partial Differential Equations*. Oxford University Press, 1965.
- [109] J.B. Smith. Shape instabilities and pattern formation in solidification: A new method for solution of the moving boundary problem. *J. Comput. Phys.*, 39:112–127, 1981.
- [110] C. Sozou. On fluid motions induced by an electric current source. *J. Fluid Mech.*, 46:25–32, 1971.
- [111] C. Sozou. On some similarity solutions in magnetohydrodynamics. *J. Fluid Mech.*, 6:331–341, 1971.
- [112] C. Sozou. Fluid motions induced by an electric current jet. *J. Fluid Mech.*, 15:272–276, 1972.
- [113] C. Sozou. On magnetohydrodynamic flows generated by an electric current discharge. *J. Fluid Mech.*, 63:665–671, 1974.
- [114] C. Sozou and H. English. Fluid motions induced by an electric current discharge. *Proc. Roy. Soc. London*, 329:71–81, 1972.

- [115] C. Sozou and W.M. Pickering. The development of magneto hydrodynamic flow due to an electric current discharge. *J. Fluid Mech.*, 70:509–517, 1975.
- [116] C. Sozou and W.M. Pickering. Magneto hydrodynamic flow due to the discharge of an electric current in a hemispherical container. *J. Fluid Mech.*, 73:641–650, 1976.
- [117] C. Sozou and W.M. Pickering. Magneto hydrodynamic flow in a container due to the discharge of an electric current from a finite size electrode. *Proc. Roy. Soc. London*, 362:509–523, 1978.
- [118] H.B. Squire. The round laminar jet. *Quart. J. Mech. and Appl. Math.*, 4:321–329, 1951.
- [119] J. Stefan. Über die theorie der eisbildung, insbesondere über die eisbildung in polarmeere. *Ann. Phys. U. Chem.*, 42:269–286, 1891.
- [120] G. Stephenson. *Mathematical Methods for Science Students*. Longman Scientific and Technical, 1988.
- [121] J. Szekely and V. Stanek. On the heat transfer and liquid mixing in the continuous casting of steel. *Met. Trans.*, 1:119, 1970.
- [122] Y. Takemoto and Y. Nakamura. A three-dimensional flow solver. *Lecture Notes in Physics*, 264:594–599, 1986.
- [123] L.N. Tao. Free boundary problems with radiation boundary conditions. *Quart. Appl. Maths.*, 37:1–10, 1979.
- [124] L.N. Tao. On solidification problems including the density jump at the moving boundary. *Quart. J. Mech. and Appl. Maths.*, 32:175–185, 1979.
- [125] A. Thom. Flow past circular cylinders at low speed. *Proc. Roy. Soc. London A*, 141:651–667, 1933.
- [126] R. Tonhardt and G. Amberg. Phase-field simulation of dendritic growth in a shear flow. *J. Crystal Growth*, 194:406–425, 1998.
- [127] J.D. Van der Waals. Verhandel. konink. akad. weten. *J. Stat. Phys.*, 20:197, 1979.
- [128] M. Van Dyke. *Perturbation Methods in Fluid Mechanics*. New York Academic Press, 1964.
- [129] S-L. Wang, R.F. Sekerka, A.A. Wheeler, B.T. Murray, S.R. Coriell, R.J. Braun, and G.B. McFadden. Thermodynamically-consistent phase-field models for solidification. *Physica D*, 69:189–200, 1993.

- [130] N.P. Weatherill. *Magnetohydrodynamic flow in a weldpool*. PhD thesis, University of Southampton, 1980.
- [131] K. Weltner and J. Grosjean et. al. *Mathematics for Engineers and Scientists*. Stanley Thornes, 1991.
- [132] A. A. Wheeler. Description of transport processes. In D. T. J. Hurle, editor, *Part B: Transport and Stability.*, volume 1 of *Handbook of Crystal Growth.*, chapter 10, pages 683–739. North-Holland, 1993.
- [133] B.T. Wheeler, A.A. Murray and R.J. Schaefer. Computation of dendrites using a phase field model. *Physica D*, 66:243–262, 1993.
- [134] D. Wilson. *Oak Ridge Natl. Lab. Rep. CSD-93*, 1982.
- [135] S.K. Wilson. The effect of a uniform magnetic field on the onset of steady Bénard-Marangoni convection in a layer of conducting fluid. *J. Eng. Math.*, 27:161–188, 1993.
- [136] D. Woods and D.R. Milner. Motion in the weld pool in arc welding. *Welding J.*, 50:163s–173s, 1971.
- [137] L.C. Woods. A note on the numerical solution of fourth order differential equations. *Aero. Quart.*, 5:176–184, 1953.
- [138] S. Yokoya and A. Matsunawa. Surface tension driven flow in semicylindrical basin. *International Institute of Welding*, Doc 212-563-83, 1983.
- [139] T. Young. *Lecture notes on Natural Philosophy, Vol.2*. Johnson, London, 1807.
- [140] T. Zacharia, S.A. David, J.M. Vitek, and T. Debroy. Weld pool development during GTA and laser beam welding of type 304 stainless steel, I - theoretical analysis. *Welding J.*, 68:499s–509s, 1989.
- [141] T. Zacharia, S.A. David, J.M. Vitek, and T. Debroy. Weld pool development during GTA and laser beam welding of type 304 stainless steel, part II - experimental correlation. *Welding J.*, 68:510s–520s, 1989.